Title
The Molecular Architecture of Spore Morphogenesis in Bacillus subtilis

Permalink
https://escholarship.org/uc/item/53h0z2p0

Author
Khanna, Kanika

Publication Date
2020

Peer reviewed|Thesis/dissertation

UNIVERSITY OF CALIFORNIA SAN DIEGO

The Molecular Architecture of Spore Morphogenesis in *Bacillus subtilis*

A dissertation submitted in partial satisfaction of the requirements for

the degree Doctor of Philosophy

in

Biology

by

Kanika Khanna

Committee in charge:

Professor Elizabeth Villa, Chair
Professor Joe Pogliano, Co-chair
Professor Matthew Daugherty
Professor Arshad Desai
Professor Susan Golden
Professor Kit Pogliano

2020

The Dissertation of Kanika Khanna is approved, and it is acceptable in quality and form for publication on microfilm and electronically:

Co-chair

Chair

University of California San Diego

2020

DEDICATION

To my parents,

Ashwani Kumar Khanna & Deepa Khanna

EPIGRAPH

“*The word cryo has cry in it for a reason.*”

- Elizabeth Villa to me (Origin: Jaochim Frank?)

“It is very easy to answer many of these fundamental biological questions; you just look at the thing!”

- Richard Feynman

“*Science knows no country, because knowledge belongs to humanity, and is the torch which illuminates the world.*”

- Louis Pasteur

TABLE OF CONTENTS

LIST OF FIGURES

LIST OF TABLES

ACKNOWLEDGEMENTS

First and foremost, I would like to thank my three wonderful supervisors – Prof. Elizabeth Villa, Prof. (or now Dean!) Kit Pogliano and Prof. Joe Pogliano for taking me in their labs and providing me with such a collaborative atmosphere to do great science. Under their mentorship, I not only learnt how to do science but also learnt a great deal about leadership. Elizabeth is a force to be reckoned with, always full of energy and transmitting the vibes throughout the lab. She has stood by me in all the highs and lows and in times of difficult "political" situations (which unfortunately sometime develop in science) like a true mentor. I am forever indebted to her for that and for teaching me so many valuable things that I am sure I will cherish as I march ahead in my scientific journey. Kit, by far has been one of the most positive persons I have encountered in my life. She can get the most positive things to look out for in the most negative data ever that will force one to think tangentially about a scientific problem. I also got the opportunity to engage in one of the most creative projects in Joe's lab as a sidekick during my thesis which has made me so much more appreciative of the unseen living world around us. Although I technically joined Joe's lab at the end of my rotation, I ended up working with Kit and Elizabeth for my thesis project. As they say, it's all in the family! A big thanks to all my committee members, Susan, Arshad and Matt for valuable suggestions and guidance during the past few years.

I don't think I would have been able to accomplish whatever I have been able to if it was not for Javi (Kit's lab). He took me under his wing and guided me in all scientific aspects, be it bench work, writing a manuscript or presenting a story. It will not be wrong of me if I say he was my fourth advisor! I am so happy for all the future scientists he will create as a leader at Max Planck Institute of Evolutionary Biology. I just aspire I could be like this to someone else! I would also like to thank Reika (Villa lab) for being a great friend during this journey from the very start. Apart from teaching me microscopy during my initial days, we have shared some great time together and am very happy the way our friendship has matured in the last five years. Her inquisitive nature and “never-being-afraid-to-learn-something-new” attitude is an inspiration and I will definitely miss her being not around. I also had the opportunity to work with two undergraduates, Yuan (Annie) and Ziyi (Andy) and I couldn’t thank them enough for the countless hours they spent segmenting my data. I am super grateful to the computational wizard Sugie for all his helpful advice and lightspeed responses in data analysis.

There are many more lab members of the three labs am thankful for, past and present, who created a wonderful lab atmosphere: Vinson (for automating everything!), Alan (for telling me not to use red ice buckets for my PCR as it is bad luck and for all his other quirks), Mike (my first mentor in the Pogliano lab), Arthur & Katrina (leaders of the phage project), Eammon, Anne, Roland, Hannah, Mac, Sergey, Martina, Matt, Digvijay.

I also have a wonderful set of friends in San Diego to thank. They have been like a second family away from home: Sunandha, Annie, Neeraja, Siddhartha, Abhay, Sourish, Tapan, Vignesh, Nandu, Prit, Swetha and Raghu or our Dinner/hike/spam (now Dinner/hike/liquid nitrogen whatsapp group). Grad school is hard and these people made it so easy with their wonderful presence. I will miss celebrating all the Indian festivals, potlucks and music with you!

Last but not the least, my fiancé Aekaansh and my parents and brother! If it was not for you guys, I would have gone insane whenever the microscope broke down. Probably they knew it before the service engineers! They could sense from my voice whenever the microscope was broken and had all the comfort to offer in those gloomy days (or months!) of the year. They are my role models and I couldn’t have asked for a better support system.

Chapter 1, in part is currently being prepared for submission for publication of the material. The manuscript in preparation is: Khanna K, Lopez-Garrido J, and Pogliano K. ‘*Bacillus subtilis* spore morphogenesis’ (in preparation). The dissertation author is the primary author of the review article.

Chapter 2, in part is currently being prepared for submission for publication of the material. The manuscript in preparation is: Khanna K, Lopez-Garrido J, Sugie J, Pogliano K, and Villa E.

‘Asymmetric localization of the divisome during *Bacillus subtilis* sporulation’ (in preparation). The dissertation author is the primary author of this material and conducted all the experiments and analysis (with input from other authors).

Chapter 3, in full, is a reprint of the material as it appears in *Cell* 2018 (Vol. 172(4) pp 758-770. e14) and in the online supplement. The manuscript is: Lopez-Garrido J, Ojkic N, Khanna K, Wagner FR, Villa E, Endres RG, and Pogliano K. ‘Chromosome translocation inflates *Bacillus* forespores and impacts cellular morphology’. The dissertation author was the secondary author and contributed towards cryo-electron tomography experiments.

Chapter 4, in full, is a reprint of the material as it appears in *eLife* 2019 (8). The manuscript is: Khanna K, Lopez-Garrido J, Zhao Z, Watanabe R, Yuan Y, Sugie J, Pogliano K, and Villa E. ‘The molecular architecture of engulfment during *Bacillus subtilis* sporulation’. The dissertation author was the primary author of the manuscript and conducted all the experiments and analysis (with input from other authors).

VITA

EDUCATION

University of California, San Diego (UCSD) 2020
PhD, Biology

Marine Biology Laboratory, Woods Hole 2017
Physical Biology of the Cell course

Indian Institute of Technology, Delhi (IITD) 2014
Bachelor and Master of Technology,
Biochemical Engineering and Biotechnology

PUBLICATIONS

1. **Khanna, K.**, Lopez-Garrido, J., Zhao, Z., Watanabe, R., Yuan, Y., Sugie, J., Pogliano, K. & Villa, E. (2019). The molecular architecture of engulfment during Bacillus subtilis sporulation. *eLife*, 8, e45257.
2. Chaikeeratisak, V., **Khanna, K.**, Egan, M., Erb, M.L.,Vavilina, A., Nguyen, K.T., Nonejuie, P., Niew-glowska, E., Pogliano, K., Agard, D.A., Villa, E., & J. Pogliano. (2019). Viral Capsid Trafficking along Tubulin Filaments in Bacteria. *Cell*, 177(7), 1771-1780.
3. Lopez-Garrido, J., Ojkic, N., **Khanna, K.**, Wagner, F. R., Villa, E., Endres, R. G., & Pogliano, K. (2018). Chromosome Translocation Inflates Bacillus Forespores and Impacts Cellular Morphology. *Cell*, 172(4), 758-770.
4. Chaikeeratisak, V., Nguyen, K., **Khanna, K.**, Brilot, A. F., Erb, M. L., Coker, J. K., Vavilina, A., Newton, G.L., Buschauer, R., Pogliano, K., Villa, E., Agard, D.A., & Pogliano, J. (2017). Assembly of a nucleus-like structure during viral replication in bacteria. *Science*, 355(6321), 194197.
5. Erwin, G. S., Grieshop, M. P., Bhimsaria, D., Do, T. J., Rodrguez-Martnez, J. A., Mehta, C., **Khanna, K.**, Swanson, S.A., Stewart, R., Thomson, J.A., Ramanathan, P. & Ansari, A.Z. (2016). Synthetic genome readers target clustered binding sites across diverse chromatin states. *Proceedings of the National Academy of Sciences*, 113(47), E7418-E7427.
6. Roy, S., Dutta, S., **Khanna, K.**, Singla, S., & Sundar, D. (2012). Prediction of DNA-binding specificity in zinc finger proteins. *Journal of Biosciences*, 37(3), 483-491.

HONORS AND AWARDS

1. Goeddel Chancellor’s Award, UCSD	2018
2. Best Poster, Gordon Research Conference, Bacterial Cell Surfaces	2016
3. Bimla Jain Medal, IITD	2014
4. Ujjal Jeevan Charitable Trust Award, IITD	2014
5. Khorana Program for Scholars Award, IUSSTF	2013
6. Kalpana Chawla Award, IITD	2013
7. Gem of Kailash (for hostel activities), IITD	2013
8. Summer Undergraduate Research Award, IITD	2012
9. Semester Merit Award, IITD	2011-2013

CONFERENCE PRESENTATIONS AND SEMINARS

(Invited and Contributed Talks)

1. The BPS Annual Meeting, California	2020
2. Young Microbiologists Symposium, John Innes Center, UK	2019
3. Mesa Cryo-EM Seminar, Salk Institute for Biological Studies	2019
4. 20th International Conference on Bacilli and Gram-Positive Bacteria, Washington DC	2019
5. Southern California Cryo-EM Symposium, California	2018
6. UCSD-Salk Retreat, California	2018
7. National Center for Biological Sciences, India	2018
8. Keystone Symposia, Cryo-EM from cells to molecules, California	2018
9. Da Vinci Convergent Science Symposium, California	2017
10. Indian Institute of Technology, Delhi, India	2016

LEADERSHIP ROLES AND OUTREACH

1. Founding Member & Secretary, BPS San Diego student chapter 2019-20
2. Chapter Coordinator & Project Coordinator 2017-19
   Asha for Education, San Diego Chapter
   (a non-profit for education of underprivileged kids in India)
3. President, Association of Indian Graduate Students, UCSD 2016-17
4. Seminar Organizer, UCSD Joint Cryo-EM meetings 2016-19
5. Seminar Organizer, Graduate student seminars in Microbiology. 2016-17
6. Teaching Assistant, UCSD: Microbiology (Fall 2017), Nutrition (Spring 2017), Phage Genomics Research Laboratory (Fall 2015)
7. Mentored 2 underrepresented high school students 2016
   ENLACE program, UCSD
8. Invited blog posts:
   a. The Microbial Menagerie – Donating your poop for science (2018)
   b. Small Things Considered – Opening Windows into the Cell (2016), A class asks questions…(2015), A Talmudic Conversation (2015)

ABSTRACT OF THE DISSERTATION

The Molecular Architecture of Spore Morphogenesis in *Bacillus subtilis*

by

Kanika Khanna

Doctor of Philosophy in Biology

University of California San Diego, 2020

Professor Elizabeth Villa, Chair
Professor Joe Pogliano, Co-chair

Many cellular processes in bacteria transpire at a scale of ~1-2 μm that are difficult to study by optical microscopy alone due to limitations imposed by diffraction properties of light. Hence, visualization of cellular structures at a high spatial resolution in the native cellular milieu in bacteria is a poorly explored field. My thesis aims to study the process of sporulation in a Gram-positive bacterium, *Bacillus subtilis*. During conditions of nutrient deprivation, *B. subtills* undergoes a developmental pathway that culminates in the production of two cells with different sizes and fates, the smaller forespore and the larger mother cell. I have studied different stages of sporulation in *B. subtilis* using novel modalities in the field of cryo-electron microscopy, namely cryo-focused ion beam milling coupled with cryo-electron tomography (or cryo-FIB-ET). Cryo-FIB-ET allows visualization of macromolecules inside the cell at a resolution of a few nanometers. Using this technique, I have elucidated important principles governing the following processes during sporulation:

(1) Polar cell division: We demonstrate that FtsAZ filaments, the major orchestrator of cell division in bacteria are localized uniformly around the leading edge of the invaginating septum during vegetative growth but present only on the mother cell side during sporulation, a process mediated by a sporulation-specific protein, SpoIIE. This asymmetry in divisome localization during sporulation dictates not only the septal thickness but also the diverse fate of the two daughter cells.

(2) Engulfment: We study the role of cell wall remodeling and chromosome translocation during engulfment. We show that the mother cell membrane migrates in finger-like projections around the forespore due to uneven cell wall degradation. We also show that the turgor pressure generated by the forespore chromosome inflates the forespore and helps it maintain its well-rounded shape. These studies have thrown light on spatiotemporal regulation of important complexes dictate architectural transformations during engulfment.

Overall, our studies have added more cases to support the observation that several complex traits to regulate critical cellular processes like division, cell migration, DNA dynamics, cell shape etc. that were previously thought to be a characteristic of only eukaryotes are also

present in prokaryotes and that cryo-FIB-ET will likely be the tool of the future to probe these and other processes at a molecular detail.

Chapter 1: Introduction

1.1 Summary

Bacillus subtilis, a Gram-positive bacterium undergoes the developmental pathway of sporulation under starvation conditions that culminates in the production of dormant and hardy endospores. Upon initiation of sporulation, the division site shifts from medial to polar site to give rise to cell types with unequal sizes and fates, the smaller forespore that is subsequently engulfed by the larger mother cell. Following engulfment, the forespore matures by developing protective coat and cortex layers and the mother cell eventually lyses. The endospores have the ability to germinate upon availability of nutrients and reinitiate the process of medial cell division. Although a lot of work has been to elucidate the genetic and biochemical basis of gene regulation during sporulation, little is known about the molecular players that mediate the architectural transformation of the forespore to a mature spore. My thesis aims to elaborate the role of key players that mediate the process of engulfment of the forespore by the mother cell, including those involved in cell division, cell wall remodeling and chromosome translocation from the mother cell to the forespore using novel techniques in the field of cryo-electron microscopy.

1.2 Introduction

The advent of electron microscopy (EM) in the 1940s propelled the field of cell biology, leading to the discovery of many eukaryotic organelles. At the same time, bacteria were considered “sac of enzymes” with random distribution of DNA and proteins. The early days of EM revealed the presence of a lipid bilayer in the cell envelope, external surface layers and appendages in bacteria (Beveridge, 1999; Beveridge and Graham, 1991; Jonson et al., 2005; Lawn, 1967; THORNLEY and HORNE, 1962). In the 1990s, application of green fluorescent protein (GFP) ushered in a new era of bacterial cell biology when it became largely recognized that bacteria are highly organized and display more similarities to eukaryotes than previously thought, for instance, directed protein movement and spatial localization, chromosome segregation and cell-cell interaction (Fu et al., 2001; Jones et al., 2001; Rudner and Losick, 2010; Southward and Surette, 2002; Visick and Fuqua, 2005; Webb et al., 1998).

However, the above techniques alone are unable to provide a complete picture of the biological phenomenon at the molecular scale. Fluorescence microscopy (FM) suffers from the drawback that complexes that lie closer than 200 nm cannot be resolved spatially owing to the diffraction properties of light (Abbe, 1873). Since the mid 2000s, technical innovations in the field have pushed this limit to ~20 nm, commencing the generation of super-resolution microscopy techniques (Baddeley and Bewersdorf, 2018). On the other hand, methods employed for “traditional” EM relied on plastic embedding, heavy staining, dehydration and chemical fixation of biological specimens (Winey et al., 2014). Such harsh treatments can affect the integrity of the sample and/or introduce artifacts in imaging. Hence, important biological context is often missing or misrepresented.

Recent technological and image processing advances place cryo-electron microscopy (cryo-EM) methods in a unique position to image cells in a frozen-hydrated state that reveals the structure and organization of macromolecules in their native cellular context (Bai et al., 2015; Milne and Subramaniam, 2009). Specifically, cryo-electron tomography (cryo-ET) provides three-dimensional (3D) views of thin biological specimens at a high resolution of a few nanometers (~ 4 nm) (Baumeister, 2002; Briggs, 2013; Milne and Subramaniam, 2009). This method is specifically crucial to decode the cellular biology of tiny bacteria as many bacterial cellular processes transpire at a scale of <1-2 μm that are difficult to resolve at a high spatial resolution using light microscopy alone. Hence, cryo-ET has the potential to become the method of choice for bacterial cell biology. Not only does it have the potential to solve structures inside the cell but also to reveal qualitative as well as quantitative aspects of spatial and temporal regulation of bacterial cellular processes by providing contextual information about the macromolecule being investigated. These studies are particularly relevant today in an era of increasing antibiotic resistance and to understand how bacteria interact with their hosts to influence their health.

My thesis aims to elaborate studies of cellular processes in bacteria that have benefitted by the application of cryo-electron tomography (cryo-ET) in complementation with FM, genetics, biochemical techniques and biophysical modeling to provide a comprehensive understanding of cellular processes during sporulation in *B. subtilis*. Certain Gram-positive bacteria belonging to the genera *Bacilli* and *Clostridia* have the ability to produce metabolically dormant cells called spores under conditions of nutrient deprivation. This process of sporulation leads to profound changes in the cellular architecture from two cells that lie side by side to a cell within a cell. Most of our current understanding of the mechanistic basis of cellular differentiation during sporulation stems from studies conducted in the model bacterium *Bacillus subtilis* (Higgins and Dworkin, 2012; Tan and Ramamurthi, 2014). The first key morphological event is the shift in the division site from medial to polar position that leads to the formation of two daughter cells of unequal sizes: the smaller cell called the forespore and the larger cell called the mother cell. The forespore is then encased inside the mother cell in a process known as engulfment which is the hallmark of endospore formation and the only example to date of phagocytosis performed by a bacterial cell. Later, the mother cell lyses and the spore, protected by cortex and coat gains resistance to any environmental assaults including radiation damage, antibiotics, desiccation etc.

These spores can remain dormant for years but have the ability to germinate into vegetative cells when subjected to nutrient-rich conditions.

The entire process of sporulation involves a complex interplay among distinct molecular mechanisms, including cell-specific gene expression, remodeling of cellular envelope, chromosome dynamics and protein localization, leading to transformation of the cellular landscape. In this review, we will focus on specific steps involved in the architectural transformation of a vegetative cell to a spore with a specific focus on engulfment and describe the key experimental approaches that have proven valuable in these studies. Considering the scope of this article, we refer the readers to other comprehensive reviews discussing sporulation gene regulation (Higgins and Dworkin, 2012; Hoch, 2017; Lopez et al., 2009; Piggot and Hilbert, 2004), asymmetric cell division event (Barák et al., 2019), assembly of cortex, coat and surface layers during later stages of spore formation (A. Driks, 2002; Adam Driks, 2002; Henriques and Moran, Jr., 2007; Mckenney et al., 2013; "The Spore Coat," 2016) and spore germination (Setlow, 2014; Setlow et al., 2017).

1.3 Chromosome dynamics

At the onset of sporulation in *B. subtilis,* the replicated chromosomes (~4.2 Mbp each) are remodeled into an elongated axial filament with origins of replication anchored to the cell poles and termini at the mid cell (Kay and Warren, 1968; Pogliano et al., 2002; Ryter, 1965). This results in uneven distribution of the forespore chromosome upon formation of the polar septum such that only one-third of the origin-proximal part of the chromosome is present in the forespore (Wu and Errington, 1998, 1994). A DNA translocase called SpoIIIE then actively transports the remaining two-thirds of the forespore chromosome from the mother cell into the forespore (Bath et al., 2000; Massey et al., 2006; Wu and Errington, 1997). The N-terminal membrane-spanning domain of SpoIIIE anchors SpoIIIE to the septal membrane while the cytoplasmic C-terminal domain with ATPase activity serves to translocate ~3 Mbp of DNA in ~15 minutes (Bath et al., 2000; Burton et al., 2007; Ptacin et al., 2008). Structural studies suggest that SpoIIIE belongs to FtsK family of translocases which crystallize as a hexameric ring with a ~3 nm central channel that can accommodate only one dsDNA and not the proteins bound to DNA (Aussel et al., 2002; Donachie, 2002; Errington et al., 2001; Yu et al., 1998). Marquis et al. later demonstrated that SpoIIIE can strip off DNA-binding proteins during translocation such that it delivers mostly naked DNA into the forespore compartment (Marquis et al., 2008). The authors argue that this may be a critical step in regulating compartment-specific gene expression by restricting transcription factors in the mother cell from entering into the forespore during DNA translocation (Marquis et al., 2008).

How does SpoIIIE assemble at the septum to translocate DNA? One of the models proposes the formation of an aqueous DNA-conducting pore via interactions between the divisome and membrane-spanning domain of SpoIIIE before the polar septum is completely formed (Fiche et al., 2013; Wu and Errington, 1997). Another model proposes that SpoIIIE can form paired channels that traverses the two opposing forespore and mother cell membranes (Burton et al., 2007; Fleming et al., 2010; Liu et al., 2006). Recently, Shin et al. showed using quantitative PALM experiments that SpoIIIE forms at least two subcomplexes each in the forespore and the mother cell with approximately equal number of molecules on each side (Shin et al., 2015). These results provide credence to the latter model in which both the arms of the chromosome are transported simultaneously across two lipid bilayers by coaxially paired channels formed by SpoIIIE molecules rather than being translocated through an aqueous pore. However, in normal conditions DNA is transported strictly in one direction, from the mother cell to the forespore. The observation that SpoIIIE can transport DNA out of the forespore when expressed only in the forespore led to the conclusion that SpoIIIE can be active in any of the compartments (Shin et al., 2015). Further studies identified that the γ domain of the C-terminus of SpoIIIE specifically recognizes certain polarized octamer sequences (GAGAAGGG) in *B. subtilis* chromosome, termed SpoIIIE recognition sequences (or SRS for short) which help establish active translocase complexes only in the mother cell to pump the DNA into the forespore

(Ptacin et al., 2008). In a mutant lacking the γ domain, SpoIIIE could pump the DNA in either direction, both into and out of the forespore (Ptacin et al., 2008).

More recently, Lopez-Garrido et al demonstrated that SpoIIIE-mediated chromosome translocation also plays a pivotal role in reshaping the forespore during engulfment (Lopez-Garrido et al., 2018). Using a combination of genetics, biophysical modeling and high-resolution imaging we showed that chromosome translocation is essential to sustain the growth in the forespore (Lopez-Garrido et al., 2018). Interestingly, forespore growth is not dependent on expression of genes that are initially excluded from the forespore when the forespore chromosome is interrupted by the polar septum. Rather, packing the ~4.2 Mbp long, negatively charged DNA into the small volume of the forespore generates an increased osmotic pressure in the forespore relative to the mother cell (Δp = ~ 20-80 kPa), mainly by sequestering water and counterions that swell the forespore chromosome. This increased osmotic pressure leads to stretching of the septal PG, allowing the newly synthesized membrane to adopt an optimal conformation as it encloses and reshapes the forespore because in the absence of this differential pressure, excess membrane accumulated at the mother cell distal tip or elsewhere in the forespore in SpoIIIE^{ATP-} sporangia (Lopez-Garrido et al., 2018). Together, this study provided the first evidence for an architectural role of DNA in mediating the transformation of the forespore from a hemisphere at polar septation to an ovoid at the completion of engulfment.

1.4. Engulfment

1.4.1 Cell wall remodeling

Genetic studies of sporulation resulted in the identification of three proteins that are essential for engulfment: SpoIID, SpoIIM and SpoIIP (henceforth referred to as D, M and P for simplicity) that are conserved across all endospore-forming bacteria (Frandsen and Stragier, 1995; Lopez-Diaz et al., 1986; Smith et al., 1993). Strains mutant in D, P or M revealed a characteristic “bulge” phenotype wherein the forespore appeared to push into the mother cell through the middle of the septum. All the three genes are under the control of σ^E regulon and are expressed only in the mother cell and together they form a complex SpoIIDMP (or DMP) which has PG degradation capability (Abanes-De Mello et al., 2002; Aung et al., 2007; Chastanet and Losick, 2007; Morlot et al., 2010).

D and P are single pass transmembrane proteins with a hydrophobic N-terminal for membrane anchoring and large extracellular domains with PG hydrolyzing activities (Abanes-De Mello et al., 2002; Aung et al., 2007; Chastanet and Losick, 2007; Frandsen and Stragier, 1995; Holland et al., 1987; Lopez-Diaz et al., 1986; Morlot et al., 2010). The amino acid sequence of D displays homology to LytB, another *B. subtilis* protein that regulates the activity of a major vegetative cell wall hydrolase with amidase activity (Blackman et al., 1998; Kuroda et al., 1992; Lopez-Diaz et al., 1986). Later biochemical studies demonstrated that D belonged to the family of lytic transglycosylases that degraded glycan strands of PG into disaccharide units (Abanes-De Mello et al., 2002; Morlot et al., 2010). P shares weak sequence homology to amidases belonging to LytC family and in vitro experiments suggested that P had both amidase and endopeptidase activities (Chastanet and Losick, 2007; Morlot et al., 2010). Hence, P can remove both stem peptides from PG as well as cleave cross-links between them. Morlot et al. further showed that D can cleave glycan strands only after the removal of stem peptides by P (termed as “denuded” glycan strands) and that D enhances the enzymatic activity of P (Morlot et al., 2010). So far, the amino acid sequence of M does not show homology to any known sequences in the database. Although its function is still unclear, M with its predicted five transmembrane segments, was found to serve as a scaffold for the assembly of the DMP complex (Aung et al., 2007; Chastanet and Losick, 2007). Together, these studies demonstrated that DMP was a highly concerted and processive PG degradation complex with D and P having complementary and sequential PG hydrolyzing activities and M serving as an anchor protein (Abanes-De Mello et al., 2002; Aung et al., 2007; Chastanet and Losick, 2007; Morlot et al., 2010).

Green fluorescent protein (GFP) fusions of D, M and P showed that all three proteins initially localized at the middle of the polar septum and were subsequently enriched at the leading edge of the engulfing mother cell membrane and remained there till the completion of engulfment (Abanes-De Mello et al., 2002). Further studies suggested that the assembly of DMP at the septal membrane follows a hierarchical pattern: M followed by P, followed by D (Aung et al., 2007; Chastanet and Losick, 2007). Simultaneously, these studies also established the role of SpoIIB (or B), another sporulation-specific protein during engulfment (Aung et al., 2007; Chastanet and Losick, 2007; Margolis et al., 1993; Perez et al., 2000). These studies showed that B served as a signal to recruit M to the septal membrane which then subsequently localized P and D to form the DMP complex (Aung et al., 2007; Chastanet and Losick, 2007). B localizes in a manner similar to DMP, moving around the forespore at the leading edge of the engulfing membrane. In the absence of B, cells were still able to complete engulfment, but more slowly as compared to wild type via an independent pathway dependent on the Q-AH zipper (discussed in section 1.3.2) to recruit DMP to the septum (Aung et al., 2007; Perez et al., 2000).

In order for the engulfing mother cell membrane to migrate around the forespore, it must overcome the steric block posed by the septal PG. Combined with earlier EM studies of thin sections of *B. subtilis* showing that engulfment-defective mutants had thicker septa than wild type sporangia, it was thought that DMP was required for the complete dissolution of the septal PG so that the mother cell membrane could migrate around the forespore (Chastanet and Losick, 2007; Illing and Errington, 1991a; Perez et al., 2000). This process, often referred to as “septal thinning” was backed up by the robust PG hydrolyzing activities of D and P (Abanes-De Mello et al., 2002; Aung et al., 2007; Chastanet and Losick, 2007; Morlot et al., 2010). However, visualization of the septum using recent high-resolution imaging technique of cryo-electron tomography (cryo-ET) (Khanna et al., 2019; Lopez-Garrido et al., 2018; Tocheva et al., 2013) challenged this idea by revealing the presence of a thin layer of peptidoglycan between the forespore and the mother cell membranes during all stages of engulfment, as opposed to the previous idea that the septum was devoid of any PG, that was highly likely a result of fixed EM sample preparation techniques. Our cryo-ET data suggested that the septa were only uniformly and slightly thinned during the morphological change from flat to curved septa which could in part be regulated by the osmotic pressure generated in the forespore by SpoIIIE-mediated chromosome translocation (Khanna et al., 2019; Lopez-Garrido et al., 2018). Instead, DMP seemed to relocalize PG synthases from the middle of the septum to the leading edges during engulfment, since in the absence of DMP, the septum was considerably thicker than wild type and several penicillin-binding proteins (PBPs) retained their localization within the septum (Khanna et al., 2019).

Meyer et al. and Ojkic et al. further showed that PG synthesis is essential for engulfment as when sporulating cells are treated with antibiotics that block PG synthesis, DMP is mislocalized and leading edge of the mother cell membrane does not migrate forward (Meyer et al., 2010; Ojkic et al., 2016). Majority of PG synthases including endopeptidases, carboxipeptidases, transpeptidases and MreB paralogues tracked the leading edge of the engulfing membrane when produced exclusively in the forespore (Ojkic et al., 2016). Together, these findings suggested that PG synthesis happens ahead of the leading edge of the migrating mother cell membrane and precedes PG degradation by mother-cell specific DMP. Biophysical modeling proposed a “make-before-break” model wherein coordination between PG insertion from the forespore and PG removal by DMP in the mother cell could move the junction between the septal PG and the lateral PG around the forespore by making room for the migrating mother cell membrane (Ojkic et al., 2016). This simple model proposes that cell wall remodeling during engulfment relies on entropic forces contributed by bond hydrolysis during PG synthesis and degradation rather than pulling or pushing forces for membrane migration. High-resolution cryo-ET images also showed that the mother cell membrane migrates around the forespore in tiny finger-like projections which are formed due to uneven degradation of PG ahead of the engulfing membrane by limited number of DMP complexes (Khanna et al., 2019). Hence, cell wall remodeling is a critical driver of engulfment which is mediated by coordinating the activities of proteins involved in degradation and synthesis of PG in space and time.

1.4.2 SpoIIQ-IIIA

The second set of proteins that play an important role in engulfment and spore formation consists of SpoIIQ (or Q), a protein encoded by the forespore and SpoIIIAA-AH (or AA-AH or A to include all 8 proteins), a set of eight proteins encoded by *spoIIIA* operon in the mother cell (Illing and Errington, 1991b; Kellner et al., 1996; Londoño-Vallejo et al., 1997). These proteins are conserved in all endospore-forming bacteria (Morlot and Rodrigues, 2018; Stragier, 2014). Q is an integral membrane protein with homology to *Staphylococcus aureus* LytM, a metalloendopeptidase but it has a degenerate active site and lacks a critical histidine residue to bind Zn^{2+} required for its endopeptidase activity (V. M. Levdikov et al., 2012; Meisner et al., 2012; Meisner and Moran, 2011). Many proteins encoded by the *spoIIIA* operon display sequence and structural similarity to different components of bacterial secretion systems (specifically type II, III and IV or TnSS where n=2,3,4) found in Gram-negative bacteria that are involved in the transport of various substrates including DNA, protein and metabolites across bacterial cell envelope, with AF-AH being homologous to ring-building motifs (RBM) and AA to ATPases of bacterial secretion system (Blaylock et al., 2004; Camp and Losick, 2008; Doan et al., 2009; Johnson et al., 2006; V. M. Levdikov et al., 2012; Meisner et al., 2012, 2008; Rodrigues et al., 2016a; Zeytuni et al., 2017a).

Both Q and A are necessary for the activation of the late forespore transcription factor, σ^G and in the absence of any of these proteins, the forespores collapse with severe membrane deformities (Blaylock et al., 2004; Broder and Pogliano, 2006; Londoño-Vallejo et al., 1997; Rubio and Pogliano, 2004; Sun et al., 2000). Although both Q and A are essential for spore production, they are essential for engulfment only under certain conditions. When sporulation is induced by resuspension in null mutant of *spoIIQ* or *spoIIIAH*, cells are still able to complete engulfment but the speed with which the mother cell membrane migrates around the forespore decreases compared to wild type (Sun et al., 2000). However, when sporulation is induced by nutrient exhaustion, the null mutants fail to complete engulfment and eventually lyse (Londoño-Vallejo et al., 1997; Sun et al., 2000). The function of Q-A is short-lived and at the completion of engulfment, Q-A is quickly degraded by SpoIVB serine protease produced in the forespore upon σ^G activation (Chiba et al., 2007; Jiang et al., 2005).

Early studies demonstrated that Q initially localizes to the septum and then spreads throughout the forespore membrane, displaying membrane-localized punctate pattern near the completion of engulfment (Londoño-Vallejo et al., 1997; Rubio and Pogliano, 2004). It has been proposed that a zipper-like interaction between the extracellular domains of Q in the forespore and AH in the mother cell across the septum help immobilize both the proteins in the septal membrane (Blaylock et al., 2004). Further protein localization and biochemical studies demonstrated that AH localizes in a similar manner as Q and that its localization is dependent on Q (Blaylock et al., 2004). The Q-AH complex can also provide an alternate route for engulfment completion under certain conditions. In the absence of SpoIIB (or B), Q-AH becomes essential for engulfment as it targets DMP to the septum via SpoIVFAB, a mother cell protein complex that is recruited to the membrane by AH (Aung et al., 2007; Jiang et al., 2005). In the absence of both B and SpoIVFAB, membrane migration is completely blocked (Aung et al., 2007). The Q-AH ratchet is also essential for engulfment in strains with reduced DMP activity and in cells wherein the peptidoglycan cell wall has been enzymatically removed to produce nascent protoplasts (Broder and Pogliano, 2006; Ojkic et al., 2014). Surprisingly, engulfment in protoplasts proceeds rapidly in ~5-20 min compared to ~45 minute in wild type and DMP is not essential for this process (Ojkic et al., 2014). Photobleaching analysis also demonstrated that SpoIIQ is stationary during engulfment and resists backward movement of the engulfing mother cell membrane. These studies provided evidence for a ratchet-like mechanism of operation of Q-AH complex that renders forward membrane movement irreversible (Broder and Pogliano, 2006).

More recent studies have suggested that Q-A could have evolved as a specialized bacterial secretion system. Using a compartmentalized biotinylation assay, Meisner et al. showed that Q and AH formed a “conduit” between the mother cell and the forespore which is open on the forespore side and gated on the mother cell side and could play an important role in mother cell-forespore communication (Meisner et al., 2008). Although the exact nature of substrate(s), if any, transported by the Q-A channel remains unknown, a working model has been proposed wherein the channel acts as a “feeding tube” that supports the forespore development through substrates provided by the mother cell (Camp and Losick, 2009; Serrano et al., 2016). In support of this, the Q-A complex mutants have a collapsed forespore and are unable to support any transcription in the forespore which may suggest possible translocation of small molecules or ions from the mother cell into the forespore that may be necessary to maintain the physiology and structural integrity of the forespore (Doan et al., 2009). These studies also provided evidence that Q and AH seem to comprise the platform of the channel onto which other proteins of the *spoIIIA* operon are thought to assemble although we do not fully understand the specific contribution of these proteins in structural determination or regulation of the channel assembly.

Recent structural studies have provided credence to the theory that the Q-A complex resembles specialized bacterial secretion systems. A ~3.5 Å resolution structure of SpoIIIAG was determined using single particle cryo-EM demonstrating that it oligomerized as a 30-mer symmetric complex resembling a “cup-and-saucer” architecture with an inner vertical β-barrel, a middle planar β-ring and an outer ring formed by repeats of a ring-building motif (RBM) with architectural similarity to bacterial T2SS and T3SS (Rodrigues et al., 2016a; Zeytuni et al., 2017b). The diameter of the hollow inner ring formed by the β-barrel corresponding to the channel diameter is ~7.5 nm. The crystal structure of three other proteins of the *spoIIIA* operon, namely, SpoIIIAB, SpoIIIAF and SpoIIIAH also demonstrated the presence of the conserved RBM of bacterial secretion systems (Vladimir M. Levdikov et al., 2012; Meisner et al., 2012; Zeytuni et al., 2018a, 2018b). Of note, the C-terminal extracellular domain of AH, which is thought to form the channel with Q displays homology to YscJ/FliF family of proteins that form inner-membrane rings in T3SS and flagellar basal body. Although the crystallized form of AH does not oligomerize in solution, its homology to RBM from T3SS prompted two independent *ab initio* ring modeling of the Q-A complex suggesting either 12-, 15- or 18-mer ring model with inner ring diameters of 6, 8 or 11 nm respectively (Vladimir M. Levdikov et al., 2012; Meisner et al., 2012). More recently, a new protein GerM was shown to have a potential role in the assembly of the Q-A complex by recruiting Q the septal membrane on the forespore side (Rodrigues et al., 2016b). GerM is produced in the mother cell by σ^E activation and its null mutant displays a similar phenotype to that of Q and A and is defective in spore formation. Future structural studies to elucidate the role of other scaffolding proteins and interactions that regulate the unidirectional transport of substrates from the mother cell to the forespore will shed light on how intracellular communication is mediated by this novel type of bacterial translocation machinery.

1.4.3 Membrane remodeling

While PG remodeling is essential to initiate the process of engulfment of the forespore, membrane remodeling becomes essential during later stages to complete engulfment by releasing the forespore into the mother cell cytoplasm. This process involves membrane fusion as well as membrane fission at the forespore tip which are topologically unique events. Recently, Doan et al identified a bitopic mother cell membrane protein, FisB (for fission protein B) that mediated membrane fission at the forespore tip during the last step of engulfment (Doan et al., 2013). The mother cell membrane migrated around the forespore similar to wild type in FisB mutant sporangia but membrane fission and hence, sporulation efficiency was severely impaired in this strain. FisB localized to the cell pole (on the side of the forespore away from the mother cell) as mobile oligomers in the mother cell membrane. Biochemical studies provided evidence for specific interaction between the extracellular domain of FisB and cardiolipin, a negatively charged lipid enriched in bacterial membranes with concave curvature (Doan et al., 2013;

Mileykovskaya and Dowhan, 2009). Based on these results, the authors proposed a model wherein FisB interacted with cardiolipin at the leading edge of the engulfing membrane, leading to membrane disruption and scission to pinch off the forespore into the mother cell cytoplasm as a double membrane bound entity (Doan et al., 2013). However, the observation that few cells devoid of FisB were still able to complete engulfment and membrane fission, albeit slowly, suggests that there might be additional mechanisms for membrane fission during sporulation (Doan et al., 2013).

1.5 Spore Morphogenesis in *Clostridium difficile*

Most of the work done so far to understand bacterial sporulation has been conducted in *B. subtilis* due to its genetic tractability while many other spore-formers have remained notoriously difficult to manipulate genetically. However, recent advances in *C. difficile* genetics have thrown light on the sporulation pathway in the clinically relevant nosocomial pathogen, highlighting similarities with and divergences from *B. subtilis.* In this section, we will explore some of these in the context of the sections discussed above to broaden the readers' perspective on bacterial spore morphogenesis. To understand the architecture of the regulatory network controlling *C. difficile* sporulation, we refer the readers to recent reviews (Fimlaid and Shen, 2015; Saujet et al., 2014; Zhu et al., 2018). We have used the subscript *bs* for genes/proteins in *B. subtilis* and *cs* for those in *C. difficile* in the subsequent text.

The essential PG degradation machinery consisting of D, P and M seems to be conserved across all spore-formers in sequence but not necessarily in function (Abecasis et al., 2013; Galperin et al., 2012; Ribis et al., 2018). Recently, Ribis et al demonstrated that P_{cd} was produced under the control of forespore-specific σ^F regulon, M_{cd} was produced at the onset of sporulation under the control of Spo0A and D_{cd} was produced from the mother cell-specific σ^E regulon (Ribis et al., 2018). In contrast, D_{bs}, P_{bs} and M_{bs} are all produced from the mother cell-specific σ^E regulon (Driks and Losick, 1991; Frandsen and Stragier, 1995; Rong et al., 1986; Smith et al., 1993).

These findings suggest different compartmentalization and possibly functional regulation of the DMP complex in *C. difficile*. Also, D_{cd} can degrade glycan strands with peptide chains in vitro in contrast to D_{bs} that strictly degrades only denuded glycan strands (Nocadello et al., 2016). Recent work also showed that only P_{cd} and D_{cd} are essential for engulfment and not M_{cd} (Dembek et al., 2018; Ribis et al., 2018). Null mutants of D_{cd} and P_{cd} were still arrested at early stages of engulfment, although interestingly, they did not display the characteristic bulging phenotype associated with mutations in DMP_{bs} in *B. subtilis* (Abanes-De Mello et al., 2002; Eichenberger et al., 2001; Frandsen and Stragier, 1995; Pogliano et al., 1999; Smith et al., 1993). Rather, the septa remained either completely flat or curved partially into the mother cell similar to wild type (Dembek et al., 2018). Biochemical evidence also suggests that P_{cd} and M_{cd} have a weak interaction as opposed to *B. subtilis* where M_{bs} recruits P_{bs}, suggesting that either M_{cd} is not essential to assemble the DMP_{cd} PG degradation complex or there might be another, as yet unidentified mechanism for proper organization of DMP_{cd}. One explanation could be that D_{cd} and P_{cd} anchored in the mother cell and forespore membranes respectively, might interact more efficiently directly across the septum like the Q-A complex in *B. subtilis* rendering M_{cd} redundant (Dembek et al., 2018; Morlot and Rodrigues, 2018). Another interesting distinction is that SpoIIB and SpoIVFA are only present in *Bacilli* and not in *Clostridia* suggesting that either the localization of DMP to the septum in *C. difficile* depends entirely on Q-AH or there is another mechanism to recruit DMP to the septum that is not dependent on B (Galperin et al., 2012).

The genes encoding the Q-A channels are conserved across all spore-forming bacteria, although they seem to play slightly distinct roles in *B. subtilis* and *C. difficile*. Both Q_{cd} and Q_{bs} have LytM zinc-binding endopeptidase domains but Q_{bs} has a non-functional active site that cannot bind Zn^{2+} in contrast to that of *C. difficile* and hence it was implicated that Q may play a direct role in PG hydrolysis during engulfment (Crawshaw et al., 2014; Meisner and Moran, 2011). However, strains with a mutation of this active site showed only minor defects in engulfment and sporulation suggesting that the endopeptidase activity may not be a critical factor for sporulation

(Crawshaw et al., 2014; Fimlaid et al., 2015; Serrano et al., 2016). Rather, there is some biochemical evidence that the active catalytic site may play a role in interacting with AH and stabilizing the complex although more structural evidence is needed to support this observation (Serrano et al., 2016). Q_{cd} and AH_{cd} are also necessary for spore production and completion of engulfment. Surprisingly, the mutant strains formed bulges and vesicles during engulfment that are reminiscent of the DMP mutant sporangia in *B. subtilis* (Fimlaid et al., 2015; Morlot and Rodrigues, 2018; Serrano et al., 2016). More specifically, loss of $AA\text{-}AF_{cd}$ can still support engulfment in 10-20% of cells but the loss of AH_{cd} or Q_{cd} has a severe defect in engulfment. Similar to *B. subtilis*, the Q_{cd} and AH_{cd} mutants are impaired in σ^G activity in the forespore and σ^K in the mother cell that may suggest a halt in metabolic cooperation between the two cells due to a defect in the assembly of the Q-A channel (Serrano et al., 2016). Q_{cd} and AH_{cd} interact both in vitro and in vivo and appear to first localize to the septum, form discrete foci during engulfment and remain associated upon completion of engulfment. Both are largely co-dependent for localization to the septal membrane but some AH_{cd} can still localize to the septum in absence of Q_{cd} (Serrano et al., 2016). This is in contrast to *B. subtilis* where the localization of AH_{bs} depends on Q_{bs} but not vice versa (Broder and Pogliano, 2006). Also, unlike *B. subtilis*, the localization of Q_{cd} or AH_{cd} was not affected in sporangia lacking either D_{cd}, M_{cd} or P_{cd} although more conclusive experiments are needed to establish the direct contribution of the Q-AH channel to engulfment and its interaction with other players in the process (Serrano et al., 2016).

1.6 References

Abanes-De Mello A, Sun YL, Aung S, Pogliano K. 2002. A cytoskeleton-like role for the bacterial cell wall during engulfment of the Bacillus subtilis forespore. *Genes Dev* **16**:3253–3264. doi:10.1101/gad.1039902

Abecasis AB, Serrano M, Alves R, Quintais L, Pereira-Leal JB, Henriques AO. 2013. A genomic signature and the identification of new sporulation genes. *J Bacteriol*. doi:10.1128/JB.02110-12

Aung S, Shum J, Mello AA-D, Broder DH, Fredlund-Gutierrez J, Chiba S, Pogliano K. 2007. Dual localization pathways for the engulfment proteins during Bacillus subtilis sporulation. *Mol Microbiol* **65**:1534–1546. doi:10.1111/j.1365-2958.2007.05887.x

Aussel L, Barre FX, Aroyo M, Stasiak A, Stasiak AZ, Sherratt D. 2002. FtsK is a DNA motor protein that activates chromosome dimer resolution by switching the catalytic state of the XerC and XerD recombinases. *Cell*. doi:10.1016/S0092-8674(02)00624-4

Barák I, Muchová K, Labajová N. 2019. Asymmetric cell division during Bacillus subtilis sporulation. *Future Microbiol* **14**:353–363.

Bath J, Ling Juan Wu, Errington J, Wang JC. 2000. Role of Bacillus subtilis SpoIIIE in DNA transport across the mother cell-prespore division septum. *Science (80-)* **290**:995–997. doi:10.1126/science.290.5493.995

Blackman SA, Smith TJ, Foster SJ. 1998. The role of autolysins during vegetative growth of Bacillus subtilis 168. *Microbiology*. doi:10.1099/00221287-144-1-73

Blaylock B, Jiang X, Rubio A, Moran CP, Pogliano K. 2004. Zipper-like interaction between proteins in adjacent daughter cells mediates protein localization. *Genes Dev* **18**:2916–2928. doi:10.1101/gad.1252704

Broder DH, Pogliano K. 2006. Forespore engulfment mediated by a ratchet-like mechanism. *Cell* **126**:917–928. doi:10.1016/j.cell.2006.06.053

Burton BM, Marquis KA, Sullivan NL, Rapoport TA, Rudner DZ. 2007. The ATPase SpoIIIE Transports DNA across Fused Septal Membranes during Sporulation in Bacillus subtilis. *Cell*. doi:10.1016/j.cell.2007.11.009

Camp AH, Losick R. 2009. A feeding tube model for activation of a cell-specific transcription factor during sporulation in Bacillus subtilis. *Genes Dev* **23**:1014–1024. doi:10.1101/gad.1781709

Camp AH, Losick R. 2008. A novel pathway of intercellular signalling in Bacillus subtilis involves a protein with similarity to a component of type III secretion channels. *Mol Microbiol* **69**:402–417. doi:10.1111/j.1365-2958.2008.06289.x

Chastanet A, Losick R. 2007. Engulfment during sporulation in Bacillus subtilis is governed by a multi-protein complex containing tandemly acting autolysins. *Mol Microbiol* **64**:139–152. doi:10.1111/j.1365-2958.2007.05652.x

Chiba S, Coleman K, Pogliano K. 2007. Impact of membrane fusion and proteolysis on SpoIIQ dynamics and interaction with SpoIIIAH. *J Biol Chem*. doi:10.1074/jbc.M606056200

Crawshaw AD, Serrano M, Stanley WA, Henriques AO, Salgado PS. 2014. A mother cell-to-forespore channel: Current understanding and future challenges. *FEMS Microbiol Lett*. doi:10.1111/1574-6968.12554

Dembek M, Kelly A, Barwinska-Sendra A, Tarrant E, Stanley WA, Vollmer D, Biboy J, Gray J, Vollmer W, Salgado PS. 2018. Peptidoglycan degradation machinery in Clostridium difficile forespore engulfment. *Mol Microbiol*. doi:10.1111/mmi.14091

Doan T, Coleman J, Marquis KA, Meeske AJ, Burton BM, Karatekin E, Rudner DZ. 2013. FisB mediates membrane fission during sporulation in bacillus subtilis. *Genes Dev*. doi:10.1101/gad.209049.112

Doan T, Morlot C, Meisner J, Serrano M, Henriques AO, Moran CP, Rudner DZ. 2009. Novel secretion apparatus maintains spore integrity and developmental gene expression in Bacillus subtilis. *PLoS Genet*. doi:10.1371/journal.pgen.1000566

Donachie W. 2002. FtsK: Maxwell's Demon? *Mol Cell*.

Driks Adam. 2002. Proteins of the Spore Core and CoatBacillus Subtilis and Its Closest Relatives. pp. 527–535. doi:10.1128/9781555817992.chap36

Driks A. 2002. Overview: Development in bacteria: Spore formation in Bacillus subtilis. *Cell Mol Life Sci*. doi:10.1007/s00018-002-8430-x

Driks A, Losick R. 1991. Compartmentalized expression of a gene under the control of sporulation transcription factor σ(E) in Bacillus subtilis. *Proc Natl Acad Sci U S A*. doi:10.1073/pnas.88.22.9934

Eichenberger P, Fawcett P, Losick R. 2001. A three-protein inhibitor of polar septation during sporulation in Bacillus subtilis. *Mol Microbiol* **42**:1147–1162. doi:10.1046/j.1365-2958.2001.02660.x

Errington J, Bath J, Wu LJ. 2001. DNA transport in bacteria. *Nat Rev Mol Cell Biol*. doi:10.1038/35080005

Fiche JB, Cattoni DI, Diekmann N, Langerak JM, Clerte C, Royer CA, Margeat E, Doan T, Nöllmann M. 2013. Recruitment, Assembly, and Molecular Architecture of the SpoIIIE DNA Pump Revealed by Superresolution Microscopy. *PLoS Biol*. doi:10.1371/journal.pbio.1001557

Fimlaid KA, Jensen O, Donnelly ML, Siegrist MS, Shen A. 2015. Regulation of Clostridium difficile Spore Formation by the SpoIIQ and SpoIIIA Proteins. *PLoS Genet*. doi:10.1371/journal.pgen.1005562

Fimlaid KA, Shen A. 2015. Diverse mechanisms regulate sporulation sigma factor activity in the Firmicutes. *Curr Opin Microbiol*. doi:10.1016/j.mib.2015.01.006

Fleming TC, Shin JY, Lee SH, Becker E, Huang KC, Bustamante C, Pogliano K. 2010. Dynamic SpoIIIE assembly mediates septal membrane fission during Bacillus subtilis sporulation. *Genes Dev* **24**:1160–1172. doi:10.1101/gad.1925210

Frandsen N, Stragier P. 1995. Identification and characterization of the Bacillus subtilis spoIIP locus. *J Bacteriol* **177**:716–722.

Galperin MY, Mekhedov SL, Puigbo P, Smirnov S, Wolf YI, Rigden DJ. 2012. Genomic determinants of sporulation in Bacilli and Clostridia: Towards the minimal set of sporulation-specific genes. *Environ Microbiol*. doi:10.1111/j.1462-2920.2012.02841.x

Henriques AO, Moran, Jr. CP. 2007. Structure, Assembly, and Function of the Spore Surface Layers. *Annu Rev Microbiol*. doi:10.1146/annurev.micro.61.080706.093224

Higgins D, Dworkin J. 2012. Recent progress in Bacillus subtilis sporulation. *Fems Microbiol Rev* **36**:131–148. doi:10.1111/j.1574-6976.2011.00310.x

Hoch JA. 2017. A Life in Bacillus subtilis Signal Transduction . *Annu Rev Microbiol*. doi:10.1146/annurev-micro-030117-020355

Holland SK, Cutting S, Mandelstam J. 1987. The possible DNA-binding nature of the regulatory proteins, encoded by spoIID and gerE, involved in the sporulation of Bacillus subtilis. *J Gen Microbiol*. doi:10.1099/00221287-133-9-2381

Illing N, Errington J. 1991a. Genetic regulation of morphogenesis in Bacillus subtilis: Roles of σ(E) and σ(F) in prespore engulfment. *J Bacteriol* **173**:3159–3169.

Illing N, Errington J. 1991b. The spoIIIA operon of Bacillus subtilis defines a new temporal class of mother-cell-specific sporulation genes under the control of the σE form of RNA polymerase. *Mol Microbiol*. doi:10.1111/j.1365-2958.1991.tb00816.x

Jiang X, Rubio A, Chiba S, Pogliano K. 2005. Engulfment-regulated proteolysis of SpoIIQ: Evidence that dual checkpoints control σK activity. *Mol Microbiol*. doi:10.1111/j.1365-2958.2005.04811.x

Johnson TL, Abendroth J, Hol WGJ, Sandkvist M. 2006. Type II secretion: From structure to function. *FEMS Microbiol Lett*. doi:10.1111/j.1574-6968.2006.00102.x

Kay D, Warren SC. 1968. Sporulation in Bacillus subtilis. Morphological changes. *Biochem J*. doi:10.1042/bj1090819

Kellner EM, Decatur A, Moran CP. 1996. Two-stage regulation of an anti-sigma factor determines developmental fate during bacterial endospore formation. *Mol Microbiol*. doi:10.1046/j.1365-2958.1996.461408.x

Khanna K, Lopez-Garrido J, Zhao Z, Watanabe R, Yuan Y, Sugie J, Pogliano K, Villa E. 2019. The molecular architecture of engulfment during Bacillus subtilis sporulation. *Elife*. doi:10.7554/eLife.45257

Kuroda A, Rashid MH, Sekiguchi J. 1992. Molecular cloning and sequencing of the upstream region of the major Bacillus subtilis autolysin gene: A modifier protein exhibiting sequence homology to the major autolysin and the spoIID product. *J Gen Microbiol*. doi:10.1099/00221287-138-6-1067

Levdikov V. M., Blagova E V., McFeat A, Fogg MJ, Wilson KS, Wilkinson AJ. 2012. Structure of components of an intercellular channel complex in sporulating Bacillus subtilis. *Proc Natl Acad*

Sci **109**:5441–5445. doi:10.1073/pnas.1120087109

Levdikov Vladimir M., Blagova E V., McFeat A, Fogg MJ, Wilson KS, Wilkinson AJ. 2012. Structure of components of an intercellular channel complex in sporulating Bacillus subtilis. *Proc Natl Acad Sci U S A*. doi:10.1073/pnas.1120087109

Liu NJL, Dutton RJ, Pogliano K. 2006. Evidence that the SpoIIIE DNA translocase participates in membrane fusion during cytokinesis and engulfment. *Mol Microbiol* **59**:1097–1113. doi:10.1111/j.1365-2958.2005.05004.x

Londoño-Vallejo JA, Fréhel C, Stragier P. 1997. spoIIQ, a forespore-expressed gene required for engulfment in Bacillus subtilis. *Mol Microbiol*. doi:10.1046/j.1365-2958.1997.3181680.x

Lopez-Diaz I, Clarke S, Mandelstam J. 1986. spoIID Operon of Bacillus subtilis: Cloning and Sequence. *Microbiology* **132**:341–354.

Lopez-Garrido J, Ojkic N, Khanna K, Wagner FR, Villa E, Endres RG, Pogliano K. 2018. Chromosome Translocation Inflates Bacillus Forespores and Impacts Cellular Morphology. *Cell* **172**:758-770.e14. doi:10.1016/j.cell.2018.01.027

Lopez D, Vlamakis H, Kolter R. 2009. Generation of multiple cell types in Bacillus subtilis. *FEMS Microbiol Rev*. doi:10.1111/j.1574-6976.2008.00148.x

Margolis PS, Driks A, Losick R. 1993. Sporulation gene spoIIB from Bacillus subtilis. *J Bacteriol*. doi:10.1128/jb.175.2.528-540.1993

Marquis KA, Burton BM, Nollmann M, Ptacin JL, Bustamante C, Ben-Yehuda S, Rudner DZ. 2008. SpoIIIE strips proteins off the DNA during chromosome translocation. *Genes Dev*. doi:10.1101/gad.1684008

Massey TH, Mercogliano CP, Yates J, Sherratt DJ, Löwe J. 2006. Double-Stranded DNA Translocation: Structure and Mechanism of Hexameric FtsK. *Mol Cell*. doi:10.1016/j.molcel.2006.06.019

Mckenney PT, Driks A, Eichenberger P. 2013. The Bacillus subtilis endospore: Assembly and functions of the multilayered coat. *Nat Rev Microbiol*. doi:10.1038/nrmicro2921

Meisner J, Maehigashi T, Andre I, Dunham CM, Moran CP. 2012. Structure of the basal components of a bacterial transporter. *Proc Natl Acad Sci U S A* **109**:5446–5451. doi:10.1073/pnas.1120113109

Meisner J, Moran CP. 2011. A LytM domain dictates the localization of proteins to the mother cell-forespore interface during bacterial endospore formation. *J Bacteriol*. doi:10.1128/JB.01270-10

Meisner J, Wang X, Serrano M, Henriques AO, Moran CP. 2008. A channel connecting the mother cell and forespore during bacterial endospore formation. *Proc Natl Acad Sci U S A* **105**:15100–15105. doi:10.1073/pnas.0806301105

Meyer P, Gutierrez J, Pogliano K, Dworkin J. 2010. Cell wall synthesis is necessary for membrane dynamics during sporulation of Bacillus subtilis. *Mol Microbiol* **76**:956-+.

Mileykovskaya E, Dowhan W. 2009. Cardiolipin membrane domains in prokaryotes and eukaryotes. *Biochim Biophys Acta - Biomembr*. doi:10.1016/j.bbamem.2009.04.003

Morlot C, Rodrigues CDA. 2018. The New Kid on the Block: A Specialized Secretion System during Bacterial Sporulation. *Trends Microbiol*. doi:10.1016/j.tim.2018.01.001

Morlot C, Uehara T, Marquis KA, Bernhardt TG, Rudner DZ. 2010. A highly coordinated cell wall degradation machine governs spore morphogenesis in Bacillus subtilis. *Genes Dev* **24**:411–422. doi:10.1101/gad.1878110

Nocadello S, Minasov G, Shuvalova LS, Dubrovska I, Sabini E, Anderson WF. 2016. Crystal structures of the spoiid lytic transglycosylases essential for bacterial sporulation. *J Biol Chem*. doi:10.1074/jbc.M116.729749

Ojkic N, Lopez-Garrido J, Pogliano K, Endres RG. 2016. Cell-wall remodeling drives engulfment during Bacillus subtiliss porulation. *Elife* **5**:30. doi:10.7554/eLife.18657

Ojkic N, López-Garrido J, Pogliano K, Endres RG. 2014. Bistable Forespore Engulfment in Bacillus subtilis by a Zipper Mechanism in Absence of the Cell Wall. *PLoS Comput Biol* **10**. doi:10.1371/journal.pcbi.1003912

Perez AR, Abanes-De Mello A, Pogliano K. 2000. SpoIIB localizes to active sites of septal biogenesis and spatially regulates septal thinning during engulfment in Bacillus subtilis. *J Bacteriol* **182**:1096–1108. doi:10.1128/jb.182.4.1096-1108.2000

Piggot PJ, Hilbert DW. 2004. Sporulation of Bacillus subtilis. *Curr Opin Microbiol*. doi:10.1016/j.mib.2004.10.001

Pogliano J, Osborne N, Sharp MD, Mello AA De, Perez A, Sun YL, Pogliano K. 1999. A vital stain for studying membrane dynamics in bacteria: A novel mechanism controlling septation during Bacillus subtilis sporulation. *Mol Microbiol* **31**:1149–1159. doi:10.1046/j.1365-2958.1999.01255.x

Pogliano J, Sharp MD, Pogliano K. 2002. Partitioning of chromosomal DNA during establishment of cellular asymmetry in Bacillus subtilis. *J Bacteriol*. doi:10.1128/JB.184.4.1743-1749.2002

Ptacin JL, Nollmann M, Becker EC, Cozzarelli NR, Pogliano K, Bustamante C. 2008. Sequence-directed DNA export guides chromosome translocation during sporulation in Bacillus subtilis. *Nat Struct Mol Biol*. doi:10.1038/nsmb.1412

Ribis JW, Fimlaid KA, Shen A. 2018. Differential requirements for conserved peptidoglycan remodeling enzymes during Clostridioides difficile spore formation. *Mol Microbiol*. doi:10.1111/mmi.14090

Rodrigues CDA, Henry X, Neumann E, Kurauskas V, Bellard L, Fichou Y, Schanda P, Schoehn G, Rudner DZ, Morlot C. 2016a. A ring-shaped conduit connects the mother cell and forespore during sporulation in Bacillus subtilis. *Proc Natl Acad Sci U S A*. doi:10.1073/pnas.1609604113

Rodrigues CDA, Ramírez-Guadiana FH, Meeske AJ, Wang X, Rudner DZ. 2016b. GerM is required to assemble the basal platform of the SpoIIIA–SpoIIQ transenvelope complex during sporulation in Bacillus subtilis. *Mol Microbiol*. doi:10.1111/mmi.13457

Rong S, Rosenkrantz MS, Sonenshein AL. 1986. Transcriptional control of the Bacillus subtilis spoIID gene. *J Bacteriol*. doi:10.1128/jb.165.3.771-779.1986

Rubio A, Pogliano K. 2004. Septal localization of forespore membrane proteins during engulfment in Bacillus subtilis. *EMBO J*. doi:10.1038/sj.emboj.7600171

Ryter A. 1965. Etude Morphologique de la sporulation de Bacillus Subtilis. *Ann Inst Pasteur (Paris)*.

Saujet L, Pereira FC, Henriques AO, Martin-Verstraete I. 2014. The regulatory network controlling spore formation in Clostridium difficile. *FEMS Microbiol Lett*. doi:10.1111/1574-6968.12540

Serrano M, Crawshaw AD, Dembek M, Monteiro JM, Pereira FC, Pinho MG, Fairweather NF, Salgado PS, Henriques AO. 2016. The SpoIIQ-SpoIIIAH complex of Clostridium difficile controls forespore engulfment and late stages of gene expression and spore morphogenesis. *Mol Microbiol*. doi:10.1111/mmi.13311

Setlow P. 2014. Germination of spores of Bacillus species: What we know and do not know. *J Bacteriol*. doi:10.1128/JB.01455-13

Setlow P, Wang S, Li Y-Q. 2017. Germination of Spores of the Orders Bacillales and Clostridiales . *Annu Rev Microbiol*. doi:10.1146/annurev-micro-090816-093558

Shin JY, Lopez-Garrido J, Lee SH, Diaz-Celis C, Fleming T, Bustamante C, Pogliano K. 2015. Visualization and functional dissection of coaxial paired SpoIIIE channels across the sporulation septum. *Elife* **4**:22. doi:10.7554/eLife.06474

Smith K, Bayer ME, Youngman P. 1993. Physical and functional characterization of the Bacillus subtilis spoIIM gene. *J Bacteriol* **175**:3607–3617.

Stragier P. 2014. A Gene Odyssey: Exploring the Genomes of Endospore-Forming BacteriaBacillus Subtilis and Its Closest Relatives. doi:10.1128/9781555817992.ch35

Sun YL, Sharp MD, Pogliano K. 2000. A dispensable role for forespore-specific gene expression in engulfment of the forespore during sporulation of Bacillus subtilis. *J Bacteriol* **182**:2919–2927. doi:10.1128/JB.182.10.2919-2927.2000

Tan IS, Ramamurthi KS. 2014. Spore formation in Bacillus subtilis. *Environ Microbiol Rep*. doi:10.1111/1758-2229.12130

The Spore Coat. 2016. The Bacterial Spore: From Molecules to Systems. doi:10.1128/microbiolspec.tbs-0023-2016

Tocheva EI, Lopez-Garrido J, Hughes H V, Fredlund J, Kuru E, VanNieuwenhze MS, Brun Y V, Pogliano K, Jensen GJ. 2013. Peptidoglycan transformations during Bacillus subtilis sporulation. *Mol Microbiol* **88**:673–686. doi:10.1111/mmi.12201

Wu LJ, Errington J. 1998. Use of asymmetric cell division and spoIIIE mutants to probe chromosome orientation and organization in Bacillus subtilis. *Mol Microbiol*. doi:10.1046/j.1365-2958.1998.00724.x

Wu LJ, Errington J. 1997. Septal localization of the SpoIIIE chromosome partitioning protein in Bacillus subtilis. *EMBO J* **16**:2161–2169. doi:10.1093/emboj/16.8.2161

Wu LJ, Errington J. 1994. Bacillus subtilis spoIIIE protein required for DNA segregation during asymmetric cell division. *Science (80-)* **264**:572–575.

Yu XC, Tran AH, Sun Q, Margolin W. 1998. Localization of cell division protein FtsK to the Escherichia coli septum and identification of a potential N-Terminal targeting domain. *J Bacteriol*.

Zeytuni N, Flanagan KA, Worrall LJ, Massoni SC, Camp AH, Strynadka NCJ. 2018a. Structural and biochemical characterization of SpoIIIAF, a component of a sporulation-essential channel in Bacillus subtilis. *J Struct Biol*. doi:10.1016/j.jsb.2018.06.002

Zeytuni N, Flanagan KA, Worrall LJ, Massoni SC, Camp AH, Strynadka NCJ. 2018b. Structural characterization of SpoIIIAB sporulation-essential protein in Bacillus subtilis. *J Struct Biol*. doi:10.1016/j.jsb.2017.12.009

Zeytuni N, Hong C, Flanagan KA, Worrall LJ, Theiltges KA, Vuckovic M, Huang RK, Massoni SC, Camp AH, Yu Z, Strynadka NC. 2017a. Near-atomic resolution cryoelectron microscopy structure of the 30-fold homooligomeric SpoIIIAG channel essential to spore formation in *Bacillus subtilis*. *Proc Natl Acad Sci* 201704310. doi:10.1073/pnas.1704310114

Zeytuni N, Hong C, Flanagan KA, Worrall LJ, Theiltges KA, Vuckovic M, Huang RK, Massoni SC, Camp AH, Yu Z, Strynadka NC. 2017b. Near-atomic resolution cryoelectron microscopy structure of the 30-fold homooligomeric SpoIIIAG channel essential to spore formation in Bacillus subtilis. *Proc Natl Acad Sci U S A*. doi:10.1073/pnas.1704310114

Zhu D, Sorg JA, Sun X. 2018. Clostridioides difficile biology: Sporulation, germination, and corresponding therapies for C. difficile infection. *Front Cell Infect Microbiol*. doi:10.3389/fcimb.2018.00029

1.7 Figures

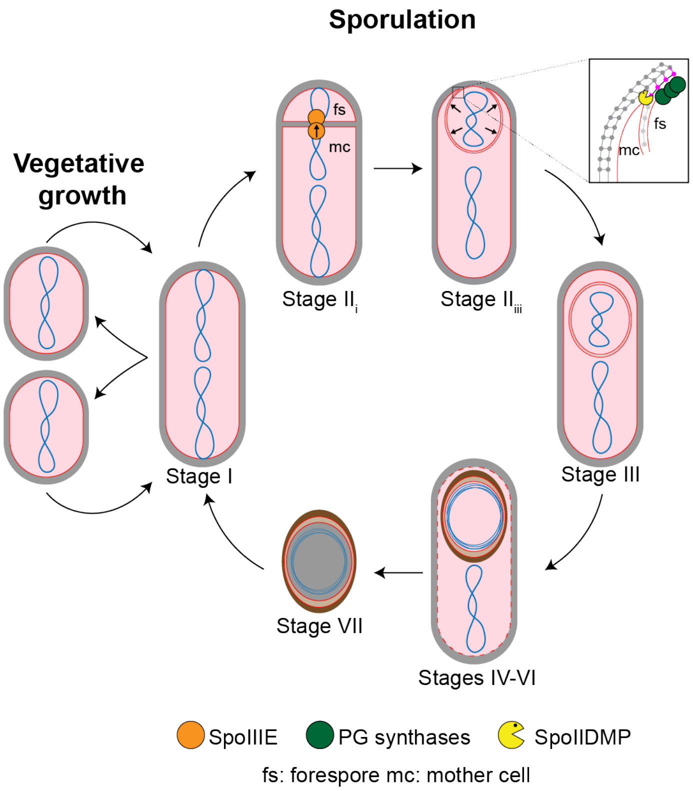

Figure 1.1. Sporulation in *Bacillus subtilis*. Schematic representing key architectural transformations during sporulation. Membranes (red), peptidoglycan (PG, grey), DNA (dark blue), SpoIIIE (orange), SpoIIDMP (yellow pacman), PG synthases (green), cortex (light brown) and coat (dark brown) are indicated. Ryter 1965 proposed the classical naming scheme to distinguish different stages of sporulation in *Bacillus subtilis* based on their morphologies in electron microscopy images(Ryter, 1965). Stage 0 represents a vegetative cell wherein the DNA replicates and extends into an axial filament in stage I. Stage II marks the formation of the asymmetric septum to form the smaller forespore and the larger mother cell. More recently, stage II has been categorized to distinguish sporulating cells with flat (stage II$_i$), curved (stage II$_{ii}$, not shown) and engulfing septum (stage II$_{iii}$). Stage II$_{\underline{iii}}$ represents completion of chromosome translocation from the mother cell to the forespore by SpoIIIE (orange) and mediation of engulfment by coordinated PG synthesis and degradation (inset). New PG (pink) is synthesized by enzymes (green) present at the leading edge of the forespore and bonds between old septal PG (light grey) and lateral PG (dark grey) are hydrolyzed by SpoIIDMP on the mother cell side (yellow pacman), providing room for membrane migration(Ojkic et al., 2016). Stage III marks completion of engulfment of the forespore by the mother cell. Stage IV is characterized by the assembly of the cortex between the membranes of the engulfed forespore and stage V by the formation of the spore coat. In stage VI, the spore matures inside the mother cell and in stage VII, the mother cell lysis to release the dormant spore to the environment. The spores can germinate to produce vegetative cells when re-exposed to nutrient-rich conditions.

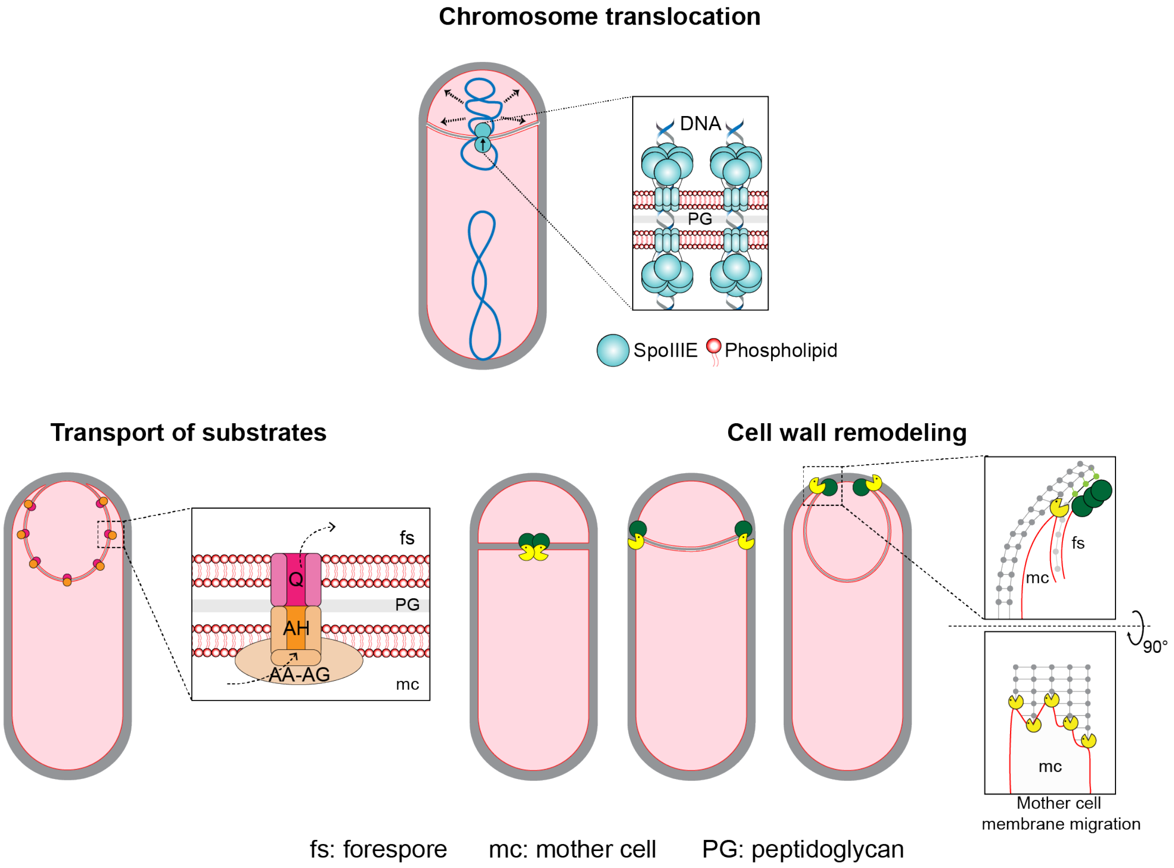

Figure 1.2. Key players in engulfment during *B. subtilis* sporulation. In all panels, PG (grey) and cell membrane (red) are highlighted. **(A)** Schematic of DNA translocation (dark blue) from the mother cell to the forespore by SpoIIIE (light blue). The DNA in the forespore generates turgor pressure due to associated ions and water molecules making the forespore uniformly round(Lopez-Garrido et al., 2018). SpoIIIE arranges as a hexamer (two each in the forespore and the mother cell) to transport the two arms of the chromosome simultaneously(Shin et al., 2015). **(B)** Schematic of the Q-AH complex (Q in the forespore, pink and AH in the mother cell, orange) that forms punctate pattern around the forespore membrane is likely involved in the transport of substrates from the mother cell to the forespore(Morlot and Rodrigues, 2018). The channel is gated on the mother cell side(Meisner et al., 2008). Other proteins belonging to *spoIIIA* operon are also represented alongside. **(C)** Schematic of the cell wall remodeling machinery during engulfment by the coordinated action of SpoIIDMP PG degradation machinery (yellow pacman) on the mother cell side and PG synthases (green) on the forespore side(Ojkic et al., 2016). Inset, top panel, lateral PG (dark grey), septal PG (light grey), new PG (light green) are highlighted. PG synthases make new PG near the forespore and DMP complex degrades the bond between lateral and old septal PG, making room for mother cell membrane migration(Ojkic et al., 2016). Inset, bottom panel, limited number of DMP complexes lead to uneven migration of the mother cell membrane giving an appearance of finger-like projection(Khanna et al., 2019).

1.8 Acknowledgements

Chapter 1, in part, is made up of material from a manuscript in preparation for publication. The manuscript is: Khanna, K., Lopez-Garrido, J., Pogliano K. *Bacillus subtilis* spore morphogenesis (*in preparation*). The dissertation author is the primary author of the manuscript in preparation.

Chapter 2: Asymmetric localization of the divisome during *Bacillus subtilis* sporulation dictates septal thickness

2.1 Summary

The mechanistic details of bacterial cytokinesis are poorly understood. *Bacillus subtilis* can divide via two modes. During vegetative growth, the division septum is formed at the mid cell to produce two equal daughter cells. However, during sporulation, the division septum is formed closer to one pole to yield a smaller forespore and a larger mother cell. We used high-resolution cryo-electron tomography to visualize the architectural differences in the organization of FtsZ filaments, the major orchestrators of bacterial cell division during these conditions. We found that during vegetative growth, FtsZ filaments are present uniformly around the leading edge of the invaginating septum but during sporulation, they are only present on the mother cell side. Our data suggest that the sporulation septum is thinner than the vegetative septum likely due to half as many FtsZ filaments tracking the division plane during sporulation as opposed to vegetative growth. We also show that a sporulation-specific protein, SpoIIE, regulates the localization of the divisome and septal thickness during sporulation. Our results provide the first evidence of asymmetric localization of the cell division machinery in bacteria leading to cell types with diverse fates, paving way for future studies in the field of prokaryotic cell division.

2.2 Introduction

Bacterial cell division involves the invagination of the cellular membrane(s) and peptidoglycan (PG) to split the cell into two progeny cells. Although conceptually simple, the molecular and mechanistic details of the process are poorly understood. In most bacteria, cell division is initiated when a tubulin homologue and GTPase, FtsZ polymerizes to form a ring-like structure, called the Z-ring at the division site (Bi and Lutkenhaus, 1991; De Boer et al., 1992; Mukherjee and Lutkenhaus, 1994). The Z-ring serves as a scaffold onto which about a dozen other proteins assemble to form a mature cell division machinery called the 'divisome' (Haeusser and Margolin, 2016). In the Gram-positive bacterium *Bacillus subtilis*, the divisome assembly proceeds in two steps. First, proteins that interact directly with FtsZ to promote its interaction with the membrane are recruited to the divisome (Gamba et al., 2009). One essential protein recruited at this stage is FtsA, an actin homologue which tethers FtsZ to the membrane via a conserved C-terminal amphipathic helix (Pichoff and Lutkenhaus, 2005; Szwedziak et al., 2014). FtsA can also form protofilaments via polymerization in an ATP-dependent manner (Szwedziak et al., 2012). Second, proteins involved in septal cell wall synthesis and remodeling are recruited to the divisome (Gamba et al., 2009). Recent studies suggest that treadmilling by FtsZ filaments serves as a platform to drive the circumferential motion of septal PG synthases in both *B. subtilis* and *E. coli*, suggesting that this dynamic property of FtsZ filaments can regulate the thickness of the division septum (Bisson et al., 2017; Yang et al., 2017).

B. subtilis is an intriguing model system to study cell division as it can divide via two possible modes. During vegetative growth, the division septum is formed at the mid cell, producing two daughter cells of equal sizes (Wang and Lutkenhaus, 1993). However, during starvation, the division septum is formed closer to one pole and the cell divides asymmetrically to yield a smaller forespore and a larger mother cell. This process, referred to as sporulation, results in the phagocytosis of the forespore by the mother cell, ultimately producing a dormant spore upon mother cell lysis (Tan and Ramamurthi, 2014). Vegetative and sporulating cells differ not only in the positioning of the division site but also in the amount of septal PG, with the medial vegetative septum being almost four times thicker than the polar sporulating septum (Illing and Errington, 1991; Tocheva et al., 2013) (~ 80 nm vs ~ 22 nm). Another distinction is the production of a sporulation-specific integral membrane protein, SpoIIE, which colocalizes with and directly interacts with FtsZ (Arigoni et al., 1995; Levin et al., 1997; Lucet, 2000). Recent evidence suggests that SpoIIE localizes only on the forespore side of the polar septum at the onset of membrane constriction before being released into the forespore membrane upon septum formation (Carniol et al., 2005; Errington, 2003; Eswaramoorthy et al., 2014; Guberman et al., 2008; Wu et al., 1998). Certain *spoIIE* mutants also form thicker polar septa compared to wild type (Barák and Youngman, 1996; Illing and Errington, 1991). These findings posit that there may be differences in the divisome organization at the forespore and the mother cell side of the septum which may play a role in regulating the septal thickness. However, we lack a mechanistic understanding of the factors regulating these processes in *B. subtilis*.

In this study, we have used cryo-electron tomography coupled with cryo-focused ion beam milling (or cryo-FIB-ET) to reveal the native architecture of the cell division machinery in *B. subtilis* during vegetative growth and sporulation at a resolution of a few nanometers. We show that FtsAZ filaments, the major players in bacterial cytokinesis are present uniformly around the leading edge of the invaginating septum in dividing vegetative cells but are localized only on the mother cell side of the septum in dividing sporulating cells. We provide evidence that there are half as many FtsZ filaments tracking the division plane during sporulation as during vegetative growth which may lead to a thinner sporulation septum as these filaments guide the insertion of cell wall material during septal biogenesis. Next, we show that the sporulation-specific protein SpoIIE is responsible for asymmetric localization of FtsAZ filaments as in its absence, the filaments localize in a manner similar to vegetative septum, uniformly around the leading edge of the invaginating septum. We anticipate that our results will pave way for future studies in the field of bacterial cell division, giving rise to testable hypothesis on how bacteria can regulate protein localization in space and time to carry out the critical process of cytokinesis under different gene expression programs.

2.3 Results

FtsAZ filaments in vegetative *B. subtilis* cells

Previously, cryo-ET images of *E. coli* and *Caulobacter crescentus* revealed the presence of a series of dots at the division site which corresponded to 2D projections of FtsZ filaments encircling the cell (Li et al., 2007; Szwedziak et al., 2014). However, the thicker *B. subtilis* cells were precluded from high-resolution tomography until recently when we incorporated a cryo-FIB milling step in the workflow to provide mechanistic details about engulfment in *B. subtilis* sporangia (Khanna et al., 2019; Lopez-Garrido et al., 2018). However, there are a few points of note when analyzing cryo-FIB-ET data. First, cryo-FIB milling employs the application of two parallel beams of gallium ions in a geometry that ablates the cellular material from the top and the bottom, leaving an electron-transparent ~100-300 nm thin slice (Fig. S2.1A). Hence, when a rod-shaped cell is milled and the resulting 3D volume rotated around the short axis by 90°, we only capture a section of the circular disk (Fig. 2.1B, S2.1A,B). Further, the cells are randomly oriented on an electron microscopy (EM) grid and different sections of the circular disk can be captured depending on the milling angle and the cell's orientation on the grid (Fig. S2.1B). Also, the range of tilt series is typically limited to ~± 60° due to the limitations of the microscope stage, restricting our angular sampling of the specimen (Fig. S2.1C). Hence, our interpretation of the data is limited to ~15-25% of the cell volume but acquisition of multiple tomograms should make the analysis more general.

First, we used cryo-FIB-ET to observe the leading edge of the invaginating septum in dividing vegetative *B. subtilis* to get insights into the divisome architecture (Fig. 2.1, S2.2). Closer inspection revealed the presence of two series of dots at the division site that were distributed uniformly along the boundary of the leading edge, a membrane-proximal series of dots (~6.5 nm from the membrane, in pink) and a membrane-distal series of dots (~14 nm from the membrane, in blue) (Fig. 2.1C-E,H, S2.2A,B,D,E). Rotation of the 3D volume around the short axis of the cell revealed that each series of dots corresponded to ~3-3.5 nm wide filamentous structures encircling the cell (Fig. 2.1F-K, 2.2C,F). In the membrane-distal series of dots, we could easily resolve individual ~4 nm dots spaced ~ 5.5 nm apart while in the membrane-proximal series of dots, there were densities comprised of even smaller proteins that were not resolved at the magnifications at which we acquired the images (Fig. 2.1D,E). Analysis of the intensities of the two rings revealed that the membrane-distal ring is denser and likely more continuous than the membrane-proximal ring which appears more patchy (Fig. 2.1F,G,L). In a few high-quality tomograms, we observed densities connecting the two series of dots in a ladder-like arrangement (S2.2D-E) and also those connecting the membrane-proximal ring to the cytoplasmic membrane (Fig. S2.2D,F).

FtsA and FtsZ comprise the membrane-proximal and the membrane-distal ring respectively

Our data suggest that two cytoskeletal rings mediate cytokinesis in *B. subtilis*, a membrane-proximal ring at a distance of ~6.5 nm from the invaginating membrane and a membrane-distal ring at a distance of ~14 nm. This arrangement is distinct from Gram-negative bacteria like *E. coli* and *C. crescentus* where only a single band of filamentous structures corresponding to FtsZ was visible at a distance of ~16 nm from the inner membrane (Li et al., 2007; Szwedziak et al., 2014). In *E. coli*, another ring composed of FtsA protofilaments was visible at a distance of ~8 nm from the membrane only when FtsA was overexpressed such that the ratio of FtsZ to FtsA altered from 5:1 in wild type to 1:1 in the modified strain (Szwedziak et al., 2014). Based on this and differences in the morphologies of the two rings highlighted in the previous section, we hypothesized that in *B. subtilis*, the membrane-proximal ring may be composed of FtsA filaments and the membrane-distal ring that of FtsZ filaments.

To unambiguously establish the identity of the Z-ring, we constructed a *B. subtilis* strain with an extra glutamine-rich linker region between the globular N-terminal domain of FtsZ and its C-terminal helix that binds FtsA (or FtsZ-linker$_{\text{Q-rich}}$, Fig. 2.3A-C), similar to a strain previously constructed in *E. coli* that led to a modest ~5 nm increase in the distance of the Z-ring from the membrane (Szwedziak et al., 2014). In *B. subtilis* FtsZ-linker$_{\text{Q-rich}}$, while the distance of the membrane-proximal ring from the invaginating membrane did not change compared to wild type, we observed large variation in the distances of membrane-distal filaments from the membrane, ranging from ~15-19 nm (Fig. 2.2A). Sometimes, we also detected "stray" filaments at a distance of ~12-20 nm from the membrane that likely corresponded to FtsZ but without a corresponding FtsA filament to tether it to the membrane as the incorporation of the long linker in the C-terminal of FtsZ may have affected this interaction (black arrows, Fig. S2.3D-J). In a few tomograms, we also observed doublets of individual protofilaments only in the membrane-distal band, an arrangement that was previously reported for FtsZ filaments in tomograms of dividing *E. coli* cells (Szwedziak et al., 2014) (Fig. S2.3D,K-N), further demonstrating that only the membrane-distal ring corresponded to the Z-ring. In one of the tomograms, we also observed an additional faint ring between the membrane-proximal and the membrane-distal rings (~14 nm from the membrane) that might correspond to few FtsZ filaments that may still interact as closely with FtsA as in wild type in spite of the longer linker region (in green, Fig. S2.4A-C). The distribution of intensity values of the rings in the mutant strain was also comparable to their counterparts in the wild type (Fig. S2.4D). Based on the above observations, we propose that the more continuous membrane-distal ring of FtsZ filaments tethered to the membrane via a patchier membrane-proximal ring of FtsA filaments and/or possibly additional divisome proteins (Fig. 2.2B).

FtsAZ filaments localize only on the mother cell side during sporulation

Next, we analyzed the divisome architecture in sporulating *B. subtilis* cells. During sporulation, the division site shifts closer to a pole as opposed to medial division during vegetative growth (Fig. 2.1A). We again observed two series of dots in dividing sporulating cells but surprisingly, they were visible along the leading edge of the invaginating polar septum only on the mother cell side (Fig. 2.2C-F). In this case, filaments could not be observed by rotation of the 3D volume of the tomogram about the short axis by 90° as they projected onto the septal PG since they were present right beneath the septal disk on the mother cell side (Fig. S2.5A,B). Rather the tomogram was rotated by 90° along the long axis of the cell at the two leading edges of the invaginating septum to observe the filaments (Fig. S2.5C,D). Of note, the leading edge of the nascent septum in the sporulating cells we imaged appeared particularly blurry and crowded, probably owing to the presence of many transmembrane cell division and sporulation-specific proteins (Fig. 2.2C,D). Hence, we could not observe the finer architectural details of FtsAZ filaments in these cells at a high-resolution. Surprisingly, we were able to better resolve FtsAZ filaments in dividing cells of SpoIIIE^{ATP-} mutant sporangia during sporulation where we observed them on the mother cell side of the septum (similar to wild type) more clearly (Fig. S2.6). In conclusion, our data suggest FtsAZ filaments mediating cell division localize differently during vegetative growth and sporulation. During vegetative growth, they span the leading edge of the invaginating septum uniformly whereas during sporulation, they localize only on the mother cell side.

FtsAZ filaments tracking the division plane may dictate septum thickness

Based on previous electron micrographs, upon closure, the polar sporulating septum is just 25% of the thickness of the medial vegetative septum (~ 22 nm vs ~ 80 nm) (Illing and Errington, 1991; Tocheva et al., 2013). Recent studies suggest that FtsZ treadmilling drives the circumferential motion of septal PG synthases and regulates the rate of PG synthesis in both *B. subtilis* and *E. coli* (Bisson et al., 2017; Yang et al., 2017). The observation that the sporulation septum is thinner than the vegetative septum and that FtsZ filaments localize differently during the two conditions led us to hypothesize that there may be a direct correlation between FtsZ filaments at the division site and the septal thickness during septal biogenesis.

To investigate this, we first measured the septal thickness in dividing sporulating and vegetative cells using our cryo-FIB-ET images to investigate if the sporulating septum is thinner than the vegetative septum as it is being formed or only upon closure as has been previously reported (Fig. 2.2G). Our data showed that the thickness of the invaginating septa in vegetative cells was ~ 50 nm as opposed to ~80 nm when the septum formation is completed. This suggests that during vegetative growth, either additional PG might be incorporated into the septum upon its closure or the already present PG might be stretched as a result of PG hydrolysis initiated during separation of the daughter cells. On the other hand, the thickness of the invaginating septa in sporulating cells was almost half of that of vegetative cells (~ 25 nm). This suggests that even at the onset of cell division, the sporulating septum is thinner than the vegetative septum.

Next, we investigated if different localization of FstZ filaments also translated into different number of FtsZ protofilaments tracking the division plane during vegetative growth and sporulation. It is difficult to count the exact number of FtsZ protofilaments from our cryo-FIB-ET data due to low signal-to-noise ratio at the division site, especially during sporulation due to blurry leading edges of the invaginating septum. Hence, we used the length spanned by the membrane-distal band of FtsZ dots (or Z-dots) as a proxy for the amount of cytoskeletal machinery mediating cell division. On average, Z-dots span twice the length in vegetative cells as compared to sporulating cells (~51 nm vs ~27 nm, Fig. 2.2H), suggesting that there are likely twice as many FtsZ filaments participating in cytokinesis during vegetative growth as compared to sporulation where they are present on only one side of the constricting septum. Based on these data we propose that the sporulation septum being thinner than the vegetative septum could be a consequence of fewer FtsZ filaments tracking the division plane during sporulation as their dynamic properties regulate the insertion of cell wall material during septal biogenesis.

SpoIIE affects the localization of FtsAZ filaments during sporulation

We next investigated factors leading to the distinct pattern of FtsAZ filament localization during vegetative growth and sporulation. For this, we focused on dissecting the role of SpoIIE (or IIE), a sporulation-specific integral membrane protein in regulating polar division for several reasons. First, IIE localizes to the dividing polar septum in an FtsZ-dependent manner (Arigoni et al., 1995; Levin et al., 1997). Biochemical evidence suggests that the central FtsZ-binding and possibly the N-terminal transmembrane domains of IIE play a role in its interaction with FtsZ (Carniol et al., 2005; Lucet, 2000). Second, previous electron micrographs demonstrated that certain *spoIIE* mutants form thicker asymmetric septa at polar sites compared to wild type sporangia (Barák and Youngman, 1996; Illing and Errington, 1991). Third, recent evidence suggests that IIE preferentially localizes to the forespore side of the dividing septum, creating an asymmetry during polar division (Eswaramoorthy et al., 2014; Guberman et al., 2008; Wu et al., 1998). Hence, we hypothesized that IIE may regulate the divisome architecture during sporulation.

To test this, we first investigated the divisome architecture in SpoIIE null mutant sporangia (or *spoIIE)*. Indeed, closer inspection of the leading edge of the invaginating septa revealed that the divisome architecture in *spoIIE* is similar to vegetative cells, with two series of dots corresponding to FtsAZ filaments present uniformly along the leading edge in contrast to wild type sporulating cells where they were present only on the mother cell side (Fig. 2.3A-C,M). Also, at ~42 nm, the invaginating polar septum in *spoIIE* sporangia was thicker than wild type sporulating septum implicating IIE in regulating the localization of the FtsAZ filaments and septal thickness during sporulation (Fig. 2.3N). Of note, even though the length spanned by FtsZ filaments in *spoIIE* sporangia was similar to wild type vegetative cells, their septa were still ~10 nm thinner suggesting there may be as of yet unidentified additional factors apart from IIE that regulate the interaction of FtsZ with PG synthases during sporulation (Fig. S2.7A).

IIE has three domains: an N-terminal transmembrane domain with 10 membrane-spanning segments (region I), a central domain that promotes oligomerization of IIE and its interaction with FtsZ (region II) and a C-terminal phosphatase domain that is involved in the activation of the forespore-specific transcription factor σ^F after septum formation (region III) (Carniol et al., 2005). Since regions I and II have been implicated in regulating the interaction of IIE with FtsZ, we imaged the following IIE mutant strains: (1) deletion in region I (or *spoIIE-ΔregI*), (2) deletion in region II (or *spoIIE-ΔregII*), and (3) replacement of 10 membrane-spanning segments with 2 membrane-spanning segments from *E. coli* MalF (or *malF-spoIIE-ΔregI*). These strains also had a deletion in *spoIIA* operon to uncouple the role of IIE in polar division from σ^F activation. As has been reported previously, $\mathrm{IIE}^{\Delta\mathrm{regI}}$-GFP appeared mostly diffuse with some cells showing enrichment or punctate patterns at the polar septum (at ~ 50% level compared to wild type) indicating some association with FtsZ, $\mathrm{IIE}^{\Delta\mathrm{regII}}$ -GFP appeared almost completely diffuse in the cytoplasm, and $\mathrm{IIE}^{\mathrm{malF}\text{-}\Delta\mathrm{regI}}$-GFP localized similar to wild type, displaying punctate patterns at the polar septum (Fig. S2.7B,C). Surprisingly, our cryo-FIB-ET data demonstrated that the organization of FtsAZ filaments at the polar septum and the septal thickness in all the three mutant strains is similar to *spoIIE* sporangia (Fig. 2.3D-N). These data suggest that both the transmembrane as well as the FtsZ-binding domain are essential to regulate the localization of FtsAZ filaments and septal thickness during sporulation.

2.4 Discussion

In this study, we elucidate the differences in the architecture of the cell division machinery in *B. subtilis* during vegetative growth and sporulation and how it impacts septal PG thickness. First, we show that during vegetative growth, two cytoskeletal rings localize uniformly around the leading edge of the invaginating medial septum to orchestrate cell division, a membrane-proximal ring of FtsA filaments that tethers the membrane-distal ring of FtsZ filaments to the membrane (Fig. 2.1,2.2A,B). Second, we demonstrate that during sporulation, FtsAZ filaments are present only on the mother cell side of the invaginating polar septum (Fig. 2.2C-F). Third, our data suggest that during septal biogenesis, the number of FtsAZ filaments tracking the sporulating septum is almost half that of the vegetative septum which likely gives rise to a thinner sporulation septum by mediating the circumferential motion of fewer PG synthases around the division plane during sporulation (Fig. 2.2G,H). Finally, we show that a sporulation-specific protein SpoIIE is essential to regulate the localization of FtsAZ filaments and septal thickness during sporulation (Fig. 2.3).

Most of our understanding of bacterial cytokinesis comes from studies in model Gram-positive and Gram-negative bacteria, namely *Bacillus subtilis* and *Escherichia coli*, respectively. Although the overall mechanism of cytokinesis is conserved in that a Z-ring that recruits other components of the divisome is formed at the division site, there are subtle differences with regards to the spatial and temporal regulation of the process and the composition of the divisome for both types of bacteria. Previously, only a single cytoskeleton ring of FtsZ was observed using cryo-ET in Gram-negative bacteria including *E. coli* and *C. crescentus* (Li et al., 2007; Szwedziak et al., 2014). However, we observed two rings corresponding to FtsA and FtsZ filaments in cryo-FIB-ET images of the Gram-positive bacterium *B. subtilis* during both vegetative growth and sporulation, even though the ratio of FtsZ to FtsA is same (5:1) in *B. subtilis* and *E. coli* (Feucht et al., 2001; Rueda et al., 2003). There are ~1000 molecules of FtsA in both *E. coli* and *B. subtilis* that are enough to form a circumferential ring but an A-ring is apparent only in *B. subtilis* although it appears more patchy than the mostly continuous Z-ring. One possible explanation for this phenomenon could be attributed to the fact that cell division in *B. subtilis* involves constriction of a septal disc composed of thicker septal PG corresponding to ~25 nm during sporulation and ~50 nm during vegetative growth. On the other hand, cell division in *E. coli* involves constriction of a septal disc composed of only a single layer of ~4 nm thick PG. Hence, cytokinesis in *B. subtilis* will likely depend on scaffolding action of multiple FtsAZ filaments to drive the circumferential motion of more molecules of PG synthases. The lateral spacing between FtsZ filaments is ~5.5 nm in *B. subtilis* which is slightly lower than the values reported in *E. coli* and *C. crescentus* (~6.5-

8 nm). Also, the distances of the Z-ring and the A-ring from the membrane in *B. subtilis* (~14 nm and ~6.5 nm respectively) are slightly shorter than the corresponding values for *E. coli* (~16 nm and ~8 nm respectively). It is possible that a tighter packing of FtsAZ filaments with each other and with the membrane in *B. subtilis* aids in efficient remodeling of the thicker septal PG. Whether these mechanisms of Z-ring and A-ring formation are also conserved in other sporulating and non-sporulating Gram-positive bacteria is yet to be explored.

Our cryo-FIB-ET data indicate that the Z-ring appears mostly continuous in the cellular sections we imaged, probably consisting of shorter overlapping filaments. 9 out of 16 tomograms of dividing vegetative cells that we captured showed more or less continuous Z-rings. The other tomograms were of significantly lower quality as they were either too thick or their orientation with respect to the tilt axis did not yield high-resolution information about the Z-ring. A previous cryo-ET study also revealed that the Z-rings are continuous in both *E. coli* and *C. crescentus* (Szwedziak et al., 2014). Howeber, superresolution microscopy data recently suggested that the organization of the Z-ring in both *B. subtilis* and *E. coli* is patchy with regions of low fluorescence intensity that indicate gaps in the ring (Holden et al., 2014; Strauss et al., 2012). This is in contrast to cryo-ET data which provides information at a resolution of a few nanometers. So far, it is difficult to ascertain the lengths of individual overlapping filaments unambiguously from our data and it is indeed possible that we do not see the gaps in our cryo-FIB-ET data as they may be present in the remainder of the cellular volume that has been ablated by cryo-FIB milling or not sampled due to missing wedge issue associated with cryo-ET data collection. However, it is unlikely as the ring appears continuous in multiple tomograms, all of which capture different parts of the septal disk.

During conditions of nutrient deprivation, *B. subtilis* initiates the sporulation pathway and the first architectural transformation that transpires is the shift in the division site from mid cell to one pole. Our data demonstrate that FtsAZ filaments are only localized on the mother cell side of the invaginating septum during sporulation. In addition, our data also reveal a correlation between number of FtsZ filaments tracking the division plane and the thickness of septal PG. The FtsZ series of dots span a length of ~50 nm in vegetative cells and ~27 nm in wild type sporulating cells which would translate to ~10 and ~5 FtsZ filament bands mediating cell division during vegetative growth and sporulation respectively (based on ~5.5 nm lateral spacing). Thinner septum during sporulation could be a likely adaptation to engulfment of the forespore by the mother cell which involves bending of the septum towards the mother cell and subsequent migration of the mother cell membrane around the forespore (Khanna et al., 2019). A thicker septum may then pose a steric block for engulfment membrane migration by being difficult to bend as has been observed in engulfment-defective strain of SpoIIDMP mutant sporangia which have considerably thicker septa than wild type sporangia.

These data indicate that during sporulation, not only is there asymmetry associated with the positioning of the division septum but also with the positioning of the division machinery. Asymmetric cell division is a common developmental theme in eukaryotes to generate progeny with diverse cellular fates (Li, 2013). During asymmetric cell division in *Caenorhabditis elegans*, the positioning of the sperm upon its entry in a newly formed zygote defines the posterior cell pole. A sperm associated signal then initiates the polarized distribution of PAR proteins which also regulate the alignment of the spindle by displacing it towards the posterior axis to ensure proper segregation of cell fate determinants. The asymmetric cleavage then produces two cells of different sizes and fates, the larger anterior cell and the smaller posterior cell (Li, 2013). Asymmetric division is also important for nervous system development in *Drosophila melanogaster* wherein neuroblasts, the precursors of the central nervous system divide asymmetrically to produce larger apical daughter which remains a neuroblast and a smaller basal ganglion mother cell (GMC). Polarity is established by differential distribution of cell fate determinants to the basal and apical cortex. In this case, the spindle itself becomes asymmetrical with apical microtubules elongating and basal microtubules shortening and the midbody positions itself asymmetrically between the spindle poles (Li, 2013).

In these and other cases of asymmetric cell division, the general theme is establishment of cell division machinery along an axis of polarity and distribution of cell fate determinants in a polarized manner along this axis. In case of *B. subtilis* sporulation, an axis of polarity is likely established when the division plane shifts from medial to polar position and cell fate determinants are differentially distributed between the future forespore and the mother cell compartments at the onset of membrane constriction. In this study, we have identified SpoIIE as a cell fate determinant that restricts FtsAZ filaments on the mother cell side for polar division by preferentially localizing on the forespore side of the invaginating septum. Although, we do not completely understand why SpoIIE localizes on the forespore side, it is possible that there are other, as of yet unidentified cell fate determinants that either recruit IIE or are recruited by IIE to the septum. This would explain why in the absence of IIE, even though the same number of FtsZ filaments track the septum as in the wild type vegetative septum, the invaginating septum is still ~10 nm thinner.

We also showed that the membrane-binding and FtsZ-binding domains of IIE are critical to regulate the divisome architecture. The case of IIE$^{malF\text{-}\Delta regI}$ is special as it is targeted to the septum similar to wild type sporangia but fails to restrict the localization of FtsAZ protofilaments to the mother cell side. IIE is only present on the forespore side even before membrane constriction begins and it is possible that IIE binding to pole-proximal FtsZ filaments and inserting its large membrane domain of 10 segments may induce a significant change in the membrane curvature. This may either render pole-proximal FtsZ filaments unavailable for other divisome proteins or conversely if the pole-proximal FtsZ is already bound to other divisome proteins, IIE may disrupt this interaction by competing for the same binding site via its large membrane-binding and/or FtsZ-binding domain. In support of this, we observed using time-lapse microscopy and structured-illumination microscopy, two puncta of fluorescently tagged FtsA at the division septum, one that constricts and another that remains at the intersection of the lateral and septal cell wall at the forespore edge in a few cells (Fig. 2.4). However, more biochemical evidence is needed to establish conclusively the mechanism by which IIE interacts with different components of the divisome to negatively regulate sporulation cell division.

Overall, our data provide a significant advancement in the understanding of the organization of the divisome, its regulators and its role in septal PG synthesis in *Bacillus subtilis*. We anticipate that future efforts to identify the molecular arrangement of FtsZ and its regulators inside the cell will aid in development of new antimicrobials targeting the cell division machinery in important pathogens.

2.5 Materials and Methods

Strain and culture conditions

Bacillus subtilis PY79 background was used for all strain constructions. A list of strains used in the study is provided in Table 2.1. All the strains were routinely grown in LB plates at 30°C overnight. For sample preparation, cells were either grown in LB media at 30°C to OD_{600} ~0.5 for vegetative growth or by growing in ¼ diluted LB to OD600 ~0.5-0.8 and then resuspending in A+B media at 37°C for inducing sporulation. For wild type sporangia, samples were prepared at an early enough time point of ~T1.5-1.75 hr after inducing sporulation to capture a mixed population of dividing cells undergoing the formation of polar septum (sporulating cells) or medial septum (vegetative cells). For other mutant sporangia, samples were also collected at ~T1.5-1.75 hr after inducing sporulation.

Cryo-FIB-ET workflow

QUANTIFOIL® R2/1 200 mesh holey carbon Cu grids (Quantifoil Micro Tools) were glow discharged using PELCO easiGlow (Ted Pella). 7-8 µl of diluted liquid culture was deposited onto the grids which were then mounted to a manual plunger (Max Planck Institute of Biochemistry). They were then manually blotted using Whatman No. 1 filter paper for 3-4 seconds from the side opposite to where the cells were deposited to remove excess resuspension media such that the cells formed a homogeneous monolayer on the grid surface. The grids were then plunge-frozen in a 50-50 mixture of liquid ethane and propane (Airgas) cooled to liquid nitrogen temperature and subsequently clipped onto Cryo-FIB Autogrids (Thermo Fisher Scientific). All subsequent transfers were performed in liquid nitrogen.

Frozen-hydrated cells were micromachined either inside Scios or Aquilos DualBeam instruments each equipped with a cryo-stage (Thermo Fisher Scientific). An integrated gas injection system (GIS) was used to deposit an organometallic platinum layer inside the FIB chamber to protect the specimen surface and avoid uneven thinning of cells. In case of specimens prepared in Aquilos, the specimen was also sputter coated with inorganic platinum layer prior to GIS deposition to prevent charging during imaging. FIB milling was then performed using two rectangular milling patterns to ablate the top and the bottom parts of the cells in steps of decreasing ion beam currents at a nominal tilt of 11^o-15^o which translates into a milling angle of 4^o-8^o. Initial rough milling was performed using ion beam currents of 0.5-0.3 nA followed by intermediate milling at 0.1 nA or 50 pA. Finally, fine milling was conducted at 30 pA. In each of the steps, the distance between the two rectangular milling patterns was sequentially decreased to get ~100-300 nm thick lamellas.

Tilt series were collected using SerialEM software (Mastronarde, 2005) either in 300-keV Tecnai G2 Polara or in 300-keV Titan Krios (Thermo Fisher Scientific), both equipped with a Quantum post-column energy filter (Gatan) and a K2 Summit 4k x 4k pixel direct detector camera (Gatan). The TEM magnification corresponded to a camera pixel size of either 0.612 nm (for data acquired on Polara) or 0.534 nm or 0.426 nm (for data acquired on Krios). The tilt series were usually collected from -61^o to $+ 61^o$ depending on the quality of the specimen with an increment ranging from 2^o-3^o with a defocus of -5 µm following either the bidirectional or the dose-symmetric tilt scheme in low dose mode. For both schemes, the zero of the tilt series was defined by taking into account the pre-tilt of the lamella. The K2 detector was operated in counting mode and images divided into frames of 0.1s. The cumulative dose for each tilt series was ~50-150 e-/Å2.

Tomogram reconstruction and segmentation

MotionCor2 (Zheng et al., 2017) was used to align the frames and dose-weigh the tilt series according to the cumulative dose. Subsequent alignment of the tilt series was done in IMOD (Kremer et al., 1996) using patch-tracking in the absence of fiducials and the tomograms reconstructed using weighted back-projection method. For purposes of representation and segmentation tomograms were binned 3x or 4x. Semi-automatic segmentation of the membranes was performed using a MATLAB script, TomosegmemTV (Martinez-Sanchez et al., 2014) which were then manually refined in Amira software package (Thermo Fisher Scientific). FtsAZ filaments were manually traced in Amira.

Image Analysis

Distribution of intensities of cytoskeletal rings

For Fig. 2.1L and Fig. S2.4D, the membrane-proximal and membrane-distal cytoskeletal rings were masked using Adobe Photoshop and the corresponding intensity values for each pixel were extracted using a custom-built MATLAB script. The distribution of these values for the two rings were depicted as box-and-whisker plot alongside those corresponding to cell membrane, cytoplasm and cell wall (PG) that were used as controls.

Distances between cytoskeletal rings and membrane

For Fig. 2.2A, a medial slice corresponding to the orthogonal view (xz) of the respective tomograms was taken from the z-stack wherein the cytoskeletal rings were clearly visible. The distances of the ring from the cell membrane were then calculated using the Fiji plugin ‘points to distance’.

Fluorescence microscopy for batch cultures

~12 µl of sample were taken at indicated time points and transferred to 1.2% agarose pads that were prepared using either sporulation resuspension media (for sporulating cultures) or ¼ LB media (for vegetative growth). Membranes were stained with 0.5 µg/ml of FM4-64 (Thermo Fisher Scientific) that was added directly to the pads. An Applied Precision DV Elite optical sectioning microscope equipped with a Photometrics CoolSNAP-HQ2 camera was used to visualize the cells. The images were deconvolved using SoftWoRx v5.5.1 (Applied Precision). For all fluorescence images, the medial focal plane of the image is shown. Excitation/emission filters were TRITC/CY5 for membrane imaging and FITC/FITC to visualize GFP or mNeonGreen signal.

3D-Structured Illumination Microscopy (3D-SIM)

For Fig. 2.4B, cells were grown as indicated above and stained with 0.5 µg/mL FM4-64. An Applied Precision/GE OMX V2.2 Microscope was then used to image them. Raw data were sequentially taken by SI-super-resolution light path to collect 1.5 mm thick specimens in 125 nm increments in the z-axis with compatible immersion oils (Applied Precision). Standard OMX SI reconstruction parameters were then used in DeltaVision SoftWoRx Image Analysis Program to reconstruct the images. To plot the graph in Fig. 2.4C, the data corresponding to membrane and mNeonGreen intensity was grouped into smaller bins of approximately equal area along the normalized length of the cell (as indicated in the inset) using a custom-built MATLAB script.

Spore titer assay

Strains were grown in triplicates in 2 ml of DSM media for 24 hr at 37^{o}C followed by heating at 80^{o}C for 20 min. Then, serial dilutions for each strain were prepared and spotted on LB plates. Number of colonies were then used as a marker to calculate spore titers.

Calculating GFP intensity

For Fig. S2.7C, ~15-16 cells with clear evidence of septal biogenesis were manually selected for each strain and all the images aligned such that the polar septum lies in the same orientation for all cells as shown in the inset of Fig. S2.7C(i). To get the linear profile of GFP intensity for each cell, the data was grouped into smaller bins of approximately equal area using a custom-built MATLAB script. Normalized GFP intensities were then plotted for each cell along its normalized length as depicted by different curves in the graphs.

2.6 References

Arigoni F, Pogliano K, Webb CD, Stragier P, Losick R. 1995. Localization of protein implicated in establishment of cell type to sites of asymmetric division. *Science (80-)*. doi:10.1126/science.270.5236.637

Barák I, Youngman P. 1996. SpoIIE mutants of Bacillus subtilis comprise two distinct phenotypic classes consistent with a dual functional role for the SpoIIE protein. *J Bacteriol*. doi:10.1128/jb.178.16.4984-4989.1996

Bi E, Lutkenhaus J. 1991. FtsZ ring structure associated with division in Escherichia coli. *Nature* **354**:161–164. doi:10.1038/354161a0

Bisson AW, Hsu YP, Squyres GR, Kuru E, Wu FB, Jukes C, Sun YJ, Dekker C, Holden S, VanNieuwenhze MS, Brun Y V, Garner EC. 2017. Treadmilling by FtsZ filaments drives peptidoglycan synthesis and bacterial cell division. *Science (80-)* **355**:739–743. doi:10.1126/science.aak9973

Carniol K, Ben-Yehuda S, King N, Losick R. 2005. Genetic dissection of the sporulation protein SpoIIE and its role in asymmetric division in Bacillus subtilis. *J Bacteriol*. doi:10.1128/JB.187.10.3511-3520.2005

De Boer P, Crossley R, Rothfield L. 1992. The essential bacterial cell-division protein FtsZ is a GTPase. *Nature*. doi:10.1038/359254a0

Errington J. 2003. Regulation of endospore formation in Bacillus subtilis. *Nat Rev Microbiol* **1**:117–126. doi:10.1038/nrmicro750

Eswaramoorthy P, Winter PW, Wawrzusin P, York AG, Shroff H, Ramamurthi KS. 2014. Asymmetric Division and Differential Gene Expression during a Bacterial Developmental Program Requires DivIVA. *PLoS Genet* **10**. doi:10.1371/journal.pgen.1004526

Feucht A, Lucet I, Yudkin MD, Errington J. 2001. Cytological and biochemical characterization of the FtsA cell division protein of Bacillus subtilis. *Mol Microbiol*. doi:10.1046/j.1365-2958.2001.02356.x

Gamba P, Veening JW, Saunders NJ, Hamoen LW, Daniel RA. 2009. Two-step assembly dynamics of the Bacillus subtilis divisome. *J Bacteriol*. doi:10.1128/JB.01758-08

Guberman JM, Fay A, Dworkin J, Wingreen NS, Gitai Z. 2008. PSICIC: Noise and asymmetry in bacterial division revealed by computational image analysis at sub-pixel resolution. *PLoS Comput Biol*. doi:10.1371/journal.pcbi.1000233

Haeusser DP, Margolin W. 2016. Splitsville: Structural and functional insights into the dynamic bacterial Z ring. *Nat Rev Microbiol*. doi:10.1038/nrmicro.2016.26

Holden SJ, Pengo T, Meibom KL, Fernandez CF, Collier J, Manley S. 2014. High throughput 3D super-resolution microscopy reveals Caulobacter crescentus in vivo Z-ring organization. *Proc Natl Acad Sci U S A*. doi:10.1073/pnas.1313368111

Illing N, Errington J. 1991. Genetic regulation of morphogenesis in Bacillus subtilis: Roles of σ(E) and σ(F) in prespore engulfment. *J Bacteriol* **173**:3159–3169.

Khanna K, Lopez-Garrido J, Zhao Z, Watanabe R, Yuan Y, Sugie J, Pogliano K, Villa E. 2019. The molecular architecture of engulfment during Bacillus subtilis sporulation. *Elife*. doi:10.7554/eLife.45257

Kremer JR, Mastronarde DN, McIntosh JR. 1996. Computer visualization of three-dimensional image data using IMOD. *J Struct Biol* **116**:71–6. doi:10.1006/jsbi.1996.0013

Levin PA, Losick R, Stragier P, Arigoni F. 1997. Localization of the sporulation protein SpoIIE in Bacillus subtilis is dependent upon the cell division protein FtsZ. *Mol Microbiol* **25**:839–846.

Li R. 2013. The art of choreographing asymmetric cell division. *Dev Cell*. doi:10.1016/j.devcel.2013.05.003

Li Z, Trimble MJ, Brun Y V., Jensen GJ. 2007. The structure of FtsZ filaments in vivo suggests a force-generating role in cell division. *EMBO J* **26**:4694–4708. doi:10.1038/sj.emboj.7601895

Lopez-Garrido J, Ojkic N, Khanna K, Wagner FR, Villa E, Endres RG, Pogliano K. 2018. Chromosome Translocation Inflates Bacillus Forespores and Impacts Cellular Morphology. *Cell* **172**:758-770.e14. doi:10.1016/j.cell.2018.01.027

Lucet I. 2000. Direct interaction between the cell division protein FtsZ and the cell differentiation protein SpoIIE. *EMBO J*. doi:10.1093/emboj/19.7.1467

Martinez-Sanchez A, Garcia I, Asano S, Lucic V, Fernandez JJ. 2014. Robust membrane detection based on tensor voting for electron tomography. *J Struct Biol* **186**:49–61. doi:10.1016/j.jsb.2014.02.015

Mastronarde DN. 2005. Automated electron microscope tomography using robust prediction of specimen movements. *J Struct Biol* **152**:36–51. doi:10.1016/j.jsb.2005.07.007

Mukherjee A, Lutkenhaus J. 1994. Guanine nucleotide-dependent assembly of FtsZ into filaments. *J Bacteriol*. doi:10.1128/jb.176.9.2754-2758.1994

Pichoff S, Lutkenhaus J. 2005. Tethering the Z ring to the membrane through a conserved membrane targeting sequence in FtsA. *Mol Microbiol*. doi:10.1111/j.1365-2958.2005.04522.x

Rueda S, Vicente M, Mingorance J. 2003. Concentration and assembly of the division ring proteins FtsZ, FtsA, and ZipA during the Escherichia coli cell cycle. *J Bacteriol*. doi:10.1128/JB.185.11.3344-3351.2003

Strauss MP, Liew ATF, Turnbull L, Whitchurch CB, Monahan LG, Harry EJ. 2012. 3D-SIM Super Resolution Microscopy Reveals a Bead-Like Arrangement for FtsZ and the Division Machinery: Implications for Triggering Cytokinesis. *PLoS Biol*. doi:10.1371/journal.pbio.1001389

Szwedziak P, Wang Q, Bharat TAM, Tsim M, Lowe J. 2014. Architecture of the ring formed by the tubulin homologue FtsZ in bacterial cell division. *Elife* **3**:52. doi:10.7554/eLife.04601

Szwedziak P, Wang Q, Freund SM, Löwe J. 2012. FtsA forms actin-like protofilaments. *EMBO J* **31**:2249–2260. doi:10.1038/emboj.2012.76

Tan IS, Ramamurthi KS. 2014. Spore formation in Bacillus subtilis. *Environ Microbiol Rep*. doi:10.1111/1758-2229.12130

Tocheva EI, Lopez-Garrido J, Hughes H V, Fredlund J, Kuru E, VanNieuwenhze MS, Brun Y V, Pogliano K, Jensen GJ. 2013. Peptidoglycan transformations during Bacillus subtilis sporulation. *Mol Microbiol* **88**:673–686. doi:10.1111/mmi.12201

Wang X, Lutkenhaus J. 1993. The FtsZ protein of Bacillus subtilis is localized at the division site and has GTPase activity that is dependent upon FtsZ concentration. *Mol Microbiol*. doi:10.1111/j.1365-2958.1993.tb01705.x

Wu LJ, Feucht A, Errington J. 1998. Prespore-specific gene expression in Bacillus subtilis is driven by sequestration of SpoIIe phosphatase to the prespore side of the asymmetric septum. *Genes Dev*. doi:10.1101/gad.12.9.1371

Yang X, Lyu Z, Miguel A, McQuillen R, Huang KC, Xiao J. 2017. GTPase activity-coupled treadmilling of the bacterial tubulin FtsZ organizes septal cell wall synthesis. *Science (80-)*. doi:10.1126/science.aak9995

Youngman P, Perkins JB, Losick R. 1984. A novel method for the rapid cloning in Escherichia coli of Bacillus subtilis chromosomal DNA adjacent to Tn917 insertions. *Mol Gen Genet* **195**:424–33.

Zheng SQ, Palovcak E, Armache JP, Verba KA, Cheng Y, Agard DA. 2017. MotionCor2: Anisotropic correction of beam-induced motion for improved cryo-electron microscopy. *Nat Methods*. doi:10.1038/nmeth.4193

2.7 Figures

Figure 2.1. Architecture of divisome in dividing vegetative *B. subtilis* cells. (A) Schematic of cell division in *B. subtilis* during (i) vegetative growth and (ii) sporulation. The thickness of the septa upon its closure is indicated for both cases. **(B)** Schematic to explain the visualization of cells in different planes in 3D. (i) Initially, the rod-shaped *Bacillus* cell lies flat on an EM grid. (ii) 3D view of a cellular section upon cryo-FIB-ET treatment using the xyz coordinate axis system. x axis represents the length along the short axis of the cell, y axis represents the length along the long axis of the cell and z axis represents the height of the cellular specimen. (iii) Top panel, projection image of the cell in the xy coordinate plane (top view). Bottom panel, the corresponding projection image in the xz coordinate plane when the cell is rotated about its short axis by 90°. The lateral and septal PG are also indicated. **(C)** Slice through a tomogram of a dividing vegetative cell. The insets (*l* for left and *r* for right side of the septum) highlight the leading edge of the invaginating septum. Scale bar: 200 nm. **(D)** Left panel, zoomed-in view of the inset in (C) corresponding to '*l*' in the xy coordinate plane. Right panel, same as left with PG (grey), cell membrane (peach), membrane-proximal series of dots (pink) and membrane-distal series of dots (blue) highlighted. The same color scheme is followed throughout. **(E)** Left panel, zoomed-in view of the inset in (C) corresponding to '*r*' in the xy coordinate plane. Right panel, same as left with different cellular parts highlighted**.** Scale bars for (D) and (E): 25 nm. **(F)** Left panel, view of the septal disk corresponding to (D) in the xz coordinate plane obtained by rotating the cell around its short axis by 90°. Right panel, same as left with PG, cell membrane, membrane-proximal ring and membrane-distal ring highlighted. **(G)** Left panel, view of the septal disk corresponding to (E) in the xz coordinate plane obtained by rotating the cell around its short axis by 90°. Right panel, same as left with different cellular parts highlighted. Scale bars for (F) and (G): 25 nm. **(H)** Schematic of the arrangement of the cytoskeletal machinery in dividing vegetative cells as seen in the xy and xz coordinate planes. All cellular parts detailed previously are highlighted in the same color scheme. **(I)** Annotation of the cell membrane, membrane-proximal ring and membrane-distal ring for the tomogram shown in (C). **(J)** and **(K)** represent zoomed-in views of the left (l) side and the right (r) side of the invaginating septum of the segmentation in (I) respectively. Scale bars are omitted from (I) – (K) owing to their perspective nature. **(L)** Box-and-whisker plot depicting the distribution of intensity values for the region traced by the membrane-distal and the membrane-proximal rings in the range of 0 to 255. A region with approximately similar area was masked for PG, cell membrane and cytoplasm as controls. Lower the intensity value of the pixel in the RGB color space, the darker it is. Also see extended data 1 and 2.

Figure 2.1

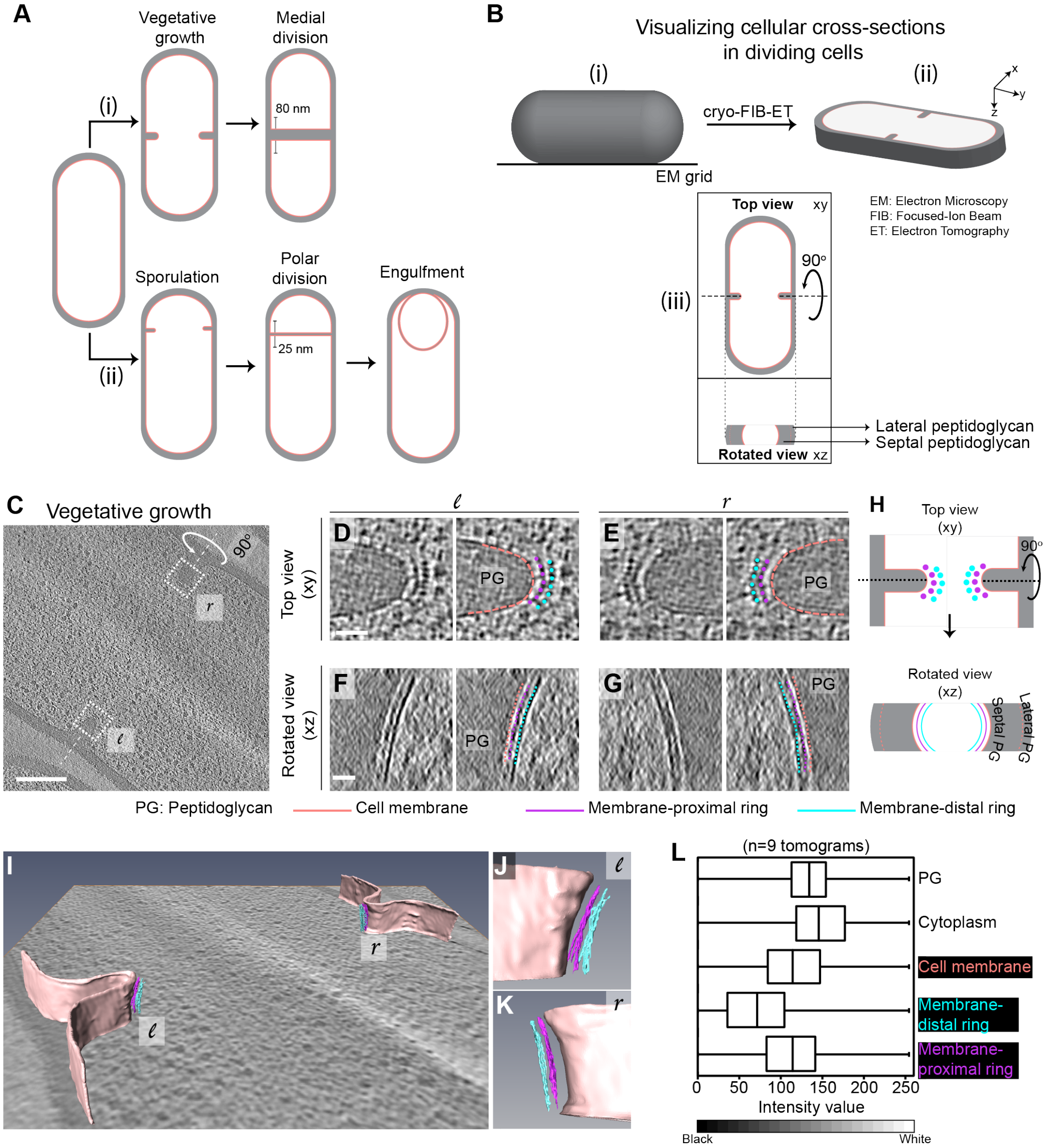
A
Vegetative growth
Medial division
(i)
80 nm
Sporulation
Polar division
Engulfment
(ii)
25 nm
B
Visualizing cellular cross-sections in dividing cells
(i)
(ii)
cryo-FIB-ET
EM grid
x
y
z
Top view xy
90°
(iii)
Rotated view xz
Lateral peptidoglycan
Septal peptidoglycan
EM: Electron Microscopy
FIB: Focused-Ion Beam
ET: Electron Tomography
C
Vegetative growth
90°
r
ℓ
ℓ
r
Top view (xy)
Rotated view (xz)
D
E
F
G
PG
H
Top view (xy)
90°
Rotated view (xz)
Septal PG
Lateral PG
PG: Peptidoglycan
Cell membrane
Membrane-proximal ring
Membrane-distal ring
I
r
ℓ
J
ℓ
K
r
L
(n=9 tomograms)
PG
Cytoplasm
Cell membrane
Membrane-distal ring
Membrane-proximal ring
0
50
100
150
200
250
Intensity value
Black
White

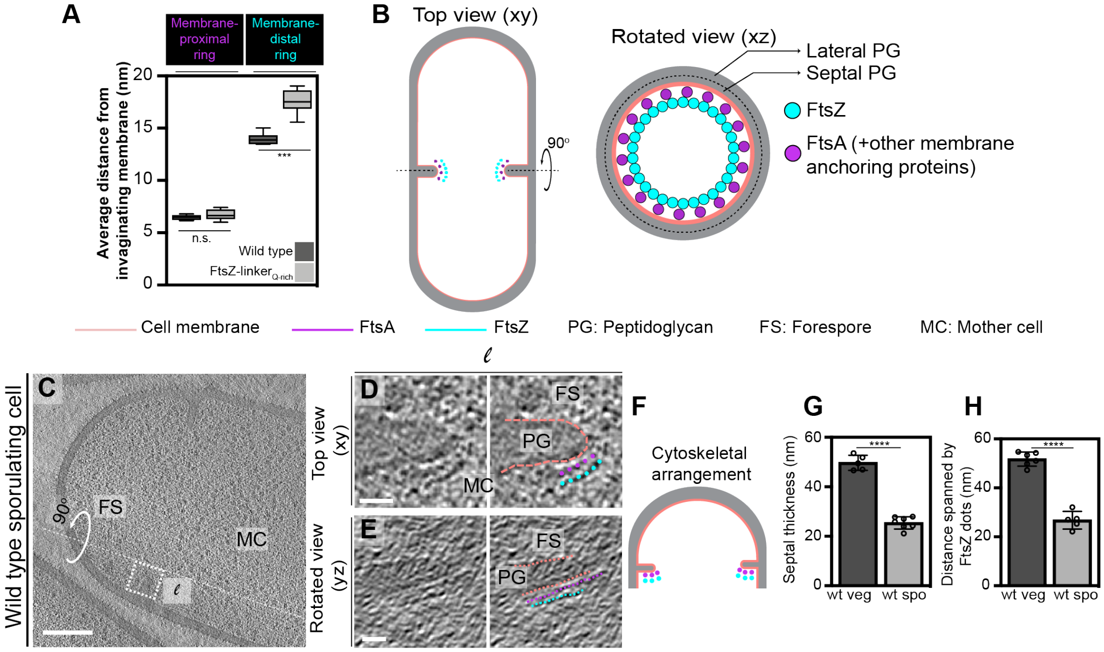

Figure 2.2. Identity of cytoskeletal filaments and their localization during sporulation. (A) Box-plot showing the distance of the membrane-proximal and the membrane-distal rings from the cell membrane in wild type and FtsZ-linker$_{Qrich}$ strains. Error bars indicate standard deviation (n.s.: p>0.05, ***: p ≤0.001, unpaired t-test). **(B)** Schematic highlighting the arrangement and identity of the cytoskeletal machinery with PG (grey), cell membrane (peach), FtsZ (blue) and FtsA (pink) highlighted. In the top view (xy coordinate plane), the cytoskeletal machinery is visible as two series of dots at the nascent septum. In the rotated view (xz coordinate plane), denser and more continuous Z-ring formed by overlapping filaments of FtsZ filaments is tethered to the membrane via a less continuous A-ring formed by FtsA filaments and likely other smaller cell division proteins. **(C)** Slice through a tomogram of a dividing sporulating cell. The forespore and mother cell compartments are indicated. Scale bar: 200 nm. **(D)** Left panel, zoomed-in view of the inset in (C) in the xy coordinate plane. Right panel, same as left with PG (grey), cell membrane (peach), FtsA series of dots (pink) and FtsZ series of dots (blue) highlighted. **(E)** Left panel, view of the septal disk corresponding to (D) in the yz coordinate plane obtained by rotating the cell around its long axis near the left side of the invaginating septum by 90°. Right panel, same as left with cellular parts and FtsAZ filaments highlighted. Scale bars for (D) and (E): 25 nm. (F) Schematic of the arrangement of cytoskeletal machinery during sporulation. **(G)** & **(H)** Bar graph depicting (G) septal thickness and (H) distance spanned by FtsZ series of dots in wild type vegetative and sporulating cells. For both, error bars indicate standard deviation. (****: p ≤0.0001, unpaired t-test). Also see extended data 3-6.

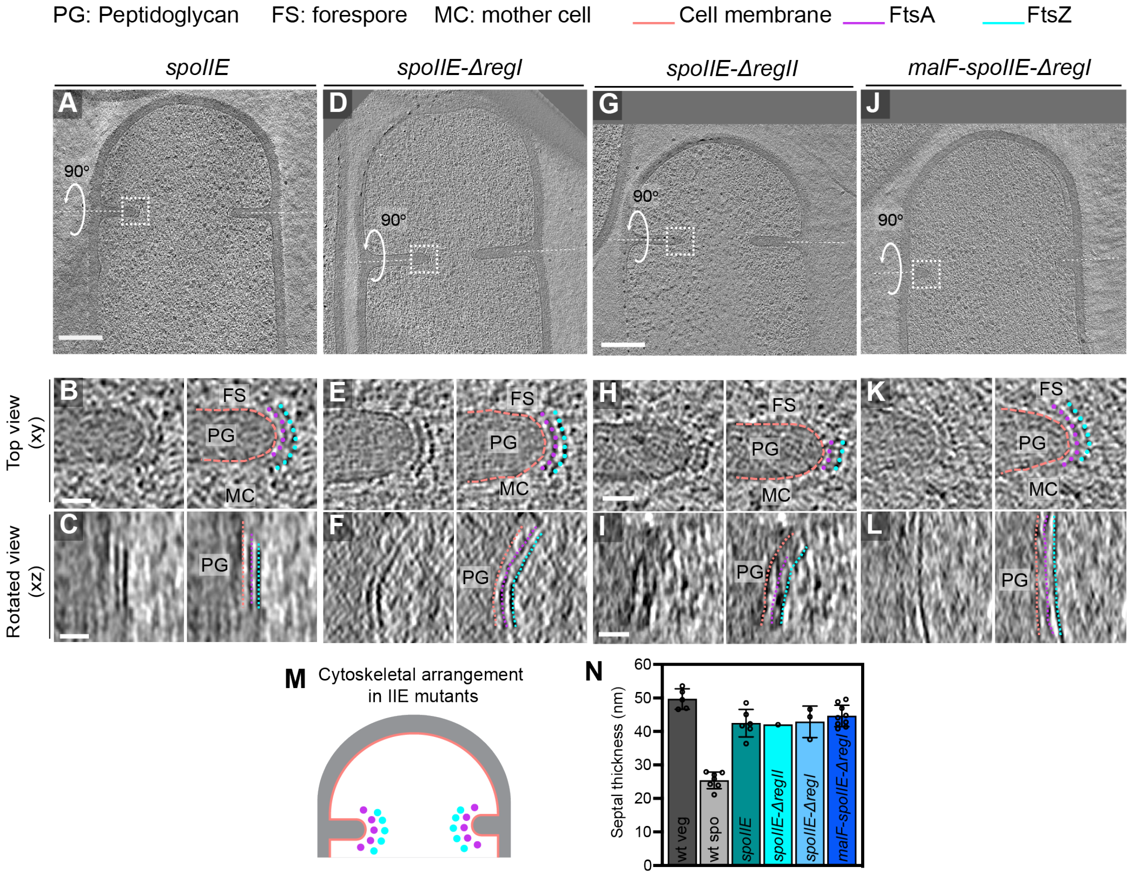

Figure 2.3. FtsAZ filaments in SpoIIE mutant sporangia. (A,D,G,J) Slice through a tomogram of a dividing **(A)** *spoIIE*, **(D)** *spoIIE-ΔregI*, **(G)** *spoIIE-ΔregII*, and **(J)** *malF-spoIIE-ΔregI* sporangia. Inset highlights the left side of the invaginating septum. **(B,E,H,K)** Left panel, zoomed-in view of the inset in (A,D,G,J) respectively in the xy coordinate plane. Right panel, same as left with the forespore (FS) and the mother cell (MC) compartments indicated in all. PG (grey), cell membrane (peach), FtsA series of dots (pink) and FtsZ series of dots (blue) are also highlighted for all. **(C,F,I,L)** Left panel, view of the septal disk corresponding to (B,E,H,K) respectively in the xz coordinate plane obtained by rotating the cell around its short axis by 90°. Right panel, same as left with cellular parts and FtsAZ filaments highlighted. Scale bars for (A,D,G,J): 200 nm and for (B,C,E,F,H,I,K,L): 25 nm. (M) Schematic of the arrangement of the cytoskeletal machinery in SpoIIE mutant sporangia from (A)-(L). PG (grey), cell membrane (peach), FtsA dots (pink) and FtsZ dots (blue) are indicated. (N) Bar graph depicting the septal thickness in wild type vegetative and sporulating cells and SpoIIE mutant sporangia. Error bars indicate standard deviation. Each dot indicates a sample point.

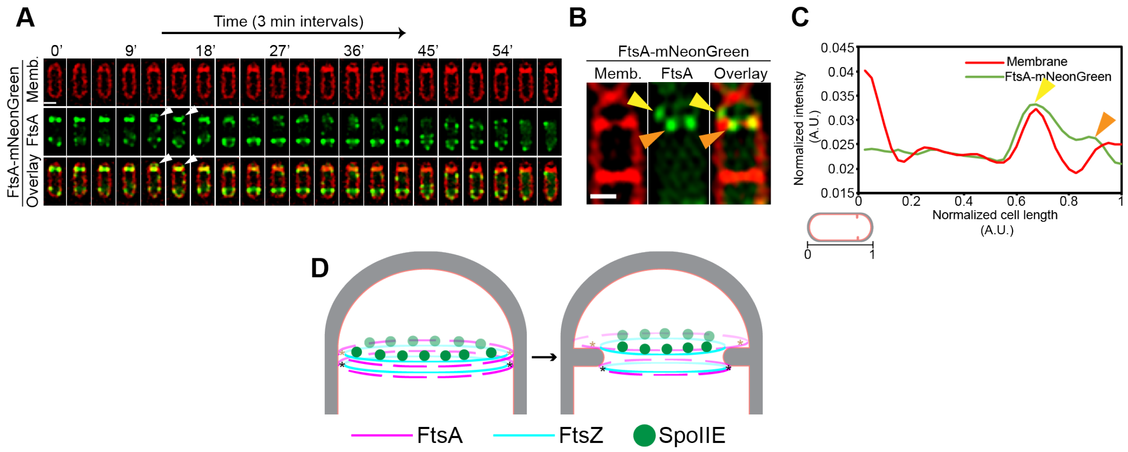

Figure 2.4. Possible model for explaining the role of SpoIIE in FtsAZ filament localization. (A) Timelapse fluorescent microscopy of dividing sporulating cell wherein FtsA (green) is tagged with mNeonGreen. Membranes (red) are stained with FM4-64. Images are taken every 3 minutes. At time point of 12 and 15 minutes, two FtsA rings are visible, one that constricts and the other that stays behind possibly on the forespore side of the septum. White arrows are used to indicate the FtsA ring on the forespore side that does not constrict. Scale bar: 1 μm. **(B)** Structured-illumination microscopy of a dividing sporulating cell where FtsA (green) is tagged with mNeonGreen. Membranes (red) are stained with FM4-64. The two dots corresponding to FtsA are more clearly visible, one on the forespore side (yellow arrow) and the other that constricts (orange arrow). Scale bar: 1 μm. **(C)** Line graph showing the normalized intensity of the membrane (red) and FtsA-mNeonGreen (green) signal along the normalized length of the cell. Two peaks corresponding to two dots of FtsA in (B) are indicated by yellow and orange arrow. **(D)** Schematic to explain a possible model of how SpoIIE (green circles) affects the localization of FtsA (pink) and FtsZ (blue) filaments during sporulation. PG (grey) and cell membrane (peach) are also highlighted. IIE molecules are preferentially present on the forespore side and hence bind to FtsZ on the forespore side (brown asterisks), preventing constriction of FtsA filaments (and likely the rest of the cell division proteins) on the forespore side while the FtsAZ filaments on the mother cell side (black asterisks) are able to constrict.

2.8 Supplemental Data

Table 2.1 Strain list for Chapter 2

Strain	Genotype or description	Reference, source or construction
PY79	Wild type	(Youngman et al., 1984)
KK240	*ftsZ-linker*$_{\textit{Q-rich}}$*Ωkan*	This study
KP69	*spoIIE::*Tn917	(Sandman et al., 1987)
KC548	*spoIIE::phleo spoIIA::cat amyE::spoIIE-ΔregII-gfp cat spc*	(Carniol et al. 2005)
KC549	*spoIIE::phleo spoIIA::cat amyE::spoIIE-ΔregI-gfp cat spc*	(Carniol et al. 2005)
KC538	*spoIIE::phleo spoIIA::spec amyE::malF-spoIIE-ΔregI gfp spc kan*	(Carniol et al. 2005)

KK240

Constructed by transformation of pKK238 (*ftsZ-linker*$_{\textit{Q-rich}}$*Ωkan*) into PY79. pKK238 was constructed by removing ssrA tag of pJLG142 and incorporating Q-rich linker from FtsN of *E. coli* at the C-terminus of FtsZ.

FtsZ-linker$_{\text{Q-rich}}$ sequence (Q-rich linker region highlighted in yellow and red):

```
MLEFETNIDGLASIKVIGVGGGGNNAVNRMIENEVQGVEYIAVNTDAQALNLSKAEVKMQIGAKLTRGLGAGANPEV
GKKAAEESKEQIEEALKGADMVFVTAGMGGGTGTGAAPVIAQIAKDLGALTVGVVTRPFTFEGRKRQLQAAGGISAM
KEAVDTLIVIPNDRILEIVDKNTPMLEAFREADNVLRQGVQGISDLIATPGLINLDFADVKTIMSNKGSALMGIGIA
TGENRAAEAAKKAISSPLLEAAIDGAQGVLMNITGGTNLSLYEVQEAADIVASASDQDVNMIFGSVINENLKDEIVV
TVIATGFIEQEKDVTKPQRPSLNQSIKTHNQSVPKREPKREEPQQQNTVSRHTSQPARQQPTQLVEVPWNEQTPEQR
QQTLQRQRQAQQLAEQQRLAQQSRTTEQSWQQQTRTSQAAPVQAQPRQSKPASSQQPYQDLLQTPAHTTAQSKPQQD
DTLDIPTFLRNRNKRG
```

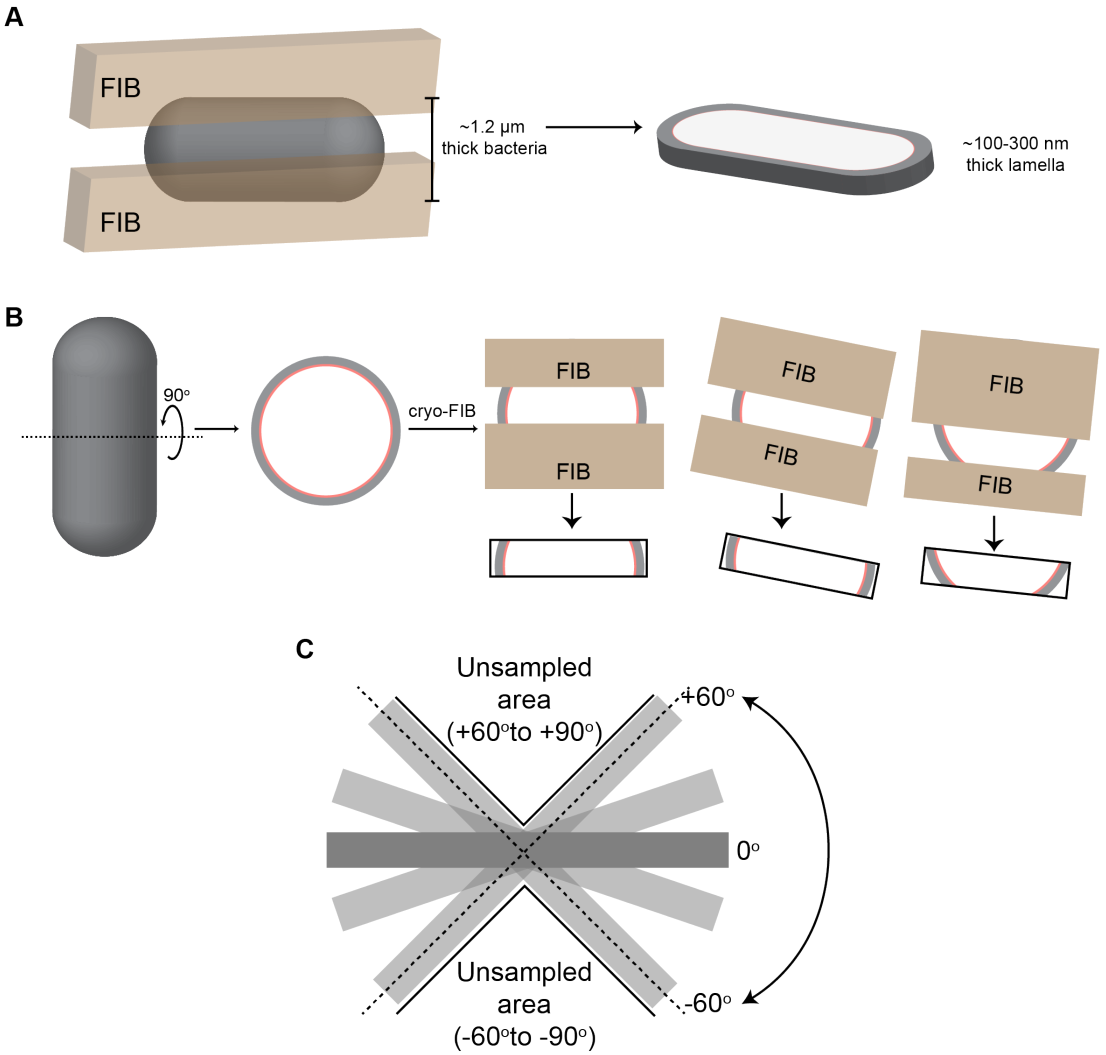

Figure S2.1. Related to Figure 1. (A) Schematic of a rod-shaped cell (grey) subjected to cryo-focused ion beam (FIB) milling. Two parallel beam of gallium ions (brown) ablate the cellular material from the top and the bottom of the cell leaving a thin slice (~100-300 nm thick) for imaging using cryo-electron tomography (cryo-ET). **(B)** Schematic depicting different sections of the septal disk that can be captured when a rod-shaped cell is FIB-milled depending on the milling angle, orientation of the cell on the EM grid and orientation of the cell with respect to the tilt axis. **(C)** Schematic depicting the missing wedge issue in cryo-ET workflow. Since we are only able to image from ~ ± 60°, the area from -60° to -90° and from +60° to +90° remains unsampled leading to missing information for these areas.

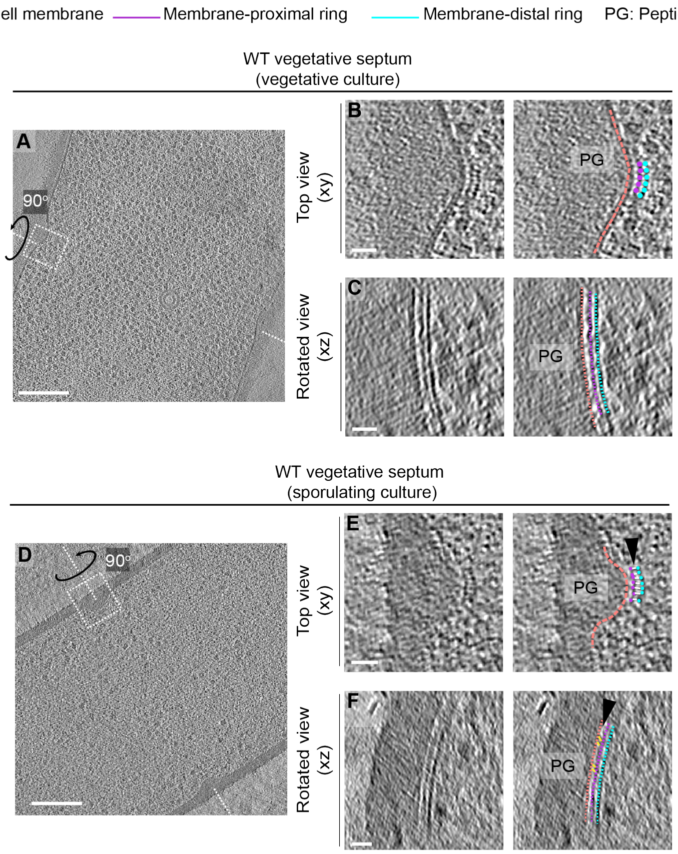

Figure S2.2. Related to Figure 1. (A) Slice through a tomogram of a dividing vegetative cell under vegetative culture conditions *(See Materials and Methods)*. The inset highlights the left side of the leading edge of the invaginating septum. Scale bar: 200 nm. **(B)** Left panel, zoomed-in view of the inset in (A) in the xy coordinate plane. Right panel, same as left with PG (peptidoglycan, gray), cell membrane (peach), membrane-proximal series of dots (pink) and membrane-distal series of dots (blue) highlighted. The same color scheme for labeling cellular parts is followed throughout. **(C)** Left panel, view of the septal disk corresponding to (B) in the xz coordinate plane obtained by rotating the cell around its short axis by 90°. Right panel, same as left with different cellular parts and FtsAZ filaments highlighted. Scale bars for (B) and (C): 25 nm. **(D)** Slice through a tomogram of a dividing vegetative cell under sporulation culture conditions *(See Materials and Methods)*. The inset highlights the left side of the leading edge of the invaginating septum. Scale bar: 200 nm. **(E)** Left panel, zoomed-in view of the inset in (A) in the xy coordinate plane. Right panel, same as left with different cellular parts highlighted. Densities connecting the membrane-proximal and membrane-distal series of dots are indicated in white (as pointed by a black arrow). **(F)** Left panel, view of the septal disk corresponding to (E) in the xz coordinate plane obtained by rotating the cell around its short axis by 90°. Right panel, same as left with different cellular parts and FtsAZ filaments highlighted. Densities connecting the membrane-proximal ring to the membrane are highlighted in yellow (as pointed by a black arrow). Scale bars for (E) and (F): 25 nm.

Figure S2.3. Related to Figure 2. **(A)** Morphology of FtsZ-linker$_{\text{Q-rich}}$ strain during vegetative growth and **(B)** sporulation. Membranes are stained with FM4-64. The cells indicated by white arrows show a filamentous phenotype. **(C)** Spore titer of wild type and FtsZ-linker$_{\text{Q-rich}}$ (see Materials and Methods). **(D)** Slice through a tomogram of FtsZ-linker$_{\text{Qrich}}$ dividing cell. The insets (*l* for left and *r* right for right side of the septum) highlight the leading edge of the invaginating septum. Scale bar: 200 nm. A schematic showing the construction of the modified strain is overlaid on the tomogram slice wherein PG (gray), cell membrane (peach) are highlighted. FtsZ (blue) is tethered to the membrane via FtsA (pink) and the two interact via a linker region (black + Q-rich linker in orange). The same color scheme is followed throughout the figure. **(E)** Left panel, zoomed-in view of the inset in (D) corresponding to '*l*' in the xy coordinate plane. Right panel, same as left with PG, cell membrane, membrane-proximal series of dots and membrane-distal series of dots highlighted**.** Black arrows indicate membrane-distal dots that are likely not tethered to the membrane via membrane-proximal dots. Green and red stars are used to differentiate the two opposite sides of the dividing septum. **(F)** Left panel, view of the septal disk corresponding to (E) in the xz coordinate plane obtained by rotating the cell around its short axis by 90°. Right panel, same as left with different cellular parts and FtsAZ filaments highlighted. Scale bar for (E) and (F): 25 nm. **(G)** Segmentation of the cell membrane (peach) corresponding to (E) & (F). Red and green stars indicate the two opposite sides. **(H)** View of the side highlighted by the green star obtained by rotating the cell by 90° as indicated in (G). Membrane-distal dots highlighted by black arrows in the right panel of (E) are highlighted. **(I)** Same as (G) except that the cell is rotated along its short axis by 90° to get a view of the septum side indicated by the red star. **(J)** View of the side highlighted by the red star. Membrane-distal dots highlighted by black arrows in the right panel of (E) are highlighted. Scale bars are omitted from (G)-(J) owing to their perspective nature. **(K)** Left panel, zoomed-in view of the inset in (D) corresponding to '*r*' in the xy coordinate plane. Right panel, same as left with different cellular parts highlighted**.** Doublets of the membrane-distal series of dots are indicated by blue arrows. **(L)** Left panel, view of the septal disk corresponding to (K) in the xz coordinate plane obtained by rotating the cell around its short axis by 90°. Right panel, same as left with different cellular parts and FtsAZ filaments highlighted. Scale bar for (K) and (L): 25 nm. **(M)** and **(N)** Two views of the annotated cell membrane, membrane-proximal and membrane-distal filaments corresponding to (K) and (L). Doublets of membrane-distal filaments highlighted by blue arrows in the right panel of (K) are indicated in (M) and (N).

Figure S2.3

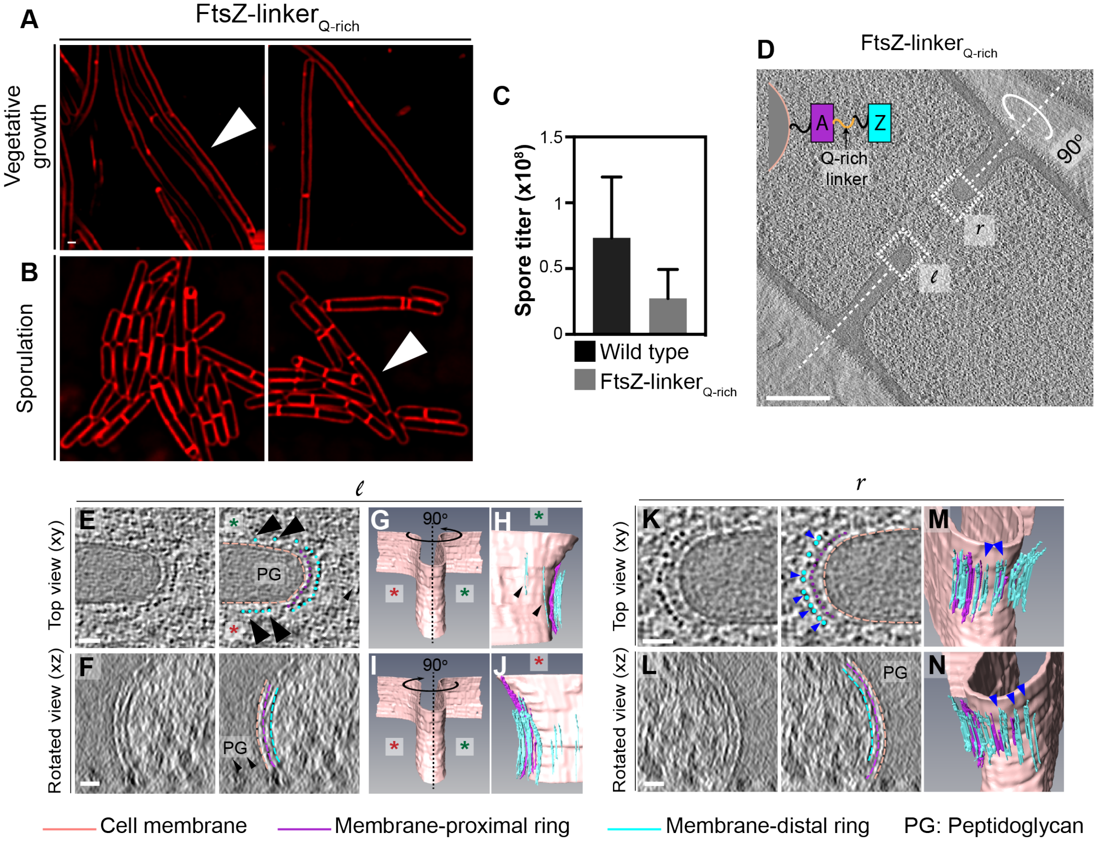
A
FtsZ-linker$_{\text{Q-rich}}$
Vegetative growth
B
Sporulation
C
Spore titer (x10^8)
1.5
1
0.5
0
Wild type
FtsZ-linker$_{\text{Q-rich}}$
D
FtsZ-linker$_{\text{Q-rich}}$
A
Z
Q-rich linker
90°
r
ℓ
ℓ
E
F
G
H
I
J
Top view (xy)
Rotated view (xz)
PG
90°
*
r
K
L
M
N
PG
Cell membrane
Membrane-proximal ring
Membrane-distal ring
PG: Peptidoglycan

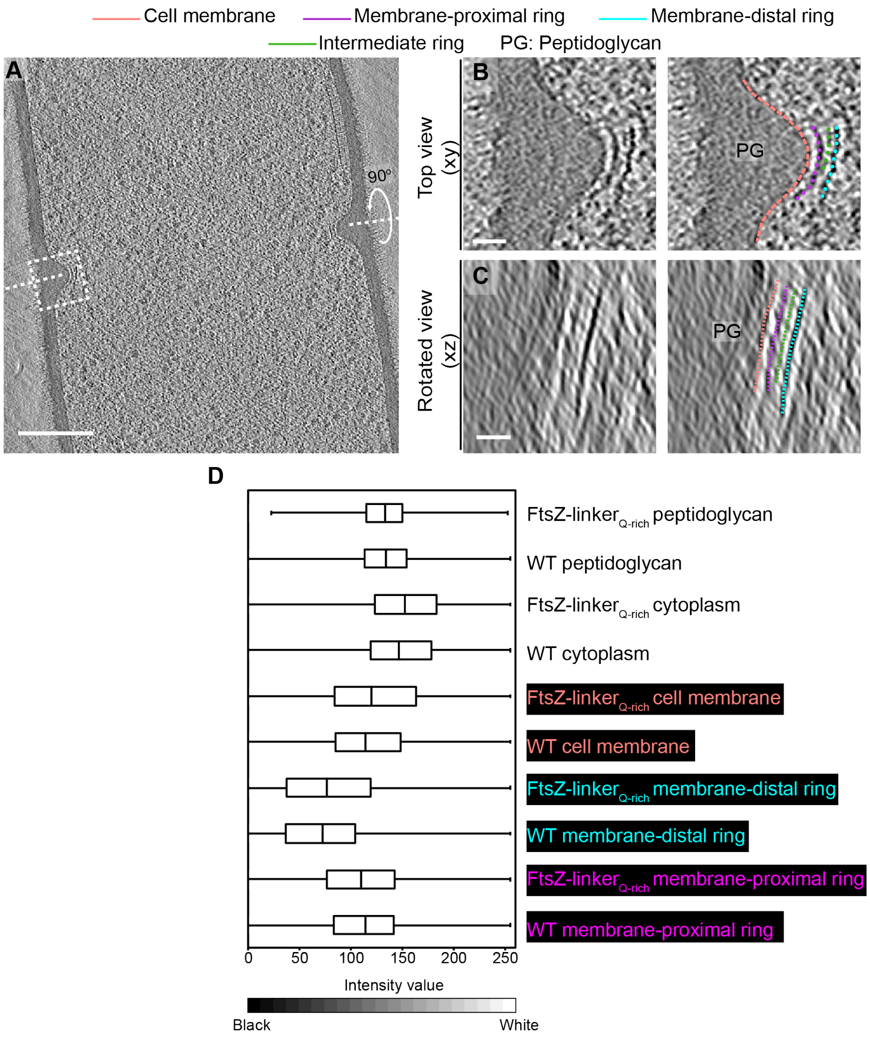

Figure S2.4. Related to Figure 2. **(A)** Slice through a tomogram of a dividing FtsZ-linker$_{\text{Q-rich}}$ vegetative cell. The inset highlights the left side of the leading edge of the invaginating septum. Scale bar: 200 nm. **(B)** Left panel, zoomed-in view of the inset in (A) in the xy coordinate plane. Right panel, same as left with PG (peptidoglycan, gray), cell membrane (peach color), membrane-proximal series of dots (pink) and membrane-distal series of dots (blue) highlighted. An intermediate series of dots between the membrane-proximal and the membrane-distal series is highlighted in green. **(C)** Left panel, view of the septal disk corresponding to (B) in the xz coordinate plane obtained by rotating the cell around its short axis by 90°. Right panel, same as left with PG, cell membrane, membrane-proximal ring, membrane-distal ring and the intermediate ring highlighted. Scale bars for (B) and (C): 25 nm. **(D)** Box-and-whisker plot depicting the distribution of intensity values for the region traced by the membrane-distal and the membrane-proximal rings for wild type and FtsZ-linker$_{\text{Q-rich}}$ in the range of 0 to 255. A region with approximately similar area was masked for PG, cell membrane and cytoplasm as controls for both strains. Lower the intensity value of the pixel in the RGB color space, the darker it is.

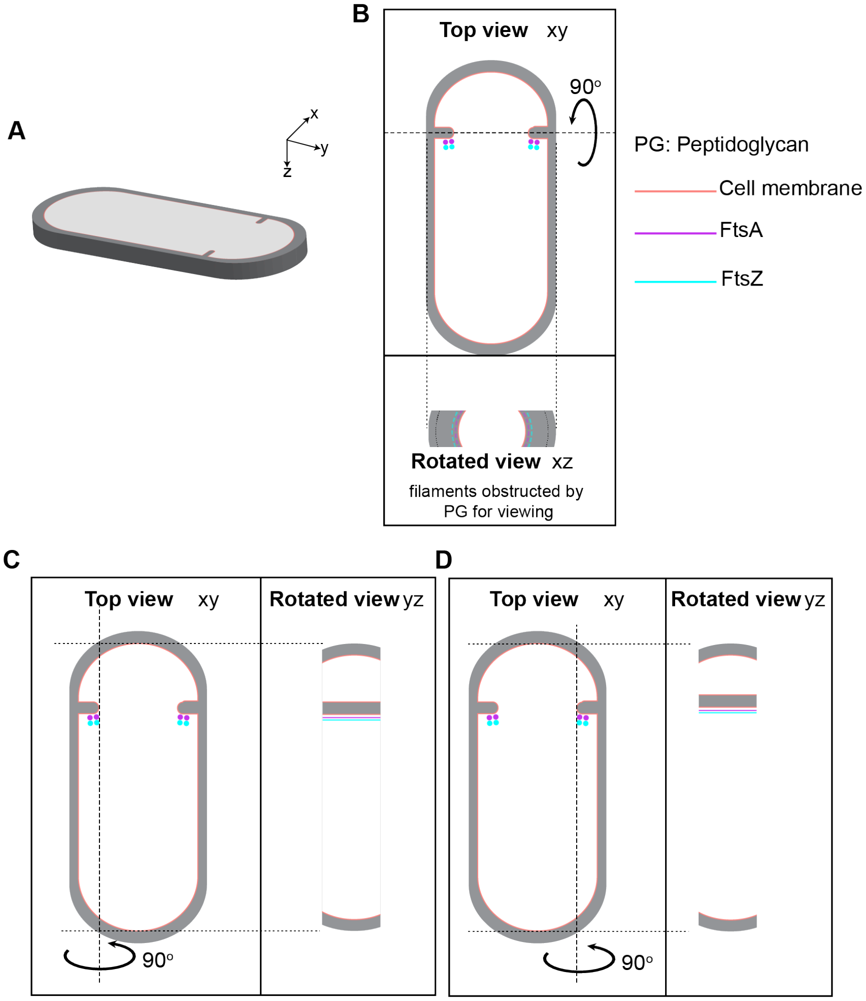

Figure S2.5. Related to Figure 2. (A) A section of a dividing sporulating cell. PG (grey), cell membrane (peach) are highlighted. The xyz coordinate axis to represent the dimensions of the 3D specimen is indicated (same as Figure 1B). **(B)** Top panel, projection image of the cell in (A) in the xy coordinate plane. FtsA (pink) and FtsZ (blue) series of dots are indicated on the mother cell side of the septum. Bottom panel, the corresponding projection image in the xz coordinate plane when the cell is rotated about its short axis by 90°. The lateral PG, septal PG and FtsAZ filaments as they project onto the orthogonal view (xz) are also highlighted. Same colo scheme is followed throughout. **(C)** Left panel, same as top panel in (B). Right panel, the corresponding projection image in the yz coordinate plane when the cell is rotated about its long axis on the left side of the invaginating septum. **(D)** Left panel, same as top panel in (B). Right panel, the corresponding projection image in the yz coordinate plane when the cell is rotated about its long axis on the right side of the invaginating septum. For both (C) and (D), FtsAZ series of dots and the corresponding filaments are also indicated.

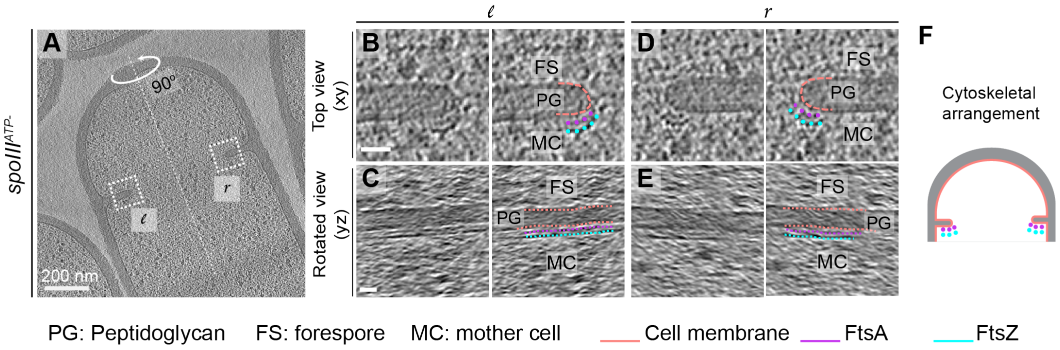

Figure S2.6. Related to Figure 2. (A) Slice through a tomogram of dividing SpoIIIE^{ATP-} sporangia. The insets correspond to the left (*l*) and right (*r*) side of the invaginating septum. Scale bar: 200 nm. **(B)** Left panel, zoomed-in view of the inset in (A) corresponding to '*l*' in the xy coordinate plane. Right panel, same as left with PG (peptidoglycan, grey), cell membrane (peach), FtsA series of dots (pink) and FtsZ series of dots (blue) highlighted. Same color scheme for labeling is followed throughout. **(C)** Left panel, view of the septal disk corresponding to (B) in the yz coordinate plane obtained by rotating the cell around its long axis near the left side of the invaginating septum by 90°. Right panel, same as left with different cellular parts and FtsAZ filaments highlighted. **(D)** Left panel, zoomed-in view of the inset in (A) corresponding to '*r*' in the xy coordinate plane. Right panel, same as left different cellular parts highlighted. **(E)** Left panel, view of the septal disk corresponding to (D) in the yz coordinate plane obtained by rotating the cell around its long axis near the right side of the invaginating septum by 90°. Right panel, same as left with different cellular parts and FtsAZ filaments highlighted. Scale bars for (B)-(E): 25 nm. **(F)** Schematic showing the arrangement of the cytoskeletal machinery in dividing SpoIIIE^{ATP-} sporangia with FtsAZ dots indicated.

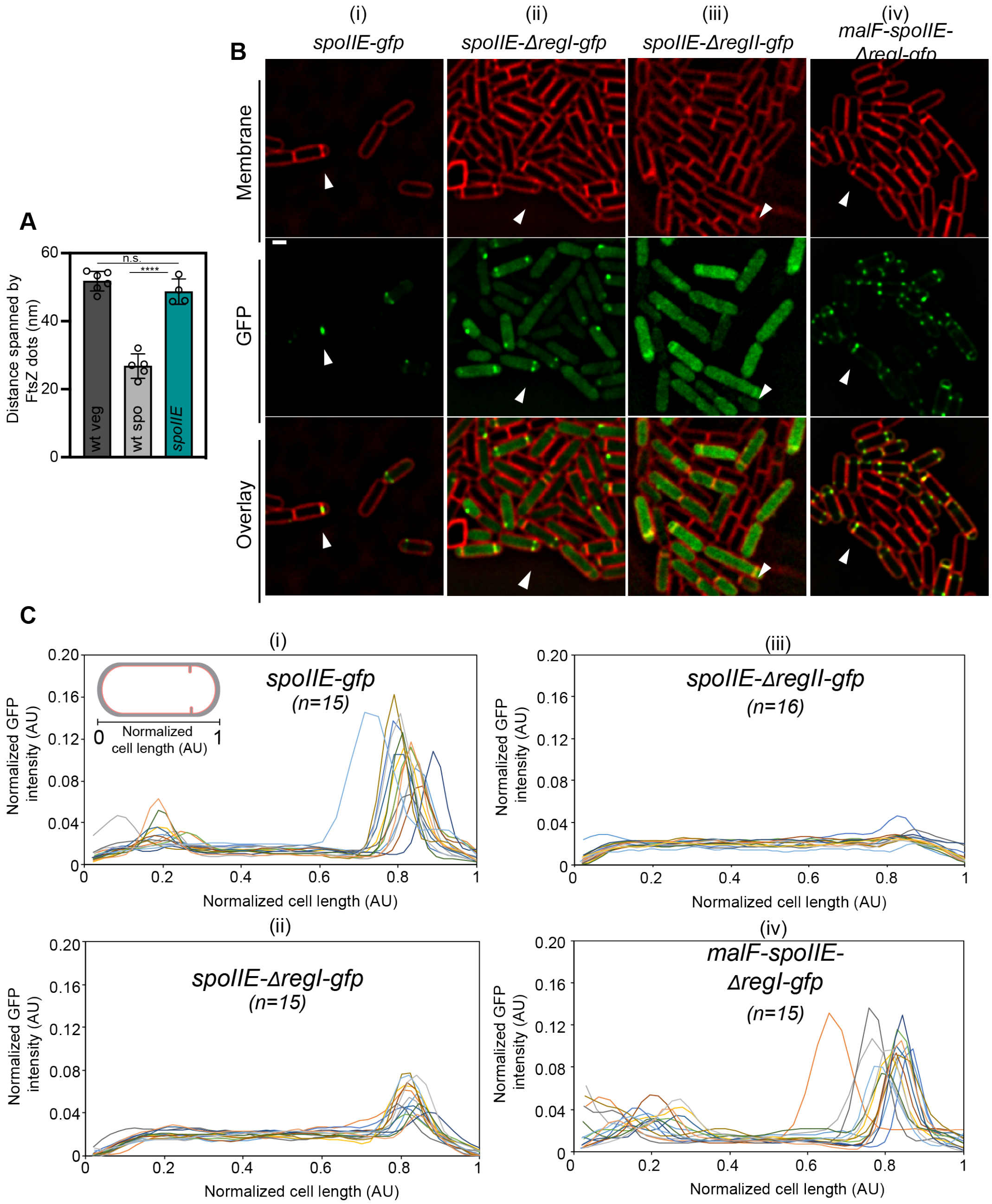

Figure S2.7. Related to Figure 3. (A) Bar graph depicting the distance spanned by FtsZ filaments in wild type vegetative and sporulating cells and SpoIIE null mutant sporangia. Error bars indicate standard deviation (n.s.: not significant, ****: p ≤0.0001, unpaired t-test). Each dot indicates a sample point. **(B)** Fluorescence microscopy of GFP-tagged (green) (i) SpoIIE, (ii) SpoIIE$^{\Delta regI}$, (iii) SpoIIE$^{\Delta regII}$, and (iv) SpoIIE$^{malF\text{-}\Delta regI}$ sporangia. Membranes are stained with FM4-64 (red). Scale bar: 1µm. White arrows indicate a representative sporulating cell for each case. **(C)** Line graphs showing normalized GFP intensity for (i) *spoIIE*, (ii) *spoIIE-ΔregI*, (iii) *spoIIE-ΔregII*, and (iv) *malF-spoIIE-ΔregI* sporangia along the normalized length of the sporangia. n indicates the number of cells analyzed for each case. Each line represents a single cell.

2.9 Acknowledgements

This chapter, in part, is currently being prepared for a manuscript in submission. The manuscript is: Khanna, K., Lopez-Garrido, J., Sugie, J., Pogliano, K., Villa, E. Asymmetric localization of the cell division machinery during *Bacillus subtilis* sporulation (*in preparation*). The dissertation author is the primary author of the manuscript in preparation and conducted all cryo-EM experiments and data analysis with input from other authors. This work was supported by National Institutes of Health Director's New Innovator Award 1DP2GM123494 (EV), the National Institutes of Health R01-GM057045 (EV and KP), the National Science Foundation MRI grant (NSF DBI 1920374). This work was performed in part at the San Diego Nanotechnology Infrastructure (SDNI) of UCSD, a member of the National Nanotechnology Coordinated Infrastructure, supported by the NSF grant (ECCS-1542148). We acknowledge the use of the UCSD Cryo-EM Facility which is supported by NIH grants to Dr. Timothy S. Baker and a gift from the Agouron Institute to UCSD. The authors thank Ethan Garner, Georgia Squyres and Niels Bradshaw for helpful discussions on the manuscript and Dr. Marcella Erb for help with 3D-SIM experiments. We thank Richard Losick, Kumaran Ramamurthi and Ethan Garner for the gift of strains.

Chapter 3: Chromosome Translocation Inflates *Bacillus* Forespores and Impacts Cellular Morphology

Article

Cell

Chromosome Translocation Inflates *Bacillus* Forespores and Impacts Cellular Morphology

Graphical Abstract

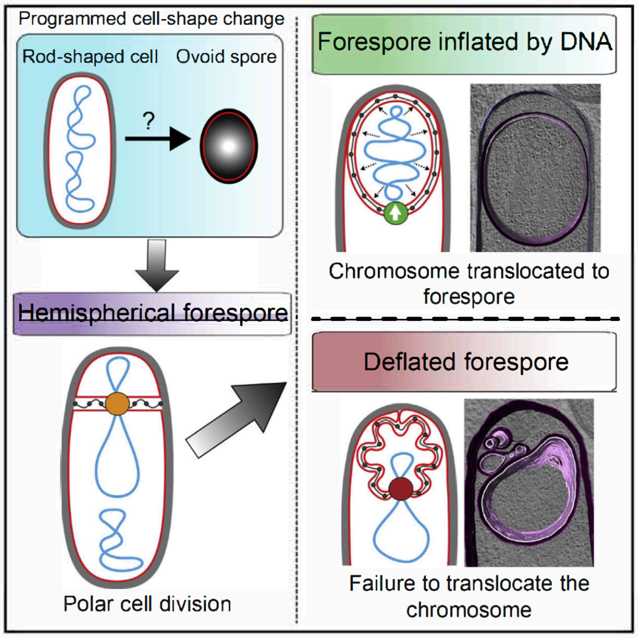

Authors

Javier Lopez-Garrido, Nikola Ojkic, Kanika Khanna, Felix R. Wagner, Elizabeth Villa, Robert G. Endres, Kit Pogliano

Correspondence

r.endres@imperial.ac.uk (R.G.E.),
kpogliano@ucsd.edu (K.P.)

In Brief

DNA generates the turgor pressure that inflates the forespore in *B. subtilis* spore development.

Highlights

- Chromosome translocation reversibly inflates the forespore
- The forespore volume increases at the expense of the mother cell volume
- Forespore growth relies on membrane, but not on peptidoglycan synthesis
- DNA-generated turgor pressure reshapes the forespore

CellPress

Chromosome Translocation Inflates *Bacillus* Forespores and Impacts Cellular Morphology

Javier Lopez-Garrido,[1,6] Nikola Ojkic,[2,3,4,6] Kanika Khanna,[1] Felix R. Wagner,[1] Elizabeth Villa,[1,5] Robert G. Endres,[2,3,5,*] and Kit Pogliano[1,5,7,*]
[1]Division of Biological Sciences, University of California, San Diego, La Jolla, CA 92093, USA
[2]Department of Life Sciences, Imperial College, London SW7 2AZ, UK
[3]Centre for Integrative Systems Biology and Bioinformatics, London SW7 2AZ, UK
[4]Present address: School of Physics and Astronomy, The University of Edinburgh, Edinburgh EN9 3FD, UK
[5]Senior author
[6]These authors contributed equally
[7]Lead Contact
*Correspondence: r.endres@imperial.ac.uk (R.G.E.), kpogliano@ucsd.edu (K.P.)
https://doi.org/10.1016/j.cell.2018.01.027

SUMMARY

The means by which the physicochemical properties of different cellular components together determine bacterial cell shape remain poorly understood. Here, we investigate a programmed cell-shape change during *Bacillus subtilis* sporulation, when a rod-shaped vegetative cell is transformed to an ovoid spore. Asymmetric cell division generates a bigger mother cell and a smaller, hemispherical forespore. The septum traps the forespore chromosome, which is translocated to the forespore by SpoIIIE. Simultaneously, forespore size increases as it is reshaped into an ovoid. Using genetics, timelapse microscopy, cryo-electron tomography, and mathematical modeling, we demonstrate that forespore growth relies on membrane synthesis and SpoIIIE-mediated chromosome translocation, but not on peptidoglycan or protein synthesis. Our data suggest that the hydrated nucleoid swells and inflates the forespore, displacing ribosomes to the cell periphery, stretching septal peptidoglycan, and reshaping the forespore. Our results illustrate how simple biophysical interactions between core cellular components contribute to cellular morphology.

INTRODUCTION

Bacterial cells display an amazing variety of cellular morphologies, which are often the defining signatures of different species (Holt et al., 1994; Young, 2006). It is generally accepted that cell shape is determined by the peptidoglycan (PG) cell wall. The molecular mechanisms involved in cell wall homeostasis are starting to be deciphered, leading to the emergence of models for the maintenance of basic shapes (Amir and Nelson, 2012; Bartlett et al., 2017; Cabeen et al., 2009; Nguyen et al., 2015; Pinho et al., 2013; Ursell et al., 2014). However, it is unclear how the cell wall and other cellular components interact to generate the shape of bacterial cells.

Some bacteria modify their shape during specific developmental processes. A paradigmatic example is sporulation in *Bacillus subtilis* (Errington, 2003; Higgins and Dworkin, 2012; Tan and Ramamurthi, 2014) during which rod shaped cells transform into ovoid spores. The study of cell shape transformations during this process can provide insights into the mechanism of cell shape generation. Sporulation starts with an asymmetrically positioned cell division event (polar septation) that generates two cells of different size and fate (Figure 1A): the smaller forespore becomes a resilient spore, whereas the larger mother cell lyses after contributing to forespore development. After polar septation, the membrane of the mother cell migrates around the forespore in a phagocytosis-like process called engulfment until the leading edges of the engulfing membrane meet and fuse, releasing the forespore into the mother cell cytoplasm.

Immediately after polar septation, the forespore is hemispherical (Figure 1A [second cell]). However, during and shortly after engulfment, it is reshaped into an ovoid (Pogliano et al., 1999). We have previously observed that a thin layer of PG persists between the mother cell and the forespore membranes throughout engulfment (Tocheva et al., 2013); this layer likely plays an important role in reshaping the forespore. Our recent data indicate that this layer originates as an extension of the septal PG by coordinated PG synthesis and degradation at the leading edge of the engulfing membrane (Figure 1B; Ojkic et al., 2016). During this process, synthesis is carried out by forespore biosynthetic complexes that move at a position that coincides with the leading edge of the engulfing mother cell membrane and PG degradation by a mother cell protein complex (SpoIIDMP) that localizes to the leading edge of the engulfing membrane. We propose that coordinated PG synthesis and degradation moves the junction between the septal PG and the lateral cell wall around the forespore, mediating membrane migration and extending the septal PG to fully enclose the forespore (Figure 1B), from now on referred to as the "extended septal PG."

Before polar septation, the chromosomes are remodeled into an elongated axial filament (Kay and Warren, 1968; Pogliano et al., 2002; Ryter, 1965), with the origins of replication at the

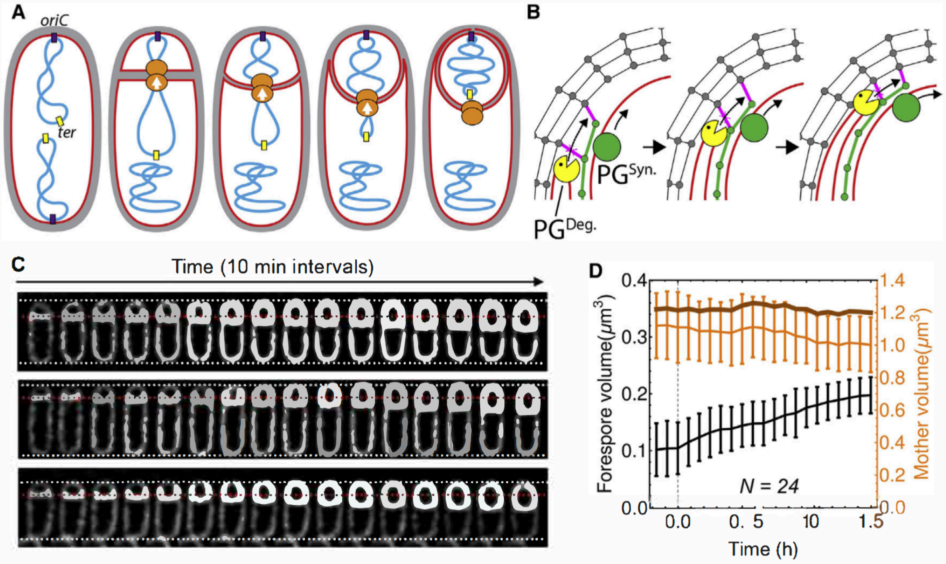

Figure 1. Forespore Growth during Sporulation

(A) Diagram of polar septation, chromosome translocation, and engulfment showing membranes (red), PG (gray), chromosomes (blue), origin of replication (purple), terminus (yellow), and SpoIIIE (orange), with translocation polarity indicated by arrows.

(B) Model for engulfment membrane migration. New PG (green) is synthesized ahead of the engulfing membrane by forespore PG-biosynthetic machineries ($PG^{Syn.}$, green circle), crosslinked (magenta) to the lateral cell wall (gray), and degraded by SpoIIDMP (yellow Pacman), extending the septal PG and moving the septal junction around the forespore.

(C) Timelapse fluorescence microscopy of three wild-type sporangia throughout engulfment showing FM4-64 stained membranes (white). Dotted lines are added as references, with white indicating the total length of the sporangium and red the original position of the septum.

(D) Average forespore volume (black line, left y axis), mother cell volume (light orange line, right y axis) and forespore plus mother cell volume (dark orange line, right y axis) of wild-type sporangia over time. Time traces were aligned so that 0 hr was the onset of septum curving. Error bars represent standard deviation. See also Figure S1 and S2.

cell poles and the termini at midcell (Figure 1A [leftmost cell]; Webb et al., 1997). As a consequence, when the septum is formed, the origin-proximal part of the forespore chromosome is inside the forespore, and the origin distal ~2/3 of the chromosome (Wu and Errington, 1994, 1998) remains in the mother cell (Figure 1A). Endospore-forming bacteria have evolved a system to deal with this topological problem: the SpoIIIE membrane protein is recruited to septal midpoint and moves the chromosome from the mother cell to the forespore (Wu and Errington, 1997; Bath et al., 2000; Massey et al., 2006). SpoIIIE assembles two subcomplexes, one in each cell (Yen Shin et al., 2015). Normally, only the mother cell subcomplex is active, transporting the chromosome into the forespore. However, in the absence of the mother cell subcomplex, the forespore subcomplex can transport the chromosome out of the forespore and into the mother cell, indicating that SpoIIIE can function as a reversible motor (Sharp and Pogliano, 2002; Yen Shin et al., 2015). DNA translocation is an energy intensive process that consumes one molecule of ATP per every two base pairs transported (or ~1.5 million ATP molecules total; Liu et al., 2015). The process commences immediately after polar septation, when the forespore is just ~0.1 μm^3, packing the chromosome into a cell that is, at the onset of this process, just 1/10 the volume of the mother cell (Figure 1). It is unclear how this tiny cell accommodates the chromosome and its associated water and counterions.

Here, we study how different core cellular components contribute to the final forespore size and morphology. We propose a model for forespore remodeling in which chromosome translocation increases forespore turgor pressure, stretching the extended septal PG so that it obtains the shape dictated by the forespore biosynthetic complexes and accommodating new membrane that is synthesized during engulfment. In the absence of DNA translocation, the membranes surrounding the forespore appear wrinkled and floppy, which might hinder the completion of engulfment by providing a more complicated membrane morphology for the engulfing membranes to traverse. Our results demonstrate that DNA contributes to forespore size and morphology, not only through the information it carries, but also through the physicochemical properties of the DNA molecule itself.

RESULTS

The Forespore Volume Increases in Detriment of the Mother Cell Volume

To visualize the transition in forespore shape from hemispherical to ovoid, we performed timelapse fluorescence microscopy using fluorescent membrane stains compatible with spore formation (Figures 1C, S1, and S2; Pogliano et al., 1999). Immediately after polar septation, the forespore volume is ~0.1 μm^3, constituting just ~10% of the total volume of the sporangium (Figures 1C and 1D). However, the forespore starts elongating toward the mother cell, increasing its volume for ~3 hr. Forespore volume doubles by engulfment completion (Figures 1C and 1D) and continues increasing until it plateaus at ~0.3 μm^3, roughly triple its initial volume (Figure S1). The mother cell volume decreases by the same amount as the forespore volume increases, therefore maintaining a constant total volume for the sporangium (Figures 1C and 1D). The reduction in mother cell volume contrasts with the ~25% increase in mother cell surface area during engulfment (Ojkic et al., 2016), which is required to allow the engulfing membrane to completely enclose the forespore.

Forespore Growth Requires Chromosome Translocation and Membrane Synthesis, but Not PG Synthesis

In previous work, we have observed that mutants impaired in chromosome translocation typically have small forespores (Becker and Pogliano, 2007; Sharp and Pogliano, 1999, 2002). To test if chromosome translocation was necessary for forespore growth, we performed timelapse microscopy of a strain unable to translocate the chromosome into the forespore due to a point mutation in SpoIIIE that abolishes ATPase activity (SpoIIIE^{ATP-}; Sharp and Pogliano, 1999). In this mutant, although chromosome translocation is blocked, SpoIIIE still assembles a translocation channel at the septum, maintaining separation of the forespore and mother cell membranes and cytoplasms (Fleming et al., 2010). Timelapse microscopy showed that SpoIIIE^{ATP-} forespores showed negligible volume increase compared to the wild-type (Figures 2A–2C, and S2). After membrane migration, an excess of membrane seemed to accumulate around the forespore, and a membrane blob was frequently observed at the mother cell distal tip of the sporangium (Figures 2B and S2). These results indicate that chromosome translocation is critical for forespore growth.

We next tested if forespore growth, like vegetative growth, relied on PG and membrane synthesis. However, these processes are essential for engulfment (Ojkic et al., 2016), complicating the analysis. In order to uncouple forespore growth from engulfment, we used engulfment-defective strains that lacked one protein in the SpoIIDMP complex (Figure 1B). In the absence of any one of these three proteins, membrane migration is blocked, but the forespore continues to grow, forming a bulge into the mother cell cytoplasm (Frandsen and Stragier, 1995; Lopez-Diaz et al., 1986; Smith et al., 1993; Figure 2D). We monitored bulge formation by timelapse microscopy in strains lacking SpoIIM (Figures 2E and S2). Bulges started to form shortly after polar septation and continued growing for ~3 hr. Importantly, chromosome translocation was also required for bulge growth, as indicated by the failure to form bulges in SpoIIIE^{ATP}-SpoIIM^{-}mutant (Figures 2E [bottom row] and S2). We then monitored bulge formation in the presence of antibiotics that block PG (cephalexin, fosfomycin, penicillin V, or bacitracin) and membrane (cerulenin) biosynthesis (Figures 2E [second and third rows] and S2) using antibiotic concentrations that affect the formation of polar septa (Ojkic et al., 2016). Bulges formed after treatment with all the PG synthesis inhibitors tested, but they failed to grow when membrane synthesis was inhibited (Figures 2E [second row] and S2). After inhibiting PG synthesis, bulges appeared unstable, collapsing or disintegrating at later time points (Figure S2). This instability would reduce the number of bulges observed in batch cultures, perhaps explaining why we previously concluded that PG synthesis was required for bulge formation (Meyer et al., 2010). Together, these results suggest that forespore growth depends on membrane synthesis and chromosome translocation, but not on PG synthesis.

Hypotheses to Explain the Requirement of Chromosome Translocation for Forespore Growth

While the requirement of membrane synthesis for forespore growth has a straightforward explanation, the role of chromosome translocation is not clear. One possibility is that growth requires the forespore expression of genes that are not initially trapped in the forespore (Figure 2F [red dots in left and middle cells]). By this hypothesis (hereafter called the gene expression model), the inhibition of forespore growth in the absence of DNA translocation would be due to the failure of genes located in the origin-distal part of the chromosome to enter and be expressed in the forespores of SpoIIIE^{ATP-} sporangia. An alternative model—the chromosome packing model (Figure 2F)—posits that forespore growth is a physical consequence of packing the ~4-megabase *B. subtilis* chromosome into the forespore, which initially comprises just ~10% (Figure 1) of the total volume of the sporangium. Packing this long, negatively charged DNA polymer into the small forespore might generate a significant turgor pressure due to the requirement for additional water molecules and positively charged counterions to neutralize the charge. These models are not necessarily mutually exclusive.

Reverse Chromosome Translocation Results in Forespore Shrinking and Collapse

We next designed experiments to tease apart the relative contribution of forespore gene expression and chromosome packing to forespore growth. First, we employed a genetic strategy to reverse SpoIIIE-mediated chromosome translocation so that DNA is first moved into and then out of the forespore (Figure 3A; Yen Shin et al., 2015). To do so, we tagged SpoIIIE with a modified ssrA* sequence that is recognized by the *E. coli* adaptor protein SspB^{Ec} and delivered to the *B. subtilis* ClpXP protease for degradation (Griffith and Grossman, 2008). We then degraded SpoIIIE in the mother cell by expressing *sspB*^{Ec} from a mother cell specific promoter (P_{spoIID}). As a consequence, degradation commences slightly after the initiation of chromosome translocation, which gives time for most sporangia to initially translocate the chromosome into the forespore, supporting forespore growth (Figure 3A). However, after mother cell SpoIIIE-ssrA* is degraded, the forespore SpoIIIE subcomplex transports the chromosome out of the forespore. If chromosome packing drives forespore growth, we expect that pumping the chromosome out of this cell would relieve the turgor pressure, causing it to shrink or collapse (Figure 3A [chromosome packing model]). However, if growth is the consequence of *de novo* synthesis of specific gene products in the forespore that mediate the cell shape change, then reverse chromosome translocation should

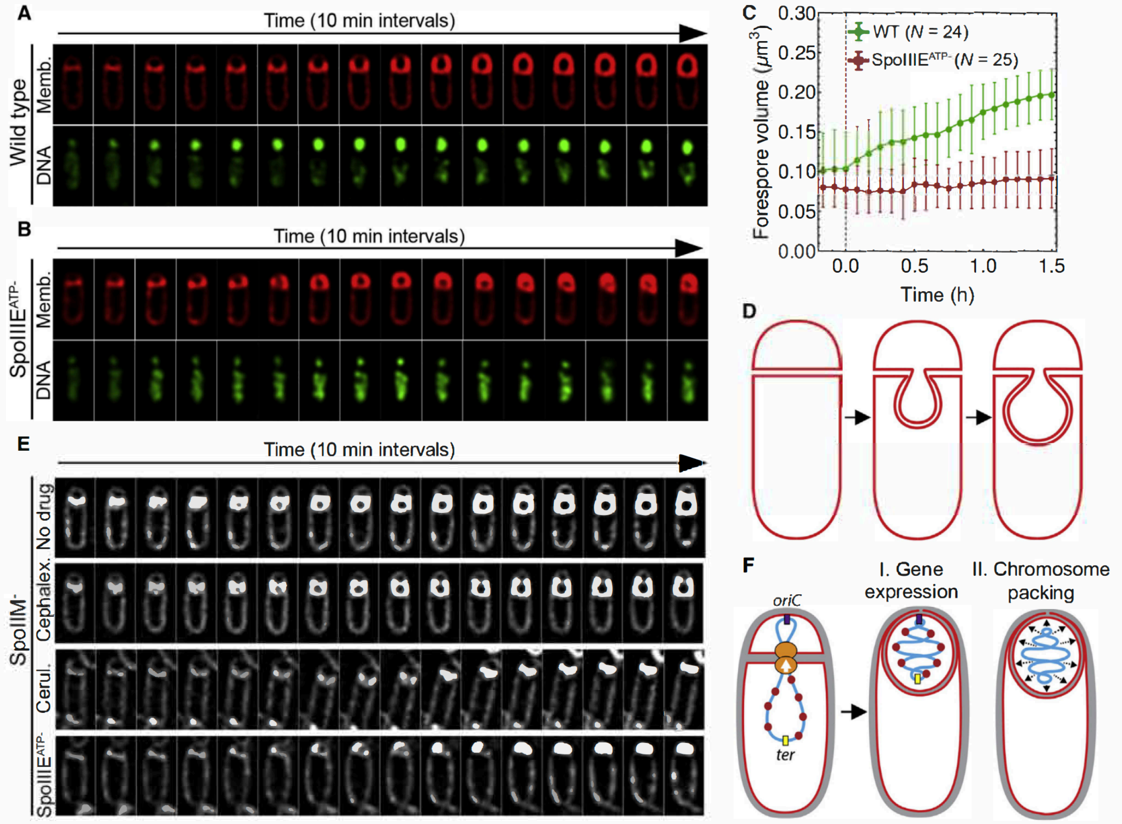

Figure 2. Processes Required for Forespore Growth

(A and B) Timelapse fluorescence microscopy of wild-type (A) and SpoIIIE^{ATP-} (B) sporangia showing FM4-64-stained membranes (red) and SYTOX-green-stained DNA (green).

(C) Change in forespore volume for wild-type (WT, green) and SpoIIIE^{ATP-} (red). Time 0 hr was set as in Figure 1. Error bars represent standard deviation.

(D) Diagram of bulge formation in *spoIID*, *spoIIM*, and *spoIIP* mutants.

(E) Timelapse microscopy of *spoIIM* sporangia without drug, or in the presence of cephalexin (50 μg/mL) or cerulenin (30 μg/mL). The last row is *spoIIM spoIIE^{ATP-}* sporangia. Membranes were stained with FM4-64. See Figure S2 for additional antibiotics.

(F) Alternative models to explain the dependence of forespore growth on chromosome translocation. For simplicity, only the forespore chromosome is shown. Additional details are provided in the main text.

See also Figure S2.

have no consequence on forespore shape, since the products would already be present in the forespore as evidenced by the initial growth of this cell (Figure 3A [gene expression model]).

We monitored chromosome translocation and forespore volume by timelapse microscopy, staining the DNA with SYTOX green and membranes with FM4-64 (Becker and Pogliano, 2007). In the absence of SpoIIIE degradation, the chromosome was translocated from the mother cell to the forespore in every sporangium with a forward translocation rate of 0.4 kb/s per chromosome arm (Figures 3B and 3C [inset]), and translocation was typically completed in less than 1 hr after polar septation (Figures 3B–3E and S3A). As expected, the forespore volume increased continuously as the chromosome was translocated to the forespore, continuing after translocation in a second phase of growth (Figures 3D, 3E, and S3A). When SpoIIIE was degraded in the mother cell, most sporangia initially showed forward chromosome translocation, which supported forespore growth (Figures 3F–3I, S3B, and S3C). After the initial forward translocation, we observed chromosome movement out of the forespore in a significant fraction of the sporangia, suggesting that the mother cell SpoIIIE subcomplex was degraded (Figures 3F–3I). We observed two distinct types of reverse translocation (Figures 3C and 3F–3I). In some sporangia, the chromosome was slowly and completely translocated out of the forespore, with a reverse translocation rate of −0.3 kb/s (Figure 3C [inset])—similar to the rate at which it had initially been

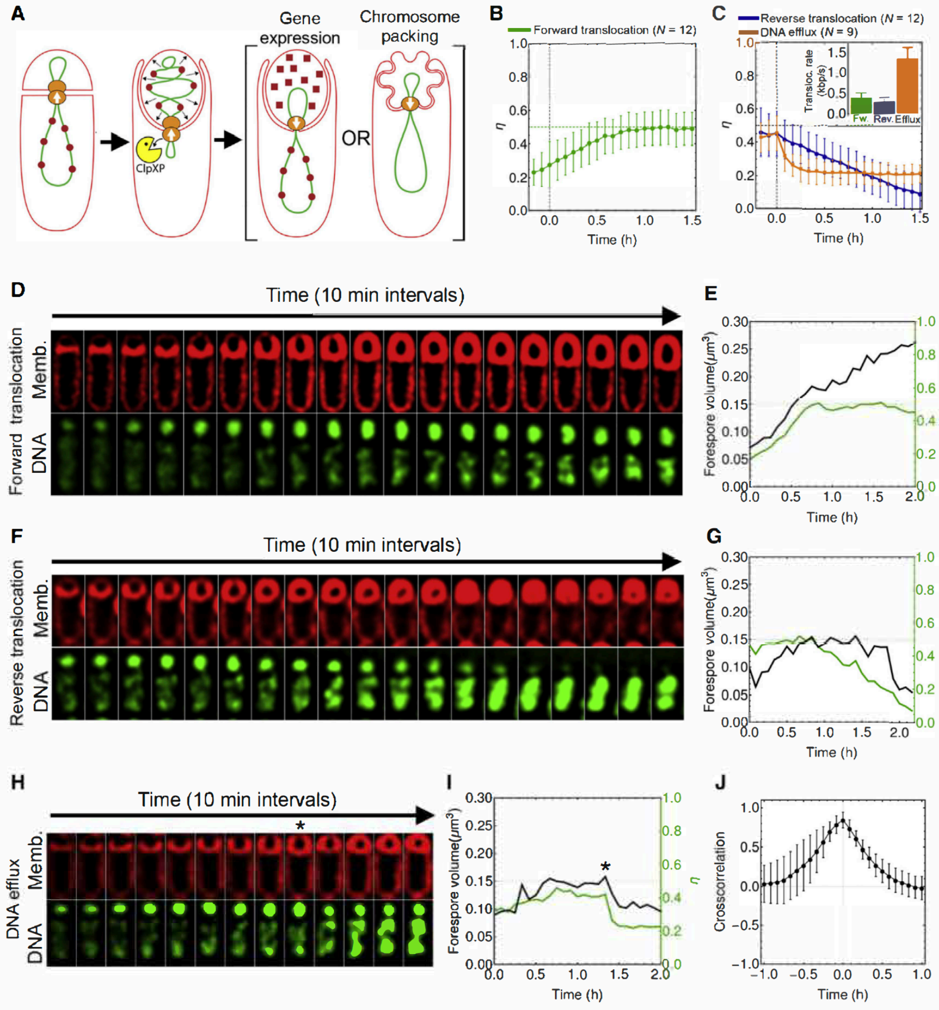

Figure 3. Reverse Chromosome Translocation Produces Forespore Shrinking and Collapse

(A) Degradation of mother cell SpoIIIE reverses chromosome translocation (Yen Shin et al., 2015), with differing impacts on forespore volume predicted by the gene expression and the chromosome packing hypotheses.

(B) Mean forespore DNA fraction (η) over time during forward chromosome translocation. The green dotted line indicates DNA fraction after chromosome translocation ($\eta = 0.5$). Error bars represent standard deviation.

(C) Mean forespore DNA fraction over time during reverse chromosome translocation and DNA efflux. The inset shows translocation rates (absolute value, kb/s per chromosome arm) during forward translocation (Fw.), reverse translocation (Rev.), and DNA efflux. Error bars represent standard deviation.

(D) Timelapse microscopy of a sporangium stained with FM4-64 (red) and SYTOX green (green) without SpoIIIE degradation.

(E) Graphs showing forespore volume (black line, left y axis) and fraction of DNA in the forespore (η, green line, right y axis) of the sporangium shown in (D).

(F–I) Examples of outcomes after SpoIIIE degradation in the mother cell. (F) Slow chromosome translocation out of the forespore. (G) Graph showing forespore volume and forespore DNA fraction for the sporangium in (F). (H) Example of abrupt DNA efflux. The asterisk indicates the onset of reverse chromosome translocation. (I) Graph showing forespore volume and forespore DNA fraction of the sporangia shown in (H).

(J) Cross-correlation between η and forespore volume during abrupt DNA efflux. Error bars represent standard deviation.

See Figure S3 for additional examples.

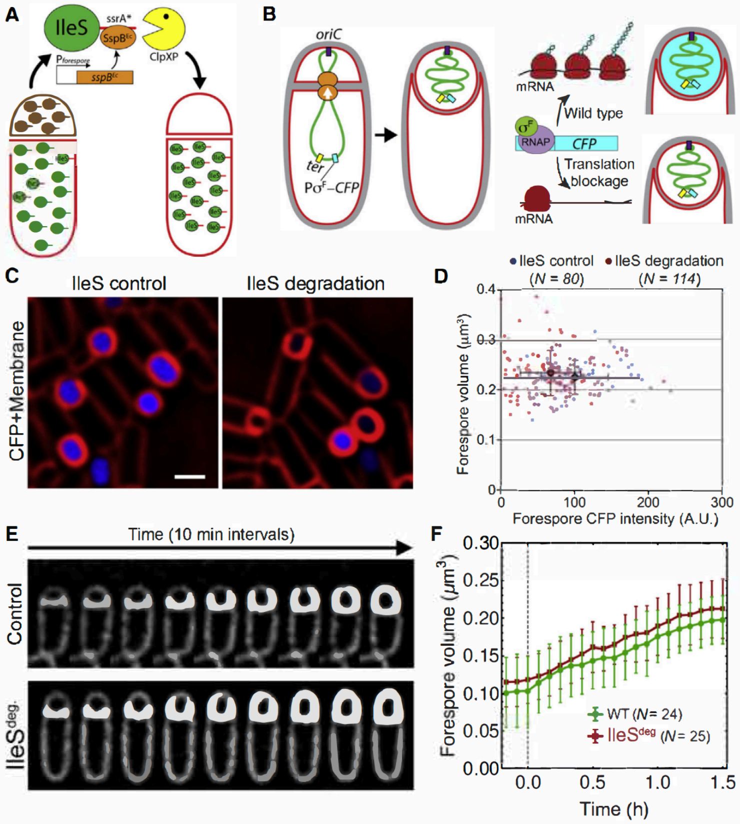

Figure 4. Sustained Protein Synthesis in the Forespore Is Not Required for Growth

(A and B) Strategies to block translation in the forespore (A) and to determine the degree to which IleS-ssrA* degradation reduces forespore translation (B).

(C) Fluorescence microscopy of sporangia expressing P_{spoIIQ}–*CFP* without IleS degradation (left) or with IleS degradation in the forespore (right). Membranes were stained with FM4-64 (red). CFP images (blue) used identical exposures and adjustments to directly compare fluorescence intensity. Scale bar, 1 µm.

(D) Total CFP fluorescence in the forespore (x axis) versus forespore volume (y axis) of sporangia without (blue) or with (red) IleS degradation in the forespore. Each dot represents an individual forespore. Solid dots represent the average CFP intensity and volume of wild-type (blue) and IleS-depleted forespores (red). Error bars represent standard deviations. IleS degradation significantly reduced CFP intensity ($p < 0.0001$) but has no effect on forespore size ($p = 4625$) compared to the control.

(E) Timelapse fluorescence microscopy of wild-type (control) and after IleS degradation in the forespore ($\text{IleS}^{\text{deg.}}$).

(F) Change in forespore volume during engulfment in wild-type (WT, green) and after forespore degradation of IleS ($\text{IleS}^{\text{deg.}}$, red). Error bars represent standard deviation.

See also Figure S4.

translocated into the forespore—as expected for SpoIIIE-mediated reverse chromosome translocation (Figures 3C, 3F, 3G, and S3B). In these cases, the forespores gradually lost volume, becoming misshapen and ultimately collapsing (Figures 3F, 3G, and S3B). In other sporangia, parts of the chromosomes quickly moved out of the forespores (−1.3 kb/s; Figure 3C), with coincident and abrupt losses of forespore volume and no subsequent movements of the remainder of the chromosomes out of the forespores (Figures 3C, 3H, 3I, and S3C). Cross-correlation analysis showed that, during DNA efflux, there was no time delay between chromosome movement out of the forespore and the loss of forespore volume, suggesting a strong coupling between both processes (Figure 3J). This abrupt DNA efflux has not been previously observed. Our prior results indicate that SpoIIIE complexes in both cells are required to assemble a stable paired channel and to maintain daughter cell separation (Yen Shin et al., 2015). It is therefore possible that degradation of mother cell SpoIIIE causes the forespore SpoIIIE channel to disassemble in some sporangia, opening a pore in the septum that allows the immediate redistribution of the chromosome between the two cells in order to minimize the repulsive and hydration forces associated with packing the chromosome into the small forespore.

Thus, the loss of the forespore chromosome correlates with decreased forespore volume over two distinct timescales, consistent with the hypothesis that DNA generates pressure within the forespore that is required to maintain its size and shape.

Sustained Translation in the Forespore Is Not Required for Growth

The above results show that chromosome packing in the forespore is critical for growth and suggest that expression of genes encoded in the region of the chromosome initially trapped in the mother cell might be dispensable for forespore growth. To further evaluate the gene expression model, we tested if sustained protein synthesis was required in the forespore to support growth. We used the cell-specific protein degradation system (Yen Shin et al., 2015) to specifically block translation in the forespore after polar septation (Figure 4A). To this end, we constructed a strain in which the sole isoleucine-tRNA synthetase, IleS, was tagged with ssrA*. The IleS-ssrA* fusion supports growth with a doubling time and cellular morphology identical to the parent strain, and production of SspB^{Ec} from a xylose-inducible promoter causes a rapid cessation of growth (Figures S4A and S4B; Lamsa et al., 2016). To block translation in the forespore, we expressed $sspB^{Ec}$ from a forespore-specific promoter ($P_{sspE(2G)}$). Degradation of IleS-ssrA* in the forespore dramatically reduced spore production, suggesting that the protein is efficiently degraded (Figure S4C).

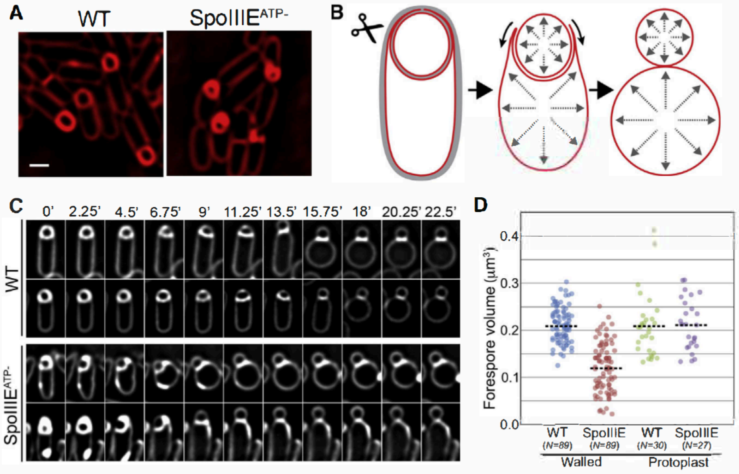

Figure 5. Chromosome Packing Increases Forespore Volume by Extending the Forespore Membrane

(A) Fluorescence microscopy of wild-type and SpoIIIE^{ATP-} sporangia. Scale bar, 1 µm.

(B) Cartoon representing the transition between a walled (left) and protoplasted (right) sporangium upon enzymatic cell wall removal with lysozyme (scissors) at low osmolarity.

(C) Timelapse microscopy showing the transition to protoplasts for wild-type (WT, upper two rows) and SpoIIIE^{ATP-} sporangia (bottom two rows).

(D) Volumes of WT and SpoIIIE^{ATP-} forespores after engulfment membrane migration for intact (walled) and protoplasted (protoplast) sporangia. Each dot represents one sporangium. Dotted line, average of each set.

To monitor the degree to which translation was impaired before chromosome translocation was completed, we placed a gene encoding the cyan fluorescent protein (CFP) under the control of a forespore-specific, σ^F-dependent promoter and integrated the construct into a site close to the chromosome terminus. Since the terminus is in the mother cell immediately after polar septation, CFP is not produced until the *cfp* gene reaches the forespore (Figure 4B). After forespore IleS degradation, we would expect a reduced CFP signal if translation was impaired by the time chromosome translocation finishes (Figure 4B). CFP intensity would therefore be indicative of the level of translation in individual forespores, allowing us to determine if there is a correlation between forespore size and the degree to which translation is inhibited. We plotted forespore CFP fluorescence versus forespore volume for individual sporangia about to complete engulfment with and without IleS degradation (Figures 4C and 4D). As expected, the average CFP intensity was shifted toward lower values after degradation (Figure 4D), and ~20% of the forespores showed negligible CFP signal, suggesting that in those forespores, translation was almost completely blocked before chromosome translocation finished. Importantly, there was no correlation between CFP intensity and forespore size, indicating that continuous protein synthesis in the forespore is not required for growth. Production of SspB^{Ec} in the forespore without ssrA* had no impact on CFP intensity or forespore size (Figure S4D).

We next performed timelapse microscopy to monitor forespore growth after IleS degradation, following only those 20% of sporangia that lacked detectable CFP expression at the end of the experiment (Figure 4E). Loss of forespore protein synthesis had no impact on forespore growth (Figures 4E and 4F). These results indicate that forespore growth does not require the continuous production of proteins in the forespore, suggesting that the chromosome packing is the main driver of forespore growth, at least during the first 1.5 hr of growth studied here.

Chromosome Packing Increases Forespore Volume by Extending the Forespore Membrane

Next, we explored if there was a connection between chromosome packing and membrane synthesis during forespore growth. It is conceivable that increased turgor pressure in the forespore triggers the synthesis of the extra membrane required for growth. Alternatively, it is possible that the excess membrane required for forespore growth and engulfment is produced independently of chromosome translocation, in which case chromosome packing might simply extend the forespore membrane to yield an effective volume increase. This second possibility seems to be supported by the accumulation of excess membrane around the forespores in the absence of chromosome translocation (Figures 2B, 5A, and S2). However, it is possible that the membrane excess is solely part of the mother cell engulfing membrane, which might wrinkle as it migrates around a smaller than normal forespore.

To distinguish between these two possibilities, we artificially extended the forespore membranes by enzymatically removing the cell wall under low-osmolarity conditions (Figures 5B and 5C). We have previously shown that sporulating cells do not lyse when the cell wall is removed in the absence of osmoprotectants (Ojkic et al., 2014). However, under those conditions, the engulfing membrane retracts (Figures 5B and 5C), suggesting that the turgor pressures of the mother cell and forespore increase (Ojkic et al., 2014), which would also allow both cells to fully extend their membranes during the transition to protoplasts. We measured the volume of wild-type and SpoIIIE^{ATP-} forespores from sporangia with an intact cell wall (Figure 5A) after completion of engulfment membrane migration, but not engulfment membrane fission (Figure 5D [walled]). As expected, the average volume of SpoIIIE^{ATP-} forespores was significantly reduced compared to wild-type forespores (Figure 5D). We then determined the volume of wild-type and SpoIIIE^{ATP-} forespores after digesting the cell wall under low-osmolarity conditions (Figure 5D [protoplast]). We monitored protoplast formation by timelapse microscopy, focusing on sporangia that had

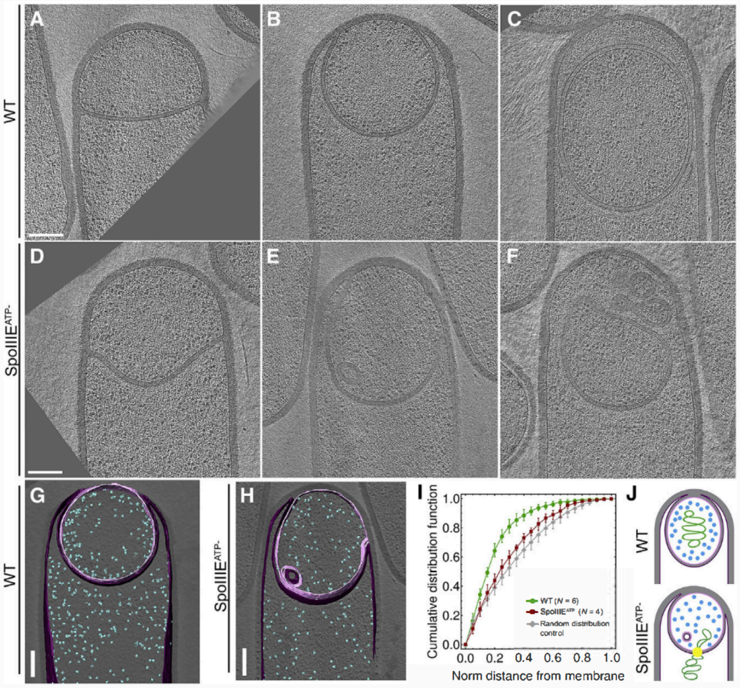

Figure 6. DNA Translocation Affects Ribosome Distribution and Membrane Topography

(A–F) Slices of cryo-electron tomograms depicting different stages of engulfment in wild-type sporangia (A–C) and corresponding states in *spoIIIE*$^{ATP-}$ sporangia (D–F). Scale bar, 200 nm.

(G and H) Segmented tomogram of WT (G) and *spoIIIE*$^{ATP-}$ (H) sporangia, showing ribosomes (blue), the forespore membrane (pink), and the mother cell membrane (purple).

(I) Cumulative distribution of ribosomes as a function of the distance from the forespore membrane in WT (green) and SpoIIIE^{ATP-} forespores. The gray line represents the cumulative distribution of randomly distributed sets of ribosomes generated *in silico*. Error bars represent standard deviation.

(J) Cartoons illustrating the exclusion of ribosomes by the forespore nucleoid.

See also Figure S5.

completed engulfment membrane migration by the time lysozyme was added (Figure 5C). As shown in Figure 5D, the average volumes of protoplasted wild-type and SpoIIIE^{ATP-} forespores are indistinguishable and equivalent to those of walled wild-type forespores. These results suggest that forespores synthesize the excess membrane required for growth independently of chromosome translocation and that chromosome packing might simply increase forespore turgor pressure to extend the forespore membrane, thereby increasing forespore volume.

The Impact of DNA Translocation on Forespore Morphology Visualized by Cryo-electron Tomography

In order to better understand the impact of chromosome translocation on forespore morphology, we visualized wild-type and SpoIIIE^{ATP-} sporangia by cryo-electron tomography (CET). *B. subtilis* cells are too thick to obtain high-resolution tomograms using CET. To circumvent this limitation, we used cryo-focused ion beam (FIB) milling to thin the samples to a thickness compatible with CET, which allows visualization of cellular structures in a near-native state, at molecular resolution (Mahamid et al., 2016; Villa et al., 2013). The tomograms of wild-type sporangia show that, during engulfment, the septum curves smoothly toward the mother cell as the mother cell membrane engulfs the forespore (Figures 6A and 6B). After engulfment, forespores are roughly ovoid, and the membranes are completely extended (Figure 6C), with a thin layer of extended septal PG between the forespore and the mother cell membranes, as we previously observed in slender *ponA* mutant sporangia (Tocheva et al., 2013).

In *spoIIIE*$^{ATP-}$ sporangia, we noted that the septum appeared wavy (Figures 6D and S5G) and less extended than wild-type. At later stages of engulfment, we observed invaginations of the double membrane that encloses the forespore (Figures 6E and 6F), and after engulfment, an excess of membrane accumulated, often at the sporangial cell pole (Figures 6F and S5H) or, sometimes, in folds of the two membranes into the forespore (Figures 6E and 6H). These observations are consistent with fluorescence microscopy results, where we typically observed membrane blobs at the mother cell distal tip of SpoIIIE^{ATP-} sporangia or elsewhere in the forespore (Figure S2). These results support the idea that, in the absence of chromosome translocation, newly synthesized forespore membrane cannot be fully extended, causing the forespore and engulfing mother cell membrane to wrinkle.

Ribosome Mapping Shows that the Hydrated Chromosome Occupies a Significant Volume of the Forespore Core

The bacterial nucleoid does not typically display a high-order organization and thus cannot be directly observed in our tomograms. However, previous studies have shown that the nucleoid excludes *B. subtilis* ribosomes (Lewis et al., 2000). The spatial organization of ribosomes therefore provides insight into the position and space occupied by the hydrated nucleoid. Ribosomes can be readily identified in our tomograms, using template matching and subtomogram averaging (Briggs, 2013). We therefore compared the spatial distribution of ribosomes in wild-type and SpoIIIE^{ATP-} sporangia (Figures 6G and 6H) and used this information to infer the space occupied by the forespore nucleoid. We focused on sporangia at late stages of engulfment to ensure that chromosome translocation was complete in wild-type and quantified ribosome distribution relative to the membrane. In SpoIIIE^{ATP-} sporangia, ribosomes were distributed uniformly across the forespore cytoplasm, indicating that the portion of the chromosome in the forespore occupies a small volume of the cell cytoplasm (Figures 6H–6J). In wild-type sporangia, forespore ribosomes were confined to the cell periphery, suggesting the full nucleoid occupies a significant fraction of the forespore core (Figures 6G, 6I, and 6J). Equivalent results were obtained by imaging GFP-labeled ribosomes with fluorescence microscopy (Figure S5).

Modeling the Impact of Chromosome-Generated Turgor Pressure on Septal PG and Forespore Shape

Taken together, our results suggest that the forespore chromosome effectively inflates the forespore, generating an increased turgor pressure that allows the cell to accommodate the additional membrane synthesized during engulfment and subsequent steps of spore formation. We estimated potential contributions of chromosome packing to the forespore turgor pressure (see STAR Methods). Our calculations indicate that packing a whole chromosome in the forespore can generate a pressure difference (Δp) between the forespore and mother cell between $\sim$20 and $\sim$80 kPa, mainly due to the osmotic effect of the counterions required to neutralize the negative charges of the DNA (Figure S6) and, to a lesser extent, due to the decreased entropy resulting from packing the chromosome into the small forespore. However, is this increase in Δp sufficient to explain observed engulfment dynamics and forespore morphology? To explore this, we modified our *in silico* mathematical model for engulfment (Ojkic et al., 2016). Briefly, using a simple model that accounts for cooperation between cell wall synthesis and degradation (Figure 1B), we proposed a mechanism for the progression of the leading edge of the engulfing membrane, in which the junction between the septal PG and the lateral cell wall moves around the forespore (Ojkic et al., 2016). Increased turgor pressure in the forespore pushes the septum and stretches the septal PG, leading to forespore expansion. It is important to note that, since the peptide-bond spring constant (k_{pep} = 50 pN/nm) is much smaller than the glycan spring constant (k_{gly} = 5570 pN/nm), the main volume change is due to elastic stretching of the peptide bond (Nguyen et al., 2015; Ojkic et al., 2016). In our model, newly synthesized peptide bonds are assumed to be relaxed and are subsequently stretched due to increasing forespore turgor pressure.

We simulated engulfment with different values of Δp between the forespore and the mother cell (Figures 7A and 7B). Our simulations assume that the same amount of extended septal PG is present in all cells and thus that any size difference is exclusively due to PG stretching. We observed drastic changes in forespore volume depending on Δp, indicating that the pressure differential between the two cells is a critical parameter in forespore size determination (Figure S7A). Our simulations with Δp around 60 kPa, which is within the Δp range that can be caused by chromosome translocation, produced forespore sizes in accordance to those found *in vivo*. Similarly, our simulations with low Δp yielded forespore sizes compatible with those found in SpoIIIE$^{\mathrm{ATP}-}$ sporangia.

To see how well this model predicted forespore volume at varying chromosome-mediated pressure differences, we took advantage of *B. subtilis* strains that have different amounts of DNA in the forespore: a translocation proficient strain in which the chromosome is fully translocated to the forespore, a SpoIIIE$^{\mathrm{ATP}-}$ strain in which only 1/3 of the chromosome is in the forespore, and a strain in which SpoIIIE is tagged with ssrA* and simultaneously degraded in the mother cell and in the forespore by producing SspB$^{\mathrm{Ec}}$ in both cells (Yen Shin et al., 2015). Due to asynchronies between the onset of chromosome translocation and SpoIIIE degradation, this last strain produces a plethora of chromosome translocation phenotypes, ranging from non-translocated to almost completely translocated (Figures 7C–7E) (Yen Shin et al., 2015). To assess the fraction of the chromosome translocated in each sporangium, we stained the DNA with SYTOX green and quantified the amount of DNA in the forespore relative to the total DNA in the sporangium (fraction of DNA in the forespore, η). We specifically selected sporangia that had completed engulfment membrane migration to compare sporangia at the same stage. By plotting η against forespore volume, we observed a clear positive correlation (correlation coefficient r = 0.74; Figure 7F). We searched for the best fit of our simulations to the data with Δp = 0 kPa corresponding to non-translocated DNA (η $\sim$0.16), finding that, when the chromosome is completely translocated (η $\sim$0.5), Δp is $\sim$58 kPa. This pressure agrees well with our theoretical estimates of DNA-mediated osmotic pressure (see STAR Methods) and *in vitro* osmotic measurements (Dobrynin and Rubinstein, 2005; Hansen et al., 2001; Raspaud et al., 2000). Finally, we found that the model was able to accurately predict forespore growth in other *Bacillus* species with different cell volumes and chromosome sizes (Figure S7). Together, our simulations with different pressures and *Bacillus* species closely match experimental data, supporting the notion that increased forespore turgor pressure due to chromosome translocation deforms and extends the septal PG, allowing the forespore to adopt its final size and shape.

DISCUSSION

To understand the mechanisms controlling cell size and shape in bacteria, it is necessary to consider both biological regulatory mechanisms and the underlying biophysical principles of the system. Here, we studied the transition in forespore shape during *B. subtilis* sporulation, from hemispherical to ovoid, using a combination of cell biology, genetics, CET, and biophysical modeling. We propose a mechanism for forespore shape generation in which the final shape of the forespore is purely achieved through physiochemical interactions between three core cellular constituents: SpoIIIE-mediated DNA translocation, which effectively inflates the forespore like air in a balloon, stimulating forespore growth by extending the forespore membranes and stretching septal PG (Figure 7G). Our results reveal an unexpected role of DNA in increasing forespore pressure, allowing it to grow within the confines of the extended septal PG to adopt its final size and shape. First, we demonstrated that the chromosome needs to be present in the forespore for this cell to adopt its extended shape (Figure 3). Second, we showed that sustained translation in the forespore is not required for growth (Figure 4). Altogether, our observations indicate that the main contribution of

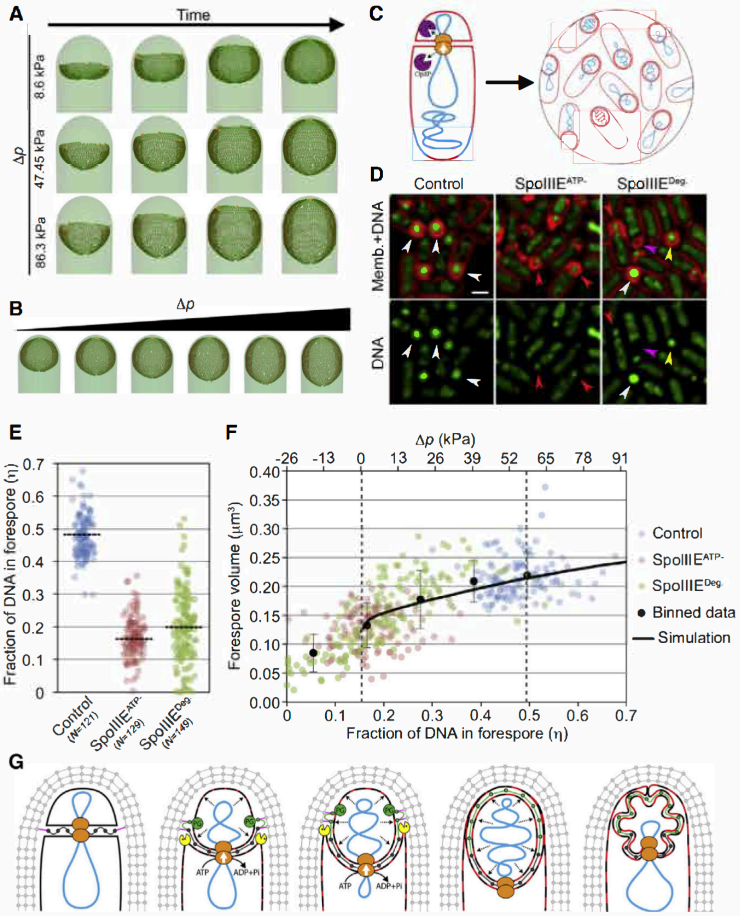

Figure 7. Modeling the Impact of Chromosome-Generated Turgor Pressure on Septal PG and Forespore Size

(A) Simulation snapshots of differing stages of engulfment at increasing pressure difference (Δp) between the forespore and mother cell. Time between frames is 0.28 hr.

(B) Simulation snapshots for Δp in the range from 8.63–86.3 kPa. All forespores have the same amount of extended septal PG. For these pressures, peptide deformations are in the linear elastic regime, with negligible nonlinear peptide deformation (see Figure S7A).

(C) Simultaneous degradation of SpoIIIE in the mother cell and forespore produces sporangia with varying amounts of DNA in the forespore.

(D) Fluorescence microscopy showing a wild-type strain (wild-type), SpoIIIE^{ATP-}, and a strain in which SpoIIIE is simultaneously degraded in the mother cell and the forespore (SpoIIIE^{Deg}). Scale bar, 1 μm. Arrowheads represent forespores with completely translocated (white), non-translocated (red), partially translocated (yellow), or no (magenta) chromosome.

(E) Fraction of forespore DNA in wild-type sporangia (blue), SpoIIIE^{ATP-} sporangia (red), and SpoIIIE^{Deg} sporangia (green). Each dot represents a different sporangium. Dotted lines, average of each set.

(F) Correlation between the fraction of DNA in the forespore (primary x axis) and forespore volume of the sporangia analyzed in (E). Binned data for all strains are shown with black dots (error bars represent standard deviation) and compared with the simulation (black line) for different Δp (secondary x axis). Vertical dotted lines indicate the average fraction of DNA in SpoIIIE^{ATP-} (left line) and wild-type (right line) forespores.

(G) Model showing engulfment and reshaping of the forespore. After polar septation, the forespore is hemispherical and is separated from the mother cell by relaxed septal PG (dark gray). Chromosome translocation increases forespore turgor pressure, stretching the septal PG and allowing the accommodation of newly synthesized membrane (red patches on the membrane). Simultaneously, coordinated PG synthesis by forespore biosynthetic proteins (PG, green) and degradation by SpoIIDMP (yellow Pacman) moves the junction between the septum and the lateral cell wall (pink peptide crosslink) around the forespore, extending the septal PG (with new PG represented in green). In the absence of chromosome translocation, forespore turgor pressure remains low, preventing stretching of the extended septal PG and the accommodation of the excess membrane produced during engulfment.

See also Figure S6 and S7.

chromosome translocation to forespore size and shape is the increase in forespore turgor pressure rather than the expression of genes located on the region of the chromosome that is initially excluded from the forespore.

According to our theoretical calculations, the main contribution of the chromosome to forespore pressure is osmotic (see STAR Methods). This can be conceptualized according to the Gibbs-Donnan effect (Figure S6; Castelnovo and Evilevitch, 2006): the translocation of a negatively charged polyelectrolyte, such as DNA, to the forespore would generate an electrostatic imbalance between the forespore and the mother cell, with the forespore negatively charged with respect to the mother cell. Such imbalance is compensated by a redistribution of the cytoplasmic cations between both cells, generating an effective osmotic Δp. Our CET images indicate that, upon chromosome translocation, the forespore nucleoid displaces the ribosomes to the cell periphery (Figure 6). This observation is compatible with the idea that the chromosome might in fact act as a sponge that swells by sequestering cations and water, causing the forespore to inflate.

Our calculations indicate that packing a full chromosome in the forespore could generate a difference of pressure between mother cell and forespore ranging from ~20 to ~80 kPa. At first sight, this Δp seems relatively minor in the context of a cell with a turgor pressure of ~2 MPa during vegetative growth (Whatmore and Reed, 1990). However, it is similar to the turgor pressure of *E. coli* cells (~30 kPa) (Deng et al., 2011), which is sufficient to deform the thin layer of septal PG from flat during division to curved after cell separation. Our CET images (Figure 6; Tocheva et al., 2013) show that the extended septal PG has a thickness similar to that of *E. coli* cell wall, suggesting that the Δp between forespore and mother cell should be sufficient to stretch the extended septal PG, making it curve into the mother cell. In agreement with this idea, our simulations indicate that PG stretching due to chromosome-generated turgor pressure is enough to explain the size difference between wild-type and SpoIIIE^{ATP-} forespores during engulfment. This is further supported by the rapid loss of forespore volume upon abrupt reverse chromosome translocation (Figures 3H–3J and S3C), which suggests that the chromosome produces an elastic deformation of the forespore. It is therefore possible that increased forespore turgor pressure does not trigger synthesis of extra PG but rather promotes the stretching of the septal PG—a hypothesis that is consistent with the independence of forespore growth from PG synthesis. A stretching-based model has also been proposed for the elongation of the *E. coli* PG sacculus (Rojas et al., 2014).

Chromosome translocation proceeds through the hydrolysis of vast amounts of ATP by the mother cell SpoIIIE subcomplex. Forespore growth could therefore be envisioned as an energy transduction process, from chemical energy stored in ATP to mechanical energy in the form of the expansion of the DNA with its associated counterions, similar to the hydration of a glass-like gel that in turn expands the membranes and stretches the septal PG (Parry et al., 2014; Taylor, 1923). In several bacteriophages, the ATP-driven packaging motor generates a force resulting in a continuous increase in internal pressure as DNA is packaged inside the phages (Evilevitch et al., 2003; Smith et al., 2001), and energy generated in this process is converted to work when the DNA is injected into the host cell. Analogously, the ATP-driven motor of SpoIIIE might also force the DNA inside the small volume of the forespore. In support of this idea, we have observed that the DNA is rapidly ejected from the forespore in some sporangia after degradation of SpoIIIE in the mother cell, presumably through an opening in the septum generated due to the disassembly of the translocation complex. The mechanical energy generated in the process of packaging the chromosome in the forespore may be converted into work done in stretching the septal PG and extending the forespore membrane to proceed with engulfment.

Overall, our results lead to a mechanism of forespore size and morphology determination in which the septal PG is stretched as a consequence of the DNA-mediated increase in forespore turgor pressure, allowing the membranes that surround the forespore to adopt an optimal smooth conformation to proceed with engulfment. Then, coordinated PG synthesis and degradation at the leading edge of the engulfing membrane allows the extension of the septal PG, moving the junction between the septal PG and lateral cell wall around the forespore and generating space for the movement of the mother cell engulfing membrane (Figure 7G). The results presented here illustrate how relatively simple biochemical processes and biophysical principles governing the interaction between core cellular components can together mediate complex processes, such as programmed changes in cellular morphology and engulfment.

STAR★METHODS

Detailed methods are provided in the online version of this paper and include the following:

- KEY RESOURCES TABLE
- CONTACT FOR REAGENT AND RESOURCE SHARING
- EXPERIMENTAL MODEL AND SUBJECT DETAILS
  - *Bacillus subtilis* PY79
  - *Bacillus megaterium* QM B1551
  - *Bacillus thuringiensis* serotype israelensis
  - *Bacillus pumilus* BL8
- METHOD DETAILS
  - Experimental procedures
  - Image analysis
  - Modeling, simulations & pressure calculations
- QUANTIFICATION AND STATISTICAL ANALYSIS

SUPPLEMENTAL INFORMATION

Supplemental Information includes seven figures, four tables, and one data set and can be found with this article online at https://doi.org/10.1016/j.cell.2018.01.027.

ACKNOWLEDGMENTS

We thank Davide Marenduzzo, Rudi Podgornik, and Rosalind Allen for discussion. This work was supported by ERC starting grant 280492-PPHPI (N.O. and R.G.E.), NIH grant R01-GM57045 (K.P.), NIH Director's New Innovator Award 1DP2GM123494-01 (E.V.), and EMBO Long Term Fellowship ALTF 1274-2011 (J.L.-G). We used the UCSD Cryo-EM Facility (supported by NIH grant R01-GM33050 to Dr. Timothy S. Baker and the Agouron Institute) and the San Diego Nanotechnology Infrastructure of UCSD (supported by the NSF grant ECCS-1542148).

AUTHOR CONTRIBUTIONS

Conceptualization, J.L.-G., N.O., R.G.E., and K.P.; Methodology, J.L.-G., N.O., and E.V.; Software, N.O.; Formal Analysis, J.L.-G., N.O., and K.K.; Investigation, J.L.-G, K.K., and F.R.W.; Writing—Original Draft, J.L.-G.; Writing—Review & Editing, all authors; Funding Acquisition, R.G.E. and K.P.

DECLARATION OF INTERESTS

K.P. is a co-founder, a shareholder, and a member of the advisory board of Linnaeus Bioscience (La Jolla, CA). The terms of this arrangement have been reviewed and are managed by the University of California, San Diego in accordance with its conflict of interest policies.

Received: July 7, 2017
Revised: October 16, 2017
Accepted: January 18, 2018
Published: February 8, 2018

SUPPORTING CITATIONS

The following references appear in the Supplemental Information: Guérout-Fleury et al. (1996); Sandman et al. (1987).

REFERENCES

Amir, A., and Nelson, D.R. (2012). Dislocation-mediated growth of bacterial cell walls. Proc. Natl. Acad. Sci. USA *109*, 9833–9838.

Bartlett, T.M., Bratton, B.P., Duvshani, A., Miguel, A., Sheng, Y., Martin, N.R., Nguyen, J.P., Persat, A., Desmarais, S.M., VanNieuwenhze, M.S., et al. (2017). A periplasmic polymer curves Vibrio cholerae and promotes pathogenesis. Cell *168*, 172–185.e15.

Bath, J., Wu, L.J., Errington, J., and Wang, J.C. (2000). Role of Bacillus subtilis SpoIIIE in DNA transport across the mother cell-prespore division septum. Science *290*, 995–997.

Becker, E.C., and Pogliano, K. (2007). Cell-specific SpoIIIE assembly and DNA translocation polarity are dictated by chromosome orientation. Mol. Microbiol. *66*, 1066–1079.

Briggs, J.A.G. (2013). Structural biology in situ–the potential of subtomogram averaging. Curr. Opin. Struct. Biol. *23*, 261–267.

Cabeen, M.T., Charbon, G., Vollmer, W., Born, P., Ausmees, N., Weibel, D.B., and Jacobs-Wagner, C. (2009). Bacterial cell curvature through mechanical control of cell growth. EMBO J. *28*, 1208–1219.

Castaño-Díez, D., Kudryashev, M., Arheit, M., and Stahlberg, H. (2012). Dynamo: a flexible, user-friendly development tool for subtomogram averaging of cryo-EM data in high-performance computing environments. J. Struct. Biol. *178*, 139–151.

Castellana, M., Hsin-Jung Li, S., and Wingreen, N.S. (2016). Spatial organization of bacterial transcription and translation. Proc. Natl. Acad. Sci. USA *113*, 9286–9291.

Castelnovo, M., and Evilevitch, A. (2006). Binding effects in multivalent Gibbs-Donnan equilibrium. Europhys. Lett. *73*, 635–641.

Deng, Y., Sun, M., and Shaevitz, J.W. (2011). Direct measurement of cell wall stress stiffening and turgor pressure in live bacterial cells. Phys. Rev. Lett. *107*, 158101.

Dobrynin, A.V., and Rubinstein, M. (2005). Theory of polyelectrolytes in solutions and at surfaces. Prog. Polym. Sci. *30*, 1049–1118.

Dobrynin, A.V., Colby, R.H., and Rubinstein, M. (1995). Scaling Theory of Polyelectrolyte Solutions. Macromolecules *28*, 1859–1871.

Errington, J. (2003). Regulation of endospore formation in Bacillus subtilis. Nat. Rev. Microbiol. *1*, 117–126.

Evilevitch, A., Lavelle, L., Knobler, C.M., Raspaud, E., and Gelbart, W.M. (2003). Osmotic pressure inhibition of DNA ejection from phage. Proc. Natl. Acad. Sci. USA *100*, 9292–9295.

Fleming, T.C., Shin, J.Y., Lee, S.H., Becker, E., Huang, K.C., Bustamante, C., and Pogliano, K. (2010). Dynamic SpoIIIE assembly mediates septal membrane fission during Bacillus subtilis sporulation. Genes Dev. *24*, 1160–1172.

Frandsen, N., and Stragier, P. (1995). Identification and characterization of the Bacillus subtilis spoIIP locus. J. Bacteriol. *177*, 716–722.

Griffith, K.L., and Grossman, A.D. (2008). Inducible protein degradation in Bacillus subtilis using heterologous peptide tags and adaptor proteins to target substrates to the protease ClpXP. Mol. Microbiol. *70*, 1012–1025.

Guérout-Fleury, A.M., Frandsen, N., and Stragier, P. (1996). Plasmids for ectopic integration in Bacillus subtilis. Gene *180*, 57–61.

Hansen, P.L., Podgornik, R., and Parsegian, V.A. (2001). Osmotic properties of DNA: critical evaluation of counterion condensation theory. Phys. Rev. E Stat. Nonlin. Soft Matter Phys. *64*, 021907.

Higgins, D., and Dworkin, J. (2012). Recent progress in Bacillus subtilis sporulation. FEMS Microbiol. Rev. *36*, 131–148.

Holt, J.H., Krieg, N.R., Sneath, P.H.A., Staley, J.T., and Williams, S.T. (1994). Bergey's manual of determinative bacteriology, Ninth Edition (Lippincott Williams & Wilkins).

Kay, D., and Warren, S.C. (1968). Sporulation in Bacillus subtilis. Morphological changes. Biochem. J. *109*, 819–824.

Kempes, C.P., Wang, L., Amend, J.P., Doyle, J., and Hoehler, T. (2016). Evolutionary tradeoffs in cellular composition across diverse bacteria. ISME J. *10*, 2145–2157.

Lamsa, A., Lopez-Garrido, J., Quach, D., Riley, E.P., Pogliano, J., and Pogliano, K. (2016). Rapid Inhibition Profiling in Bacillus subtilis to identify the mechanism of action of new antimicrobials. ACS Chem. Biol. *11*, 2222–2231.

Lewis, P.J., Thaker, S.D., and Errington, J. (2000). Compartmentalization of transcription and translation in Bacillus subtilis. EMBO J. *19*, 710–718.

Liu, N., Chistol, G., and Bustamante, C. (2015). Two-subunit DNA escort mechanism and inactive subunit bypass in an ultra-fast ring ATPase. eLife *4*, 1–20.

Lo, C.J., Leake, M.C., and Berry, R.M. (2006). Fluorescence measurement of intracellular sodium concentration in single Escherichia coli cells. Biophys. J. *90*, 357–365.

Lopez-Diaz, I., Clarke, S., and Mandelstam, J. (1986). spoIID operon of Bacillus subtilis: cloning and sequence. J. Gen. Microbiol. *132*, 341–354.

Mahamid, J., Pfeffer, S., Schaffer, M., Villa, E., Danev, R., Cuellar, L.K., Förster, F., Hyman, A.A., Plitzko, J.M., and Baumeister, W. (2016). Visualizing the molecular sociology at the HeLa cell nuclear periphery. Science *351*, 969–972.

Manning, G.S. (2006). The persistence length of DNA is reached from the persistence length of its null isomer through an internal electrostatic stretching force. Biophys. J. *91*, 3607–3616.

Martinez-Sanchez, A., Garcia, I., Asano, S., Lucic, V., and Fernandez, J.J. (2014). Robust membrane detection based on tensor voting for electron tomography. J. Struct. Biol. *186*, 49–61.

Massey, T.H., Mercogliano, C.P., Yates, J., Sherratt, D.J., and Löwe, J. (2006). Double-stranded DNA translocation: structure and mechanism of hexameric FtsK. Mol. Cell *23*, 457–469.

Mastronarde, D.N. (1997). Dual-axis tomography: an approach with alignment methods that preserve resolution. J. Struct. Biol. *120*, 343–352.

Meyer, P., Gutierrez, J., Pogliano, K., and Dworkin, J. (2010). Cell wall synthesis is necessary for membrane dynamics during sporulation of Bacillus subtilis. Mol. Microbiol. *76*, 956–970.

Nguyen, L.T., Gumbart, J.C., Beeby, M., and Jensen, G.J. (2015). Coarse-grained simulations of bacterial cell wall growth reveal that local coordination alone can be sufficient to maintain rod shape. Proc. Natl. Acad. Sci. USA *112*, E3689–E3698.

Ojkic, N., López-Garrido, J., Pogliano, K., and Endres, R.G. (2014). Bistable forespore engulfment in Bacillus subtilis by a zipper mechanism in absence of the cell wall. PLoS Comput. Biol. *10*, e1003912.

Ojkic, N., López-Garrido, J., Pogliano, K., and Endres, R.G. (2016). Cell-wall remodeling drives engulfment during Bacillus subtilis sporulation. eLife *5*, e18657.

Parry, B.R., Surovtsev, I.V., Cabeen, M.T., O'Hern, C.S., Dufresne, E.R., and Jacobs-Wagner, C. (2014). The bacterial cytoplasm has glass-like properties and is fluidized by metabolic activity. Cell *156*, 183–194.

Pelletier, J., Halvorsen, K., Ha, B.-Y., Paparcone, R., Sandler, S.J., Woldringh, C.L., Wong, W.P., and Jun, S. (2012). Physical manipulation of the Escherichia coli chromosome reveals its soft nature. Proc. Natl. Acad. Sci. USA *109*, E2649–E2656.

Pereira, M.C.F., Brackley, C.A., Lintuvuori, J.S., Marenduzzo, D., and Orlandini, E. (2017). Entropic elasticity and dynamics of the bacterial chromosome: A simulation study. J. Chem. Phys. *147*.

Pinho, M.G., Kjos, M., and Veening, J.-W. (2013). How to get (a)round: mechanisms controlling growth and division of coccoid bacteria. Nat. Rev. Microbiol. *11*, 601–614.

Podgornik, R., Aksoyoglu, M.A., Yasar, S., Svenšek, D., and Parsegian, V.A. (2016). DNA equation of state: In vitro vs in Viro. J. Phys. Chem. B *120*, 6051–6060.

Pogliano, J., Osborne, N., Sharp, M.D., Abanes-De Mello, A., Perez, A., Sun, Y.L., and Pogliano, K. (1999). A vital stain for studying membrane dynamics in bacteria: a novel mechanism controlling septation during Bacillus subtilis sporulation. Mol. Microbiol. *31*, 1149–1159.

Pogliano, J., Sharp, M.D., and Pogliano, K. (2002). Partitioning of chromosomal DNA during establishment of cellular asymmetry in Bacillus subtilis. J. Bacteriol. *184*, 1743–1749.

Purohit, P.K., Kondev, J., and Phillips, R. (2003). Mechanics of DNA packaging in viruses. Proc. Natl. Acad. Sci. USA *100*, 3173–3178.

Raspaud, E., da Conceiçao, M., and Livolant, F. (2000). Do free DNA counterions control the osmotic pressure? Phys. Rev. Lett. *84*, 2533–2536.

Rigort, A., Bäuerlein, F.J., Villa, E., Eibauer, M., Laugks, T., Baumeister, W., and Plitzko, J.M. (2012). Focused ion beam micromachining of eukaryotic cells for cryoelectron tomography. Proc. Natl. Acad. Sci. USA *109*, 4449–4454.

Rojas, E., Theriot, J.A., and Huang, K.C. (2014). Response of Escherichia coli growth rate to osmotic shock. Proc. Natl. Acad. Sci. USA *111*, 7807–7812.

Ryter, A. (1965). MORPHOLOGIC STUDY OF THE SPORULATION OF BACILLUS SUBTILIS. Ann. Inst. Pasteur (Paris) *108*, 40–60.

Sandman, K., Losick, R., and Youngman, P. (1987). Genetic analysis of Bacillus subtilis spo mutations generated by Tn917-mediated insertional mutagenesis. Genetics *117*, 603–617.

Sharp, M.D., and Pogliano, K. (1999). An in vivo membrane fusion assay implicates SpoIIIE in the final stages of engulfment during Bacillus subtilis sporulation. Proc. Natl. Acad. Sci. USA *96*, 14553–14558.

Sharp, M.D., and Pogliano, K. (2002). Role of cell-specific SpoIIIE assembly in polarity of DNA transfer. Science *295*, 137–139.

Smith, K., Bayer, M.E., and Youngman, P. (1993). Physical and functional characterization of the Bacillus subtilis spoIIM gene. J. Bacteriol. *175*, 3607–3617.

Smith, D.E., Tans, S.J., Smith, S.B., Grimes, S., Anderson, D.L., and Bustamante, C. (2001). The bacteriophage straight phi29 portal motor can package DNA against a large internal force. Nature *413*, 748–752.

Smith, M.B., Li, H., Shen, T., Huang, X., Yusuf, E., and Vavylonis, D. (2010). Segmentation and tracking of cytoskeletal filaments using open active contours. Cytoskeleton *67*, 693–705.

Tan, I.S., and Ramamurthi, K.S. (2014). Spore formation in Bacillus subtilis. Environ. Microbiol. Rep. *6*, 212–225.

Tang, G., Peng, L., Baldwin, P.R., Mann, D.S., Jiang, W., Rees, I., and Ludtke, S.J. (2007). EMAN2: an extensible image processing suite for electron microscopy. J. Struct. Biol. *157*, 38–46.

Taylor, C.V. (1923). The contractile vacuole in Euplotes: An example of the sol-gel reversibility of cytoplasm. J. Exp. Zool. *37*, 259–289.

Tocheva, E.I., López-Garrido, J., Hughes, H.V., Fredlund, J., Kuru, E., Vannieuwenhze, M.S., Brun, Y.V., Pogliano, K., and Jensen, G.J. (2013). Peptidoglycan transformations during Bacillus subtilis sporulation. Mol. Microbiol. *88*, 673–686.

Ursell, T.S., Nguyen, J., Monds, R.D., Colavin, A., Billings, G., Ouzounov, N., Gitai, Z., Shaevitz, J.W., and Huang, K.C. (2014). Rod-like bacterial shape is maintained by feedback between cell curvature and cytoskeletal localization. Proc. Natl. Acad. Sci. USA *111*, E1025–E1034.

Villa, E., Schaffer, M., Plitzko, J.M., and Baumeister, W. (2013). Opening windows into the cell: focused-ion-beam milling for cryo-electron tomography. Curr. Opin. Struct. Biol. *23*, 771–777.

Webb, C.D., Teleman, A., Gordon, S., Straight, A., Belmont, A., Lin, D.C., Grossman, A.D., Wright, A., and Losick, R. (1997). Bipolar localization of the replication origin regions of chromosomes in vegetative and sporulating cells of *B. subtilis*. Cell *88*, 667–674.

Whatmore, A.M., and Reed, R.H. (1990). Determination of turgor pressure in Bacillus subtilis: a possible role for K+ in turgor regulation. J. Gen. Microbiol. *136*, 2521–2526.

Wu, L.J., and Errington, J. (1994). Bacillus subtilis SpoIIIE protein required for DNA segregation during asymmetric cell division. Science *264*, 572–575.

Wu, L.J., and Errington, J. (1997). Septal localization of the SpoIIIE chromosome partitioning protein in Bacillus subtilis. EMBO J. *16*, 2161–2169.

Wu, L.J., and Errington, J. (1998). Use of asymmetric cell division and spoIIIE mutants to probe chromosome orientation and organization in Bacillus subtilis. Mol. Microbiol. *27*, 777–786.

Yen Shin, J., Lopez-Garrido, J., Lee, S.-H., Diaz-Celis, C., Fleming, T., Bustamante, C., and Pogliano, K. (2015). Visualization and functional dissection of coaxial paired SpoIIIE channels across the sporulation septum. eLife *4*, e06474.

Young, K.D. (2006). The selective value of bacterial shape. Microbiol. Mol. Biol. Rev. *70*, 660–703.

Youngman, P., Perkins, J.B., and Losick, R. (1984). A novel method for the rapid cloning in Escherichia coli of Bacillus subtilis chromosomal DNA adjacent to Tn917 insertions. Mol. Gen. Genet. *195*, 424–433.

STAR★METHODS

KEY RESOURCES TABLE

REAGENT or RESOURCE	SOURCE	IDENTIFIER
Chemicals, Peptides, and Recombinant Proteins		
FM4-64	Thermo Fisher Scientific	Cat#T13320
SYTOX Green	Thermo Fisher Scientific	Cat#S7020
Fosfomycin	MilliporeSigma	Cat#P5396
Bacitracin	MilliporeSigma	Cat#B0125
Penicillin V	MilliporeSigma	Cat#1504489
Cephalexin	MilliporeSigma	Cat#C4895
Cerulenin	MilliporeSigma	Cat#C2389
Rifampicin	MilliporeSigma	Cat#R3501
Experimental Models: Organisms/Strains		
Bacillus subtilis PY79	Youngman et al., 1984	Tax. ID:1415167
Bacillus megaterium QM B1551	Dr. Peter Setlow at UConn Health	Tax. ID:545693
Bacillus thuringiensis subsp. israelenis	*Bacillus* Genetic Stock Center	4Q2; Tax. ID:339854
Bacillus pumilus BL8	Dr. Louise Temple at James Madison University	Tax. ID:1189615
See Table S1 for a complete list of strains used in this paper, including all the *Bacillus subtilis* PY79 variants	N/A	N/A
Oligonucleotides		
See Table S2 for oligonucleotides	N/A	N/A
Recombinant DNA		
Plasmid: pJLG38: *GFPΩkan*	This paper	N/A
Plasmid: pJLG82: *amyE::PsspE(2G)-sspBΩcat*	This paper	N/A
Plasmid: pJLG113: *ileS-ssrAΩkan*	This paper	N/A
Plasmid: pER226: *rpsB-GFPΩkan*	This paper	N/A
Software and Algorithms		
JFilament	Smith et al., 2010	http://athena.physics.lehigh.edu/jfilament/
volumeestimator	Ojkic et al., 2016	https://elifesciences.org/articles/18657/figures#SD2-data
intensityestimator	This paper	Data S1
IMOD	Mastronarde, 1997	http://bio3d.colorado.edu/imod/; RRID: SCR_003297
TomoSegMemTV	Martinez-Sanchez et al., 2014	https://sites.google.com/site/3demimageprocessing/tomosegmemtv
Amira	Commercial software by Thermo Scientific (formerly FEI)	https://www.fei.com/software/amira-3d-for-life-sciences/; RRID: SCR_014305
EMAN2	Tang et al., 2007	http://blake.bcm.edu/emanwiki/EMAN2
Dynamo	Castaño-Díez et al., 2012	https://wiki.dynamo.biozentrum.unibas.ch/w/index.php/Main_Page

CONTACT FOR REAGENT AND RESOURCE SHARING

Further information and requests for resources and reagents should be directed to and will be fulfilled by the Lead Contact, Kit Pogliano (kpogliano@ucsd.edu).

EXPERIMENTAL MODEL AND SUBJECT DETAILS

We used four different *Bacillus* species as experimental models: *Bacillus subtilis* PY79, *Bacillus megaterium* QM B1551, *Bacillus thuringiensis* serotype israelensis, and *Bacillus pumilus* BL8. All of them were routinely grown in LB plates at 30°C. Sporulation was induced in two different ways: (i) For *B. subtilis* PY79, sporulation was induced by resuspension in A+B medium, after growing the bacteria in 1/4 diluted LB to O.D.$_{600}$ ~0.5. For strains carrying an integration in *thrC*, the resuspension medium was supplemented with 50 μg/ml of threonine. Sporulation cultures were grown at 37°C for batch culture and protoplast experiments, and at 30°C for timelapse experiments. (ii) For comparing forespore sizes of all the model organisms (Figure S7), sporulation was induced by exhaustion in Difco Sporulation Medium (DSM) at 30°C. Relevant details about the different experimental models are provided below:

Bacillus subtilis PY79

Most of the work was done using this model, since it is highly genetically tractable. A list of the different *Bacillus subtilis* PY79 strains used in his study is provided in Table S1. The plasmids and oligonucleotides used to construct the different strains are provided in Tables S2 and S3, respectively. Table S4 includes detailed descriptions of plasmid construction.

Chromosome size: 4.03 megabases.

No plasmids.

Bacillus megaterium QM B1551

Chromosome size: 5.10 megabases.

Seven plasmids, with a combined size of 0.43 megabases.

Bacillus thuringiensis serotype israelensis

Chromosome size: 5.50 megabases.

Six plasmids, with a combined size of 0.84 megabases.

Bacillus pumilus BL8

Chromosome size: ~3.7-3.8 megabases.

METHOD DETAILS

Experimental procedures

Fluorescence microscopy from batch cultures

Cells were visualized on an Applied Precision DV Elite optical sectioning microscope equipped with a Photometrics CoolSNAP-HQ^2 camera and deconvolved using SoftWoRx v5.5.1 (Applied Precision). For imaging, cells (12 μl) were transferred to 1.2% agarose pads prepared using sporulation resuspension medium. Cells were typically imaged ~3 hours after sporulation induction at 37°C. The median focal plane is shown. When appropriate, membranes were stained with 0.5 μg/ml of FM4-64, added directly to the agarose pad. DNA was stained with 0.5 μM of SYTOX green, added to the sporulating cultures ~1 hour after resuspension and to the agarose pad.

To observe ribosome distribution using a RPS2-GFP after transcription blockage with rifampicin (Figure S5), sporulating cultures of a strain expressing *rpsB-GFP* were split 2 hours after sporulation induction and incubated with and without 0.25 μg/ml of rifampicin for one extra hour. Cells were then imaged as described above.

Timelapse fluorescence microscopy

Sporulation was induced at 30°C. To visualize DNA, the culture was supplemented with 0.5 μM SYTOX green ~one hour after sporulation induction. SYTOX green is typically used as an indicator of dead cells, as it has a limited ability to cross the membrane of living cells. However, when added to sporulating cultures several hours before imaging, SYTOX green stains the chromosomes yielding a readily detectable fluorescence signal, without affecting the sporulation process. To visualize the membranes, 0.5 μg/ml FM4-64 was added to the culture ~2 hours after sporulation induction and incubation continued for another hour. Seven μl samples were taken 3 hours after resuspension and transferred to agarose pads prepared as follows: 2/3 volume of supernatant from the sporulation culture; 1/3 volume 3.6% agarose in fresh A+B sporulation medium; 0.17 μg/ml FM4-64; 0.17 μM SYTOX green. When appropriate, antibiotics were added to the pads to the final concentrations indicated in the figure legends. Pads were partially dried, covered with a glass slide and sealed with petroleum jelly to avoid dehydration during timelapse imaging. Petroleum jelly is not toxic and cannot be metabolized by *B. subtilis*, which poses an advantage over other commonly used sealing compounds, such as glycerol, which can be used as a carbon source and inhibit the initiation of sporulation. Pictures were taken in an environmental chamber at 30°C every 5 min for at least 5 hours. Excitation/emission filters were TRITC/CY5 for membrane imaging, and FITC/FITC for DNA imaging. Excitation light transmission was set to 5% to minimize phototoxicity. Exposure time was 0.1 s. For presentation purposes, sporangia were aligned vertically (with forespore on top) by rotating them using Photoshop.

Protoplast timelapse fluorescence microscopy

Sporulation was induced at 37°C. Samples were taken 3-4 hours after resuspension, spun at 7000 x g for 10 s, and resuspended in 25 μl of a buffer containing 20 mM maleic acid and 20 mM $MgCl_2$, pH 6.5. 10 μl of the resuspended culture were placed on a poly-L-lysine-treated coverslip and mixed with lysozyme and FM 4–64 (final concentrations 1 mg/ml and 5 μg/ml, respectively). Images were taken at room temperature, every 45 s for one hour. Excitation light transmission was set to 32%. Exposure time was 0.1 s.

Cryo-Electron Tomography

Holey carbon coated QUANTIFOIL R 2/1 copper grids were glow discharged using Pelco easiGlow glow discharge cleaning system and sporulating *B. subtilis* PY79 cells were deposited on these grids. Samples were taken approximately 2-3 hours after resuspension for wild-type sporulating cells and at 2.5 hours after resuspension for *spoIIIE*$^{ATP-}$ strain. Excess resuspension media was removed by manual blotting using Whatman No. 1 filter paper from the reverse side so that cells form a monolayer on the grids. Grids were then plunge-frozen using a custom-built vitrification device (Max Planck Institute for Biochemistry, Munich) by rapid immersion in ethane/propane mixture cooled by liquid nitrogen.

Grids were mounted into modified FEI Autogrids after vitrifcation. This prevents any mechanical damage to the delicate grids during subsequent transfer steps. Then, these clipped grids were transferred into a dual-beam (cryo-FIB/SEM) microscope (Scios, Thermo Fisher Scientific, formerly FEI) equipped with a cryogenic stage. Thin sections of 100-250 nm, or lamellae, were prepared as previously described in Rigort et al., 2012 (see protocol for lamella preparation, not wedges). Each lamella contains ~10-12 cells.

Tilt-series were collected from typically −66° to +66° with a tilt increment of 1.5° or 2° using SerialEM in a 300-keV Tecnai G2 Polara (Thermo Fisher Scientific, formerly FEI) equipped with post-column Quantum Energy Filter (Gatan) and a K2 Summit 4k x 4k direct detector camera (Gatan). Images were recorded at a nominal magnification of 34,000 with a pixel size of 0.61 nm or 22,500 with a pixel size of 0.92 nm. The dose rate was set to 10-12 e^{-}/physical pixel at the camera level. Frame exposure was set to 0.1 s, with a total exposure in a frame set to be determined by an algorithm targeting an average count number. The total dose in a tomogram was typically ~100-150 e^{-}/A^{o2} with a defocus ranging from −5 to −6 μm. A total of 24 tomograms from 14 FIB-milled lamellae were collected for wild-type sporulating cells and 16 tomograms from 6 FIB-milled lamellae for *spoIIIE*$^{ATP-}$ cells.

Tomograms were reconstructed in IMOD (Mastronarde, 1997) using patch tracking.

Image analysis

Determination of cell volume

To determine the volumes of the forespore and the mother cell, we extracted the membrane contours of the forespore and the mother cell using microscopy images in which membranes were stained with FM4-64. For this purpose, we used the semi-automated active contour software JFilament, available as ImageJ plugin (Smith et al., 2010). In the case of timelapse movies, the membrane position was extracted for every time frame. We then used a custom-built *Mathematica* software (volumeestimator) to calculate 3D volumes of forespore, by assuming rotational symmetry around the axis connecting the center of masses of forespore and mother cell. The code is available in Ojkic et al., 2016. In the case of the forespore volumes reported in Figures 4D, 5D, and S4D, forespore volume was extracted without considering the center of masses to determine the rotational axis. Instead, since we only focused on the fully engulfed forespores that have typical ovoid shape, the rotational axis was estimated by finding axis of rotation as minimum moment of inertia axis. This method was validated by comparing forespore volumes using the two different methods giving $R^2 > 0.99$ (graph not shown).

Estimation of chromosome translocation

The forespore and mother cell contours were determined using JFilament, as above. We extended the *Mathematica* software to extract the total fluorescence intensity of the pixels enclosed by the contours (intensityestimator). In the case of timelapse movies, we used one optical section per time frame, and the total forespore and mother cell SYTOX green intensities were tracked over time. For measurements from batch culture microscopy experiments, we added the SYTOX green intensities of six consecutive optical sections, covering a total thickness of 0.75 μm. The background intensity was calculated using a rolling radius of 3.2 μm (ImageJ). From the total SYTOX green intensity within the forespore and the mother cell, we subtracted the total background intensity to obtain the net SYTOX green intensity in each cell. We defined the fraction of DNA in forespore (η) as [total net SYTOX green intensity in FS / (total net SYTOX green intensity in FS + total net SYTOX green intensity in MC)]. When chromosome translocation is completed, η is ~0.5 (Figures 3B and 7E).

Translocation rate measurements

From the measurement of fraction of DNA in the forespore (η) over time (see previous section) we calculated translocation speed per chromosome arm as $v = N\, d\eta/dt$, where N is the number of bp per DNA, and t is time. During forward and slow reverse translocation, chromosomes are translocated with constant rate (Figure 3B and 3C). For each cell, we determined $d\eta/dt$ using linear fit from η versus time graph, and we calculated the average ± SD of the different cells. The fast reverse translocation rate was calculated similarly as above, but for each cell the slopes were determined from three consecutive time points separated by 5 min intervals, after the onset of the reverse translocation.

Forespore CFP fluorescence intensity

To determine the CFP intensity in the forespore, the intensity of five optical sections was added, covering a total thickness of 0.6 μm. The forespore contour and the CFP intensity enclosed by it were calculated using intensityestimator, as explained in "Estimation of chromosome translocation" subsection.

Fluorescently labeled ribosome distribution

Forespore and mother cell contours were extracted using the ImageJ plugin JFilament, as above. The long axis of every sporangium was rotated to be parallel with *y*-axis, with the forespore pointing up. Then, we aligned the centers of mass of every forespore, and normalized RPS2-GFP fluorescence at the medial focal plane. To calculate average fluorescence distribution of many forespores, we created a square grid with a meshwork size of 16 nm. For each meshwork point we binned pixel intensities that were within a radius of 64 nm. Subsequently, we calculated the average fluorescence for each meshwork point and plotted as a density plot (Figure S5J). Normalized intensity through the center of the forespore and perpendicular to the long axis of the cell (along $y = 0$ line) is plotted in Figure S5K.

Ribosome distribution in CET

Semi-automatic segmentation of membranes was done using TomosegmemTV (Martinez-Sanchez et al., 2014) and then manual refinement in Amira (FEI Visualization Sciences Group). Subtomograms containing ribosomes were manually picked using EMAN2 (Tang et al., 2007) and averaged, classified and placed in their original positions in the tomogram using Dynamo (Castaño-Díez et al., 2012) and Amira. We analyzed the distribution of the ribosomes in tomograms of six wild-type and four SpoIIIE^{ATP-} forespores. We determined the shortest distance between each ribosome and the segmented surface of the forespore in 3D. For each case, the distance between the ribosome and the forespore membrane was normalized to the largest possible distance from the membrane determined numerically for each forespore in 3D. As a control, we generated random distributions of ribosomes within the SpoIIIE^{ATP-} forespores wherein the same number of ribosomes (as found in the respective tomogram) were initiated randomly within the membrane region. The number of random sets for each SpoIIIE^{ATP-} forespores was ~300. A cumulative distribution of ribosomes (normalized to the total number of ribosomes) was then plotted against distance from the membrane for each forespore.

DNA mesh pore size calculation

Estimates for DNA mesh pore size in the forespore were made based on calculations in SI appendix, section S4 in Castellana et al., 2016. L denotes the total length of forespore DNA (~4.03 megabases or ~1.37 mm) and V is the volume of the forespore (0.1-0.2 μm^3) wherein DNA is confined. As an approximation, DNA can be thought of as occupying a cubic lattice of volume V that consists of N cubic pores each with edge length a (pore size) so that $V = Na^3$ and DNA length, L is given by $L = 3aN$ for close packing. This provides an estimate of pore size as $a = \sqrt{(3V/L)}$

Based on these calculations, the forespore nucleoid can be thought of as a DNA mesh with an average pore diameter of ~15-20 nm.

Modeling, simulations & pressure calculations

Engulfment model and simulations are described in detail in Ojkic et al., 2016. Different *Bacillus* species were simulated using different initial forespore sizes, by varying the radius of the forespore to be 0.26, 0.32, 0.55 and 0.6 μm corresponding to *B. pumilus*, *B. subilis*, *B. thuringiensis*, and *B. megaterium*, respectively. The cell sizes were derived from fluorescence microscopy images of sporangia of the different species (Figures S7B and S7C). Below there is a detailed description of how chromosome-generated turgor pressure was calculated for *B. subtilis*. The same calculations where used for different species, taking into account their respective cell and genome sizes.

In *B. subtilis,* packing a long ~4-megabase DNA polymer into a forespore that is initially ~0.1 μm^3 (Figure 1) creates a DNA concentration (C_{DNA}) of ~45 g/l. Each base pair (bp) of the chromosome accompanies two negative phosphate charges, which makes the DNA molecule highly negatively charged. Based on those premises we explored entropic, elastic, electrostatic, and osmotic contributions to the total forespore pressure.

Entropic contribution

By packing the chromosome into the forespore the number of potential DNA conformations is reduced, leading to the increased entropic pressure. When fully translocated, DNA volume fraction (DNA volume divided by forespore volume) is ~6.2%. This produces an entropic pressure of ~2 kPa, estimated using Langevin simulations (Pereira et al., 2017). This estimate is in a good agreement with the experimental measurements in *E. coli*, which suggest that the entropic pressure generated by a 4.6-megabase chromosome is ~4 kPa (Pelletier et al., 2012). However, this estimated entropic pressure is not large enough to significantly deform peptidoglycan meshwork (Figure S7).

Elastic contribution

The DNA elastic bending stiffness tends to restore bent DNA molecules to their straight configuration. The DNA persistence length, l_p~50 nm, is much smaller than the typical linear size of the forespore, $\sim \sqrt[3]{V_{fspore}} = 460$ nm. Additionally, the DNA persistence length decreases in ionic solutions (Manning, 2006). Since the forespore size is about an order of magnitude larger than the DNA persistence length, the DNA elastic bending contribution to the forespore pressure is negligible.

Electrostatic contribution

DNA is negatively charged and the electrostatic repulsion depends on the spacing between neighboring DNA strands. To estimate average DNA radial separation d, we approximate the DNA molecule by a cylinder of the same length as a whole molecule: $d^2\ L_{DNA} = V_{fspore}$, where L_{DNA} is the total DNA length (Purohit et al., 2003). Since bp linear size is 0.34 nm (Kempes et al., 2016; Raspaud et al., 2000), we obtain that the typical distance between two neighboring DNA strands is ~8.4 nm. DNA electrostatic interactions are screened in the ionic solutions due to counterions and the typical Debye's electrostatic screening length of about 0.8 nm (Podgornik et al., 2016; Raspaud et al., 2000). Since the calculated distance d between neighboring DNA strands is much larger than the Debye's screening length, the electrostatic contribution to the pressure is also negligible.

Osmotic contribution

DNA is negatively charged and attracts positively charged counterions that contribute to osmotic pressure. The DNA volume fraction in the forespore is ~6.2% corresponding to a semi-dilute polymer solution. In this regime, the osmotic pressure (p) has polymeric (p_p) and an ionic contribution of the DNA counterions (p_i) (Dobrynin and Rubinstein, 2005; Dobrynin et al., 1995). For DNA forespore concentrations, the polymeric contribution is negligible (Raspaud et al., 2000) therefore $p \approx p_i$. The expression for the osmotic pressure of DNA counterions is given by:

$$p = \frac{RT\phi C_c}{1 + \frac{4C_s}{\phi C_c}},$$

where R is the ideal gas constant, T is the temperature, ϕ is the osmotic coefficient, C_c is the counterion concentration, and C_s is the salt concentration (Dobrynin et al., 1995). The counterion concentration is equal to the DNA phosphate concentration (Raspaud et al., 2000). The above expression fits well with experimentally measured counterion osmotic pressure with $\phi = (0.245 \pm 0.020)$ (Raspaud et al., 2000). Note that the dependence of the osmotic pressure due to DNA counterions on C_s accounts for the classical Gibbs-Donnan effect. Using experimentally measured salt concentration in *E. coli* (Lo et al., 2006) in the range of 2-20 mM and applying above expression we obtain that the forespore osmotic pressure is in the range 26-70 kPa. This estimate agrees with *in vitro* measurement of osmotic pressure of 63 kPa for the C_s = 10 mM and DNA forespore concentration (Hansen et al., 2001; Raspaud et al., 2000). In the lower range of salt concentration, Debye's electrostatic screening length remains smaller than the typical distance between neighboring DNA strands.

QUANTIFICATION AND STATISTICAL ANALYSIS

For each experiment we had at least two biological replicas, and each one contained at least three technical replicas. Averages of individual cells, but not the averages of different replicas are reported. The number of cells analyzed (N) is indicated in each figure. Data represent the mean of N cells. The standard deviation is shown as dispersion measurement.

Supplemental Figures

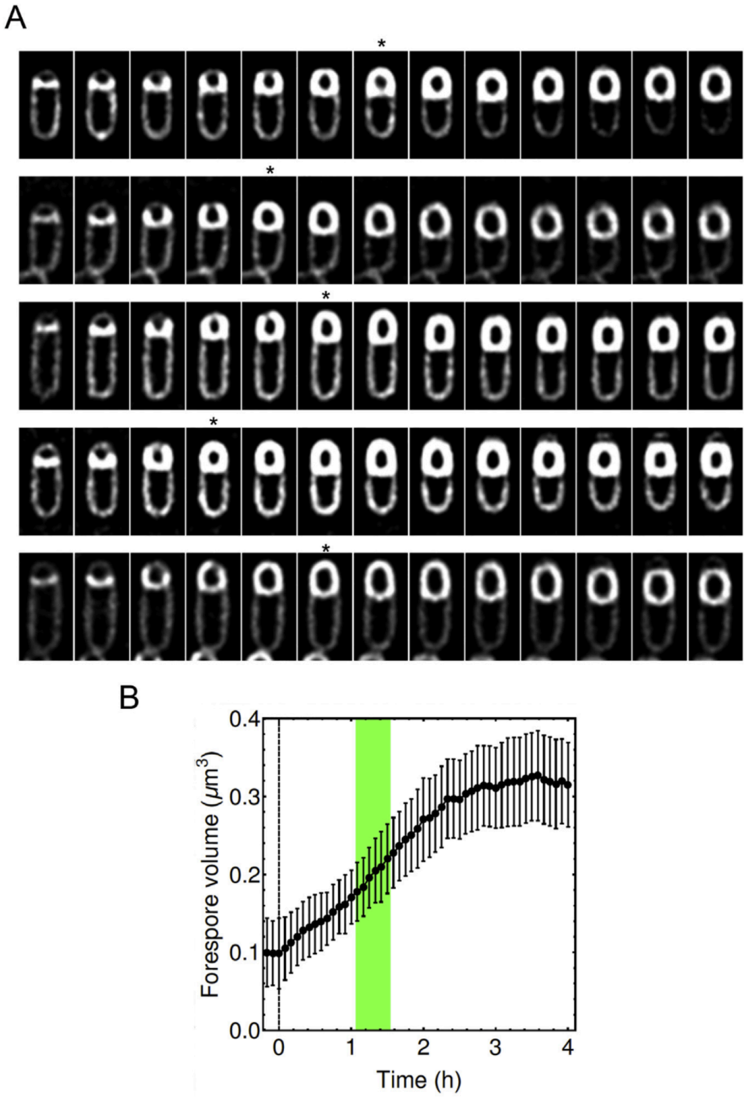

Figure S1. Forespore Growth over Longer Time, Related to Figure 1

(A) Timelapse fluorescence microscopy of wild-type sporangia stained with the membrane dye FM4-64. Each row is a different sporangium. The time between two consecutive snapshots is 20 min, and the total time of each series is 4 hours. The asterisk indicates the time point at which engulfment completes.

(B) Change in forespore volume over time, extracted from timelapse movies. For each time point, the average and standard deviation of 41 sporangia is shown. The green vertical band indicates the time interval at which engulfment membrane migration is completed for the analyzed sporangia. The timelapses were aligned so that 0 h was the time immediately before the time point at which the flat sporulation septum started to curve.

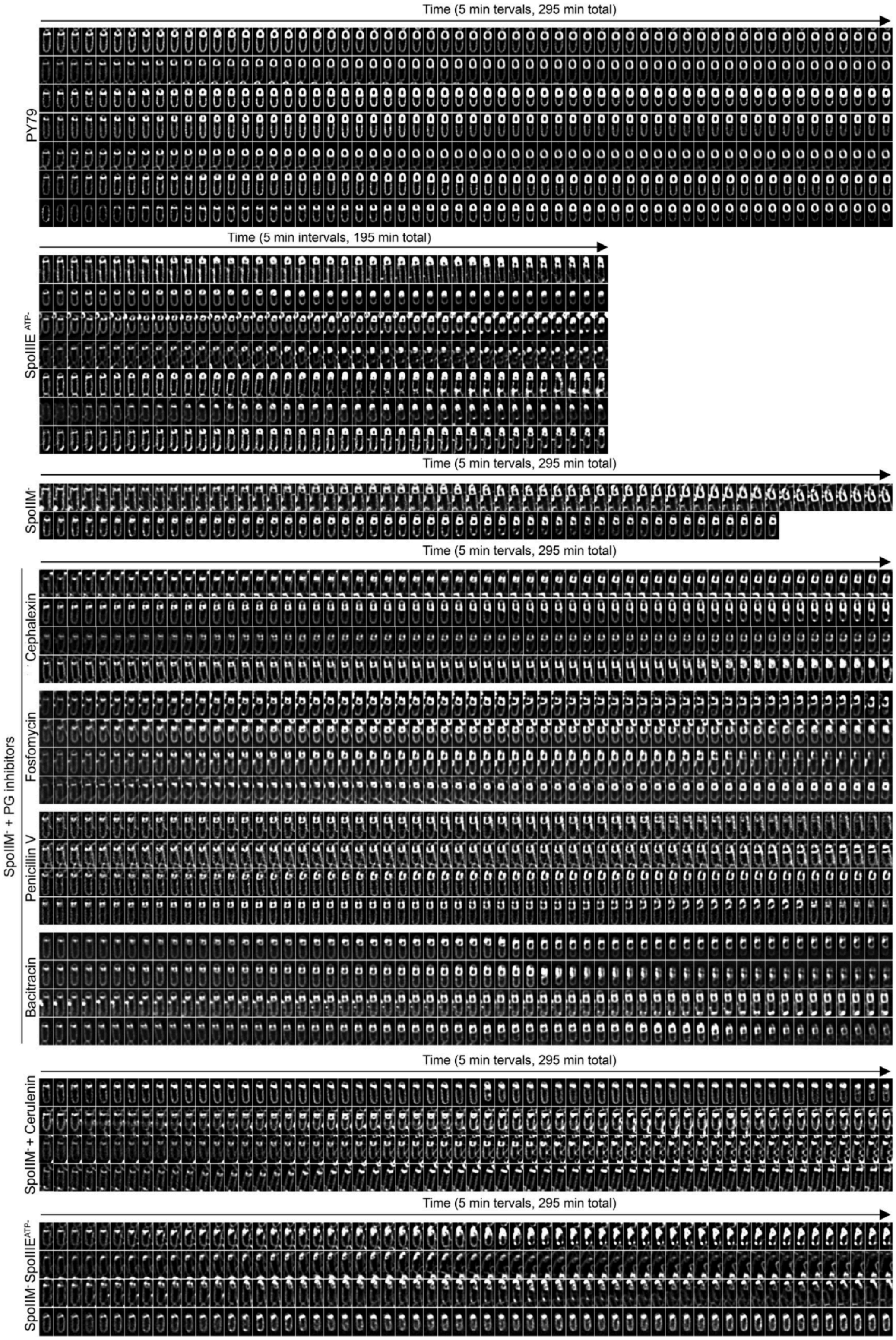

(legend on next page)

Figure S2. Full Timelapse Microscopy Series, Related to Figures 1 and 2

This figure is provided at high-resolution and zoom-in is recommended for proper visualization. Timelapse microscopy of wild-type sporangia, SpoIIIE^{ATP-} sporangia, SpoIIM^{-} sporangia, SpoIIM^{-} sporangia treated with cephalexin (50 μg/ml), fosfomycin (6900 μg/ml), penicillin V (500 μg/ml), bacitracin (50 μg/ml) or cerulenin (30 μg/ml), and SpoIIM^{-} SpoIIIE^{ATP-} sporangia. Images were collected at 30°C every 5 minutes for a total of up to 295 minutes. Each row represents a different sporangium and all the collected time points are shown. Membranes were stained with FM4-64.

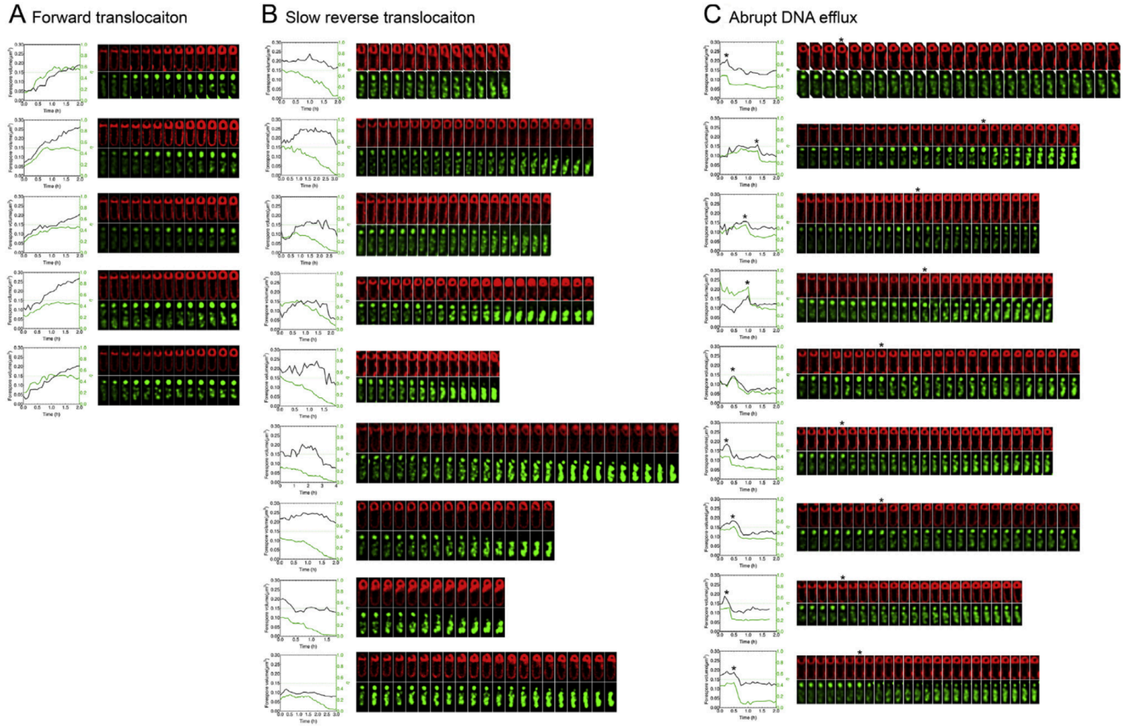

Figure S3. Forward and Reverse Chromosome Translocation, Related to Figure 3

This figure is provided at high-resolution and zoom-in is recommended for proper visualization. Examples of control sporangia (A) in which the chromosome is completely translocated from the mother cell to the forespore, and sporangia in which SpoIIIE is degraded in the mother cell (B and C) and the chromosome is slowly (B) or abruptly (C) translocated out of the forespore. Membranes are stained with FM4-64 and DNA with SYTOX green. Snapshots taken every 10 min are shown for (A) and (B), and every 5 min for (C). Graphs show forespore volume (black line, left y axis) and fraction of DNA intensity in the forespore, η (green line, right y axis), over time of the sporangium immediately next to them. The green dotted line represents the fraction DNA intensity in the forespore corresponding to full chromosome translocation. The asterisks in (C) indicate the onset of the chromosome abrupt transport out of the forespore.

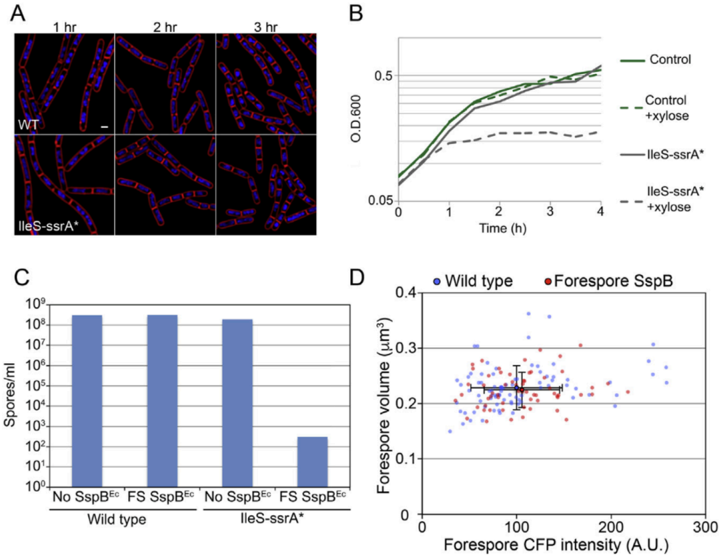

Figure S4. IleS-ssrA* Is Efficiently Degraded and *sspB^{Ec}* Expression in the Forespore Does Not Affect Either Translation or Forespore Size, Related to Figure 4

(A) Fluorescence microscopy of non-sporulating wild-type and IleS-ssrA* strains. Membranes were stained with FM4-64 and DNA with DAPI. Scale bar, 1 μm. Images were taken at the indicated time points after diluting a late exponential culture to O.D.$_{600}$ = 0.2.

(B) Growth curves of strains producing SspB^{Ec} under the control of a xylose-dependent promoter (P_{xylA}), in a background in which IleS is not tagged with ssrA* (control, green lines), or in a background in which IleS is tagged with ssrA* (IleS-ssrA*, gray lines). Late-exponential cultures of each strain were diluted to O.D.$_{600}$ = 0.2, either in the absence of xylose (solid lines) or in the presence of 1% xylose (dotted lines). O.D.$_{600}$ measurements were taken every 30 minutes for 4 hours. Production of SspB^{Ec} in the control does not interfere with growth. However, production of SspB^{Ec} in the IleS-ssrA* background abolishes growth, suggesting that IleS-ssrA* is efficiently degraded.

(C) Spore titers of wild-type and IleS-ssrA* strains in the absence of SspB^{Ec} (No SspB^{Ec}) or when SspB^{Ec} is produced in the forespore from $P_{sspE(2G)}$ (FS SspB^{Ec}). Production of SspB^{Ec} in the forespore does not interferes with spore formation in wild-type background, but produces a dramatic reduction (~10^6 folds) in spore titers in IleS-ssrA* background. The averages of three independent experiments are shown.

(D) Plot representing the total CFP fluorescence intensity in the forespore (x axis) versus forespore volume (y axis) of wild-type sporangia (blue dots), or of sporangia in which SspB^{Ec} is produced in the forespore, but in which no protein is tagged with ssrA* (red dots). Each dot represents an individual forespore. The solid dots represent the average CFP intensity and volume of wild-type sporangia (blue, N = 141) and sporangia in which SspB^{Ec} is produced in the forespore (red, N = 61). The error bars represent the standard deviations. No significant differences are observed on the CFP intensity (p = 0.4345) or forespore size (p = 0.4812) between the two strains.

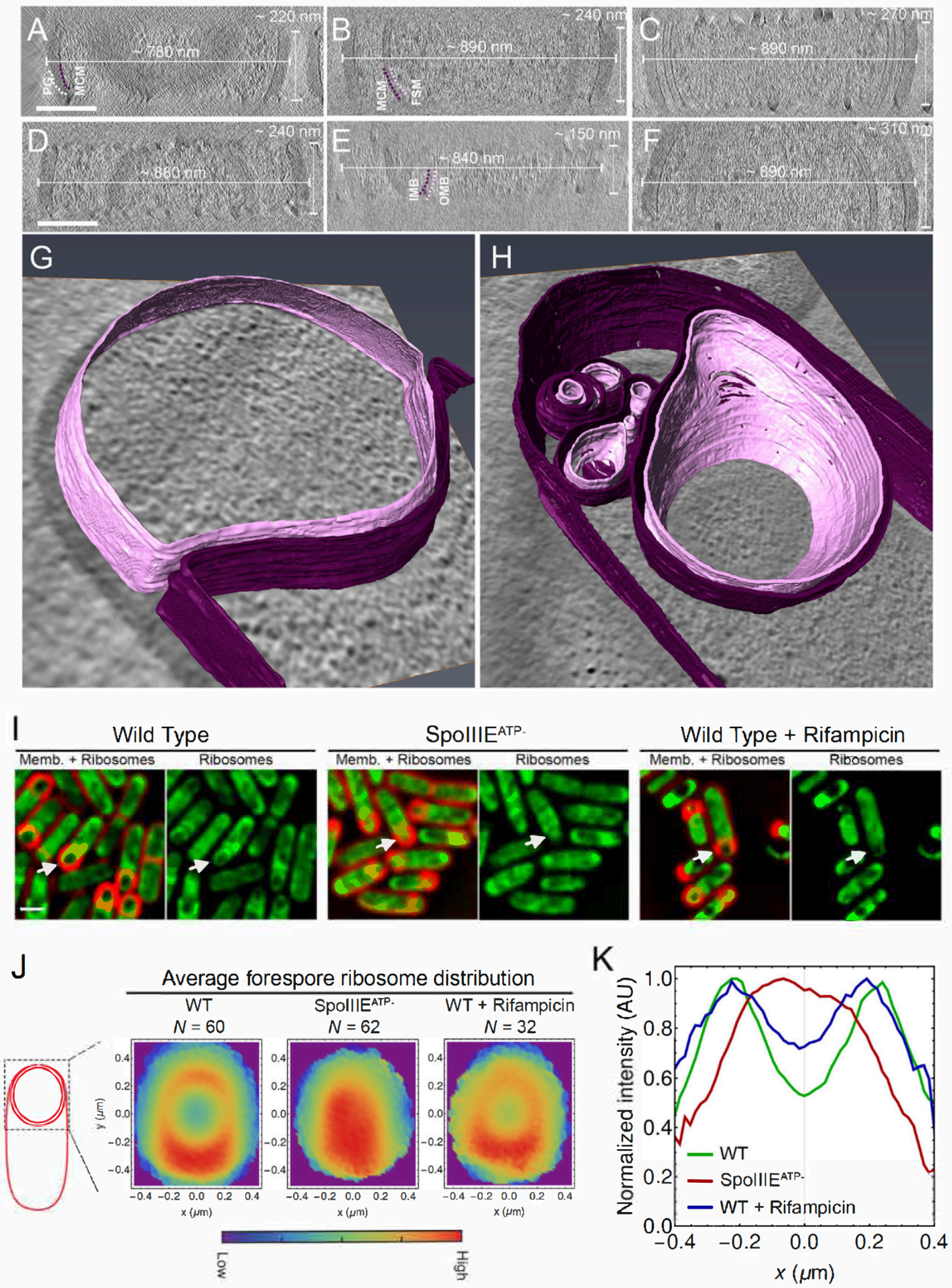

Figure S5. FIB-CE Tomograms Thickness and Membrane Segmentation, Related to Figure 6

(A–F) Cells shown in Figure 6A–6F have been rotated 90° around the short axis of the respective cell. The mother cell membrane (MCM) and forespore membrane (FSM) are highlighted with magenta and pink dotted lines, and PG with white dotted lines. Inner membrane of the bleb (IMB) and outer membrane of the bleb (OMB) for the tomogram shown in Figure 6E are highlighted with magenta and pink dotted lines, respectively, in the rotated view in shown in S5E. The thickness of each lamella as well as the approximate width of the plane at which the slice of the tomogram was taken for Figure 6A–6F is shown for each cell. The volumes

(legend continued on next page)

enclosed by the milled forespores shown in Figure 6B (and B) and Figure 6E (and E) are ∼0.062 μm^3 and ∼0.046 μm^3, respectively (measured by segmenting the forespore in Amira), and there are ∼167 and ∼79 ribosomes in those volumes. Scale bars, 200 nm.

(G) Segmentations of the forespore and mother cell membranes of the sporangium shown in Figure 6D (and S5D) with a wavy appearance.

(H) Segmentations of the forespore and mother cell membranes of the sporangium shown in Figure 6F (and S5F). Excess membrane that accumulates at the mother cell distal pole has also been shown. The forespore membrane is shown in pink, the mother cell membrane in magenta. Scale bars have been omitted in panels G and H as a perspective view of the cells is shown.

(I) Fluorescence microscopy of wild-type sporangia (left), SpoIIIE^{ATP-} sporangia (middle) and wild-type sporangia treated with rifampicin (0.25 μg/ml) for one hour (right) to stop transcription, expressing a GFP fusion to the ribosomal protein S2 (encoded by *rpsB*) to visualize ribosome distribution. The concentration of rifampicin used is five times higher than the minimal inhibitory concentration (Lamsa et al., 2016). The arrows point at representative forespores. Membranes were stained with FM4-64. Scale bar, 1 μm.

(J) Average ribosome distribution in wild-type forespores (WT, right), SpoIIIE^{ATP-} forespores (middle), and wild-type forespores treated with rifampicin (WT + Rifampicin, left).

(K) Normalized fluorescence intensity along a horizontal line that cross (at $y = 0$) the averaged forespores shown in (J). Fluorescently-labeled ribosomes localize to the forespore periphery in wild-type sporangia, but are homogenously distributed in SpoIIIE^{ATP-} forespores, in agreement with CET results (Figure 6G–6J). Ribosomes still tend to localize to the forespore periphery after treatment with rifampicin for one hour, suggesting that the peripheral localization of the ribosomes is not entirely due to the presence of transcriptionally active loops at the forespore periphery. It is likely that the compacted chromosome physically excludes ribosomes due to an excluded volume effect: Forespores are only 0.1-0.2 μm^3 in volume (compared to 1 μm^3 for mother cells), and we estimate that packing a ∼4-megabase chromosome into this small volume will create a DNA mesh with an average pore diameter of < 20 nm (see STAR Methods for calculation details), significantly smaller than what has been estimated for *E. coli* cells (∼50 nm; Castellana et al., 2016). *Bacillus* ribosomes have a diameter of ∼20 nm, and therefore would be unable to freely diffuse inside the nucleoid.

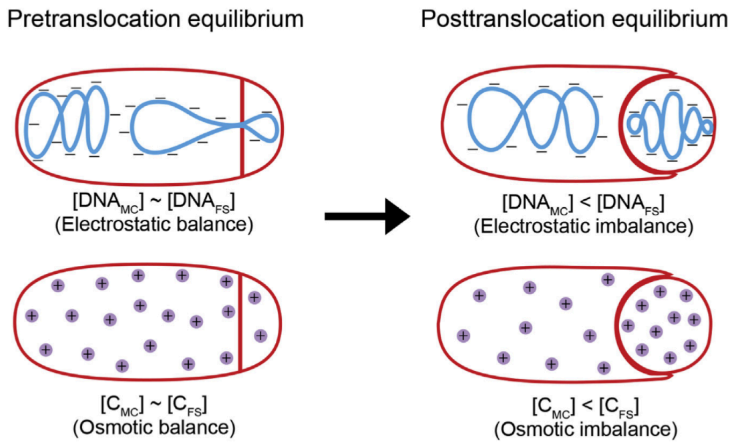

Figure S6. Gibbs-Donnan Effect to Explain the Osmotic Difference between Mother Cell and Forespore, Related to Figure 7

Right after polar septation, the forespore and mother cell are in both electrostatic and osmotic equilibrium, as the same concentration of charges and ions are present in both cells. The translocation of the polyanionic chromosome to the forespore generates an electrostatic imbalance, since the concentration of DNA in the forespore is higher than in the mother cell, due to the size difference of both cells. Because the DNA cannot diffuse freely between the forespore and the mother cell, the electrostatic imbalance is compensated by the redistribution of positively-charged ions (purple circles), which become more concentrated in the forespore. In turn, this creates an osmotic difference between both cells, which ultimately results in a net water flow to the forespore, leading to an increase in turgor pressure.

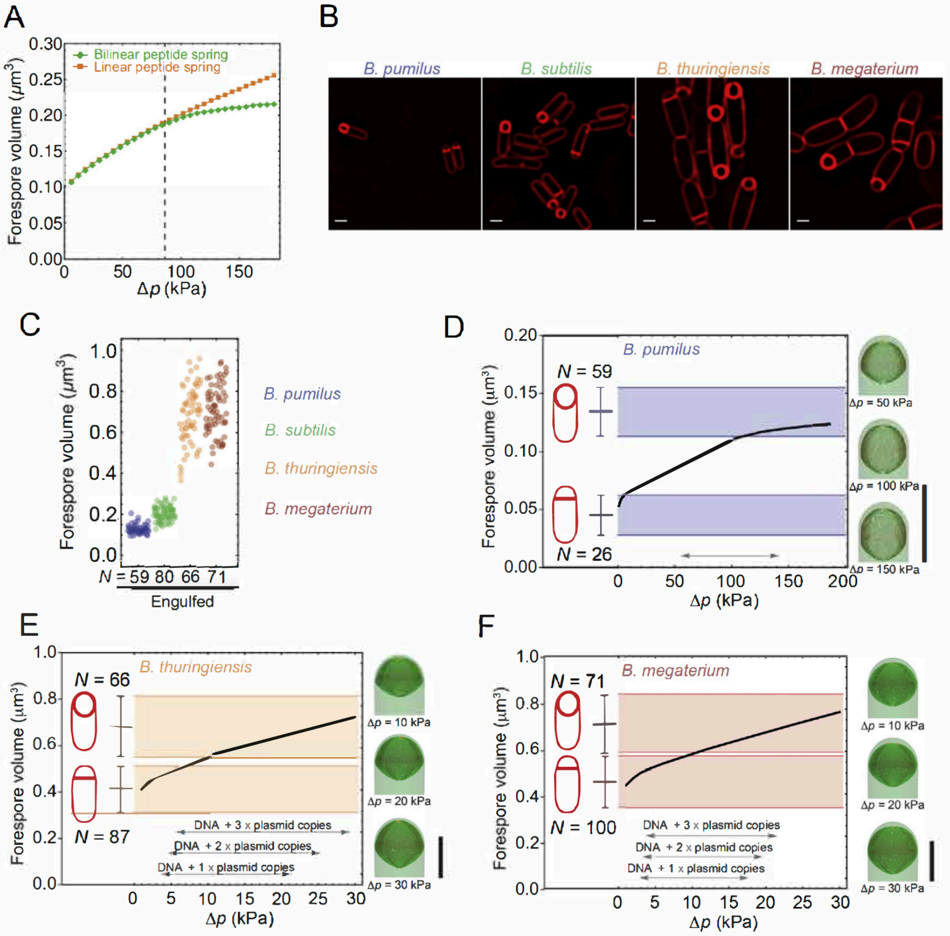

Figure S7. Simulations for Different Peptide Models and Different *Bacillus* Species, Related to Figure 7

(A) Forespore volume at the end of engulfment versus pressure difference (Δ*p*) between forespore and mother cell. Peptides are modeled as linear springs with effective spring constant k_{pep} = 25 pN/nm, or bilinear peptide springs with effective spring constants k_{pep1} = 25 pN/nm for peptide elongation up to 50% natural spring length, and k_{pep2} = 1100 pN/nm for elongations larger than 50% natural spring length (Nguyen et al., 2015; Ojkic et al., 2016). Simulations with linear or bilinear peptides show no significant difference up to pressures of ~100 kPa. In our simulations we used bilinear spring constants. Vertical line represents maximum pressures used to simulate engulfment in Figure 7.

(B) Fluorescence microscopy images of *B. pumilus*, *B. subtilis*, *B. thuringiensis,* and *B. megaterium* sporulating cultures. Membranes were stained with FM4-64. The scale bars are identical for every species (1 μm).

(C) Forespore volume of sporangia that completed engulfment membrane migration (engulfed) for different *Bacillus* species: *B. pumilus* (blue), *B. subtilis* (green), *B. thuringiensis* (orange) and *B. megaterium* (red). Each dot represents a different forespore. The number of forespores measured in each set (*N*) is indicated at the bottom of the graph.

(D–F) Simulated forespore volume after engulfment (black lines) for *B. pumilus* (D), *B. thuringiensis* (E) and *B. megaterium* (F) as a function of Δ*p*. *B. subtilis* simulations are shown in Figure 7. The average forespore volume of sporangia that just underwent polar septation (flat septa) and of sporangia that completed engulfment membrane migration (engulfed) is shown on the left side of each graph. The error bars represent the standard deviation, and the number of forespores measured (*N*) is indicated inside the graph. The difference in volume between engulfed and flat septum sporangia provides a rough estimate of how much forespores grow during engulfment. On the right side of each graph, the horizontal bands represent average volume ± STD of forespores with flat septa (lower band) and fully engulfed forespores (higher band). Theoretically calculated ranges of osmotic pressures generated by genome packing in the forespore are shown with gray arrow bars at the bottom of the graphs. Chromosome sizes of the different species are provided in the STAR Methods. For *B. thuringiensis*, and *B. megaterium*, which contain large plasmids, theoretically calculated ranges of osmotic pressures are shown taking into account uncertainties in forespore plasmid numbers in the forespore. Simulations show that osmotic pressure due to packing the genome in the forespore is enough to explain forespore growth during engulfment in the different *Bacillus* species. Simulation snapshots for different Δ*p* are shown to the right of each graph. Scale bars, 1 μm.

Acknowledgement

Chapter 3, in full, is a reprint of the material as it appears in *Cell* 2018 (Vol. 172(4) pp 758-770. e14) and in the online supplement. The manuscript is: Lopez-Garrido, J., Ojkic, N., Khanna, K., Wagner, F.R., Villa, E., Endres, R.G., Pogliano, K. ‘Chromosome translocation inflates *Bacillus* forespores and impacts cellular morphology’. The dissertation author was the secondary author and performed cryo-ET experiments and analysis.

Chapter 4: The molecular architecture of engulfment during *Bacillus subtilis* sporulation

eLIFE
elifesciences.org

RESEARCH ARTICLE

The molecular architecture of engulfment during *Bacillus subtilis* sporulation

Kanika Khanna, Javier Lopez-Garrido, Ziyi Zhao, Reika Watanabe, Yuan Yuan, Joseph Sugie, Kit Pogliano*, Elizabeth Villa*

Division of Biological Sciences, University of California, San Diego, La Jolla, United States

Abstract The study of bacterial cell biology is limited by difficulties in visualizing cellular structures at high spatial resolution within their native milieu. Here, we visualize *Bacillus subtilis* sporulation using cryo-electron tomography coupled with cryo-focused ion beam milling, allowing the reconstruction of native-state cellular sections at molecular resolution. During sporulation, an asymmetrically-positioned septum generates a larger mother cell and a smaller forespore. Subsequently, the mother cell engulfs the forespore. We show that the septal peptidoglycan is not completely degraded at the onset of engulfment. Instead, the septum is uniformly and only slightly thinned as it curves towards the mother cell. Then, the mother cell membrane migrates around the forespore in tiny finger-like projections, whose formation requires the mother cell SpoIIDMP protein complex. We propose that a limited number of SpoIIDMP complexes tether to and degrade the peptidoglycan ahead of the engulfing membrane, generating an irregular membrane front.

DOI: https://doi.org/10.7554/eLife.45257.001

Introduction

From an architectural point of view, bacterial cells are among the simplest forms of life on the planet. Their cytoplasm is typically devoid of membrane bound organelles, and their cellular morphology relies upon a semi-rigid peptidoglycan (PG) cell wall that imposes its shape on the malleable cell membrane(s). Bacterial cells are inflated by their high internal turgor pressure, which pushes the membranes against the cell wall, causing the PG to stretch and the cell to adopt its appropriate shape. Despite the apparent simplicity, studies in the past few decades have demonstrated that bacterial cellular architecture is far more complex than previously thought, in terms of both its ultrastructure and dynamic capabilities (***Hawver et al., 2016***; ***Wagstaff and Löwe, 2018***; ***Wang et al., 2013***).

Endospore formation in *Bacillus subtilis* represents a striking example of the dynamic capabilities of bacterial cells, as it entails dramatic changes in cellular architecture. First, the division site shifts to polar position, generating a sporangium comprised of two cells: a larger mother cell and a smaller forespore (***Figure 1A***; ***Errington, 2003***; ***Higgins and Dworkin, 2012***; ***Tan and Ramamurthi, 2014***). The polar septum traps the forespore chromosome, which is subsequently transported to the forespore by SpoIIIE, a membrane-anchored ATPase that assembles a translocation complex at septal midpoint (***Bath et al., 2000***; ***Yen Shin et al., 2015***; ***Wu and Errington, 1994***; ***Wu and Errington, 1997***). Chromosome translocation increases the turgor pressure in the forespore, causing it to inflate and expand into the mother cell (***Lopez-Garrido et al., 2018***). Simultaneously, the mother cell engulfs the forespore in a process that resembles eukaryotic phagocytosis (***Figure 1A***). After engulfment, the forespore is fully enclosed within the cytoplasm of the mother cell, where it matures in a process that involves the synthesis of protective layers of cortex and coat, and the partial dehydration of the forespore cytoplasm. Finally, the mother cell lyses and the mature spore is released to the environment, where it remains dormant until the conditions are appropriate for germination.

***For correspondence:**
kpogliano@ucsd.edu (KP);
evilla@ucsd.edu (EV)

Competing interests: The authors declare that no competing interests exist.

Funding: See page 18

Received: 29 January 2019
Accepted: 04 July 2019
Published: 08 July 2019

Reviewing editor: Tâm Mignot, CNRS-Aix Marseille University, France

eLife digest Much of what happens in biology occurs at scales so small that the microscopy methods traditionally used by biologists cannot visualize them. One such process is bacterial sporulation: in stressful conditions, bacteria like *Bacillus subtilis* can divide to produce a smaller cell called a forespore, which the larger mother cell then engulfs. The forespore matures into a hardy spore, which is able to survive in harsh environments and only transform into an active bacterium when conditions improve.

Bacterial cells are surrounded by a stiff layer of a material called peptidoglycan. This wall sits outside of the bacterium's thin flexible membrane and determines the bacterium's shape. At the beginning of sporulation, the forespore is separated from the mother cell by a peptidoglycan wall. Engulfment of the spore by the mother cell requires a dramatic change in the shape of this partition. Microbiologists had thought that all the rigid peptidoglycan must be degraded to allow the partition to deform flexibly during engulfment; however, no one had yet observed the tiny structures involved.

Khanna et al. directly visualized sporulation in *B. subtilis* using a technique called cryo-electron tomography (or cryo-ET for short). In cryo-ET, samples are cooled to low temperatures and then imaged with a beam of electrons. Cryo-ET requires thin samples, thinner even than most bacteria. By combing cryo-ET with another methodology that allowed them to focus in on thin sections of their sample, Khanna et al. generated high resolution images, which provided a look at forespore engulfment in unprecedented detail.

These images revealed that the peptidoglycan wall separating the mother cell from forespore is not completely degraded: a thin layer of peptidoglycan persists. Comparing these images to cryo-ET images of cells treated with drugs that block the production of peptidoglycan suggested a new engulfment mechanism. This includes a cycle of peptidoglycan production and degradation that accompanies the advancing mother cell membrane as it surrounds the forespore during engulfment. Khanna et al. could also see that the mother cell's membrane formed finger-like projections as it moved around the forespore, something that was not visible with previous techniques.

This detailed engulfment mechanism is an important advance in the understanding of bacterial spore formation. Additionally, Khanna et al. have generated a collection of images, methods and analyses that may prove useful to a wide community of biologists attempting to understand sporulation and other fundamental processes that occur on a small scale.

DOI: https://doi.org/10.7554/eLife.45257.002

Engulfment represents a major rearrangement of the sporangium, from two cells that lie side by side to a cell within a cell. Such rearrangement likely involves a profound remodeling of the PG cell wall around the forespore, which would otherwise constrain the movement of the engulfing membrane. At the onset of engulfment, the engulfing mother cell membrane must circumvent the physical barrier posed by the septal PG in order to migrate around the forespore. This has led to the logical proposal that engulfment must entail the complete dissolution of the septal PG, a process often referred to as 'septal thinning' (***Chastanet and Losick, 2007***; ***Illing and Errington, 1991***; ***Perez et al., 2000***). This proposal was supported by early electron microscopy studies of fixed and stained sporangia showing that engulfment-defective mutants had thicker septa than wild type sporangia (***Holt et al., 1975***; ***Illing and Errington, 1991***; ***Rousseau and Hermier, 1975***). Further studies showed that engulfment requires three mother cell proteins: SpoIID, SpoIIM and SpoIIP, which form a complex (DMP) with PG degradation activity (***Abanes-De Mello et al., 2002***; ***Aung et al., 2007***; ***Chastanet and Losick, 2007***; ***Morlot et al., 2010***). In principle, DMP could mediate the complete dissolution of the septal PG to remove the steric block to the movement of the mother cell membrane around the forespore.

The idea that septal PG is completely degraded has been more recently challenged by cryo-electron tomography (cryo-ET) images showing that a thin PG layer is present between the forespore and the mother cell membranes throughout engulfment (***Tocheva et al., 2013***). It has also been shown that DMP-mediated PG degradation is required and rate-limiting for membrane migration even after the septal barrier has been bypassed, suggesting that DMP plays a role separate from the

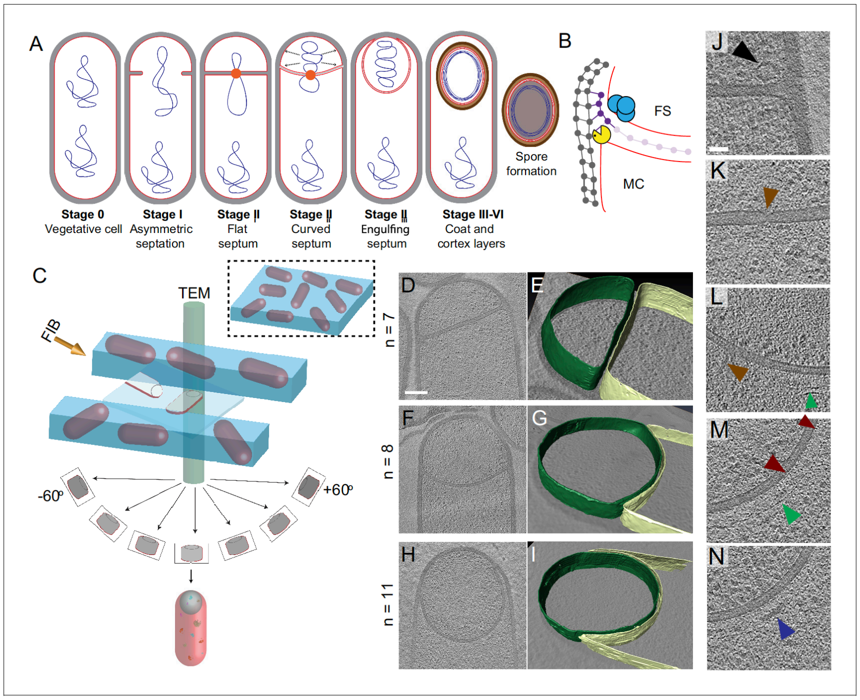

Figure 1. Visualizing the 3D architecture of engulfment during sporulation in *B. subtilis*. (**A**) Schematic illustrating the process of polar septation, chromosome translocation, engulfment and spore maturation. Membranes (red), PG (gray), chromosomes (blue), SpoIIIE (orange) and coat proteins (shades of brown) are highlighted. Outward arrows in the stage II_{ii} forespore indicate increased turgor pressure due to chromosome translocation. (**B**) Revised engulfment model (***Ojkic et al., 2016***): new PG (purple) is synthesized ahead of the leading edge of the engulfing membrane by forespore-associated PG biosynthetic enzymes (blue) and is subsequently degraded by DMP (yellow pacman), making room for the engulfing membrane to advance. The coordinated synthesis and degradation of PG at the leading edge of the engulfing membrane can move the junction between the septum (pink) and the lateral cell wall (gray) around the forespore. (**C**) Schematic illustrating cryo-FIB-ET methodology for bacterial samples (see Materials and methods). (**D–I**) Slices through cryo-electron tomograms representing different stages of engulfment: (**D**) flat polar septum (Stage II_i), (**F**) curved septum (Stage II_{ii}) and (**H**) engulfing septum (Stage II_{iii}). Scale bar for (D,F,I): 200 nm. The corresponding forespore membrane (green) and the mother cell membrane (yellow) are annotated in (**E,G,I**) respectively. n indicates the number of tomograms acquired for each cell type. Scale bars have been omitted for (E,G,I) as cells are shown in perspective views . (**J–N**) Zoomed-in slices through cryo-electron tomograms showing (**J**) a large ellipsoidal complex adjacent to the forespore membrane (black arrow), (**K**) a putative SpoIIIE channel (brown arrow) and (**L**) another putative channel (brown arrow), (**L,M**) coat filaments (green arrows), (**M**) basement coat layer (maroon arrow) and (**N**) amorphous coat proteins (purple arrow). Scale bar for (J-N): 50 nm.

DOI: https://doi.org/10.7554/eLife.45257.003

The following figure supplements are available for figure 1:

Figure supplement 1. Slices through cryo-electron tomograms representing different stages of engulfment in wild type sporulating *B. subtilis* cells.

DOI: https://doi.org/10.7554/eLife.45257.004

Figure supplement 2. Slices through cryo-electron tomograms representing later stages of sporulation when the forespore is completely inside the mother cell.

DOI: https://doi.org/10.7554/eLife.45257.005

Figure supplement 3. Unidentified complexes during sporulation in *B. subtilis*.

DOI: https://doi.org/10.7554/eLife.45257.006

dissolution of septal PG (***Abanes-De Mello et al., 2002***; ***Gutierrez et al., 2010***). In addition, the movement of the mother cell membrane also requires PG synthesis at the leading edge of the engulfing membrane (***Meyer et al., 2010***; ***Ojkic et al., 2016***). Based on these observations, we proposed a revised model for engulfment membrane migration in which coordinated PG synthesis and degradation at the leading edge of the engulfing mother cell membrane moves the junction between the septum and the lateral cell wall around the forespore, making room for the engulfing membrane to advance (**Figure 1B**; **Ojkic et al., 2016**). This model eliminates the need for complete dissolution of the septal PG and predicts that PG synthesis happens ahead of the leading edge of the engulfing membrane. Then, the mother cell DMP degrades this new PG to mediate membrane migration. However, due to the limited resolution of optical microscopy, conclusive evidence that PG synthesis occurs ahead of PG degradation is lacking.

Cryo-ET allows the visualization of three-dimensional (3D) architecture of bacterial membranes and cell wall in a hydrated near-native state that cannot be achieved by methods reliant on chemical fixation and staining (**Ben-Harush et al., 2010**; **Matias and Beveridge, 2005**; **Oikonomou et al., 2016**). However, a limitation of cryo-ET is that the samples must be less than ~500 nm thick to obtain high-resolution tomograms, constraining its application to only a handful of bacteria that are either naturally slender, or, as in the case of *B. subtilis*, for which slender mutant strains are available (**Tocheva et al., 2013**). But the latter typically contain mutations in genes involved in PG metabolism and may not be ideal to study cell wall remodeling. Recent application of cryo-focused ion beam (cryo-FIB) milling has produced artifact-free thin sample sections of ~100–300 nm, which allows the acquisition of high-resolution tomograms of sections of wild type cells (**Figure 1C**; **Marko et al., 2007**; **Rigort et al., 2012**; **Villa et al., 2013**). Cryo-FIB milling coupled with cryo-ET (or cryo-FIB-ET) is therefore becoming the method of choice for studies of cellular architecture of both eukaryotic and prokaryotic cells (**Chaikeeratisak et al., 2017**; **Engel et al., 2015**; **Lopez-Garrido et al., 2018**; **Mahamid et al., 2016**).

Here, we have used cryo-FIB-ET to study sporulation in *B. subtilis*, revealing the different stages of engulfment with a resolution that has not been achieved previously. We have analyzed wild type sporangia, engulfment mutants, and sporangia treated with PG synthesis inhibitors to obtain new mechanistic insights into the PG transformations that occur during engulfment. First, we provide evidence that septal PG is not degraded completely at the onset of engulfment. Second, we show that during membrane migration, the newly synthesized PG deforms the forespore membrane ahead of the leading edge of the engulfing mother cell membrane, indicating that PG synthesis precedes PG degradation. Third, we observe that the mother cell membrane migrates around the forespore by forming tiny finger-like projections, the formation of which depends on DMP complexes tethering to and degrading the PG ahead of the engulfing membrane. The methodology, images and analyses presented here will provide valuable resources for future studies of spore assembly and other fundamental cell biological processes.

Results

Visualizing sporulation in wild type *B. subtilis* at molecular resolution

Recently, we used cryo-FIB-ET to illustrate the role of DNA translocation in inflating the forespore (**Lopez-Garrido et al., 2018**). These data confirmed the presence of a thin layer of PG between the forespore and the mother cell membranes in the wild type strain, as previously visualized by cryo-ET of a slender *ponA* mutant of *B. subtilis* (**Tocheva et al., 2013**). We expanded our cryo-FIB-ET studies to investigate the architecture of *B. subtilis* cells during different stages of sporulation (**Figure 1C**; see Materials and methods). We acquired high-quality data of wild type cells during engulfment (Stage II, **Figure 1D–I**; **Figure 1—figure supplement 1**) and during later stages of sporulation, when cortex and coat were being assembled (Stages III-VI, **Figure 1—figure supplement 2**). Data of very late stages of

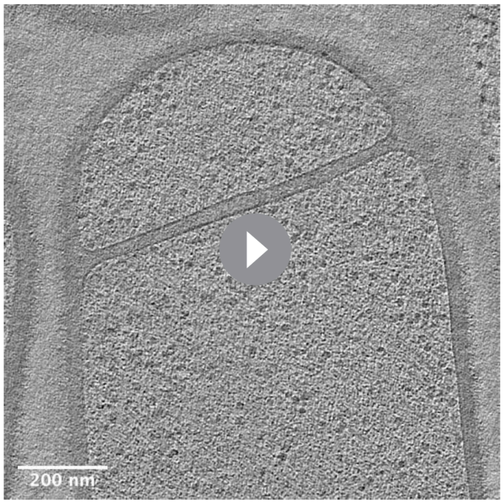

Video 1. Movie showing slices through a cryo-electron tomogram of *B. subtilis* wild type sporangium (flat septum, Stage II_i) shown in **Figure 1D**.
DOI: https://doi.org/10.7554/eLife.45257.007

Video 2. Movie showing slices through a cryo-electron tomogram of *B. subtilis* wild type sporangium (curved septum, Stage II_{ii}) shown in ***Figure 1F***.
DOI: https://doi.org/10.7554/eLife.45257.008

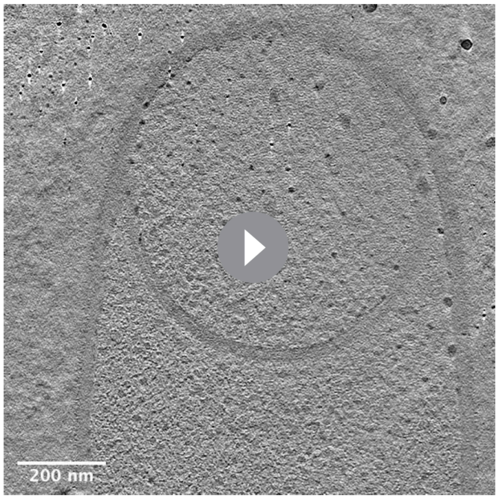

Video 3. Movie showing slices through a cryo-electron tomogram of *B. subtilis* wild type sporangium (engulfing septum, Stage II_{iii}) shown in ***Figure 1H***.
DOI: https://doi.org/10.7554/eLife.45257.009

sporulation failed to provide high-resolution information inside the forespore, likely due to the dehydration of this cell, which increases sensitivity of cryo-ET samples to the electron beam (***Wu et al., 2012***).

Our data showed that the external cell wall of sporulating cells was ~20–30 nm thick, consistent with other EM studies (***Matias and Beveridge, 2005***; ***Tocheva et al., 2013***). The polar septum formed close (within 500 nm) to one cell pole, and was initially flat (***Figure 1D,E***, ***Figure 1—figure supplement 1A–D***, ***Video 1***). Eventually, the septum bent smoothly into the mother cell (***Figure 1F, G***, ***Figure 1—figure supplement 1E–H***, ***Video 2***) and the mother cell membrane moved forward to engulf the forespore, at which stage the forespore was roughly rounded (***Figure 1H,I***, ***Figure 1—figure supplement 1I–L***, ***Video 3***).

Visual inspection of tomograms also revealed several structures that have not been characterized previously. Immediately after polar septation, we observed ellipsoidal complexes that were present only in the forespore, adjacent to the membrane and often close to the intersection between the septum and the lateral cell wall (***Figure 1J***, ***Figure 1—figure supplement 3A–C***). These structures were observed in 2 out of 7 tomograms of wild type sporangia with flat septa, with ~4 ellipsoidal complexes observed in ~200 nm slices. The 3D reconstruction of these complexes revealed that the ellipsoidal structures had a mean radius of ~45 nm (***Figure 1—figure supplement 3A–C***, see Materials and methods). The molecular identity of these structures remains undetermined. We also identified a region approximately in the center of a flat septum where the two membranes are closer together than elsewhere on the septum (14 nm vs. 23 nm, ***Figure 1K***, ***Figure 1—figure supplement 3D,E***). This constriction may correspond to paired hexameric SpoIIIE channels (***Fleming et al., 2010***; ***Liu et al., 2006***; ***Yen Shin et al., 2015***). We also observed structures that appear to be channels crossing the septum (***Figure 1L***) that may correspond to SpoIIIA-SpoIIQ complexes (***Blaylock et al., 2004***; ***Levdikov et al., 2012***; ***Morlot and Rodrigues, 2018***; ***Zeytuni et al., 2017***). We observed this thin region in the polar septum and channel-like features (***Figure 1K,L***) in 2 out of 15 tomograms of wild type sporangia with flat and curved septa. The low frequency of observation could be attributed to the fact that we are imaging only ~150–250 nm slices of cells that are over 1 µm wide. So, many tomograms would not include low abundance structures such as SpoIIIE, which is comprised of two adjacent channels. Next, we observed a basement coat layer adjacent to the outer forespore membrane that is likely comprised of SpoVM and/or SpoIVA (***Figure 1M***; ***Ramamurthi and Losick, 2009***). This layer is visible as an array of dots spaced ~4–6 nm apart, similar to that observed previously in *Acetonema longum* sporulating cells (***Tocheva et al., 2011***). Moving outward, we observed

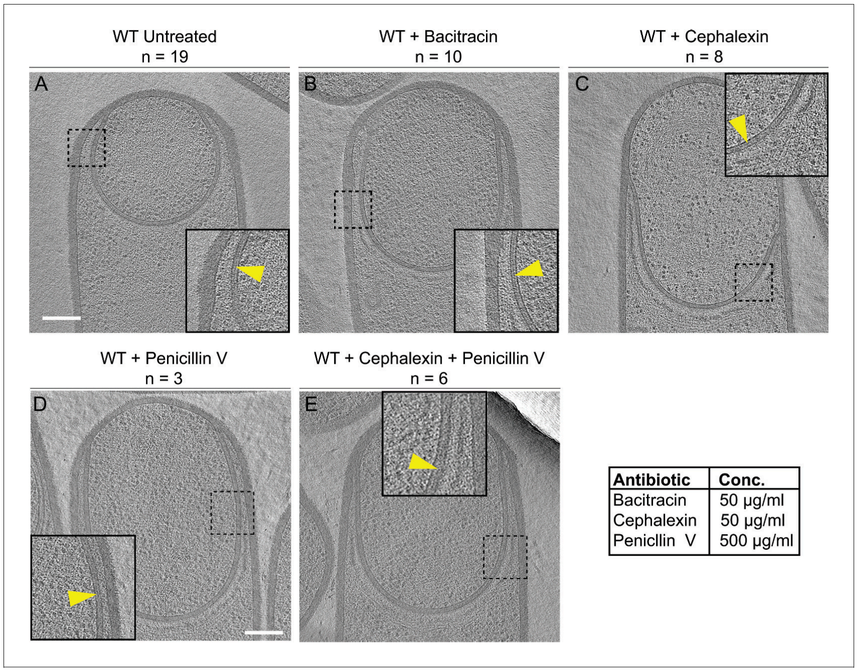

Antibiotic	Conc.
Bacitracin	50 μg/ml
Cephalexin	50 μg/ml
Penicllin V	500 μg/ml

Figure 2. Septal PG is not completely degraded at the onset of engulfment. (**A–C**) Slices through cryo-electron tomograms of wild type engulfing sporangia that are (**A**) untreated, (**B**) bacitracin-treated, (**C**) cephalexin-treated, (**D**) penicillin V-treated and (**E**) penicillin V- and cephalexin-treated. The thin layer of septal PG is indicated by yellow arrows in the zoom-in panels for each of the tomographic slices. n indicates the number of tomograms acquired for each cell type. Antibiotic concentrations used for the experiments are indicated in the bottom right. Scale bar: 200 nm.

DOI: https://doi.org/10.7554/eLife.45257.010

The following figure supplements are available for figure 2:

Figure supplement 1. Quantification of cell length upon antibiotic treatment.

DOI: https://doi.org/10.7554/eLife.45257.011

Figure supplement 2. Thin layer of septal peptidoglycan persists in wild type and antibiotic-treated sporangia.

DOI: https://doi.org/10.7554/eLife.45257.012

a dense amorphous layer and a filamentous layer (***Figure 1L–N***, ***Figure 1—figure supplement 3F, G***) that may contain CotE, SpoIVA and other coat proteins that are recruited to the outer forespore membrane during engulfment (***McKenney et al., 2013***). Further studies are required to determine the molecular identity of these structures unambiguously.

Septal PG is not completely degraded at the onset of engulfment

The cryo-FIB-ET images provided high-resolution details of the septum and the engulfing membrane. Hence, we focused on those details to obtain mechanistic insights about engulfment. The complete degradation of the septal PG

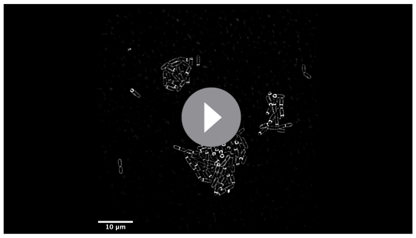

Video 4. Time-lapse microscopy of untreated sporulating *B. subtilis* cells stained with the membrane dye FM4-64. Pictures were taken every 5 minutes for 2 hours (related to ***Figure 2—figure supplement 1***).

DOI: https://doi.org/10.7554/eLife.45257.013

during septal thinning has been traditionally considered a prerequisite for engulfment (***Abanes-De Mello et al., 2002***; ***Chastanet and Losick, 2007***; ***Eichenberger et al., 2001***; ***Perez et al., 2000***). However, we observed a thin PG layer between the mother cell and the forespore membranes throughout engulfment in both wild type (***Figure 2A***; ***Lopez-Garrido et al., 2018***) and a slender *ponA* mutant (***Tocheva et al., 2013***), suggesting that the septal PG is either not completely degraded or is quickly resynthesized after degradation.

To probe this, we imaged engulfing sporangia after treatment with antibiotics that block PG synthesis. When PG synthesis is inhibited, engulfment membrane migration does not continue, although the septum still stretches and curves into the mother cell (***Ojkic et al., 2016***). We reasoned that, if the septal PG was completely degraded, we would observe sporangia lacking PG between the mother cell and the forespore membranes after antibiotic treatment. However, if the septal PG was not completely degraded, the sporangia would show a layer of PG around the forespore, independent of antibiotic treatment.

To inhibit PG synthesis, we treated the cells with bacitracin, cephalexin, penicillin V or a combination of penicillin V and cephalexin (***Figure 2***). We previously assessed the extent of PG inhibition after antibiotic treatment by determining the frequency of division events, which rely on the synthesis of new PG (***Ojkic et al., 2016***). As expected, our results showed that untreated cells continued to grow and divide under the experimental conditions (***Figure 2—figure supplement 1A***) but when treated with cephalexin and penicillin V, cell division was completely blocked. These results also indicated that PG synthesis was inhibited within a few minutes of antibiotic treatment, because cells that were already undergoing septation were unable to complete septum formation (***Figure 2—figure supplement 1B–D***, top panels). To complement this analysis, we tested if these drugs also inhibited elongation, which also depends on PG synthesis (***Spratt, 1975***). To do so, we measured the elongation of vegetative cells present in sporulating cultures over a period of one hour after antibiotic treatment (***Figure 2—figure supplement 1E***, see Materials and methods). The length of wild type untreated vegetative cells increased by ~35% in an hour, but when treated with cephalexin or penicillin V alone, they elongated only ~10%. Furthermore, when treated with a combination of cephalexin and penicillin V, the cells elongated negligibly, indicating complete blockage of both septation and elongation (***Figure 2—figure supplement 1***, ***Videos 4–7***).

For cryo-FIB-ET, we added the antibiotics two hours after inducing sporulation, when ~ 40–50% of the cells have undergone polar septation (***Ojkic et al., 2016***), and plunge froze the samples either one (for bacitracin) or two hours (for cephalexin, penicillin V, and combination of cephalexin and penicillin V) later. Indeed, we observed a thin PG layer in both untreated and antibiotic-treated sporangia (***Figure 2***, ***Figure 2—figure supplement 2***), suggesting that septal PG is not completely degraded at the onset of engulfment.

Septal thickness decreases slightly and uniformly across the entire septum during engulfment

The above observation prompted us to re-evaluate the process of septal thinning. The current model for septal thinning proposes that DMP initially localizes to the septal midpoint, where it starts degrading the septal PG as it moves towards the edge of the septal disk (***Abanes-De Mello et al., 2002***; ***Chastanet and Losick, 2007***; ***Illing and Errington, 1991***; ***Meyer et al., 2010***). This enzymatic septal thinning model predicts that, during the transition from flat to curved septa, the septum should be thinner in the middle than at the edges (***Figure 3A***). To test this, we measured the distance between the forespore and the mother cell membranes across the length of the septum (see Materials and methods) for cells with flat (Stage $\mathrm{II_{i}}$), curved (Stage $\mathrm{II_{ii}}$) and engulfing (Stage $\mathrm{II_{iii}}$) septa (***Figure 3B–D***, ***Figure 3—figure supplement 1***). Sporangia with flat septa had an average septal thickness of ~23 nm±3.3 nm (***Figure 3B,E,F***) with 3 out of 5 septa being thicker at the middle (~28 nm) than at the edges (~22 nm) (***Figure 3B,E***, ***Figure 3—figure supplement 1A***), contrary to what is proposed by the enzymatic septal thinning model. The septal thickness decreased by ~25% to~18 nm during later stages of engulfment (***Figure 3C–F***, ***Figure 3—figure supplement 1B,C***) and a thin layer of PG was observed in all septa (***Figure 2A***, ***Figure 2—figure supplement 2A–C***). Importantly, septal thickness was uniform across the entire septum during later stages (***Figure 3C,D,E***, ***Figure 3—figure supplement 1B,C***) and no septum was thinner in the middle than in the edges. These results show that the transition from thick to thin septum is homogenous, contrary to the prediction of the enzymatic septal thinning model, and consistent with the model that DNA translocation dependent forespore growth stretches septal PG.

SpoIIDMP is essential to maintain a thin, flexible septum

Next, we tested whether DMP was required to mediate the slight thinning observed during the transition from flat to curved septum. To address this question, we measured septal thickness in DMP mutants. In single mutants lacking D, M or P, engulfment is blocked but the septum bulges towards the mother cell, which complicates the analysis (***Figure 3—figure supplement 2***). However, bulge formation is largely abolished in a triple mutant lacking functional versions of D, M and P simultaneously (***Eichenberger et al., 2001***). Therefore, we imaged the DMP triple mutant by cryo-FIB-ET and measured its septal thickness (***Figure 3G–I***, ***Figure 3—figure supplement 3***).

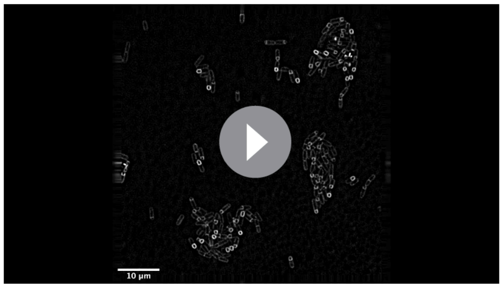

Video 5. Time-lapse microscopy of penicillin V-treated (500 μg/ml) sporulating *B. subtilis* cells stained with the membrane dye FM4-64. Pictures were taken every 5 minutes for 2 hours (related to ***Figure 2—figure supplement 1***).

DOI: https://doi.org/10.7554/eLife.45257.014

Most sporulation septa of the DMP triple mutant were either flat or slightly curved into the mother cell (***Figure 3G–I***, ***Figure 3—figure supplement 3A–D***). In some cells, we observed membrane accumulation in the mother cell (***Figure 3H,I***, ***Figure 3—figure supplement 3A,B***) and small bulges approximately in the middle of the septum (***Figure 3—figure supplement 3C,D***, ***Video 8***). Septal thickness ranged from ~25 nm to ~45 nm, with an average thickness of 28 nm ±2.09 nm (***Figure 3E–G***, ***Figure 3—figure supplement 3E***), which is ~5 nm greater than that of wild type sporangia with flat septa. Importantly, there were no significant differences in septal thickness between flat and curved septa in DMP mutant sporangia (***Figure 3G***, ***Figure 3—figure supplement 3E***), indicating that DMP is in fact necessary for the slight thinning of the septum observed in wild type sporangia.

Surprisingly, the thickness of individual DMP mutant septum was irregular across the septal length, with thicker regions of more than 45 nm, that were not observed in wild type cells (***Figure 3G***, ***Figure 3—figure supplement 3E***). One possible explanation for this finding is that in the absence of DMP, proteins involved in PG synthesis persist at the septum, and their continued activity leads to thicker and less flexible septal regions (***Figure 3J***). To test this model, we stained wild type and DMP mutant sporangia with BOCILLIN-FL, a fluorescent-derivative of penicillin V with affinity for multiple penicillin-binding proteins (PBPs) (***Zhao et al., 1999***, see Materials and methods). We observed continuous fluorescent signal around the septa in both strains, but the signal was

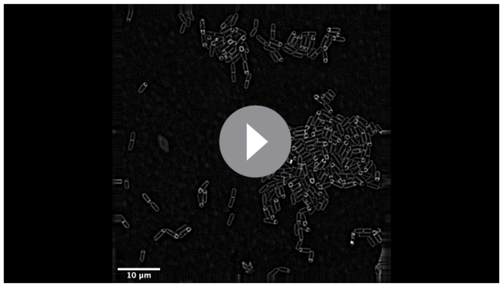

Video 6. Time-lapse microscopy of cephalexin-treated (50 μg/ml) sporulating *B. subtilis* cells stained with the membrane dye FM4-64. Pictures were taken every 5 minutes for 2 hours (related to ***Figure 2—figure supplement 1***).

DOI: https://doi.org/10.7554/eLife.45257.015

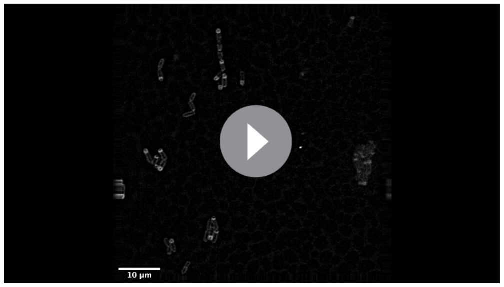

Video 7. Time-lapse microscopy of cephalexin- (50 μg/ml) and penicillin V- (500 μg/ml) treated sporulating *B. subtilis* cells stained with the membrane dye FM4-64. Pictures were taken every 5 minutes for 2 hours (related to ***Figure 2—figure supplement 1***).

DOI: https://doi.org/10.7554/eLife.45257.016

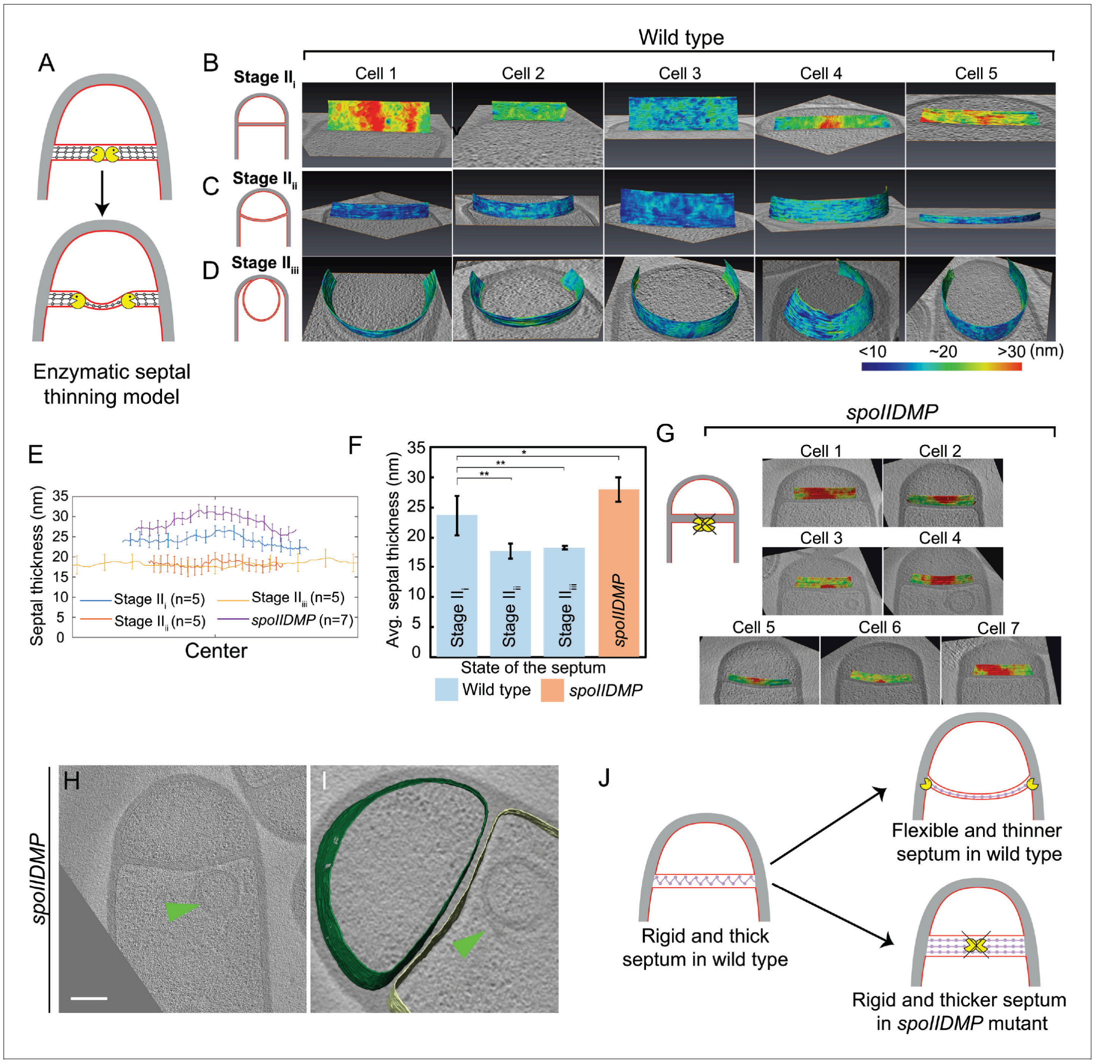

Figure 3. Septum is uniformly and only slightly thinned during engulfment and SpoIIDMP is required to maintain a thin flexible septum. (**A**) Schematic illustrating the model of septal thinning driven by septal PG (black meshwork) degradation by the DMP complex (yellow pacman) with membranes (red) and lateral PG (gray) highlighted. (**B–D**) Septal disc is color-coded according to the distance between the forespore and the mother cell membranes in five wild type sporangia with (**B**) flat, (**C**) curved and (**D**) engulfing septa. Schematic representing the morphology of each cell type is shown on the far left. (**E**) Average thickness of the septum across the forespore surface for the cells shown in (**B–D,G**). Error bars indicate standard deviation. n indicates the number of tomograms used for calculating septal distances in each case. (**F**) Average septal thickness for wild type flat (Stage II$_i$), curved (Stage II$_{ii}$) and engulfing (Stage II$_{iii}$) sporangia and *spoIIDMP* mutant sporangia. Error bars indicate standard deviation (n.s.: $p>0.05$; *: $p\leq0.05$; **: $p\leq0.01$; ***: $p\leq0.001$, unpaired t-test). (**G**) Septal disc is color-coded according to the distance between the forespore and the mother cell membranes in seven *spoIIDMP* mutant sporangia. Scale bars have been omitted in distance plots as perspective views are shown. (**H**) Slice through a cryo-electron tomogram of *spoIIDMP* mutant sporangia. Scale bar: 200 nm. (**I**) Annotated forespore (green) and mother cell (yellow) membranes for the tomogram in (**H**). Excess membrane accumulation is highlighted by green arrows. (**J**) Schematic representing the role of DMP (yellow pacman) in septal thinning with membranes (red), lateral PG (gray) and septal PG (pink) highlighted. The rigid and thick septum in wild type can curve into the mother cell during engulfment but that of DMP becomes even thicker and does not curve into the mother cell.

Figure 3 continued on next page

Figure 3 continued

DOI: https://doi.org/10.7554/eLife.45257.017

The following source data and figure supplements are available for figure 3:

Source data 1. Raw data of septal distances in wild type *B. subtilis* sporangia and sporangia of engulfment-defective mutants used to plot the bar graph in ***Figure 3F***.

DOI: https://doi.org/10.7554/eLife.45257.022

Figure supplement 1. Septal thickness during engulfment in wild type *B. subtilis.*

DOI: https://doi.org/10.7554/eLife.45257.018

Figure supplement 2. Septal thickness in *spoIIP* mutant sporangia.

DOI: https://doi.org/10.7554/eLife.45257.019

Figure supplement 3. Septal thickness in *spoIIDMP* sporangia.

DOI: https://doi.org/10.7554/eLife.45257.020

Figure supplement 4. Observing peptidoglycan synthesis using BOCILLIN-FL.

DOI: https://doi.org/10.7554/eLife.45257.021

---

brightest at the leading edge in wild type sporangia (***Ojkic et al., 2016***) and at different positions across the septum in DMP mutant sporangia (***Figure 3—figure supplement 4***). This mislocalization might allow ongoing synthesis of septal PG, leading to abnormally thick sporulation septa.

PG is synthesized ahead of the leading edge of the engulfing membrane

Once the septum curves, the mother cell membrane starts to migrate around the forespore. Since the PG is not completely degraded, it will represent a major obstacle for the advancement of the engulfing membrane. To explain how cells overcome this hurdle, we previously proposed a conceptually new model for engulfment in which coordinated PG synthesis and degradation at the leading edge of the engulfing membrane moves the junction between the septum and the lateral cell wall around the forespore, making room for the engulfing mother cell membrane to advance (***Figure 1B***; ***Ojkic et al., 2016***). In this 'make before break' model, new PG would be synthesized ahead of the engulfing membrane by forespore-associated PG biosynthetic complexes and subsequently degraded by DMP. To test this model, we first focused on the shape of the forespore membrane opposing the leading edge of the engulfing mother cell membrane. In wild type sporangia, the forespore membrane was rounded immediately ahead of the engulfing membrane (***Figure 4A***). This could be due to accumulation of additional PG at this site, which might push and deform the forespore membrane, introducing a broader curve. To confirm this, we analyzed the shape of the forespore membrane of sporangia in which PG synthesis was blocked with either bacitracin or cephalexin (***Figure 4B***, ***Figure 4—figure supplement 1***, see Materials and methods). The forespore membrane was less rounded and had a sharp corner with a radius of curvature that was four times smaller than that of untreated cells (~30 nm vs. ~120 nm, ***Figure 4C***). These results indicate that new PG is indeed synthesized ahead of the leading edge of the engulfing membrane, and that it deforms the forespore membrane at the junction between the septum and the lateral cell wall.

To exclude the possibility that new PG synthesis also happened behind the leading edge of the engulfing membrane, we analyzed septal thickness in sporangia treated with cephalexin and a combination of cephalexin and penicillin V using cryo-FIB-ET. If the septum is thinner in the presence of antibiotics, it would suggest that additional septal PG is synthesized after the DMP complex advances and degrades the PG ahead of the leading edge of the engulfing membrane. However, if septal thickness is independent of the presence of antibiotics, it would suggest that PG is not normally synthesized behind the DMP complex. Our data showed that the septal thickness of cells treated with cephalexin was comparable to that of untreated cells. Surprisingly, the septal thickness of cells treated with a combination of cephalexin and penicillin V was ~3 nm greater than that of untreated cells (***Figure 4—figure supplement 2***). This modest increase in septal thickness is of a magnitude that is consistent with recent molecular dynamics simulations which show that relaxed PG is thicker than stretched PG (***Beeby et al., 2013***). It is possible that treatment with antibiotics blocking PG synthesis inhibits the stretching of septal PG due to the absence of membrane migration which could pull the septal PG around the forespore. Alternatively, the residual DMP might partially cleave septal PG, releasing the tension and leading to slightly thicker septa. Taken together, in both cases of antibiotic treatment the septal thickness did not decrease compared to untreated sporangia, suggesting that PG is not synthesized behind the DMP complex.

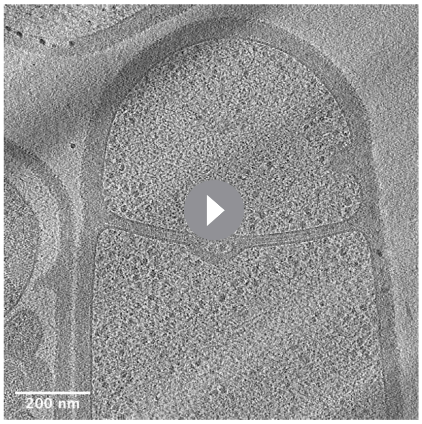

Video 8. Movie showing slices through a cryo-electron tomogram of *spoIIDMP* mutant sporangium shown in ***Figure 3—figure supplement 3C***.

DOI: https://doi.org/10.7554/eLife.45257.023

3D architecture of the leading edge of the engulfing membrane

The new PG synthesized ahead of the leading edge of the engulfing membrane might interfere with the movement of the engulfing membrane, until it is degraded by DMP. To obtain insights about the movement of the engulfing membrane, we annotated the forespore and the mother cell membranes in our tomograms to visualize the architecture of the leading edge in 3D. Our data showed that the leading edge of the engulfing membrane in wild type sporulating cells moved around the forespore in tiny finger-like projections (***Figure 4D–G***, ***Figure 4—figure supplement 3***). The projections were ~10–30 nm wide and ~5–20 nm long, with significant variations from cell to cell. We hypothesized that those projections could be due to the uneven degradation of PG ahead of the leading edge of the engulfing membrane. To test this possibility, we imaged *spoIIP* mutant sporangia, which lack a functional DMP complex. As expected, the septum bulged towards the mother cell cytoplasm, but the mother cell membrane did not move forward in these cells. No membrane projections anywhere were observed in the mother cell membrane in any of the tomograms that were annotated (***Figure 4H–K***, ***Figure 4—figure supplement 4***, ***Video 9***). Also, no projections were observed in the DMP triple mutant, most of which did not form bulges (***Figure 4—figure supplement 5***). These findings suggest that SpoIIDMP is necessary for the formation of finger-like projections in the engulfing mother cell membrane.

We next tested whether PG synthesis was also required for the formation of finger-like projections. To study this possibility, we focused on sporangia in which PG synthesis was blocked using cephalexin (***Figure 4L–O***, ***Video 10***). When treated with antibiotics that block PG synthesis, membrane migration is blocked although the forespore continues to grow into the mother cell (***Ojkic et al., 2016***). The case of cephalexin-treated cells is more complicated than other antibiotics, because after the septum curves into the mother cell, the leading edge sometimes retracts on one side while advancing slightly on the other (***Video 10***; ***Ojkic et al., 2016***). This appears to consist of rotation of the 'cup' formed by the bulging septum relative to the lateral cell wall, rather than membrane migration, because the distance between the leading edges does not decrease during this process. Thus, rotation of the septal cup does not reflect the degree to which the forespore is engulfed. Cephalexin inhibits the earliest stages of cell division (***Eberhardt et al., 2003***; ***Kocaoglu and Carlson, 2015***), and therefore we speculate that it might be required to tether the extending septum to the lateral cell wall. In the absence of these bridges, the septum might be free to rotate according to Brownian motion, perhaps anchored by the Q-AH ratchet that can also mediate engulfment in the absence of the cell wall (***Broder and Pogliano, 2006***). We used cryo-FIB-ET to compare the architecture of both sides of the engulfing membrane in cephalexin-treated sporangia (***Figure 4L–O***). We did not observe finger-like projections in the side of the membrane that retracts (***Figure 4M***) but observed a few projections in the opposite side (***Figure 4N***), which might remain tethered to PG ahead of the engulfing membrane. Also, when cells were treated with penicillin V, we observed fewer projections that were shorter compared to untreated cells (***Figure 4—figure supplement 6***). Taken together, these results suggest that the finger-like projections at the leading edge of the engulfing membrane might be caused by tethering of the engulfing membrane to the PG via DMP (***Figure 4P***).

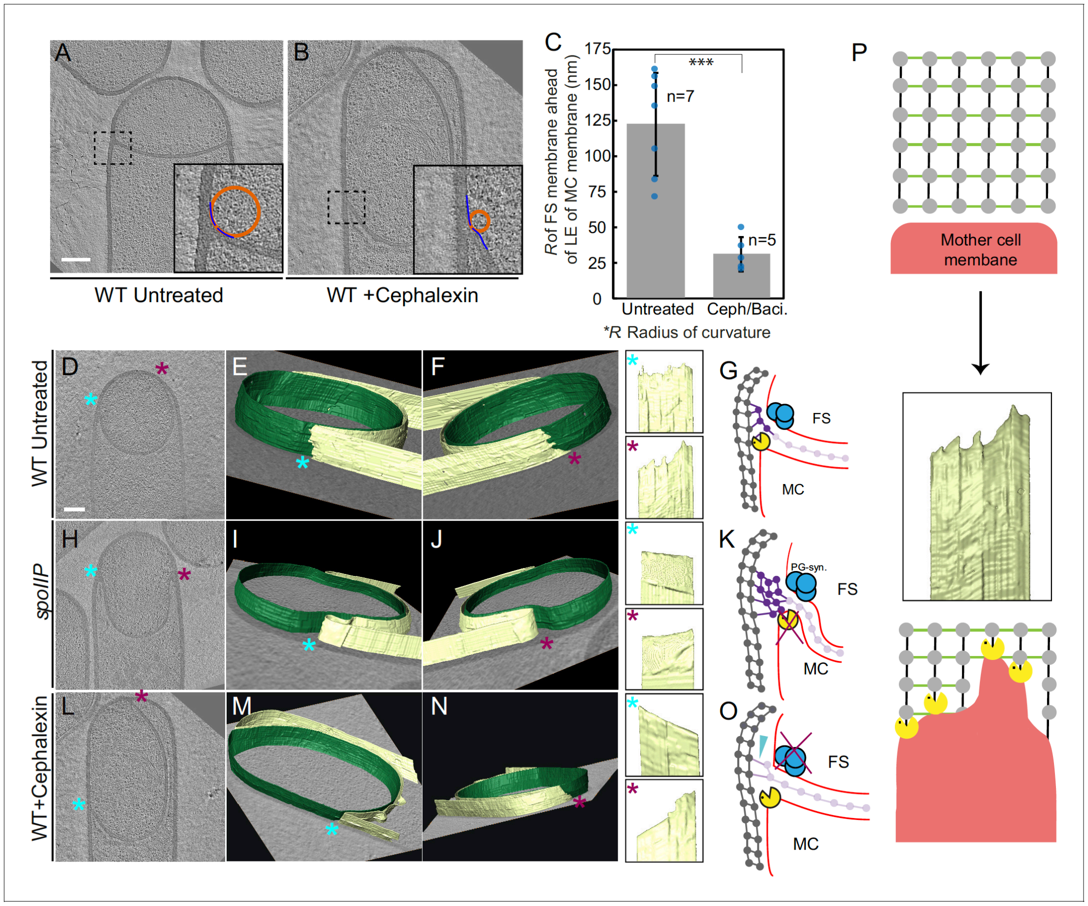

Figure 4. Architecture of the leading edge of the engulfing membrane. (**A**,**B**) Slices through cryo-electron tomograms of wild type (**A**) untreated and (**B**) cephalexin-treated sporangia. The radius of curvature (orange circle) of the forespore membrane (blue spline) ahead of the leading edge of the engulfing membrane is highlighted in the respective insets. (**C**) Plot showing the average radius of curvature (nm) of the forespore membrane ahead of the leading edge of the engulfing membrane for untreated and antibiotic-treated sporangia. Blue dots indicate individual data points (as also indicated by n); black bars indicate the standard deviation (***: p<0.001, unpaired t-test). (**D**) Slice through a cryo-electron tomogram of wild type *B. subtilis* sporangium. (**E**,**F**) Annotated forespore (green) and mother cell (yellow) membranes for the tomogram shown in (**D**) as viewed from both the left (blue asterisk) and the right (maroon asterisk) sides respectively, with insets of zoomed-in views of the leading edge of the engulfing membrane of both sides. Similar labeling scheme is followed through *(H–N)*. *(G)* Schematic showing the localization of DMP PG degradation machinery (yellow pacman) and PG synthases (blue circles). Membranes (red), lateral PG (gray), septal PG (pink) and new PG (purple) are also highlighted. (**H**) Slice through a cryo-electron tomogram of *spoIIP* mutant sporangium. (**I**,**J**) Annotated membranes for the tomogram shown in (**H**) with insets of zoomed-in views of the leading edge of the engulfing membrane of both sides. (**K**) Schematic representing a cell in which the DMP complex (yellow pacman) does not assemble. (**L**) Slice through a cryo-electron tomogram of cephalexin-treated sporangium. (**M**,**N**) Annotated membranes for the tomogram shown in (**L**) with insets of zoomed-in views of the leading edge of the engulfing membrane of both sides. (**O**) Schematic representing a cell in which PG synthesis (blue circles) has been inhibited. Scale bar for (**D**,**H**,**L**): 200 nm. Scale bars have been omitted for surface rendered images owing to their perspective nature. (**P**) Model for mother cell membrane migration. DMP complexes (yellow pacman) present at different positions on the mother cell membrane (red) tether the membrane to the PG (gray) synthesized ahead. Due to a limited number of DMP complexes, the engulfing membrane may move forward in finger-like projections. This is indicated by a representative annotated mother cell membrane (yellow) from ***Figure 4F***.

DOI: https://doi.org/10.7554/eLife.45257.024

The following figure supplements are available for figure 4:

Figure 4 continued on next page

Figure 4 continued

Figure supplement 1. Quantification of radius of curvature of the forespore membrane.
DOI: https://doi.org/10.7554/eLife.45257.025

Figure supplement 2. Graph depicting the septal thickness of wild type untreated and antibiotic-treated sporangia (cephalexin and a combination of cephalexin and penicillin V) according to concentrations specified in ***Figure 2—figure supplement 1***.
DOI: https://doi.org/10.7554/eLife.45257.026

Figure supplement 3. Membrane architecture in wild type.
DOI: https://doi.org/10.7554/eLife.45257.027

Figure supplement 4. Membrane architecture in spoIIP sporangia.
DOI: https://doi.org/10.7554/eLife.45257.028

Figure supplement 5. Membrane architecture in *spoIIDMP* sporangia.
DOI: https://doi.org/10.7554/eLife.45257.029

Figure supplement 6. Membrane architecture in antibiotic-treated sporangium.
DOI: https://doi.org/10.7554/eLife.45257.030

Discussion

In this study, we have visualized the developmental process of sporulation in *Bacillus subtilis* using cryo-FIB-ET. We have obtained images of cells during different stages of sporulation at a resolution of a few nanometers, revealing new details about the architecture of spore assembly, as well as several hitherto unknown structures inside and around the developing spore (***Figure 1***). Our results also provide mechanistic insights into engulfment, including the early step of septal thinning (***Figures 2*** and ***3***) and membrane migration (***Figure 4***) which are captured in the model presented in ***Figure 5***.

We provide evidence that the septal PG is not completely degraded at the onset of engulfment. Instead, the septum gets slightly (~25%) thinner as it curves into the mother cell, with PG continuously present between the mother cell and the forespore membranes. In addition, the whole septum transitions from thick to thin homogenously, contrary to previous results that suggested that septal thinning started in the middle and progressed towards the edges. The homogenous thinning of the septum can be explained by our previous finding that septal PG is stretched as the forespore grows towards the mother cell due to increased turgor pressure caused by SpoIIIE-mediated chromosome translocation (***Lopez-Garrido et al., 2018***). Thus, septal thinning could simply represent a change in the conformation of the septal PG, from a relaxed to a stretched state, triggered by the increased turgor pressure in the forespore. This is consistent with recent molecular dynamics simulations on Gram-positive cell walls, which show that relaxed PG fragments are ~25% thicker than those in a strained conformation (***Beeby et al., 2013***).

Our results also indicate that DMP is required to maintain a flexible septum that can curve as the forespore grows into the mother cell (***Figure 3***). We found that the septa of DMP triple mutants have irregular thickness and are on average thicker than wild type septa (***Figure 3E–G***). Since DMP is produced after polar septation, the septa of DMP mutant sporangia must have thickened after they have been formed. Thus, it is possible that DMP prevents septal thickening by clearing PG synthases from the septum, where they would accumulate after polar septation. This model is consistent with the increased

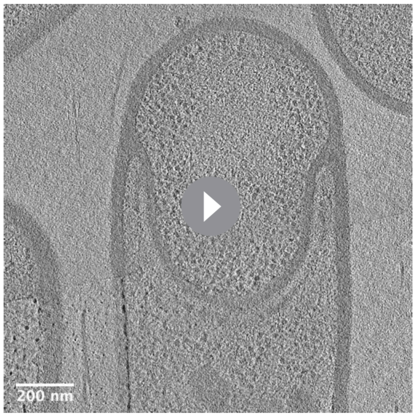

Video 9. Movie showing slices through a cryo-electron tomogram of *spoIIP* mutant sporangium shown in ***Figure 4H***.
DOI: https://doi.org/10.7554/eLife.45257.031

localization of PBPs throughout the septum in DMP mutants (***Figure 3—figure supplement 4***). Nevertheless, we cannot rule out the possibility that DMP degrades the septal PG partially to generate a flexible septum. If this was the case, the partial degradation should happen simultaneously across the whole septum to enable the homogenous transition from thick to thin. However, since DMP is rate limiting for engulfment, it seems unlikely that there may be enough DMP complexes to mediate the homogeneous thinning of the septum. We therefore favor the model that septal thinning is primarily driven by stretching of septal peptidoglycan.

Our data also provide insights into the mechanism of membrane migration during engulfment. Using fluorescence microscopy, we previously observed that new PG is synthesized at the leading edge of the engulfing membrane (***Ojkic et al., 2016***; ***Tocheva et al., 2013***). We also showed that many forespore penicillin binding proteins (PBPs) can track the leading edge of the engulfing mother cell membrane (***Ojkic et al., 2016***), suggesting that PG synthesis at the leading edge of the engulfing membrane is carried out by forespore PBPs. The cryo-FIB-ET images presented here provide further support to this idea: the comparison of the architecture of the leading edge of the engulfing membrane between native sporangia and sporangia in which PG synthesis is blocked by antibiotics shows that new PG deforms and rounds the forespore membrane ahead of the leading edge of the engulfing membrane (***Figure 4A–C***), indicating that new PG is synthesized by forespore PBPs immediately ahead of the leading edge of the engulfing mother cell membrane. We propose that DMP complexes at the leading edge of the engulfing membrane target this new PG for degradation, making room for the engulfing membrane to advance (***Figures 1B*** and ***5C***). This relatively simple model suggests that engulfment could have evolved by developing new mechanisms to spatially and temporally regulate the conserved protein machineries that synthesize and degrade peptidoglycan.

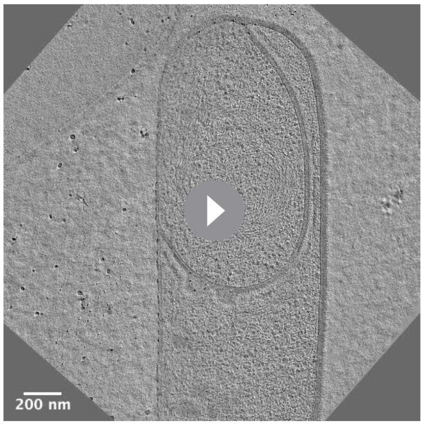

Video 10. Movie showing slices through a cryo-electron tomogram of wildtype *B. subtilis* sporangium treated with cephalexin shown in ***Figure 4L***.

DOI: https://doi.org/10.7554/eLife.45257.032

The 3D reconstruction of the leading edge of the engulfing mother cell membrane shows the presence of finger-like projections that resemble the filopodia of eukaryotic cells (***Mattila and Lappalainen, 2008***). In eukaryotic cells, these membrane projections are produced by cytoskeletal proteins, and the projections are typically a few micrometers wide. In contrast, no cytoskeletal elements contributing to engulfment have been described so far (or visualized in our tomograms) and the finger-like projections at the leading edge of the engulfing membrane are only a few nanometers wide. Instead, our results demonstrate that DMP is required for the formation of these finger-like projections. The simplest model to explain these data is that DMP tethers the engulfing membrane to the PG ahead of the leading edge of the engulfing membrane, as it degrades the new PG to make room for the engulfing membrane to expand. DMP activity is rate limiting for membrane migration (***Abanes-De Mello et al., 2002***; ***Meyer et al., 2010***), suggesting that there is a discrete number of DMP complexes to remove the steric barrier posed by the newly synthesized PG ahead of the leading edge. The limited number of DMP complexes might cause the PG to be degraded irregularly, generating an uneven membrane front in the form of finger-like projections. The distance between the tips of the finger-like projections is ~5–20 nm, which would require that some DMP complexes are ahead of others by 2 to 8 glycan strands (***Turner et al., 2018***). Our observations are consistent with the hypothesis that the finger-like projections are produced via the tethering of the DMP complex to existing peptidoglycan, since short fingers are observed when PG synthesis is inhibited, and that these fingers are either stabilized or enhanced by binding newly synthesized peptidoglycan, since longer fingers are observed in the presence of ongoing PG synthesis. This is supported by prior studies of the two enzymes that degrade peptidoglycan (D and P), which have

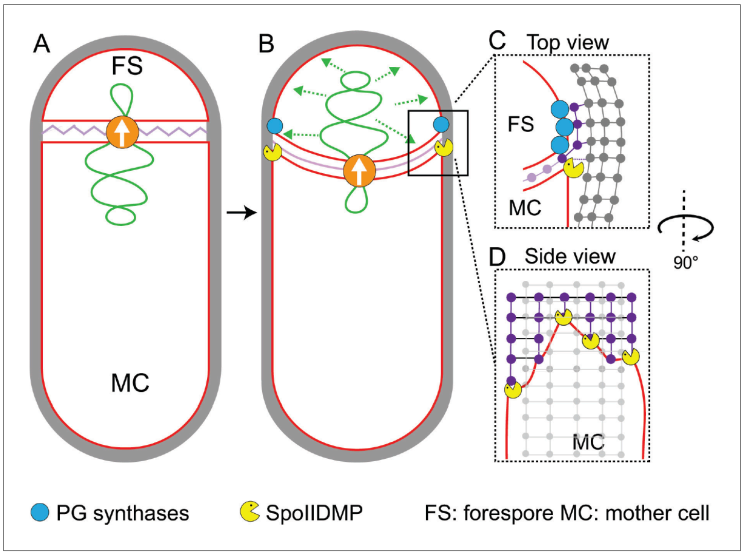

Figure 5. Model for septal thinning and membrane migration. (**A**) Schematic of a sporulating cell with a flat septum and relaxed septal PG (pink). Membranes (red), lateral PG (gray), SpoIIIE (orange) and forespore chromosome (green) are also highlighted. (**B**) As SpoIIIE translocates the chromosome to the forespore, the septal PG is stretched which may contribute to septal thinning. (**C**) Top view of the sporulating cell wherein coordinated PG degradation by DMP (yellow pacman) and PG synthesis by PG biosynthetic enzymes (blue) at the leading edge provide room for the engulfing mother cell membrane migration. (**D**) Side view depicting the proposed membrane migration model with mother cell membrane (red), PG synthesized ahead of the membrane (purple) and lateral PG (gray) highlighted. During engulfment, DMP complexes present at different locations on the mother cell membrane may move forward by degrading the PG ahead and their rate-limiting activity may lead to the formation of tiny finger-like projections. FS: Forespore; MC: mother cell.

DOI: https://doi.org/10.7554/eLife.45257.033

shown that these comprise a processive enzyme complex in which P binds and cleaves PG first, allowing D to bind and cleave PG (***Morlot et al., 2010***). Our cell biological data showed that localization of P to the leading edge of the engulfing membrane is decreased but not completely absent when PG synthesis is inhibited (***Ojkic et al., 2016***), suggesting that P can bind to existing PG, but that high affinity binding requires newly synthesized peptidoglycan. This increased binding of P would likely allow the formation of longer finger-like projections. From a functional perspective, we speculate that the finger-like projections could be compared to 'friction ridges', the minutely raised ridges of the epidermis that provide a grasping surface on our fingers (***Tomlinson et al., 2007***). During engulfment, these membrane projections may provide the engulfing membrane a tighter lateral grip while moving around the forespore, hence serving as a ratchet that prevents backward movement of the membrane.

The application of cryo-FIB-ET has been instrumental in allowing us to visualize and accurately measure structural details of engulfing sporangia, which transpire at a scale of a few nanometers. Our studies support a mechanistic model for the enigmatic process of engulfment, while revealing novel architectural details about engulfment and spore assembly, including intriguing new molecular structures that will require further study to unambiguously identify them. Our findings reveal details about sporulation at an unprecedented resolution and further illustrate the potential of cryo-FIB-ET to reveal critical new information about dynamic biological processes.

Materials and methods

Key resources table

Reagent type (species) or resource	Designation	Source or reference	Identifiers	Additional information
Strain, strain background (*Bacillus subtilis* PY79)	PY79	(**Youngman et al., 1984**)	Tax. ID:1415167	Wild type
Strain, strain background (*Bacillus subtilis* PY79)	*ΔspoIIP::tet*	(**Frandsen and Stragier, 1995**)		KP513
Strain, strain background (*Bacillus subtilis* PY79)	*spoIID298, spoIIM-mls, ΔspoIIP::tet*	(**Broder and Pogliano, 2006**)		KP4188
Chemical compound, drug	FM4-64	Thermo Fisher Scientific	Cat#T13320	
Chemical compound, drug	Bacitracin	MilliporeSigma	Cat#B0125	Conc. used: 50 µg/ml
Chemical compound, drug	Penicillin V	MilliporeSigma	Cat#1504489	Conc. used: 500 µg/ml
Chemical compound, drug	Cephalexin	MilliporeSigma	Cat#C4895	Conc. used: 50 µg/ml
Software, algorithm	JFilament	(**Smith et al., 2010**)	http://athena.physics.lehigh.edu/jfilament/	
Software, algorithm	IMOD	(**Mastronarde, 1997**)	http://bio3d.colorado.edu/imod/; RRID: SCR_003297	
Software, algorithm	TomoSegMemTV	(**Martinez-Sanchez et al., 2014**)	https://sites.google.com/site/3demimageprocessing/tomosegmemtv	
Software, algorithm	Amira	Commercial software by Thermo Scientific (formerly FEI)	https://www.fei.com/software/amira-3d-for-life-sciences/; RRID: SCR_014305	
Software, algorithm	SerialEM	(**Mastronarde, 2005**)	http://bio3d.colorado.edu/SerialEM/	
Software, algorithm	Matlab code to calculate septal distances of sporangia	This paper; ***Source code 1***		
Software, algorithm	Matlab code to calculate cell length using fluorescence microscopy images	This paper; ***Source code 2***		

Strains and culture conditions

We used *Bacillus subtilis* PY79 background for all data acquisition. The strains (see *Key Resources Table*) were grown in LB plates at 30˚C. The bacteria were first grown in ¼ diluted LB to OD_{600} ~0.5–0.7. Sporulation was then induced by resuspension in A + B media at 37˚C. For cryo-FIB-ET, we collected wild type sporulating cells 1.5–3 hr after sporulation induction. For cells treated with antibiotics, 50 µg/ml of bacitracin, 50 µg/ml of cephalexin and 500 µg/ml of penicillin V were used. Antibiotics were added two hours after induction of sporulation and samples for cryo-FIB-ET were collected either one (for bacitracin) or two hours (for cephalexin, penicillin V and a combination of cephalexin and penicillin V) later. For *spoIIP* and *spoIIDMP* mutant sporangia, cells were collected 2.5 hr after induction of sporulation for cryo-ET.

Cryo-FIB-ET and image processing

7 µl of diluted liquid culture was deposited onto glow-discharged (using Pelco easyGlow) holey carbon coated QUANTIFOIL R 2/1 200 mesh copper grids. Manual blotting was performed using Whatman No. one filter paper from the reverse side to remove excess resuspension media such that cells form a monolayer on the grids. They were then immediately plunge-frozen into a liquid ethane/propane mixture cooled by liquid nitrogen using a custom-built vitrification device (Max Planck Institute for Biochemistry, Munich). These grids were then stored in storage boxes in liquid nitrogen until further use.

Vitrified bacterial samples forming a monolayer on the grids were mounted into modified autogrids (Max Planck Institute for Biochemistry) for milling inside a Thermo Scientific Scios DualBeam (cryo-FIB/SEM) (Materials and methods). 100–250 nm thin sections or lamellae (12–15 µm in width) were then prepared using rectangular milling patterns and beam current of 0.1 nA or 0.3 nA for rough milling and 10 pA or 30 pA for fine milling as described in ***Chaikeeratisak et al. (2017)***. Tilt series were collected in a 300-keV Tecnai G2 Polara (Thermo Scientific) equipped with a K2 Summit direct detection camera (Gatan) and a post-column Quantum energy filter (Gatan). The samples were usually tilted from −66˚ to +66˚ (the range per tilt series depending on the quality of the lamellae) with an increment of 1.5˚ or 2˚. The tilt series were acquired using SerialEM (***Mastronarde, 2005***). The images were recorded at a defocus of −5 to −6 µm at nominal magnifications of 34,000 (pixel size: 0.61 nm) or 41,000 (pixel size: 0.49 nm) with a cumulative dose of ~60–130 $e^{-}/Å^{2}$. Images for later stages of sporulation (***Figure 1—figure supplement 2B***) were acquired at nominal magnification of 22,500 (pixel size: 0.92 nm) as these samples were highly sensitive to radiation damage.

The patch-tracking feature of IMOD was used to reconstruct the tilt-series (***Kremer et al., 1996***). TomosegmemTV (***Martinez-Sanchez et al., 2014***) was used for semi-automatic segmentation of membranes followed by manual refinement in the Amira software package.

Measuring mean radius of ellipsoidal complexes

The mean radius (r) of an ellipse is given by:

$$r = \sqrt{\frac{a^2 + b^2}{2}}$$

where *a* is the semi-major axis of the ellipse and *b* is the semi-minor axis of the ellipse. For ellipsoidal complexes observed in our tomograms (***Figure 1J***, ***Figure 1—figure supplement 3A–C***), average value of *a* is ~45 nm and that of *b* is ~42 nm.

Calculating septal distances

'Surface distance' feature of Amira was used to calculate the septal distances between the forespore and mother cell membranes. The septal-disc was color coded according to these values (***Figure 3B–D,G***, ***Figure 3—figure supplement 2E***). Five tomograms each of wild type cells representing different stages of engulfment (flat, curved and engulfing septa) were used for analysis. For engulfment mutants, five *spoIIP* sporangia and seven *spoIIDMP* sporangia were analyzed. For antibiotic treated cells, six cephalexin-treated sporangia and five cephalexin- and penicillin V- combination treated sporangia were analyzed. To get the linear profiles of the distances, the data was grouped into smaller bins of approximately equal area for each tomogram. Then the average of the distance within a bin was used to represent the distance between the membranes at that location of the bin (see ***Source code 1***). ***Figure 3E*** represents an average of all the profiles for each cell type in ***Figure 3—figure supplement 1*** and ***Figure 3—figure supplement 3E***.

Fluorescence microscopy

Cells were visualized on an Applied Precision DV Elite optical sectioning microscope equipped with a Photometrics CoolSNAP-HQ2 camera and deconvolved using SoftWoRx v5.5.1 (Applied Precision). For experiment outlined in ***Figure 3—figure supplement 4***, the median focal plane of the image is shown. Membranes were stained with 0.5 µg/ml of FM4-64 (Thermo Fisher Scientific) that was added directly to 1.2% agarose pads prepared using sporulation resuspension medium. 10 µg/µl of BOCILLIN-FL was added to 1 ml of culture aliquoted ~2.5 hr after sporulation induction (at 37˚C) and washed with sporulation resuspension medium three times. 12 µl of washed cells were then transferred to agarose pads for imaging.

For time-lapse microscopy, sporulation was induced at 30˚C. 0.5 µg/ml FM4-64 was added to the cultures ~1.5 hr after sporulation induction and incubation continued for another hour. Composition of agarose pads for time-lapse microscopy is as follows: 2/3 vol of supernatant from the sporulation culture, 1/3 vol 3.6% agarose in fresh A + B sporulation medium, 0.17 µg/ml FM4-64, supplemented with antibiotics according to concentrations mentioned above in '*Strains and culture conditions*'. 12 µl samples were taken 3 hr after resuspension and transferred to the agarose pads. Pads were covered with a glass slide and sealed with petroleum jelly to avoid dehydration during time-lapse imaging. Pictures were taken in an environmental chamber at 30˚C every 5 min for ~5 hr. Excitation/emission filters were TRITC/CY5 for membrane imaging. Excitation light transmission was set to 5% to minimize phototoxicity and exposure time was set to 0.1 s.

Calculating cell length using fluorescence microscopy images

To determine the length of vegetative cells over time (***Figure 2—figure supplement 1E***), membrane contours were extracted from microscopy images for each time frame (up to 60 min post treatment with antibiotics) using semi-automated active contour software JFilament, available as a Fiji plugin (***Schindelin et al., 2012***; ***Smith et al., 2010***). The cell length was then calculated by measuring along the long axis of the contours using a custom-built MATLAB script (see ***Source code 2***). To plot the average cell length, the data was normalized to the initial cell length for each of the cases.

Calculating radius of curvature

To calculate radius of curvature (***Figure 4A–C***, ***Figure 4—figure supplement 1***), a slice was taken approximately from the center of the z-stack for each of the tomograms. 'Measure spline curvature' feature of sabl_mpl (***Yao et al., 2017***) was then used to plot radii of curvatures around the forespore membranes just ahead of the leading edge for seven native sporangia and five antibiotic-treated sporangia wherein membrane migration appears to be blocked.

Acknowledgements

This work was supported by National Institutes of Health Director's New Innovator Award 1DP2GM123494 (EV), and the National Institutes of Health R01-GM057045 (EV and KP). We used the UC San Diego Cryo-EM Facility (partially supported by a gift from the Agouron Institute to Tim Baker), and the San Diego Nanotechnology Infrastructure of UC San Diego (supported by the NSF grant ECCS-1542148). The authors would like to thank Antonio Martínez-Sánchez for useful insights into data analysis.

Additional information

Funding

Funder	Grant reference number	Author
National Institutes of Health	National Institute of Health's Director's New Innovator Award (1DP2GM123494)	Elizabeth Villa
National Institutes of Health	RO1-GM057045	Kit Pogliano Elizabeth Villa

The funders had no role in study design, data collection and interpretation, or the decision to submit the work for publication.

Author contributions

Kanika Khanna, Javier Lopez-Garrido, Conception and design, Data acquisition, Data analysis, Writing—original draft; Ziyi Zhao, Yuan Yuan, Joseph Sugie, Data analysis; Reika Watanabe, Assistance with cryo-EM; Kit Pogliano, Elizabeth Villa, Conception and design, Data analysis, Writing—review and editing

Author ORCIDs

Kanika Khanna https://orcid.org/0000-0001-7150-0350
Javier Lopez-Garrido https://orcid.org/0000-0002-8907-502X
Ziyi Zhao https://orcid.org/0000-0003-4455-3224
Reika Watanabe http://orcid.org/0000-0002-7427-7702
Yuan Yuan https://orcid.org/0000-0002-9509-9167
Joseph Sugie https://orcid.org/0000-0003-2911-1807
Kit Pogliano https://orcid.org/0000-0002-7868-3345
Elizabeth Villa https://orcid.org/0000-0003-4677-9809

Decision letter and Author response

Decision letter https://doi.org/10.7554/eLife.45257.044
Author response https://doi.org/10.7554/eLife.45257.045

Additional files

Supplementary files

- Source code 1. Matlab code to calculate septal distances of sporangia.

DOI: https://doi.org/10.7554/eLife.45257.034

- Source code 2. Matlab code to calculate cell length using fluorescence microscopy images.

DOI: https://doi.org/10.7554/eLife.45257.035

- Transparent reporting form

DOI: https://doi.org/10.7554/eLife.45257.036

Data availability

The authors have created a library of *B. subtilis* tomograms accessible at: http://villalab.ucsd.edu/research/engulfment. The authors have also deposited three representative tilt-series to Electron Microscopy Data Bank (EMDB) in the form of 4x binned tomograms. The IDs are EMD-20335, EMD-20336, EMD-20337 for Figure 1D,F,H respectively.

The following datasets were generated:

Author(s)	Year	Dataset title	Dataset URL	Database and Identifier
Khanna K, Lopez-Garrido J, Zhao Z, Watanabe R, Yuan Y, Sugie J, Pogliano K, Villa E	2019	Representative tilt-series	http://www.ebi.ac.uk/pdbe/entry/emdb/EMD-20335	Electron Microscopy Data Bank, EMD-20335
Khanna K, Lopez-Garrido J, Zhao Z, Watanabe R, Yuan Y, Sugie J, Pogliano K, Villa E	2019	Representative tilt-series	http://www.ebi.ac.uk/pdbe/entry/emdb/EMD-20336	Electron Microscopy Data Bank, EMD-20336
Khanna K, Lopez-Garrido J, Zhao Z, Watanabe R, Yuan Y, Sugie J, Pogliano K, Villa E	2019	Representative tilt-series	http://www.ebi.ac.uk/pdbe/entry/emdb/EMD-20337	Electron Microscopy Data Bank, EMD-20337

References

Abanes-De Mello A, Sun YL, Aung S, Pogliano K. 2002. A cytoskeleton-like role for the bacterial cell wall during engulfment of the *Bacillus subtilis* forespore. *Genes & Development* **16**:3253–3264. DOI: https://doi.org/10.1101/gad.1039902, PMID: 12502745

Aung S, Shum J, Abanes-De Mello A, Broder DH, Fredlund-Gutierrez J, Chiba S, Pogliano K. 2007. Dual localization pathways for the engulfment proteins during *Bacillus subtilis* sporulation. *Molecular Microbiology* **65**:1534–1546. DOI: https://doi.org/10.1111/j.1365-2958.2007.05887.x, PMID: 17824930

Bath J, Wu LJ, Errington J, Wang JC. 2000. Role of *Bacillus subtilis* SpoIIIE in DNA transport across the mother cell-prespore division septum. *Science* **290**:995–997. DOI: https://doi.org/10.1126/science.290.5493.995, PMID: 11062134

Beeby M, Gumbart JC, Roux B, Jensen GJ. 2013. Architecture and assembly of the Gram-positive cell wall. *Molecular Microbiology* **88**:664–672. DOI: https://doi.org/10.1111/mmi.12203, PMID: 23600697

Ben-Harush K, Maimon T, Patla I, Villa E, Medalia O. 2010. Visualizing cellular processes at the molecular level by cryo-electron tomography. *Journal of Cell Science* **123**:7–12. DOI: https://doi.org/10.1242/jcs.060111, PMID: 20016061

Blaylock B, Jiang X, Rubio A, Moran CP, Pogliano K. 2004. Zipper-like interaction between proteins in adjacent daughter cells mediates protein localization. *Genes & Development* **18**:2916–2928. DOI: https://doi.org/10.1101/gad.1252704, PMID: 15574594

Broder DH, Pogliano K. 2006. Forespore engulfment mediated by a ratchet-like mechanism. *Cell* **126**:917–928. DOI: https://doi.org/10.1016/j.cell.2006.06.053, PMID: 16959571

Chaikeeratisak V, Nguyen K, Khanna K, Brilot AF, Erb ML, Coker JK, Vavilina A, Newton GL, Buschauer R, Pogliano K, Villa E, Agard DA, Pogliano J. 2017. Assembly of a nucleus-like structure during viral replication in bacteria. *Science* **355**:194–197. DOI: https://doi.org/10.1126/science.aal2130, PMID: 28082593

Chastanet A, Losick R. 2007. Engulfment during sporulation in *Bacillus subtilis* is governed by a multi-protein complex containing tandemly acting autolysins. *Molecular Microbiology* **64**:139–152. DOI: https://doi.org/10.1111/j.1365-2958.2007.05652.x, PMID: 17376078

Eberhardt C, Kuerschner L, Weiss DS. 2003. Probing the catalytic activity of a cell division-specific transpeptidase in vivo with beta-lactams. *Journal of Bacteriology* **185**:3726–3734. DOI: https://doi.org/10.1128/JB.185.13.3726-3734.2003, PMID: 12813065

Eichenberger P, Fawcett P, Losick R. 2001. A three-protein inhibitor of polar septation during sporulation in *Bacillus subtilis*. *Molecular Microbiology* **42**:1147–1162. DOI: https://doi.org/10.1046/j.1365-2958.2001.02660.x, PMID: 11886548

Engel BD, Schaffer M, Kuhn Cuellar L, Villa E, Plitzko JM, Baumeister W. 2015. Native architecture of the Chlamydomonas chloroplast revealed by in situ cryo-electron tomography. *eLife* **4**:e04889. DOI: https://doi.org/10.7554/eLife.04889, PMID: 25584625

Errington J. 2003. Regulation of endospore formation in *Bacillus subtilis*. *Nature Reviews Microbiology* **1**:117–126. DOI: https://doi.org/10.1038/nrmicro750, PMID: 15035041

Fleming TC, Shin JY, Lee SH, Becker E, Huang KC, Bustamante C, Pogliano K. 2010. Dynamic SpoIIIE assembly mediates septal membrane fission during *Bacillus subtilis* sporulation. *Genes & Development* **24**:1160–1172. DOI: https://doi.org/10.1101/gad.1925210, PMID: 20516200

Frandsen N, Stragier P. 1995. Identification and characterization of the *Bacillus subtilis* spoIIP locus. *Journal of Bacteriology* **177**:716–722. DOI: https://doi.org/10.1128/jb.177.3.716-722.1995, PMID: 7836306

Gutierrez J, Smith R, Pogliano K. 2010. SpoIID-mediated peptidoglycan degradation is required throughout engulfment during *Bacillus subtilis* sporulation. *Journal of Bacteriology* **192**:3174–3186. DOI: https://doi.org/10.1128/JB.00127-10, PMID: 20382772

Hawver LA, Jung SA, Ng WL. 2016. Specificity and complexity in bacterial quorum-sensing systems. *FEMS Microbiology Reviews* **40**:738–752. DOI: https://doi.org/10.1093/femsre/fuw014, PMID: 27354348

Higgins D, Dworkin J. 2012. Recent progress in *Bacillus subtilis* sporulation. *FEMS Microbiology Reviews* **36**:131–148. DOI: https://doi.org/10.1111/j.1574-6976.2011.00310.x, PMID: 22091839

Holt SC, Gauther JJ, Tipper DJ. 1975. Ultrastructural studies of sporulation in Bacillus sphaericus. *Journal of Bacteriology* **122**:1322–1338. PMID: 1097399

Illing N, Errington J. 1991. Genetic regulation of morphogenesis in *Bacillus subtilis*: roles of sigma E and sigma F in prespore engulfment. *Journal of Bacteriology* **173**:3159–3169. DOI: https://doi.org/10.1128/jb.173.10.3159-3169.1991, PMID: 1902463

Kocaoglu O, Carlson EE. 2015. Profiling of β-Lactam selectivity for Penicillin-Binding proteins in Escherichia coli strain DC2. *Antimicrobial Agents and Chemotherapy* **59**:2785–2790. DOI: https://doi.org/10.1128/AAC.04552-14

Kremer JR, Mastronarde DN, McIntosh JR. 1996. Computer visualization of three-dimensional image data using IMOD. *Journal of Structural Biology* **116**:71–76. DOI: https://doi.org/10.1006/jsbi.1996.0013, PMID: 8742726

Levdikov VM, Blagova EV, McFeat A, Fogg MJ, Wilson KS, Wilkinson AJ. 2012. Structure of components of an intercellular channel complex in Sporulating *Bacillus subtilis*. *PNAS* **109**:5441–5445. DOI: https://doi.org/10.1073/pnas.1120087109, PMID: 22431604

Liu NJ, Dutton RJ, Pogliano K. 2006. Evidence that the SpoIIIE DNA translocase participates in membrane fusion during cytokinesis and engulfment. *Molecular Microbiology* **59**:1097–1113. DOI: https://doi.org/10.1111/j.1365-2958.2005.05004.x, PMID: 16430687

Lopez-Garrido J, Ojkic N, Khanna K, Wagner FR, Villa E, Endres RG, Pogliano K. 2018. Chromosome translocation inflates *Bacillus* forespores and impacts cellular morphology. *Cell* **172**:758–770. DOI: https://doi.org/10.1016/j.cell.2018.01.027, PMID: 29425492

Mahamid J, Pfeffer S, Schaffer M, Villa E, Danev R, Cuellar LK, Förster F, Hyman AA, Plitzko JM, Baumeister W. 2016. Visualizing the molecular sociology at the HeLa cell nuclear periphery. *Science* **351**:969–972. DOI: https://doi.org/10.1126/science.aad8857, PMID: 26917770

Marko M, Hsieh C, Schalek R, Frank J, Mannella C. 2007. Focused-ion-beam thinning of frozen-hydrated biological specimens for cryo-electron microscopy. *Nature Methods* **4**:215–217. DOI: https://doi.org/10.1038/nmeth1014, PMID: 17277781

Martinez-Sanchez A, Garcia I, Asano S, Lucic V, Fernandez JJ. 2014. Robust membrane detection based on tensor voting for electron tomography. *Journal of Structural Biology* **186**:49–61. DOI: https://doi.org/10.1016/j.jsb.2014.02.015, PMID: 24625523

Mastronarde DN. 1997. Dual-axis tomography: an approach with alignment methods that preserve resolution. *Journal of Structural Biology* **120**:343–352. DOI: https://doi.org/10.1006/jsbi.1997.3919, PMID: 9441937

Mastronarde DN. 2005. Automated electron microscope tomography using robust prediction of specimen movements. *Journal of Structural Biology* **152**:36–51. DOI: https://doi.org/10.1016/j.jsb.2005.07.007, PMID: 16182563

Matias VR, Beveridge TJ. 2005. Cryo-electron microscopy reveals native polymeric cell wall structure in *Bacillus subtilis* 168 and the existence of a periplasmic space. *Molecular Microbiology* **56**:240–251. DOI: https://doi.org/10.1111/j.1365-2958.2005.04535.x, PMID: 15773993

Mattila PK, Lappalainen P. 2008. Filopodia: molecular architecture and cellular functions. *Nature Reviews Molecular Cell Biology* **9**:446–454. DOI: https://doi.org/10.1038/nrm2406, PMID: 18464790

McKenney PT, Driks A, Eichenberger P. 2013. The *Bacillus subtilis* endospore: assembly and functions of the multilayered coat. *Nature Reviews Microbiology* **11**:33–44. DOI: https://doi.org/10.1038/nrmicro2921, PMID: 23202530

Meyer P, Gutierrez J, Pogliano K, Dworkin J. 2010. Cell wall synthesis is necessary for membrane dynamics during sporulation of *Bacillus subtilis*. *Molecular Microbiology* **76**:956–970. DOI: https://doi.org/10.1111/j.1365-2958.2010.07155.x, PMID: 20444098

Morlot C, Uehara T, Marquis KA, Bernhardt TG, Rudner DZ. 2010. A highly coordinated cell wall degradation machine governs spore morphogenesis in *Bacillus subtilis*. *Genes & Development* **24**:411–422. DOI: https://doi.org/10.1101/gad.1878110, PMID: 20159959

Morlot C, Rodrigues CDA. 2018. The new kid on the block: a specialized secretion system during bacterial sporulation. *Trends in Microbiology* **26**:663–676. DOI: https://doi.org/10.1016/j.tim.2018.01.001, PMID: 29475625

Oikonomou CM, Chang YW, Jensen GJ. 2016. A new view into prokaryotic cell biology from electron cryotomography. *Nature Reviews Microbiology* **14**:205–220. DOI: https://doi.org/10.1038/nrmicro.2016.7, PMID: 26923112

Ojkic N, López-Garrido J, Pogliano K, Endres RG. 2016. Cell-wall remodeling drives engulfment during *Bacillus subtilis* sporulation. *eLife* **5**:e18657. DOI: https://doi.org/10.7554/eLife.18657, PMID: 27852437

Perez AR, Abanes-De Mello A, Pogliano K. 2000. SpoIIB localizes to active sites of septal biogenesis and spatially regulates septal thinning during engulfment in *Bacillus subtilis*. *Journal of Bacteriology* **182**:1096–1108. DOI: https://doi.org/10.1128/JB.182.4.1096-1108.2000, PMID: 10648537

Ramamurthi KS, Losick R. 2009. Negative membrane curvature as a cue for subcellular localization of a bacterial protein. *PNAS* **106**:13541–13545. DOI: https://doi.org/10.1073/pnas.0906851106, PMID: 19666580

Rigort A, Bäuerlein FJ, Villa E, Eibauer M, Laugks T, Baumeister W, Plitzko JM. 2012. Focused ion beam micromachining of eukaryotic cells for cryoelectron tomography. *PNAS* **109**:4449–4454. DOI: https://doi.org/10.1073/pnas.1201333109, PMID: 22392984

Rousseau M, Hermier J. 1975. Wall polysaccharides in sporulating bacteria: localization by electron microscopy [Localisation en microscopie electronique des polysaccharides de la paroi chez les bacteries en sporulation]. *Journal de Microscopie et de Biologie Cellulaire* **23**:237–248.

Schindelin J, Arganda-Carreras I, Frise E, Kaynig V, Longair M, Pietzsch T, Preibisch S, Rueden C, Saalfeld S, Schmid B, Tinevez JY, White DJ, Hartenstein V, Eliceiri K, Tomancak P, Cardona A. 2012. Fiji: an open-source platform for biological-image analysis. *Nature Methods* **9**:676–682. DOI: https://doi.org/10.1038/nmeth.2019, PMID: 22743772

Smith MB, Li H, Shen T, Huang X, Yusuf E, Vavylonis D. 2010. Segmentation and tracking of cytoskeletal filaments using open active contours. *Cytoskeleton* **67**:693–705. DOI: https://doi.org/10.1002/cm.20481, PMID: 20814909

Spratt BG. 1975. Distinct penicillin binding proteins involved in the division, elongation, and shape of Escherichia coli K12. *PNAS* **72**:2999–3003. DOI: https://doi.org/10.1073/pnas.72.8.2999, PMID: 1103132

Tan IS, Ramamurthi KS. 2014. Spore formation in *Bacillus subtilis*. *Environmental Microbiology Reports* **6**:212–225. DOI: https://doi.org/10.1111/1758-2229.12130, PMID: 24983526

Tocheva EI, Matson EG, Morris DM, Moussavi F, Leadbetter JR, Jensen GJ. 2011. Peptidoglycan remodeling and conversion of an inner membrane into an outer membrane during sporulation. *Cell* **146**:799–812. DOI: https://doi.org/10.1016/j.cell.2011.07.029, PMID: 21884938

Tocheva EI, López-Garrido J, Hughes HV, Fredlund J, Kuru E, Vannieuwenhze MS, Brun YV, Pogliano K, Jensen GJ. 2013. Peptidoglycan transformations during *Bacillus subtilis* sporulation. *Molecular Microbiology* **88**:673–686. DOI: https://doi.org/10.1111/mmi.12201, PMID: 23531131

Tomlinson SE, Lewis R, Carré MJ. 2007. Review of the frictional properties of finger-object contact when gripping. *Proceedings of the Institution of Mechanical Engineers, Part J: Journal of Engineering Tribology* **221**: 841–850. DOI: https://doi.org/10.1243/13506501JET313

Turner RD, Mesnage S, Hobbs JK, Foster SJ. 2018. Molecular imaging of glycan chains couples cell-wall polysaccharide architecture to bacterial cell morphology. *Nature Communications* **9**:1263. DOI: https://doi.org/10.1038/s41467-018-03551-y, PMID: 29593214

Villa E, Schaffer M, Plitzko JM, Baumeister W. 2013. Opening windows into the cell: focused-ion-beam milling for cryo-electron tomography. *Current Opinion in Structural Biology* **23**:771–777. DOI: https://doi.org/10.1016/j.sbi.2013.08.006, PMID: 24090931

Wagstaff J, Löwe J. 2018. Prokaryotic cytoskeletons: protein filaments organizing small cells. *Nature Reviews Microbiology* **16**:187–201. DOI: https://doi.org/10.1038/nrmicro.2017.153, PMID: 29355854

Wang X, Montero Llopis P, Rudner DZ. 2013. Organization and segregation of bacterial chromosomes. *Nature Reviews Genetics* **14**:191–203. DOI: https://doi.org/10.1038/nrg3375, PMID: 23400100

Wu W, Thomas JA, Cheng N, Black LW, Steven AC. 2012. Bubblegrams reveal the inner body of bacteriophage φkz. *Science* **335**:182. DOI: https://doi.org/10.1126/science.1214120, PMID: 22246767

Wu LJ, Errington J. 1994. *Bacillus subtilis* SpoIIIE protein required for DNA segregation during asymmetric cell division. *Science* **264**:572–575. DOI: https://doi.org/10.1126/science.8160014, PMID: 8160014

Wu LJ, Errington J. 1997. Septal localization of the SpoIIIE chromosome partitioning protein in *Bacillus subtilis*. *The EMBO Journal* **16**:2161–2169. DOI: https://doi.org/10.1093/emboj/16.8.2161, PMID: 9155041

Yao Q, Jewett AI, Chang YW, Oikonomou CM, Beeby M, Iancu CV, Briegel A, Ghosal D, Jensen GJ. 2017. Short FtsZ filaments can drive asymmetric cell envelope constriction at the onset of bacterial cytokinesis. *The EMBO Journal* **36**:1577–1589. DOI: https://doi.org/10.15252/embj.201696235, PMID: 28438890

Yen Shin J, Lopez-Garrido J, Lee SH, Diaz-Celis C, Fleming T, Bustamante C, Pogliano K. 2015. Visualization and functional dissection of coaxial paired SpoIIIE channels across the sporulation septum. *eLife* **4**:e06474. DOI: https://doi.org/10.7554/eLife.06474, PMID: 25950186

Youngman P, Perkins JB, Losick R. 1984. A novel method for the rapid cloning in Escherichia coli of *Bacillus subtilis* chromosomal DNA adjacent to Tn917 insertions. *MGG Molecular & General Genetics* **195**:424–433. DOI: https://doi.org/10.1007/BF00341443, PMID: 6088944

Zeytuni N, Hong C, Flanagan KA, Worrall LJ, Theiltges KA, Vuckovic M, Huang RK, Massoni SC, Camp AH, Yu Z, Strynadka NC. 2017. Near-atomic resolution cryoelectron microscopy structure of the 30-fold homooligomeric SpoIIIAG channel essential to spore formation in *Bacillus subtilis*. *PNAS* **114**:E7073–E7081. DOI: https://doi.org/10.1073/pnas.1704310114, PMID: 28784753

Zhao G, Meier TI, Kahl SD, Gee KR, Blaszczak LC. 1999. BOCILLIN FL, a sensitive and commercially available reagent for detection of Penicillin-Binding proteins. *Antimicrobial Agents and Chemotherapy* **43**:1124–1128. DOI: https://doi.org/10.1128/AAC.43.5.1124

Supplemental Files

Figure 1—figure supplement 1

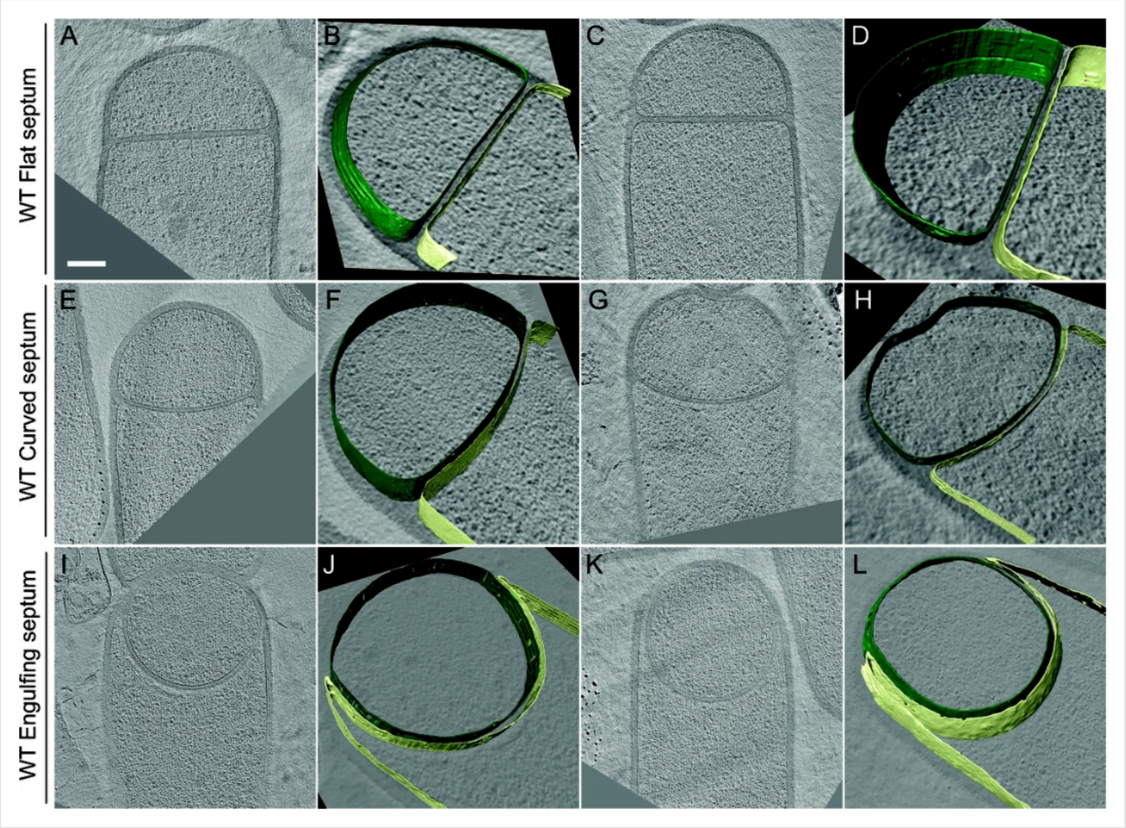

Slices through cryo-electron tomograms representing different stages of engulfment in wild type sporulating *B. subtilis* cells.

The forespore (green) and the mother cell (yellow) membranes are annotated and shown adjacent to each tomogram. (**A–D**) represent flat septum (Stage II_{i}) sporangia, (**E–H**) represent curved septum (Stage II_{ii}) sporangia and (**I–L**) represent engulfing septum (Stage II_{iii}) sporangia. Scale bar for the tomogram slices (**A,C,E,G,I,K**): 200 nm. Scale bars have been omitted for all segmented images as cells are displayed in perspective mode.

Figure 1—figure supplement 2

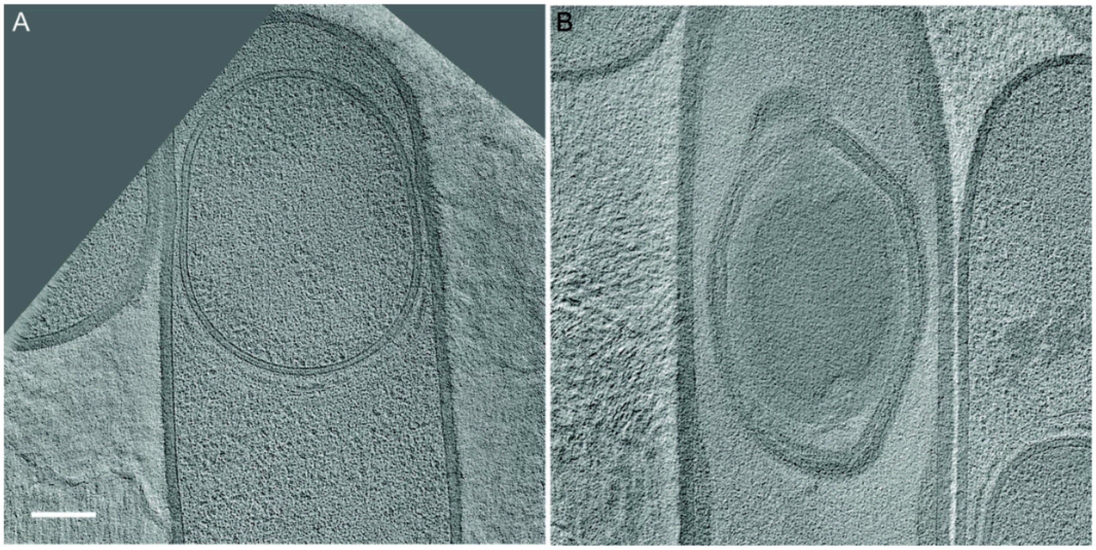

Slices through cryo-electron tomograms representing later stages of sporulation when the forespore is completely inside the mother cell.

(**A**) represents an earlier stage than (**B**). A dense spore with coat and cortex layers is observed in (**B**). Scale bar: 200 nm.

https://doi.org/10.7554/eLife.45257.005

Figure 1—figure supplement 3

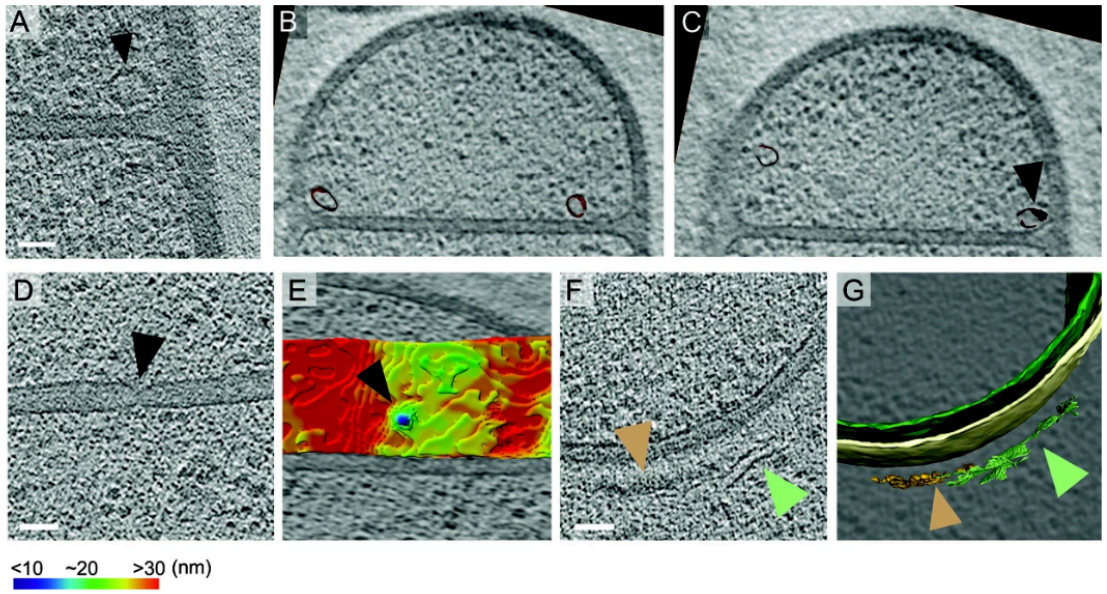

Unidentified complexes during sporulation in *B. subtilis.*

(**A**) Ellipsoidal structure (black arrow) seen in the forespore shortly after septum formation as shown in Figure 1J. Scale bar: 50 nm. (**B,C**) 2 different slices through the same cryo-electron tomogram shown in (**A**) depicting the 3D annotation of the ellipsoidal structures (maroon). The structure highlighted in (**A**) in black arrow is pointed out at in (**C**). (**D**) Slice through a cryo-electron tomogram with putative SpoIIIE channel (black arrow) highlighted as in Figure 1K and (**E**) shows the corresponding color-coded distance of the forespore membrane from the mother cell membrane. The putative channel corresponds to a septal thickness of ~14 nm. (**F**) Slice through a cryo-electron tomogram with coat filaments (green arrow) and amorphous dense coat layer (orange arrow) highlighted. (**G**) shows the corresponding 3D annotations of the filaments (green) and the coat layer (orange), along with the forespore membrane (green) and the mother cell membrane (yellow). Scale bar for (**D,F**): 50 nm. Scale bars have been omitted for all segmented images as cells are displayed in perspective mode.

Figure 2—figure supplement 1

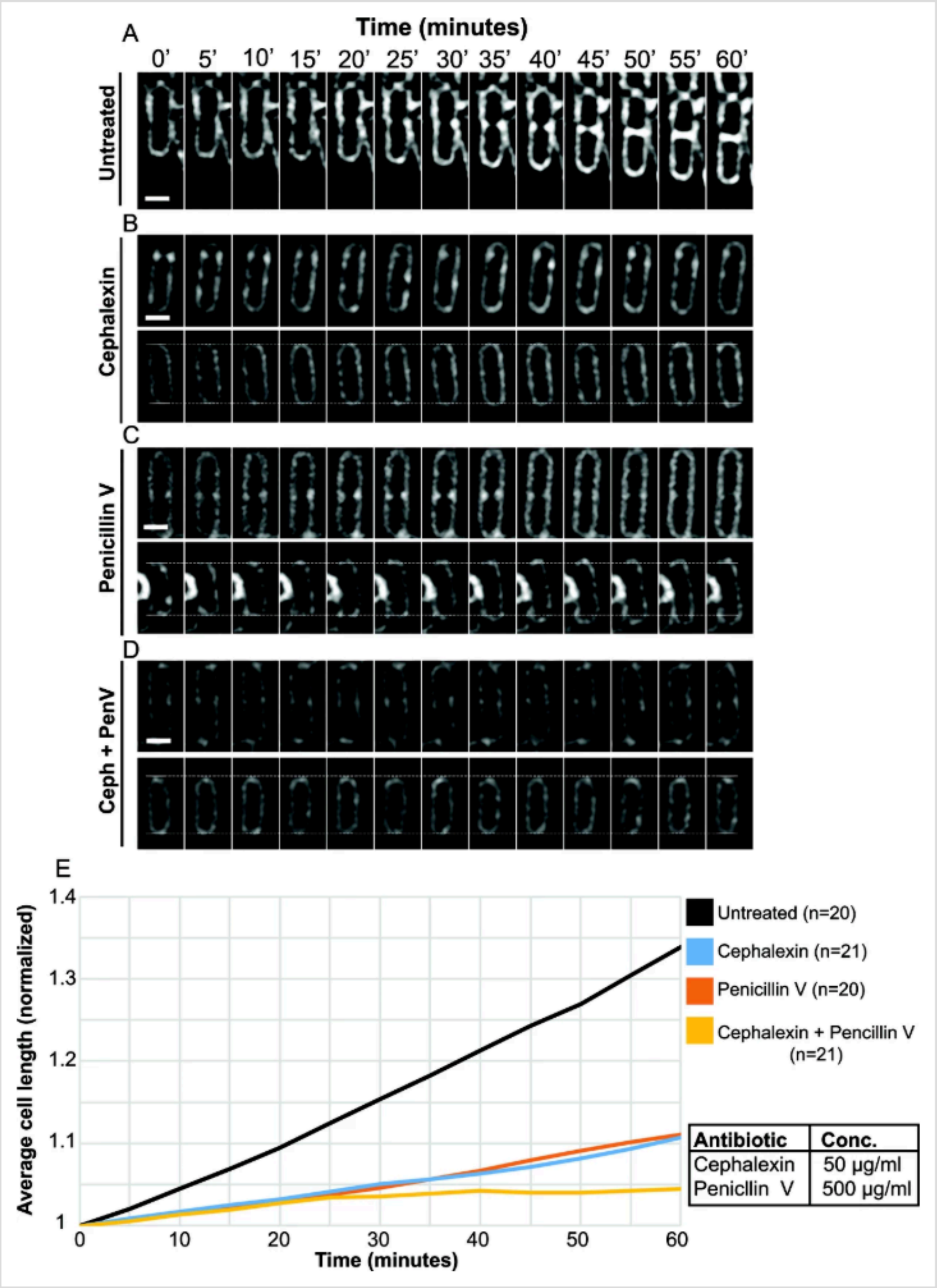

Antibiotic	Conc.
Cephalexin	50 µg/ml
Penicllin V	500 µg/ml

Quantification of cell length upon antibiotic treatment.

(**A–D**) Time-lapse microscopy showing the growth of wild type vegetative *B. subtilis* cells that are (**A**) untreated, (**B**) cephalexin-treated, (**C**) penicillin V-treated and (**D**) treated with a combination of cephalexin and penicillin V. The cells at the top in panels (**B–D**) had initiated septation before imaging, but the formation of the septum is interrupted upon exposure to the antibiotics, indicating that the blockage of PG synthesis happens on a time scale of a few minutes. An abortive polar septum close to the upper cell pole is observed in the cell in top panel (**B**), and abortive vegetative septa in the middle of the cell are observed in top panels (**C**) and (**D**). The cells at the bottom in panels (**B–D**) have dotted lines plotted along the lower and the upper pole of the cell from where the time-lapse experiment starts (0 min time point) to provide visual cue for the change in cell length over the course of time. Scale bars for (**A–D**): 1 µm. (**E**) Average length of vegetative cells (normalized) plotted as a function of time for untreated and different antibiotic-treated cases. n indicates the number of cells analyzed for each case and antibiotic concentrations used in the study are indicated alongside.

Figure 2—figure supplement 2

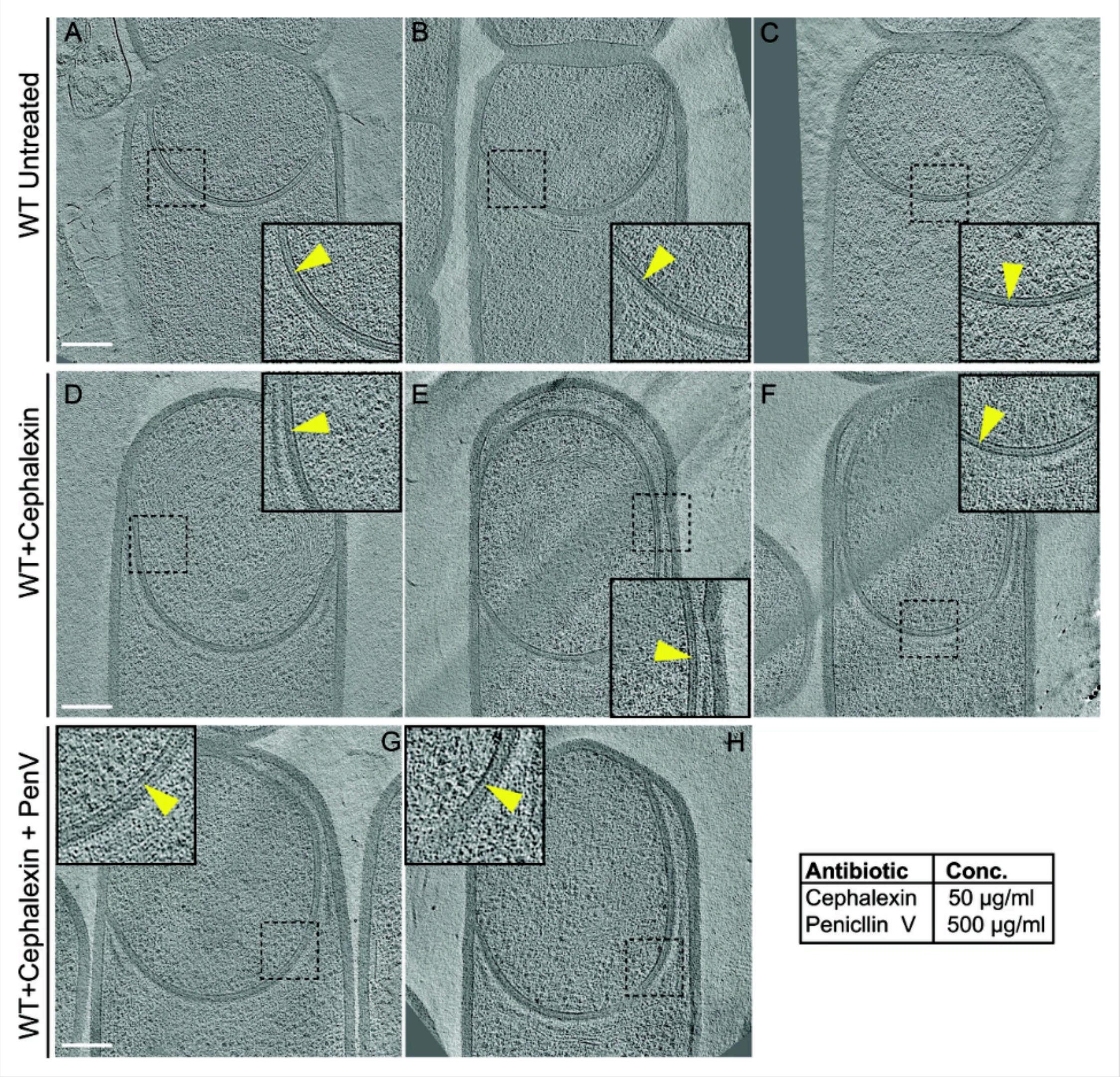

Antibiotic	Conc.
Cephalexin	50 µg/ml
Penicllin V	500 µg/ml

Thin layer of septal peptidoglycan persists in wild type and antibiotic-treated sporangia.

(**A–C**) Slices through cryo-electron tomograms of wild type untreated *B. subtilis* sporangia, (**D–F**) cephalexin-treated) sporangia, and (**G,H**) cephalexin- and penicillin V-treated sporangia. The thin layer of PG between the forespore and the mother cell membranes is indicated by yellow arrows in the zoom-in panels for each tomographic slice. Antibiotic concentrations used are indicated in the bottom right. Scale bars for (**A–H**): 200 nm.

Figure 3—figure supplement 1

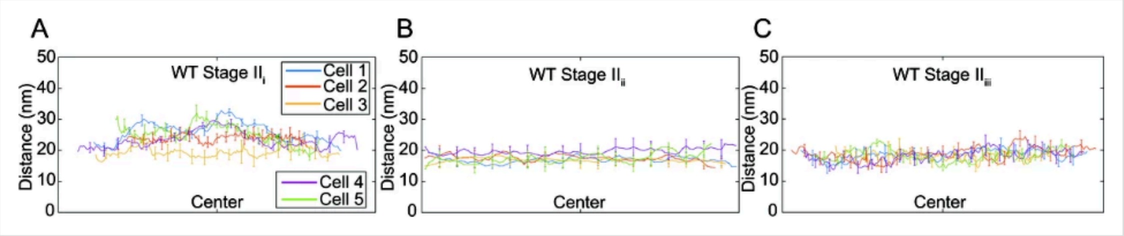

Septal thickness during engulfment in wild type *B. subtilis.*

(**A**) Average thickness of the septum across the forespore surface for five wild type Stage II$_i$ sporangia shown in Figure 3B. (**B**) Average thickness of the septum across the forespore surface for five wild type Stage II$_{ii}$ sporangia shown in Figure 3C. (**C**) Average thickness of the septum across the forespore surface for five wild type Stage II$_{iii}$ sporangia shown in Figure 3D.

Figure 3—figure supplement 2

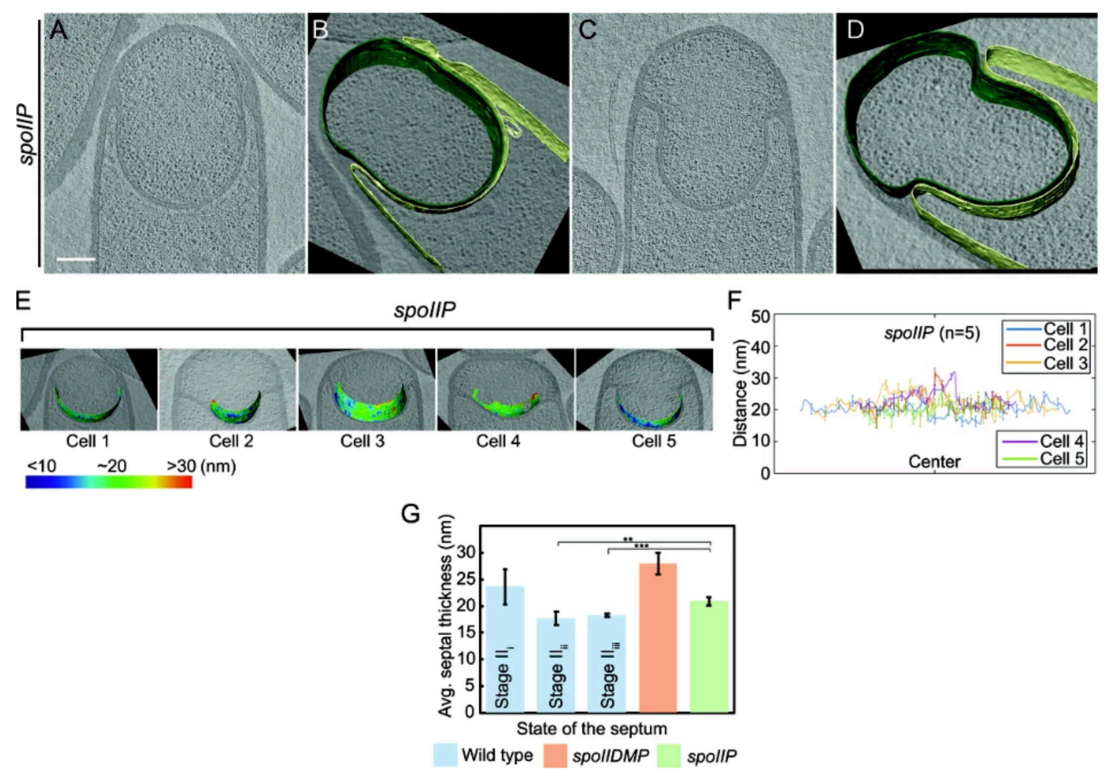

Septal thickness in *spoIIP* mutant sporangia.

(**A–D**) Slices through cryo-electron tomograms of *spoIIP* sporangia with annotations of the forespore membrane (green) and the mother cell membrane (yellow) adjacent to each tomogram. Scale bars for tomogram slices in (**A,C**): 200 nm. Scale bars have been omitted in segmented images owing to their perspective nature. The septum of *spoIIP* sporangia typically contains a bulge in the middle, and a thicker, flat region at the edges that does not bulge towards the mother cell. The distance between the membranes was only determined for the part of the setum that bulges towards the mother cell, but not for the thicker part at the edges that does not bulge. (**E**) Color-coded distance of the forespore membrane from the mother cell membrane along the length of the septum for *spoIIP* mutant sporangia. (**F**) Average thickness of the septum across the forespore surface for five *spoIIP* mutant sporangia shown in (**E**). (**G**) Average septal thickness for wild type stages II$_{i\text{-}iii}$ and *spoIIDMP* and *spoIIP* mutant sporangia. Error bars indicate standard deviation (n.s.: p>0.05; *: p≤0.05; **: p≤0.01; ***: p≤0.001, unpaired t-test).

Figure 3—figure supplement 3

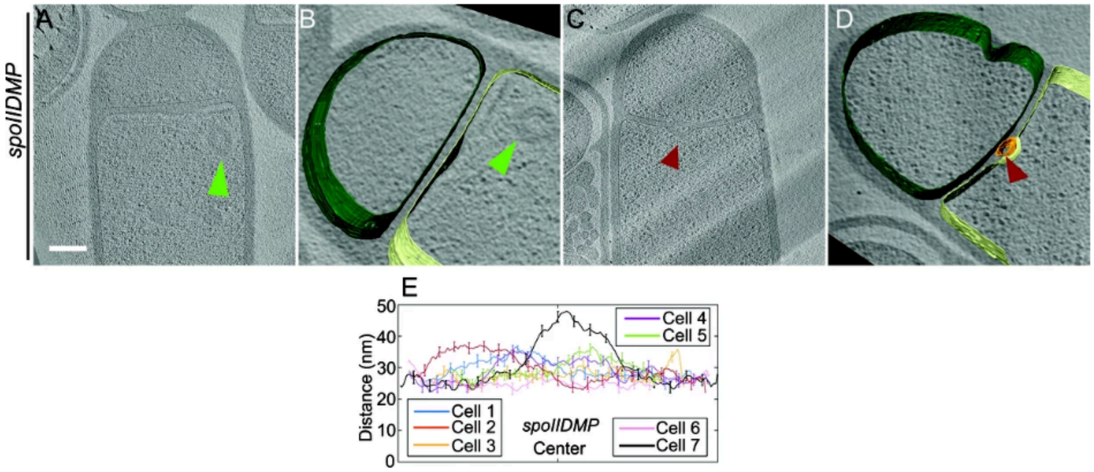

Septal thickness in *spoIIDMP* sporangia.

(**A–D**) Slices through cryo-electron tomograms of *spoIIDMP* mutant sporangia with annotations of the forespore membrane (green) and the mother cell membrane (yellow) adjacent to each tomogram. Bulges are indicated by green arrows in (**A,B**) and in red arrows in the middle of the septum in (**C,D**). Scale bars for tomogram slices in (**A,C**): 200 nm. Scale bars are omitted for all segmented images due to their perspective nature. (**E**) Average thickness of the septum across the forespore surface for seven *spoIIDMP* sporangia shown in Figure 3G.

Figure 3—figure supplement 4

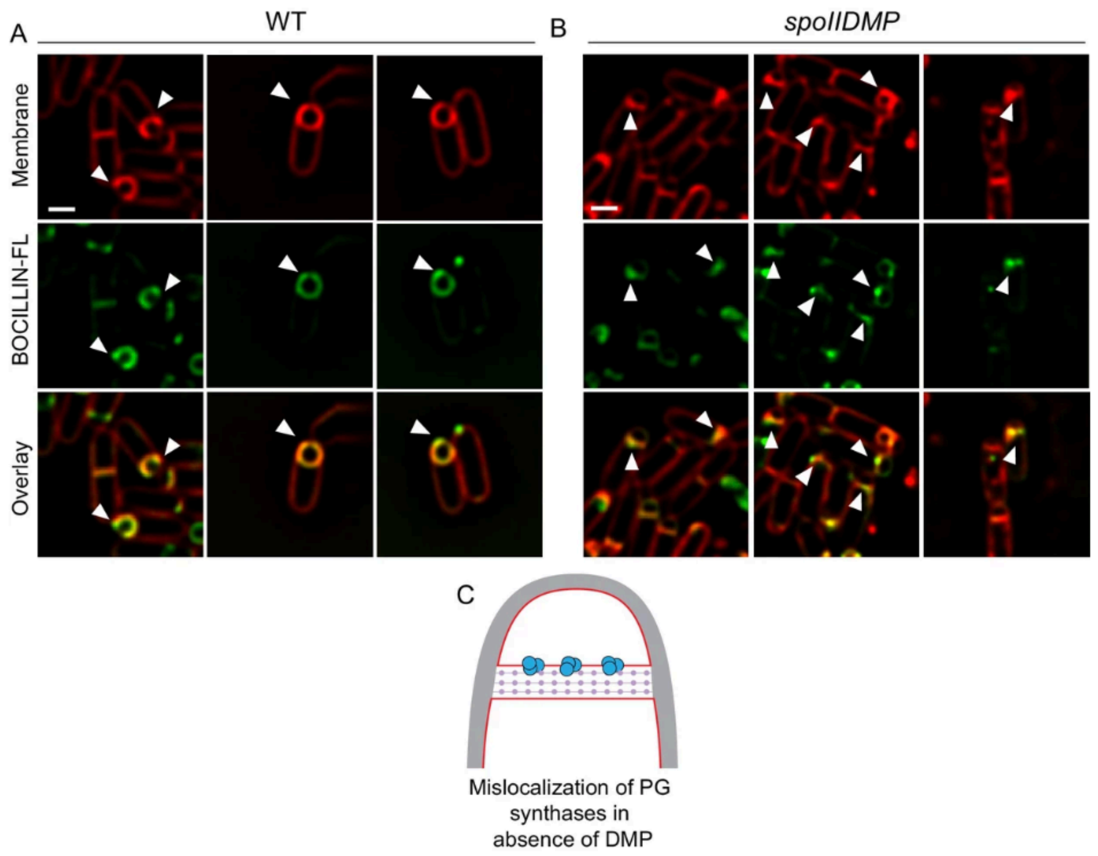

Observing peptidoglycan synthesis using BOCILLIN-FL.

(**A**) Wild type sporulating cells stained with a green fluorescent derivative of penicillin V (BOCILLIN-FL). Membranes were stained with FM 4–64 (red). White arrows indicate cells with enhanced fluorescent signal at the leading edges of the engulfing membrane. (**B**) *spoIIDMP* mutant sporangia stained with BOCILLIN-FL (green). Membranes were stained with FM 4–64 (red). White arrows indicate cells with enhanced fluorescent signal in variable regions of the septum. Scale bars: 1 µm. (**C**) Schematic to explain accumulation of PG synthases in the septum (blue circles) in the absence of DMP as opposed to being localized near the leading edges in wild type sporangia. Membranes (red), lateral PG (gray) and septal PG (pink circles) are also highlighted.

Figure 4—figure supplement 1

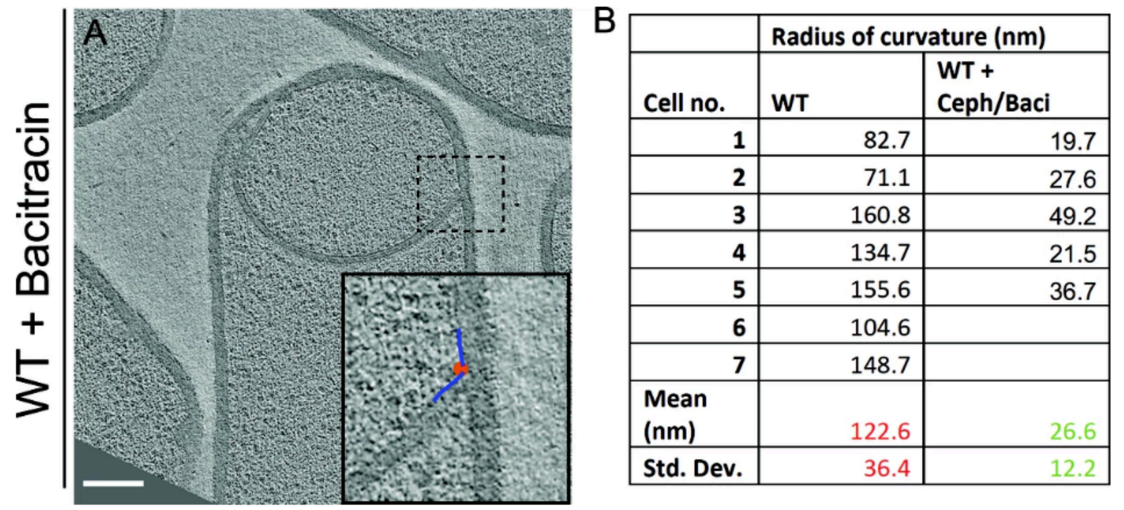

	Radius of curvature (nm)	
Cell no.	**WT**	**WT + Ceph/Baci**
1	82.7	19.7
2	71.1	27.6
3	160.8	49.2
4	134.7	21.5
5	155.6	36.7
6	104.6	
7	148.7	
Mean (nm)	122.6	26.6
Std. Dev.	36.4	12.2

Quantification of radius of curvature of the forespore membrane.

(**A**) Slice through a cryo-electron tomogram of a wild type sporangium treated with bacitracin (50 µg/ml) with the radius of curvature of the forespore membrane ahead of the leading edge of the engulfing membrane highlighted. Scale bar: 200 nm. (**B**) Raw data for radius of curvature of the forespore membrane of wild type sporangia and antibiotic (cephalexin and bacitracin) treated sporangia with mean and standard deviation indicated.

Figure 4—figure supplement 2

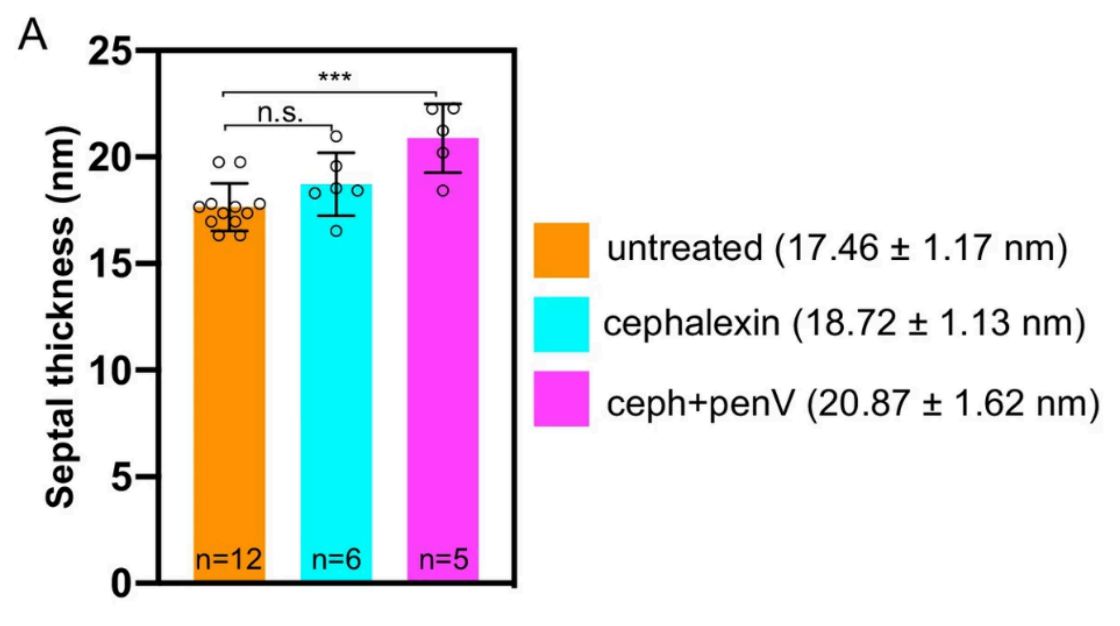

Graph depicting the septal thickness of wild type untreated and antibiotic-treated sporangia (cephalexin and a combination of cephalexin and penicillin V) according to concentrations specified in Figure 2—figure supplement 1.

n indicates the number of tomograms analysed. The mean and standard deviation for each case is indicated.

https://doi.org/10.7554/eLife.45257.026

Figure 4—figure supplement 3

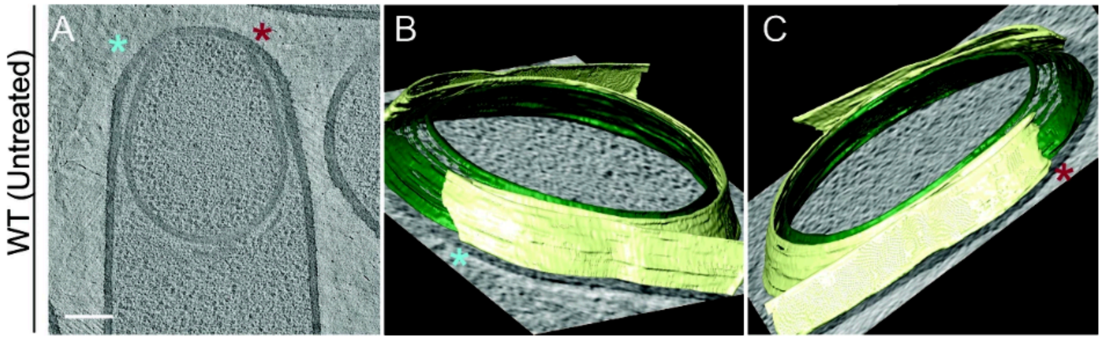

Membrane architecture in wild type.

(**A**) Slice through a cryo-electron tomogram of a wild type sporangium. (**B,C**) Annotation of membranes for the tomogram shown in (**A**). Forespore membrane is shown in green and mother cell membrane in yellow and both sides of the engulfing mother cell membrane are indicated by blue and maroon asterisks respectively. Scale bar for (**A**): 200 nm. Scale bars are omitted for annotated panels that are shown in perspective mode.

Figure 4—figure supplement 4

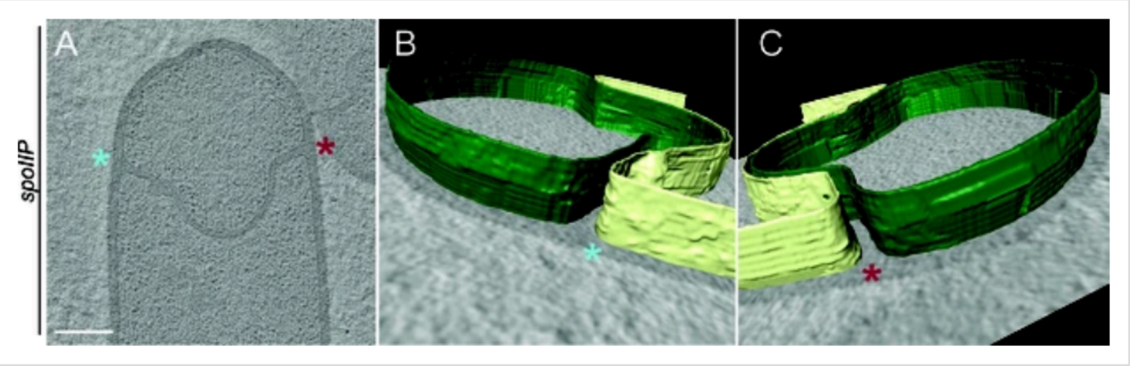

Membrane architecture in spoIIP sporangia.

(**A**) Slice through a cryo-electron tomogram of a *spoIIP* sporangium. (**B,C**) Annotation of membranes for the tomogram shown in (**A**). Forespore membrane is shown in green and mother cell membrane in yellow and both sides of the engulfing mother cell membrane are indicated by blue and maroon asterisks respectively. Scale bar for (**A**): 200 nm. Scale bars are omitted for annotated panels that are shown in perspective mode.

Figure 4—figure supplement 5

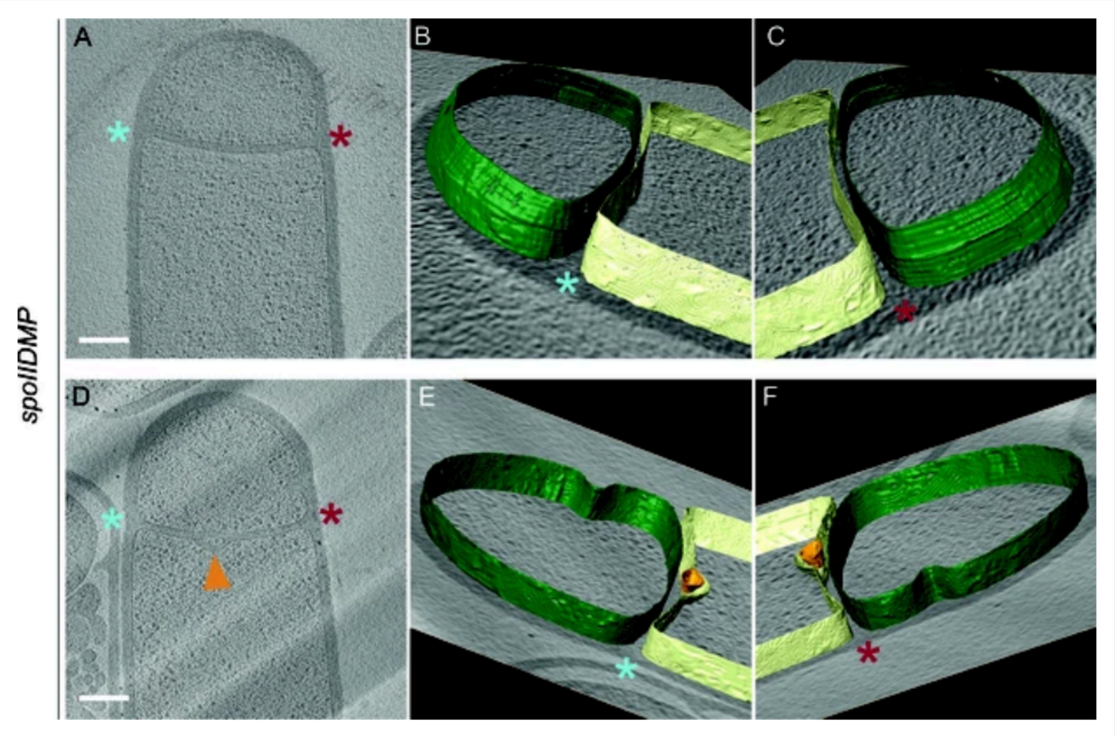

Membrane architecture in *spoIIDMP* sporangia.

(**A,D**) Slices through cryo-electron tomograms of *spoIIDMP* sporangia. (**B,C**) Annotation of membranes for the tomogram shown in (**A**). (**E,F**) Annotation of membranes for the tomogram shown in (**D**). Forespore membrane is shown in green and mother cell membrane in yellow and both sides of the engulfing mother cell membrane are indicated by blue and maroon asterisks respectively. A bulge in the middle of the septum (orange arrow) in (**D**) is highlighted in orange in (**E**) and (**F**). Scale bars for (**A,D**): 200 nm. Scale bars are omitted for annotated panels that are shown in perspective mode.

Figure 4—figure supplement 6

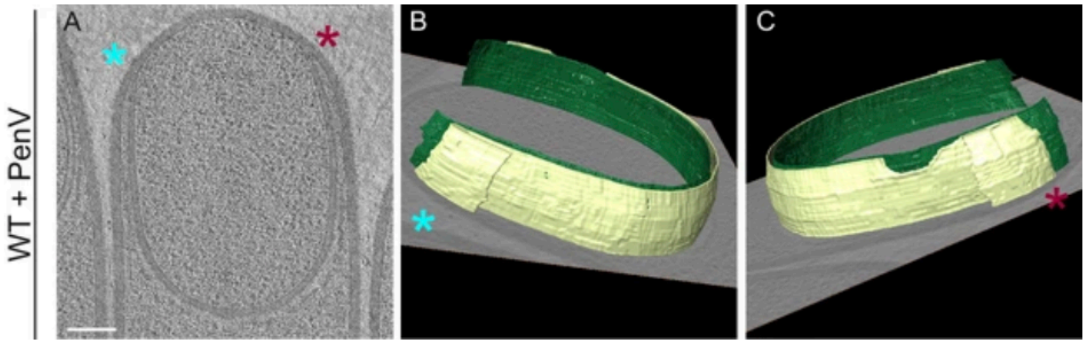

Membrane architecture in antibiotic-treated sporangium.

(**A**) Slice through a cryo-electron tomogram of a wild type sporangium treated with penicillin V. (**B,C**) Annotation of membranes for the tomogram shown in (**A**). Forespore membrane is shown in green and mother cell membrane in yellow and both sides of the engulfing mother cell membrane are indicated by blue and maroon asterisks respectively. Scale bar for (**A**): 200 nm. Scale bars are omitted for annotated panels that are shown in perspective mode.

Acknowledgements

Chapter 4, in full, is a reprint of the material as it appears in *eLife* 2019 (8). The manuscript is: Khanna, K., Lopez-Garrido, J., Zhao, Z., Watanabe, R., Yuan, Y., Sugie, J., Pogliano, K., Villa, E. ‘The molecular architecture of engulfment during *Bacillus subtilis* sporulation’. The dissertation author was the primary author of the manuscript and conducted all cryo-EM experiments and analysis with input from other authors.

Chapter 5: Toroidal packaging of DNA during sporulation in *Bacillus subtilis*

5.1 Summary

There is limited knowledge about how protein binding modulates the architecture and dynamic properties of DNA inside the cells. During sporulation in *B. subtilis*, the cell divides into a smaller forespore which is ultimately engulfed by the larger mother cell. After engulfment, the forespore DNA condenses into a toroidal shape when a class of proteins termed small, acid-soluble proteins (SASP) bind to it. This condensation is thought to protect the spore DNA from environmental assaults. However, there is limited knowledge about how SASP binding modulates the architecture and dynamic properties of the forespore DNA. In this study, we have elaborated the role of major α/β-type SASP in changing the conformation of DNA from random coil to condensed state during sporulation. We show using timelapse fluorescence microscopy and cryo-electron tomography that upon SASP binding, the forespore DNA adopts a twisted toroid confirmation and discuss the implications the binding interaction may have on DNA regulation and architecture.

5.2 Introduction

Deoxyribonucleic acid or DNA is the central feature of all life forms, encoding the genetic information to carry out cellular processes. While the DNA in eukaryotes is enclosed in a membrane-bound compartment, the DNA and its associated molecules in prokaryotes occupy a distinct region in the cytoplasm called the ‘nucleoid’. The enzymatic details of DNA replication and transcription in bacteria have been studied in great detail, but we have a limited understanding of how the dynamics and architecture of DNA regulate these processes.

Bacillus subtilis, a rod-shaped Gram-positive bacterium, packs a circular chromosome of ~4.2 Mbp in ~1 μm^3 cell volume (Kunst et al., 1997). During vegetative growth, *B. subtilis* divides into two equal daughter cells each with its own copy of chromosome. However, during starvation, the cells switch to sporulation which is characterized by the formation of an asymmetrically positioned (polar) septum (Higgins and Dworkin, 2012; Tan and Ramamurthi, 2014). This leads to the formation of two daughter cells of unequal sizes: the smaller cell called the forespore which is ultimately engulfed by the larger cell called the mother cell. At the onset of sporulation, the segregating chromosomes are remodeled into an elongated structure called the axial filament, with the origins of replication at the cell poles and the termini at mid cell (Kay and Warren, 1968; Pogliano et al., 2002; Ryter, 1965; Webb et al., 1997). The polar septum forms before the origin-distal part of the chromosome enters into the forespore. Hence, after polar septation, the forespore chromosome is trapped at the sporulation septum such that only the one-third origin-proximal part of the chromosome is present in the forespore while the rest two-thirds remains in the mother cell (L J Wu and Errington, 1994; Wu and Errington, 1998). A membrane-anchored and ATP-powered motor called SpoIIIE then pumps the remaining chromosome from the mother cell to the forespore (Bath et al., 2000; Massey et al., 2006; Wu and Errington, 1997). We recently showed that chromosome translocation is essential for the growth of the forespore and that packing this long, negatively charged DNA polymer into the small volume of the forespore generates significant turgor pressure in the forespore (Lopez-Garrido et al., 2018).

Later in sporulation when the forespore is encased inside the mother cell, a set of proteins known as the small acid-soluble proteins (SASP), that are produced specifically in the forespore bind to and saturate the forespore chromosome (Driks, 2014; Setlow, 2007, 2006). SASP are encoded by genes termed *ssp* that are expressed under the control of the forespore-specific σ factor, σ^G. They make up about 10% protein content of dormant spores and are highly conserved among endospore-forming bacteria (Driks, 2014; Setlow, 2006, 1995, 1994). They are usually 60-75 residues in length and bind DNA in a non-specific and highly cooperative manner. The majority of SASP (~75%) are composed of three proteins: SASP-α, SASP-β and SASP-γ. Previous studies have shown that the α/β-type SASP are associated with the forespore chromosome and together they form a compact ring-like structure during later stages of forespore development (Francesconi et al., 1988; Pogliano et al., 1995).

Previous spectroscopic analysis indicated that binding of α/β-type SASP changes the configuration of DNA from B-like form to A-like form (Donnellan and Stafford, 1968; Stafford and Donnellan, 1968). However, electron microscopy data suggested that the DNA helix bound to SASPs has mixed features, with rise per base pair in DNA identical to B-form, and twist, width of the minor groove and sugar puckering identical to A-form (Frenkiel-Krispin et al., 2004; Ki et al., 2008). Another important characteristic of SASP-bound DNA is the significant increase in its persistence length, making the DNA rigid and less prone to damage by UV radiation, heat and genotoxic chemicals (Griffith et al., 1994). Although substantial studies have been done to understand the role of SASPs in mediating DNA protection and in modulating DNA properties, little is known about the high-resolution architecture and dynamics of regulation of SASP-DNA binding in vivo.

In this study we have used timelapse fluorescence microscopy and cryo-focused ion beam milling coupled with cryo-electron tomography (or cryo-FIB-ET) to get insights into forespore DNA architecture upon SASP-binding at high resolution in the native state and the dynamics of SASP-

DNA interaction. We show that SASP-binding changes the forespore DNA conformation from random coil to a twisted toroid and discuss the possible implications it may have in protecting the forespore DNA from harsh environmental conditions.

5.3 Results

SASP adopt twisted toroidal configuration inside forespores

Previous cytological evidence using indicated that α/β-type SASP adopt a toroidal ring-like configuration inside forespores (Francesconi et al., 1988; Pogliano et al., 1995). To get better insights about SASP-DNA binding, we visualized strains containing functional GFP fusions of the major SASP, SspA and SspB using timelapse fluorescence microscopy (Fig. 5.1). For both SspA and SspB, we observed GFP signal in the forespore compartment before the completion of engulfment. Also, both SASP adopt a configuration resembling twisted toroid instead of a ring-like doughnut shaped as has been previously reported by immunofluorescence and immunoelectron microscopy (Francesconi et al., 1988; Pogliano et al., 1995). In fact, these twisted toroids continuously rotate inside the forespore as they are being formed and even after fully adopting the toroidal configuration and eventually become static ~ 2.5 hours after they have been formed (Fig. 5.1).

We also tested the fate of SASP in a SpoIIIE^{ATP-} mutant (Sharp and Pogliano, 1999) wherein the forespore DNA remains trapped at the septum due to a point mutation in SpoIIIE, rendering its ATPase activity non-functional (Fig. S5.1). In both the GFP strains, we observe diffuse fluorescence throughout the cytoplasm in both the forespore and the mother cell, probably due to non-specific activation of σ^G in both the compartments.

Architecture of toroidal forespore DNA using cryo-FIB-ET

It is difficult to visualize ~2 nm thin DNA inside the cells in a native state with the current pool of available electron microscopy techniques unless it displays any high-order organization.

For instance, the arrangement of condensed DNA in viruses can be readily revealed by cryo-ET (Cyrklaff et al., 2007; Grünewald and Cyrklaff, 2006). For prokaryotic cells, previous studies have indicated that the nucleoid excludes ribosomes and other major cellular complexes (Bakshi et al., 2015; Chai et al., 2014; Lewis et al., 2000; Luef et al., 2015). Since ribosomes can be easily identified using cryo-ET, this information can be used to assign localization to DNA based on the areas that are excluded by the ribosomes, an approach we had used earlier to define the role of DNA in shaping the forespore in *B. subtilis* (Lopez-Garrido et al., 2018).

Since SASP are known to saturate and condense the forespore DNA, we anticipated that we may be able to capture higher-order arrangement of SASP-bound DNA inside the forespore using cryo-FIB-ET. We imaged the cells roughly 4 hours after sporulation induction at which stage majority of the forespores are engulfed and growing inside the mother cell. Our data indicated that initially, the forespore ribosomes are distributed in the periphery of the forespore (Fig. S5.2). Since the excluded space is occupied by the DNA, it seems to be packed in a random coil configuration in the center of the forespore as we did not detect any higher order arrangement at this stage. As the forespore develops further inside the mother cell, it grows in volume and we have previously shown that this value gradually increases from 0.2 μm^3 upon engulfment completion to ~0.3 μm^3 when it plateaus (Lopez-Garrido et al., 2018). At this stage, the condensed forespore DNA is clearly visible in cryo-FIB-ET images (Fig. 5.2A-C). Depending on the orientation of the cells on the electron microscopy grids and positioning of the rectangular milling patterns inside the FIB, we captured different views of the twisted toroidal DNA, either complete rings or half or three-fourths ring (Fig. 5.2A-C, S5.3). The condensed DNA consisted of tightly packed spirals encircling the inside of the forespore with a spacing of ~ 6-9 nm between the strands. The ribosomes were densely packed in the center of the forespore in these cells. In many of the forespores, we observed a highly electron-dense circular region of ~60-70 nm diameter and it appeared that the DNA was wound around it (Fig. 5.2C). Currently, we do not know the identity of these complexes.

Next, we imaged a strain mutant for both SspA and SspB, the major SASP. We did not observe any obvious condensed or toroidal DNA arrangement in these mutant sporangia (Fig. 5.2D-F). However, in some sporangia we observed the electron-dense region similar to wild type and a few short regions of condensed structures likely reflecting residual DNA packaging due to other minor SASP (Fig. 5.2F).

5.4 Discussion

It has been previously established that 3-4 hours after onset of sporulation, α/β-type small acid soluble proteins (SASPs) accumulate to a high level inside the spore, saturate the forespore DNA by binding nonspecifically in a highly cooperative manner and drive the transformation of DNA from random coil state to toroidal configuration. In this study, we demonstrated that binding of α/β-type SASP to the forespore DNA changes its configuration to that of a twisted toroid and elaborated upon the architecture of the packaged DNA using fluorescence microscopy and cryo-FIB-ET (Fig. 5.3).

After SpoIIIE translocates DNA into the forespore, the forespore contains one copy of circular chromosome of ~ 4.2 Mbp, that would translate to a total length ~1.5 mm. Our cryo-FIB-ET data indicate that the twisted toroids are ~150 nm wide. Assuming that the diameter of the forespore is ~1000 nm and toroid occupies the forespore periphery, this would mean that the DNA is wounded circumferentially as in a rope for ~400-500 rounds. Since DNA segments are highly negatively charged, they would repel each other strongly under normal conditions. However, the positively charged SASP molecules synthesized in the forespore with a copy number of ~ 1 million, bind to the forespore DNA and mediate the attraction between the DNA strands.

The finding that both SspA and SspB are expressed before engulfment completion is surprising because *ssp* genes encoding SASP are under the control of forespore-specific transcription factor, σ^G, the activation of which is thought to be linked to engulfment completion

(Regan et al., 2012). However, recently there has been contrary evidence and debate in the field about this claim (Doan et al., 2013, 2009). Specifically, half of the sporangia that are mutant for a protein mediating membrane fission are still able to activate σ^G suggesting that engulfment completion and σ^G activation are likely not coupled (Doan et al., 2013). Our observation that the major SASP are expressed before engulfment membrane fission also lends credence to the latter claim.

Our timelapse fluorescence microscopy data indicate that the twisted toroids formed by major SASP rotate inside the forespore as engulfment membrane migration proceeds. In many cases, protein binding can significantly bend the DNA (Schultz et al., 1991). This bending would then introduce strain in the DNA segment such that when the circular DNA closes upon itself upon joining of its two ends, it would deform into a twisted shape like a figure eight as is the case in supercoiled DNA. Perhaps, the bending of the forespore DNA when many molecules of SASP bind to it introduces sufficient strain to twist the toroid. Previous studies show that many of the proteins that bind non-specifically to DNA exhibit a rotation-coupled sliding along DNA helical pitch (Ando and Skolnick, 2014; Blainey et al., 2009). Hence, it is possible that the rotation of the toroid that we see in our timelapse experiment reflects the period when the newly expressed SASP are still searching for their binding sites on the DNA. Notably, the rotation happens prior to engulfment completion when we do not see any evidence of condensed DNA in our cryo-FIB-ET images. It is possible the end of the rotation of the twisted toroid is somehow coupled to the expression of SASP. When SASP expression has reached its maximum, it is possible that the molecular crowding prevents them from sliding any further on the condensed DNA. Alternatively, the rotation of SASP on DNA is facilitated by some factor in the forespore and once that factor has degraded, the SASP molecules stop rotating. More data are needed to test these hypotheses and establish biophysical basis for how SASP cooperatively search for their target binding regions in the forespore DNA resulting in changes in the DNA topology.

Majority of the dsDNA viruses pack their genome under a very high pressure to overcome the repulsion between negatively charged DNA strands with the help of an ATP-powered motor protein. In such cases, the spacing between the adjacent strands is ~2.5-3 nm which is lower than the value of 6-9 nm that we report in the SASP-bound DNA filaments in *B. subtilis*. However, more recently the structural studies of filamentous viruses and an archaeal virus that harbor dsDNA in A-form suggest that their genome packaging is facilitated by a virion protein that decorates the DNA and the spacing between the nucleoprotein filaments is slightly larger in these cases at ~4.3 nm (DiMaio et al., 2015; Wang et al., 2019).

Ring-like structures of DNA condensates have previously been observed in the case of sperm DNA packaging by protamines, a family of small arginine-rich proteins that prevent DNA from various stresses like sonication and boiling (Eickbush and Moudrianakis, 1978). Doughnut-shaped complexes have also been observed when histone H1 was mixed with DNA (Hsiang and Cole, 1977). Our observation that the forespore DNA is wrapped around an electron-dense region in many cells (Fig. 5.2C) is reminiscent of DNA wrapping around histones in eukaryotes. Although we only observe roughly one such electron-dense region in ~200 nm slices of cells prepared by cryo-FIB-ET, it is possible that there are more of these in the entire ~1.2 μm wide cell. In fact, it was previously shown that *B. subtilis* histone-like protein, HBsu colocalized with α/β-type SASP on the forespore nucleoid but unlike SASP did not form complete rings (Ross and Setlow, 2000). Margery & Ross further demonstrated in vitro that HBsu modulated the effects of SASP binding on DNA including protection from DNase damage and DNA supercoiling and persistence length (Ross and Setlow, 2000). It is possible that these electron-dense regions may be aggregrates of HBsu although more conclusive evidence is needed.

Collectively, our results demonstrate the higher-order architectural information about DNA packaging mediated by SASP during *B. subtilis* sporulation, a process that is thought to preserve the spore genome from harsh environmental conditions including UV irradiation, antibiotics, oxidative damage etc. We anticipate that this study combined with further biophysical modeling and structural studies will enable us to understand the basic principles underlying protein-DNA interactions in extreme environments. This will be an important step towards designing cell-based therapies that can protect DNA in many other cell types to increase their resistance and improve chances of their survival under stressful conditions.

5.5 Materials and Methods

Strains and culture conditions

Bacillus subtilis PY79 or 168 background was used for all strain constructions. A list of strains used in the study is provided in Table 5.1. All the strains were routinely grown in LB plates at 30°C overnight. For sample preparation, cells were grown in in ¼ diluted LB to OD600 ~0.5-0.8 and then resuspended in A+B media at 37°C for inducing sporulation.

Table 5.1 Strain list for Chapter 5

Strain	**Genotype or description**	**Reference, source or construction**
PY79	Wild type	(Youngman et al., 1984)(Youngman et al., 1984)
KK233	*sspA-sfGFPΩkan*	pKK229 → PY79 (Kan, This study)
KK234	*sspB-sfGFPΩkan*	pKK231 → PY79 (Kan, This study)
KP53	*ΔsspA ΔsspB*	(Mason & Setlow, 1986)(Mason and Setlow, 1986)
KP541	*spoIIIE*$^{ATP-}$ (G467S; ATPase mutant)	(Sharp & Pogliano, 1999)(Sharp and Pogliano, 1999)
KK377	*sspA-sfGFP spoIIIE*$^{ATP-}$	KK233 → KP541* (Kan)
KK379	*sspB-sfGFP spoIIIE*$^{ATP-}$	KK234 → KP541* (Kan)

*Genomic or plasmid DNA of the strain on the left side of the arrow transformed into competent cells of the strain on the right side of the arrow. The selection antibiotics are indicated alongside.

Table 5.2 Oligo list for Chapter 5

Primer	Sequence
JLG-7	AATTGGGACAACTCCAGTG
JLG-77	GCTAGCAGCGCAAGCGC
JLG-95	CATGGATTACGCGTTAACCC
JLG-96	GCACTTTTCGGGGAAATGTG
KK82	*gggttaacgcgtaatccatg*GAGCGTGGCCGTAATGATTTC*
KK83	*cttgcgcttgcgctgctagc*TTGAACTCTGCCGCCCATTTG*
KK86	*cactggagttgtcccaatt*AATATATGGCTATAGAGGGC*
KK87	*cacatttccccgaaaagtgc*ATCGGGAATCTAGGATCC*
KK88	*gggttaacgcgtaatccatg*TGTTCATTTCTTCAGCCCG*
KK89	*cttgcgcttgcgctgctagc*GAATTGTCCTCCGCCCATG*
KK90	*cactggagttgtcccaatt*ACAATTTCACATAATGGCTTAG*
KK91	*cacatttccccgaaaagtgc*GACGATATCCTTTTCAGAAATG*

*****Capital letters indicate regions of the primer that anneal to the template and lowercase italicized letters indicate the homologous regions for Gibson assembly.

Plasmid construction

pKK229: This plasmid was constructed by assembling the following 4 fragments by Gibson Assembly (New England Bioloabs): (i) a DNA fragment encompassing the spectinomycin resistance gene, the origin of replication, and the ampicillin resistance gene from pDG1662(Guérout-Fleury et al., 1996) amplified with primers JLG-95 and JLG-96, (ii) a 682 bp region upstream of *sspA* coding sequence and the 207 bp of *sspA* coding sequence (not including the stop codon) amplified with KK88 and KK89 from *B. subtilis* PY79 genomic DNA (iii) *sfGFPΩkan* from pJLG36(Shin et al., 2015) amplified with JLG7 and JLG77, and (iv) a region of 820 bp immediately downstream of *sspA* stop codon amplified with KK90 and KK91.

pKK231: This plasmid was constructed by assembling the following 4 fragments by Gibson Assembly (New England Bioloabs): (i) a DNA fragment encompassing the spectinomycin resistance gene, the origin of replication, and the ampicillin resistance gene from pDG1662(Guérout-Fleury et al., 1996) amplified with primers JLG-95 and JLG-96, (ii) a 431 bp region upstream of *sspB* coding sequence and the 201 bp of *sspB* coding sequence (not including the stop codon) amplified with KK82 and KK83 from *B. subtilis* PY79 genomic DNA (iii) *sfGFPΩkan* from pJLG36(Shin et al., 2015) amplified with JLG7 and JLG77, and (iv) a region of 593 bp immediately downstream of *sspB* stop codon amplified with KK86 and KK87.

Fluorescence microscopy for batch cultures

Please refer to Section 2.5 (Fluorescence microscopy for batch cultures) for more details.

Timelapse fluorescence microscopy

0.5 μg/ml FM4-64 was added to cultures ~2 hours after sporulation induction to visualize the membranes. The cultures were then incubated for another hour before collecting the samples for timelapse microscopy (~ 3 hours after sporulation induction). 1.5 ml of the culture at ~3 hours was spun at ~6000 rpm for 1 min and 1ml of the supernatant collected which was mixed with 0.5 ml of 3.6% agarose prepared in A+B sporulation media to make pads for timelapse microscopy. 7 μl of the culture was then added to these pads, let to dry and the slides covered with a glass coverslip and sealed with petroleum jelly. Pictures were taken in an environmental chamber at

30°C every 5 min for ~5 hours. TRITC/CY5 filters were used for membrane imaging and FITC/FITC for sfGFP. For each image, exposure time was set to 0.1 and excitation light transmission to 5%.

Cryo-FIB-ET workflow

Samples for cryo-FIB-ET were collected 4 hours after induction of sporulation. For details regarding the procedures for plunge-freezing, cryo-FIB milling and cryo-ET, please refer to Section 2.5 (cryo-FIB-ET workflow).

Tomogram reconstruction and segmentation

Please refer to Section 2.5 (Tomogram reconstruction and segmentation) for more details. For ribosome segmentation, please refer to the procedure outlined before in Chaikeeratisak et al., 2017 (Materials and Methods)(Chaikeeratisak et al., 2017).

5.6 References

Ando T, Skolnick J. 2014. Sliding of Proteins Non-specifically Bound to DNA: Brownian Dynamics Studies with Coarse-Grained Protein and DNA Models. *PLoS Comput Biol*. doi:10.1371/journal.pcbi.1003990

Bakshi S, Choi H, Weisshaar JC. 2015. The spatial biology of transcription and translation in rapidly growing Escherichia coli. *Front Microbiol* **6**:15. doi:10.3389/fmicb.2015.00636

Bath J, Ling Juan Wu, Errington J, Wang JC. 2000. Role of Bacillus subtilis SpoIIIE in DNA transport across the mother cell-prespore division septum. *Science (80-)* **290**:995–997. doi:10.1126/science.290.5493.995

Blainey PC, Luo G, Kou SC, Mangel WF, Verdine GL, Bagchi B, Xie XS. 2009. Nonspecifically bound proteins spin while diffusing along DNA. *Nat Struct Mol Biol*. doi:10.1038/nsmb.1716

Chai Q, Singh B, Peisker K, Metzendorf N, Ge XL, Dasgupta S, Sanyal S. 2014. Organization of Ribosomes and Nucleoids in Escherichia coli Cells during Growth and in Quiescence. *J Biol Chem* **289**:11342–11352. doi:10.1074/jbc.M114.557348

Chaikeeratisak V, Nguyen K, Khanna K, Brilot AF, Erb ML, Coker JKC, Vavilina A, Newton GL, Buschauer R, Pogliano K, Villa E, Agard DA, Pogliano J. 2017. Assembly of a nucleus-like structure during viral replication in bacteria. *Science (80-)* **355**:194–197. doi:10.1126/science.aal2130

Cyrklaff M, Linaroudis A, Boicu M, Chlanda P, Baumeister W, Griffith G, Krijnse-Locker J. 2007. Whole cell cryo-electron tomography reveals distinct disassembly intermediates of vaccinia virus. *PLoS One*. doi:10.1371/journal.pone.0000420

DiMaio F, Yu X, Rensen E, Krupovic M, Prangishvili D, Egelman EH. 2015. A virus that infects a hyperthermophile encapsidates A-form DNA. *Science (80-)*. doi:10.1126/science.aaa4181

Doan T, Coleman J, Marquis KA, Meeske AJ, Burton BM, Karatekin E, Rudner DZ. 2013. FisB mediates membrane fission during sporulation in bacillus subtilis. *Genes Dev*. doi:10.1101/gad.209049.112

Doan T, Morlot C, Meisner J, Serrano M, Henriques AO, Moran CP, Rudner DZ. 2009. Novel secretion apparatus maintains spore integrity and developmental gene expression in Bacillus subtilis. *PLoS Genet*. doi:10.1371/journal.pgen.1000566

Donnellan JE, Stafford RS. 1968. The Ultraviolet Photochemistry and Photobiology of Vegetative Cells and Spores of Bacillus megaterium. *Biophys J*. doi:10.1016/S0006-3495(68)86471-9

Driks A. 2014. Proteins of the Spore Core and CoatBacillus Subtilis and Its Closest Relatives. doi:10.1128/9781555817992.ch36

Eickbush TH, Moudrianakis EN. 1978. The compaction of DNA helices into either continuous supercoils or folded-fiber rods and toroids. *Cell*. doi:10.1016/0092-8674(78)90198-8

Francesconi SC, MacAlister TJ, Setlow B, Setlow P. 1988. Immunoelectron microscopic localization of small, acid-soluble spore proteins in sporulating cells of Bacillus subtilis. *J Bacteriol*

170:5963–5967.

Frenkiel-Krispin D, Sack R, Englander J, Shimoni E, Eisenstein M, Bullitt E, Horowitz-Scherer R, Hayes CS, Setlow P, Minsky A, Wolf SG. 2004. Structure of the DNA-SspC complex: Implications for DNA packaging, protection, and repair in bacterial spores. *J Bacteriol* **186**:3525–3530. doi:10.1128/JB.186.11.3525-3530.2004

Griffith J, Makhov a, Santiago-Lara L, Setlow P. 1994. Electron microscopic studies of the interaction between a Bacillus subtilis alpha/beta-type small, acid-soluble spore protein with DNA: protein binding is cooperative, stiffens the DNA, and induces negative supercoiling. *Proc Natl Acad Sci U S A* **91**:8224–8228. doi:10.1073/pnas.91.17.8224

Grünewald K, Cyrklaff M. 2006. Structure of complex viruses and virus-infected cells by electron cryo tomography. *Curr Opin Microbiol*. doi:10.1016/j.mib.2006.06.016

Guérout-Fleury AM, Frandsen N, Stragier P. 1996. Plasmids for ectopic integration in Bacillus subtilis. *Gene*. doi:10.1016/S0378-1119(96)00404-0

Higgins D, Dworkin J. 2012. Recent progress in Bacillus subtilis sporulation. *FEMS Microbiol Rev*. doi:10.1111/j.1574-6976.2011.00310.x

Hsiang MW, Cole RD. 1977. Structure of histone H1-DNA complex: Effect of histone H1 on DNA condensation. *Proc Natl Acad Sci U S A*. doi:10.1073/pnas.74.11.4852

Kay D, Warren SC. 1968. Sporulation in Bacillus subtilis. Morphological changes. *Biochem J*. doi:10.1042/bj1090819

Ki SL, Bumbaca D, Kosman J, Setlow P, Jedrzejas MJ. 2008. Structure of a protein-DNA complex essential for DNA protection in spores of Bacillus species. *Proc Natl Acad Sci U S A*. doi:10.1073/pnas.0708244105

Kunst F, Ogasawara N, Moszer I, Albertini AM, Alloni G, Azevedo V, Bertero MG, Bessières P, Bolotin A, Borchert S, Borriss R, Boursier L, Brans A, Braun M, Brignell SC, Bron S, Brouillet S, Bruschi C V., Caldwell B, Capuano V, Carter NM, Choi SK, Codani JJ, Connerton IF, Cummings NJ, Daniel RA, Denizot F, Devine KM, Düsterhöft A, Ehrlich SD, Emmerson PT, Entian KD, Errington J, Fabret C, Ferrari E, Foulger D, Fritz C, Fujita M, Fujita Y, Fuma S, Galizzi A, Galleron N, Ghim SY, Glaser P, Goffeau A, Golightly EJ, Grandi G, Guiseppi G, Guy BJ, Haga K, Haiech J, Harwood CR, Hénaut A, Hilbert H, Holsappel S, Hosono S, Hullo MF, Itaya M, Jones L, Joris B, Karamata D, Kasahara Y, Klaerr-Blanchard M, Klein C, Kobayashi Y, Koetter P, Koningstein G, Krogh S, Kumano M, Kurita K, Lapidus A, Lardinois S, Lauber J, Lazarevic V, Lee SM, Levine A, Liu H, Masuda S, Mauël C, Médigue C, Medina N, Mellado RP, Mizuno M, Moestl D, Nakai S, Noback M, Noone D, O'Reilly M, Ogawa K, Ogiwara A, Oudega B, Park SH, Parro V, Pohl TM, Portetelle D, Porwollik S, Prescott AM, Presecan E, Pujic P, Purnelle B, Rapoport G, Rey M, Reynolds S, Rieger M, Rivolta C, Rocha E, Roche B, Rose M, Sadaie Y, Sato T, Scanlan E, Schleich S, Schroeter R, Scoffone F, Sekiguchi J, Sekowska A, Seror SJ, Serror P, Shin BS, Soldo B, Sorokin A, Tacconi E, Takagi T, Takahashi H, Takemaru K, Takeuchi M, Tamakoshi A, Tanaka T, Terpstra P, Tognoni A, Tosato V, Uchiyama S, Vandenbol M, Vannier F, Vassarotti A, Viari A, Wambutt R, Wedler E, Wedler H, Weitzenegger T, Winters P, Wipat A, Yamamoto H, Yamane K, Yasumoto K, Yata K, Yoshida K, Yoshikawa HF, Zumstein E, Yoshikawa H, Danchin A. 1997. The complete genome sequence of the gram-positive bacterium Bacillus subtilis. *Nature*. doi:10.1038/36786

Lewis PJ, Thaker SD, Errington J. 2000. Compartmentalization of transcription and translation in Bacillus subtilis. *Embo J* **19**:710–718. doi:10.1093/emboj/19.4.710

Lopez-Garrido J, Ojkic N, Khanna K, Wagner FR, Villa E, Endres RG, Pogliano K. 2018. Chromosome Translocation Inflates Bacillus Forespores and Impacts Cellular Morphology. *Cell* **172**:758-770.e14. doi:10.1016/j.cell.2018.01.027

Luef B, Frischkorn KR, Wrighton KC, Holman H-YN, Birarda G, Thomas BC, Singh A, Williams KH, Siegerist CE, Tringe SG, Downing KH, Comolli LR, Banfield JF. 2015. Diverse uncultivated ultra-small bacterial cells in groundwater. *Nat Commun* **6**:6372. doi:10.1038/ncomms7372

Mason JM, Setlow P. 1986. Essential role of small, acid-soluble spore proteins in resistance of Bacillus subtilis spores to UV light. *J Bacteriol*. doi:10.1128/jb.167.1.174-178.1986

Massey TH, Mercogliano CP, Yates J, Sherratt DJ, Löwe J. 2006. Double-Stranded DNA Translocation: Structure and Mechanism of Hexameric FtsK. *Mol Cell*. doi:10.1016/j.molcel.2006.06.019

Pogliano J, Sharp MD, Pogliano K. 2002. Partitioning of chromosomal DNA during establishment of cellular asymmetry in Bacillus subtilis. *J Bacteriol*. doi:10.1128/JB.184.4.1743-1749.2002

Pogliano K, Harry E, Losick R. 1995. Visualization of the subcellular location of sporulation proteins in Bacillus subtilis using immunofluorescence microscopy. *Mol Microbiol* **18**:459–70. doi:10.1111/j.1365-2958.1995.mmi_18030459.x

Regan G, Itaya M, Piggot PJ. 2012. Coupling of σG Activation to Completion of Engulfment during Sporulation of Bacillus subtilis Survives Large Perturbations to DNA Translocation and Replication. *J Bacteriol*. doi:10.1128/JB.01470-12

Ross MA, Setlow P. 2000. The Bacillus subtilis Hbsu protein modifies the effects of α/β-type, small acid-soluble spore proteins on DNA. *J Bacteriol*. doi:10.1128/JB.182.7.1942-1948.2000

Ryter A. 1965. Etude Morphologique de la sporulation de Bacillus Subtilis. *Ann Inst Pasteur (Paris)*.

Schultz S, Shields G, Steitz T. 1991. Crystal structure of a CAP-DNA complex: the DNA is bent by 90 degrees. *Science (80-)*. doi:10.1126/science.1653449

Setlow P. 2007. I will survive: DNA protection in bacterial spores. *Trends Microbiol*. doi:10.1016/j.tim.2007.02.004

Setlow P. 2006. Spores of Bacillus subtilis: Their resistance to and killing by radiation, heat and chemicalsJournal of Applied Microbiology. pp. 514–525. doi:10.1111/j.1365-2672.2005.02736.x

Setlow P. 1995. Mechanisms for the Prevention of Damage to DNA in Spores of Bacillus Species. *Annu Rev Microbiol* **49**:29–54. doi:10.1146/annurev.mi.49.100195.000333

Setlow P. 1994. Mechanisms which contribute to the long-term survival of spores of Bacillus species. *J Appl Bacteriol* **76**:49S-60S. doi:10.1111/j.1365-2672.1994.tb04357.x

Sharp MD, Pogliano K. 1999. An in vivo membrane fusion assay implicates SpoIIIE in the final stages of engulfment during Bacillus subtilis sporulation. *Proc Natl Acad Sci U S A* **96**:14553–14558. doi:10.1073/pnas.96.25.14553

Shin JY, Lopez-Garrido J, Lee SH, Diaz-Celis C, Fleming T, Bustamante C, Pogliano K. 2015. Visualization and functional dissection of coaxial paired SpoIIIE channels across the sporulation septum. *Elife* **4**:22. doi:10.7554/eLife.06474

Stafford RS, Donnellan JE. 1968. Photochemical evidence for conformation changes in DNA during germination of bacterial spores. *Proc Natl Acad Sci U S A*. doi:10.1073/pnas.59.3.822

Tan IS, Ramamurthi KS. 2014. Spore formation in Bacillus subtilis. *Environ Microbiol Rep*. doi:10.1111/1758-2229.12130

Wang F, Liu Y, Su Z, Osinski T, de Oliveira GAP, Conway JF, Schouten S, Krupovic M, Prangishvili D, Egelman EH. 2019. A packing for A-form DNA in an icosahedral virus. *Proc Natl Acad Sci U S A*. doi:10.1073/pnas.1908242116

Webb CD, Teleman A, Gordon S, Straight A, Belmont A, Lin DCH, Grossman AD, Wright A, Losick R. 1997. Bipolar localization of the replication origin regions of chromosomes in vegetative and sporulating cells of B. subtilis. *Cell*. doi:10.1016/S0092-8674(00)81909-1

Wu LJ, Errington J. 1998. Use of asymmetric cell division and spoIIIE mutants to probe chromosome orientation and organization in Bacillus subtilis. *Mol Microbiol*. doi:10.1046/j.1365-2958.1998.00724.x

Wu LJ, Errington J. 1997. Septal localization of the SpoIIIE chromosome partitioning protein in Bacillus subtilis. *EMBO J* **16**:2161–2169. doi:10.1093/emboj/16.8.2161

Wu L J, Errington J. 1994. Bacillus subtilis spoIIIE protein required for DNA segregation during asymmetric cell division. *Science (80-)* **264**:572–575.

Wu Ling Juan, Errington J. 1994. Bacillus subtilis spoIIIE protein required for DNA segregation during asymmetric cell division. *Science (80-)*. doi:10.1126/science.8160014

Youngman P, Perkins JB, Losick R. 1984. A novel method for the rapid cloning in Escherichia coli of Bacillus subtilis chromosomal DNA adjacent to Tn917 insertions. *Mol Gen Genet* **195**:424–33.

5.7 Figures

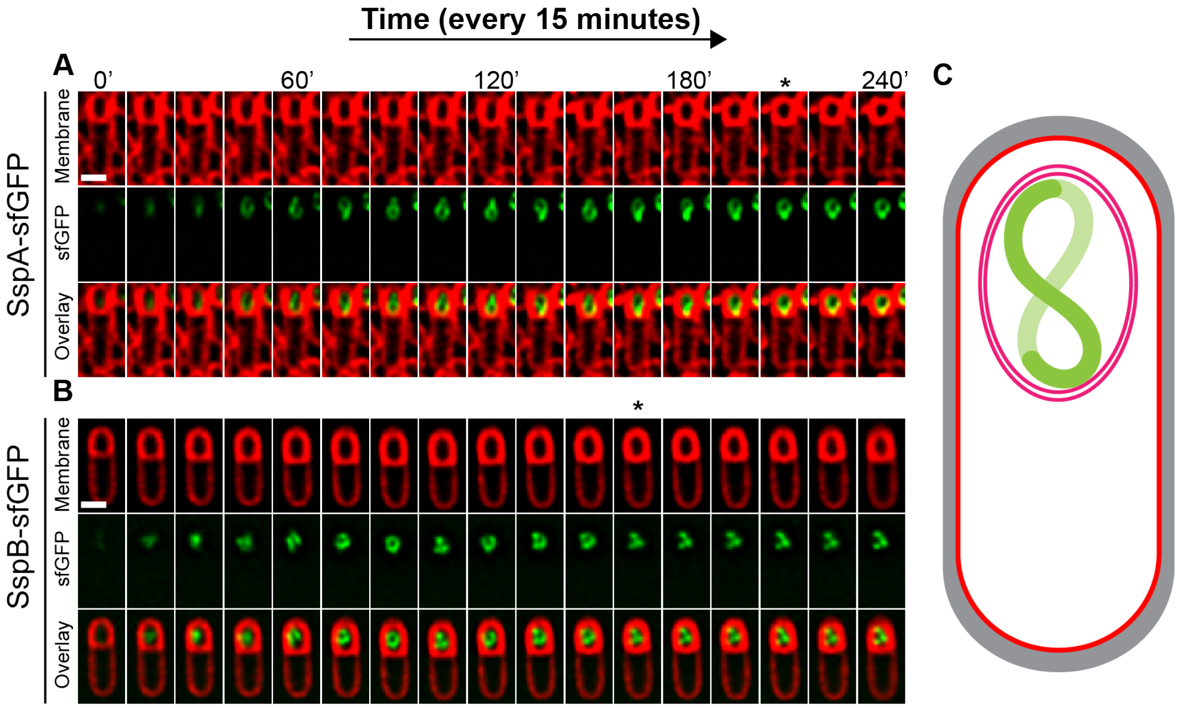

Figure 5.1. α/β-type SASP form twisted toroids in vivo. Timelapse fluorescence microscopy of **(A)** SspA-sfGFP and **(B)** SspB-sfGFP sporangia showing membranes stained with FM4-64 (red) and the sfGFP-tagged proteins, SspA and SspB (green). Time between two consecutive images is 15 minutes and the total time of each series is 2 hours. Astereik indicates the time point at which twisted toroids stop rotating. Scale bar: 1 μm. **(C)** Schematic of twisted toroid formed by SASP in the forespore with the cell wall (grey), mother cell membrane (red), inner and outer forespore membranes (pink) and twisted toroidal arrangement of SASP (green) highlighted.

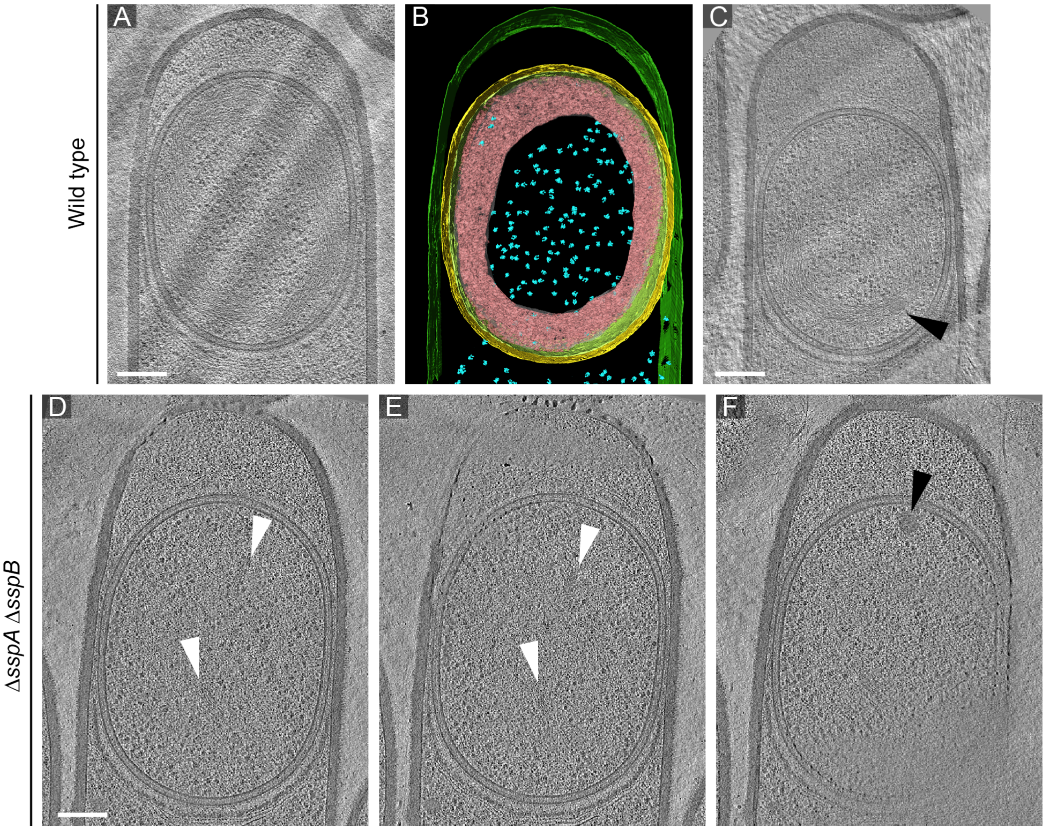

Figure 5.2. SASP-DNA packaging visualized using cryo-FIB-ET. (A) Slice through a tomogram of a wild type sporangium. **(B)** Segmentation of the tomogram shown in (A) with the mother cell membrane (green), the inner forespore membrane (light green), the outer forespore membrane (yellow), ribosomes (blue) and toroidal DNA (pink) highlighted. **(C)** Slice through a tomogram of another wild type sporangium. Black arrow indicates the electron-dense region around which the DNA seems to be wound. Scale bar for (A) and (C): 200 nm. Scale bar has been omitted from (B) owing to its perspective nature. **(D)-(F)** Different slices through the same tomogram of a *sspA sspB* double mutant sporangium. White arrows indicate the small patches of condensed DNA visible in the mutant sporangium and black arrows indicate the electron dense region similar to the one indicated in (C). Scale bars (D) to (F): 200 nm.

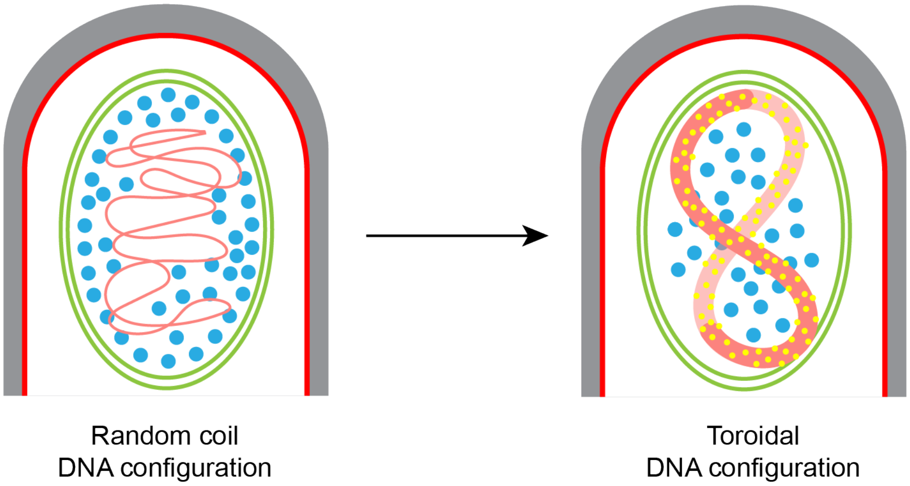

Figure 5.3. Conformational change in SASP-bound DNA. Schematic representing the change in the configuration of the DNA (peach) from random coil state to a twisted toroidal state upon SASP (yellow) binding. Initially, the ribosomes (blue) are distributed throughout the cytoplasm with preferential localization towards the forespore periphery as the DNA occupies a large central volume. Upon SASP binding, the ribosomes localize preferentially to the center of the forespore in the space occluded by the condensed DNA (shown in 3D in peach in the right panel) which localized to the periphery. The cell wall (grey), mother cell membrane (red) and the inner and outer forespore membranes (green) are also highlighted.

5.8 Supplemental Figures

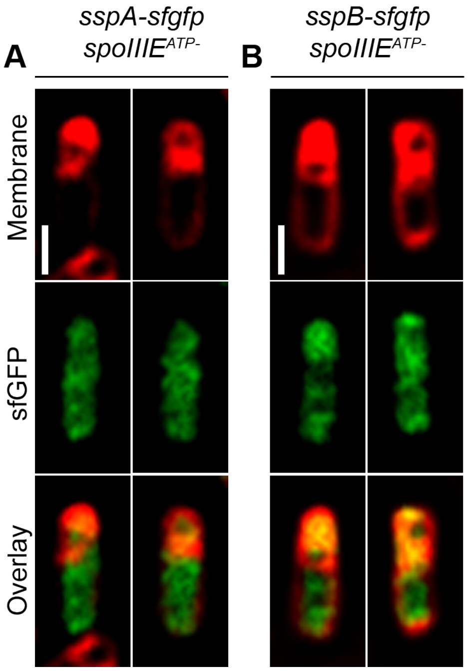

Figure S5.1. Related to Fig. 1. **(A)** & **(B)** In SpoIIIE^{ATP-} sporangia, the forespore DNA remains trapped at the septum such that only one-third of the DNA is present in the forespore and the remaining in the mother cell(Bath et al., 2000; Massey et al., 2006; Ling Juan Wu and Errington, 1994; Wu and Errington, 1998, 1997). As the ATPase activity of SpoIIIE is abolished, it is unable to translocate the rest of the DNA from the mother cell into the forespore and eventually the forespore collapses(Lopez-Garrido et al., 2018). In such cases, σ^G that controls the activation of *sspA* and *sspB* genes encoding α/β-type SASP is not activated in a compartment-specific manner and hence we see diffuse GFP signal (green) for the two proteins in (A) and (B). Membranes are stained with FM4-64. Scale bar: 1 μm.

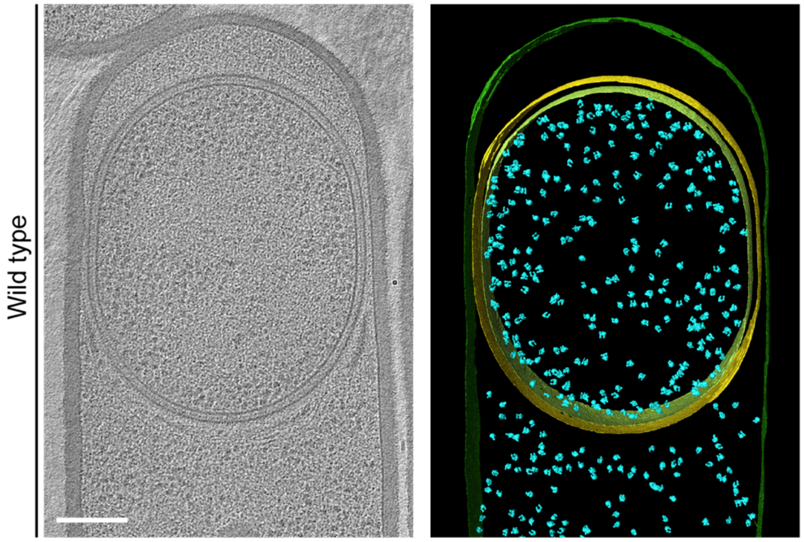

Figure S5.2. Related to Fig. 5.2. (A) Slice through a tomogram of a wild type sporangia wherein the forespore is inside the mother cell but the DNA is not condensed yet. Scale bar: 200 nm. (B) Segmentation of the tomogram in (A) with the mother cell membrane (green), the inner forespore membrane (light green), the outer forespore membrane (yellow) and ribosomes (blue) highlighted.

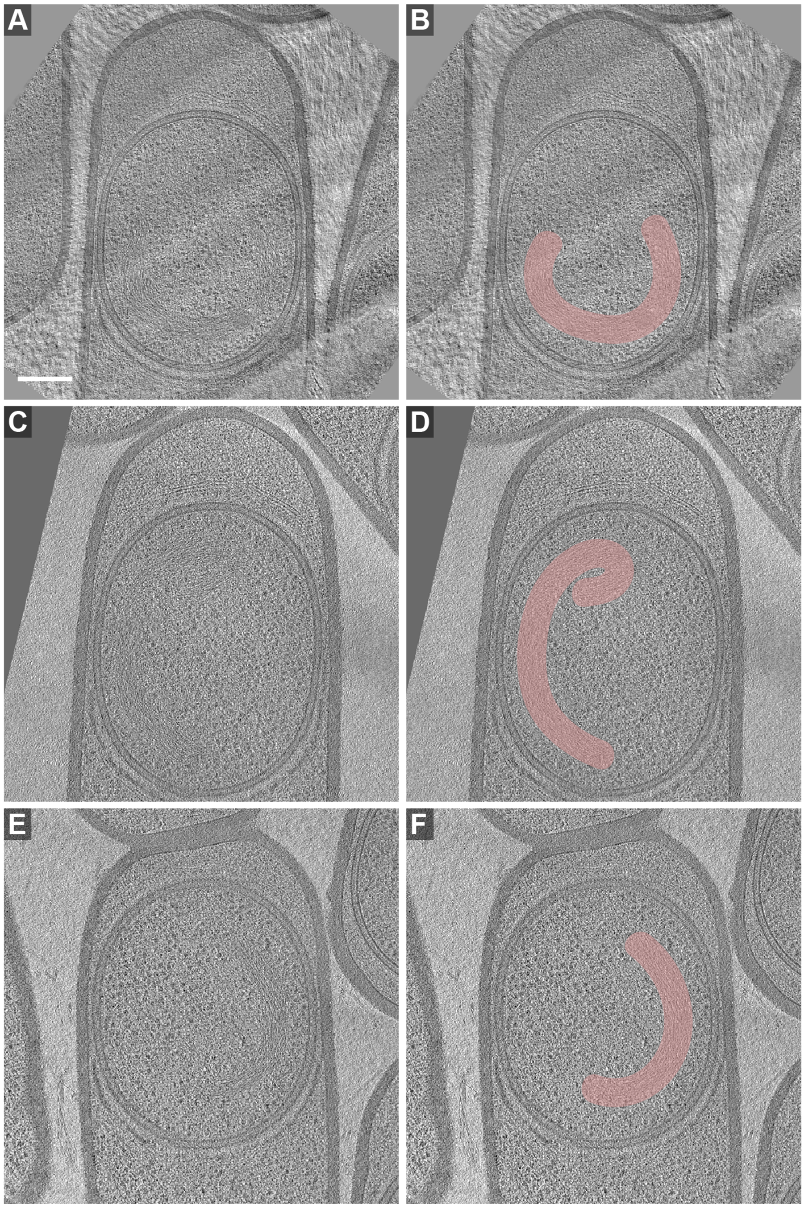

Figure S5.3. Related to Fig. 5.2. Visualized of SASP-bound condensed DNA inside the forespore. (A), (C) & (E) Slices through additional tomograms of wild type sporangia with different orientations in which the condensed DNA has been captured. (B), (D) & (F) Same as (A), (C) & (E) respectively with the condensed DNA traced in peach. Scale bars for (A) to (F): 200 nm.

5.9 Acknowledgements

This work was supported by National Institutes of Health Director’s New Innovator Award 1DP2GM123494 (EV), the National Institutes of Health R01-GM057045 (EV and KP), the National Science Foundation MRI grant (NSF DBI 1920374). This work was performed in part at the San Diego Nanotechnology Infrastructure (SDNI) of UCSD, a member of the National Nanotechnology Coordinated Infrastructure, supported by the NSF grant (ECCS-1542148). We acknowledge the use of the UCSD Cryo-EM Facility which is supported by NIH grants to Dr. Timothy S. Baker and a gift from the Agouron Institute to UCSD. We thank Dr. Kumaran Ramamurthi (NIH) for valuable suggestions on experiments and data.

Chapter 6: Discussion

6.1 Introduction

My thesis aims to elaborate studies of cellular processes in bacteria that have benefitted by the application of cryo-electron tomography (cryo-ET) in complementation with FM, genetics, biochemical techniques and biophysical modeling to provide a comprehensive understanding of cellular processes. In this discussion section, I will first discuss new sample preparation techniques for cryo-ET that have accelerated the pace of discoveries by making suitable thin samples and imaging the target of interest. Then, I will summarize some of the recent studies that have employed these cutting-edge methods to answer intriguing biological questions in bacteria, with a special focus on sporulation in *B. subtilis*, phage infection in bacterial hosts and bacterial cytoskeleton.

6.2 Sample preparation strategies for cryo-ET

Cryo-EM involves the imaging of frozen hydrated specimens preserved in a vitreous, glass-like ice layer in an ultra-high vacuum in a transmission electron microscope (TEM). Cryo-ET is an application of cryo-EM wherein multiple images of the specimen are taken by tilting it with respect to the electron beam which can then be combined to obtain a high resolution (~a few nanometers) 3D view of the specimen (Baumeister, 2002). An image is formed when the electron beam interacts with the specimen that can result in one of three scenarios: (1) the electron passes through the specimen uninterrupted without interacting with any atom, or (2) the electron can be scattered without any loss in energy (elastic scattering), or (3) the electron transfers some of its energy to the specimen (inelastic scattering). The last case contributes to noise in the image which increases with the thickness of the specimen. This becomes a problem especially during acquisition of images at higher tilts in cryo-ET when the thickness of the specimen is effectively greater. These factors limit the imaging of bacterial specimens to slender strains typically < 1 µm in thickness (like *C. crescentus*, *E. coli* and spirochetes).

It is possible to make thinner bacterial samples for higher resolution imaging either prior to or post-vitrification. For the former case, genetic manipulations can be introduced in bacteria to construct slender mutant strains. For instance, minicells (small cells without genomes) in the order of ~500 nm have been generated previously for *E. coli* and *S. enterica* by manipulating genes that result in aberrant cell division events. They have been used in cryo-ET studies of chemoreceptor arrays, flagellar motors, injectisomes, phage-host interactions and cell division (Briegel et al., 2012; Farley et al., 2016; Liu et al., 2012; Szwedziak et al., 2014). In *B. subtilis*, deletion of a gene encoding for a penicillin-binding protein (*ponA*) resulted in thinner cells of ~700 nm that were used to study peptidoglycan remodeling during sporulation (Tocheva et al., 2011). Biochemical modifications to thin specimens prior to freezing include gently lysing the cells using either antibiotic, lysozyme or an inducible phage gene to deplete the cells of their cytoplasm producing ghost cells with intact cell membranes. This approach has been used to study cell membranes and protein complexes embedded in the membranes in their native context (Briegel et al., 2012, 2009; Fu et al., 2014). However, such genetic or biochemical modifications can affect the very process under study, hence distorting the interpretations of the results.

In order to obtain insights unhindered by manipulations to the bacterial specimen prior to vitrification, it is preferable to thin them for cryo-ET post-vitrification. Currently, there are two widely adopted approaches for the same. The first one relies on sectioning the specimen using a cryo-ultramicrotome. However, the method suffers from several drawbacks. It is technically challenging and results in artefacts including knife marks, compressions along the direction of cutting and crevasses perpendicular to it, physically distorting the specimen (Matias et al., 2003; McDowall et al., 1983; Salje et al., 2009). The more recent approach to thin the specimens post-vitrification involves the application of a focused beam of gallium ions to ablate the cellular material from the top and bottom of the specimen, leaving a section of ~100-300 nm of the specimen for cryo-ET data acquisition (Böck et al., 2017; Chaikeeratisak et al., 2019, 2017; Khanna et al., 2018; Lopez-Garrido et al., 2018; Marko et al., 2007; Weiss et al., 2019). This method, known as cryo-

FIB milling provides artefact-free views of the biological specimen, enabling high-resolution structural determination of macromolecules of interest. Recent development of automated pipelines for cryo-FIB milling is also paving way for it to become more routine and high-throughput (Buckley et al., 2019; Zachs et al., 2019).

In spite of these specimen-thinning approaches, it is difficult to unambiguously identify most of the macromolecules of interest from black and white cryo-ET images even where prior knowledge about their feature or localization is available. So far, in situ cryo-ET is limited to larger complexes like ribosomes or those that display a higher-order organization like bacterial secretion systems or cytoskeletal filaments or the more definitive cellular envelope. One way to localize the molecule of interest would be to combine the strengths of two complementary approaches by first visualizing it using FM using genetically encoded fluorophores and then finding its corresponding location in the cells using cryo-EM, a technique referred to as cryo-correlative light and electron microscopy (or cryo-CLEM) which can be especially useful when only few cells express the molecule of interest (Wolff et al., 2016; Zhang, 2013). This step is typically incorporated prior to cryo-FIB milling in the experimental workflow as exposure to electron or ion beam could potentially bleach the fluorophore prior to TEM imaging. For samples that are thinned using cryo-ultramicrotome, however, this step could be incorporated after sectioning and prior to TEM imaging.

Integration of cryo-FM basically involves another transfer step during the imaging pipeline with potential for additional contamination and/or devitrification of specimens. Moreover, due to the very small sizes of bacteria, the level of precision of localization of the fluorescent signal is pretty low. Techniques incorporating super-resolution light microscopy at liquid nitrogen temperatures may hopefully lead to better localization precision in the future (Chang et al., 2014). Another alternative can be do endogenously tag the macromolecule of interest with a label that is easily identifiable in EM images. Resolving different features of interest in cryo-EM images depends on the contrast generated when atoms with different scattering properties interact with the electron beam to generate different intensities. Hence, the tags developed for EM so far have been mostly heavy metal based which are more electron-dense than the background and readily visible in EM images (Bouchet-Marquis et al., 2012; Wang et al., 2011), although an equivalent of a widely applicable endogenous GFP tag for localization of protein complexes using cryo-ET still does not exist. Recently, a promising progress made in the direction came in the form of a genetically encoded label corresponding to iron loaded ferritin FtnA protein of *E. coli* (Wang et al., 2011). As a test, ferritin tag was fused to bacterial proteins with known subcellular locations as well as GFP for localization in both FM and EM simultaneously. For instance, when tagged to a cell division protein or a protein of the chemotaxis system, the label localized to the division septum or the cell pole respectively, with the same localization pattern as observed with FM (Wang et al., 2011). However, the large size (~12 nm diameter) and the multivalent nature of ferritin particles can potentially affect the localization pattern and/or the structure of the macromolecule of interest. Hence, the tag may not be suitable for all complexes/model systems. Moreover, to visualize iron loaded FtnA molecules, cells have to be grown in the presence of iron which can be toxic, further limiting the applicability of this tag.

6.3 Phage-host interaction

Bacteriophages (or phages) are perhaps one of the most abundant entities in the biosphere and carry out important ecological roles by influencing the genomes of the bacteria they infect and have also been implicated in the evolution of pathogenic bacteria (Clokie et al., 2011). Recently, there has been a renewed interest in phages as they can be an alternative to antibiotics to treat multi-drug resistant bacterial infections, a concept referred to as phage therapy (Dedrick et al., 2019). Phages are extremely small entities with size ranging from 25-200 nm and hence cryo-ET is a viable technique to study spatiotemporal regulation of host infection by phages in native context due to the high resolution offered by the method in comparison to other microscopy techniques.

The first study to employ cryo-ET to study phage-host interaction involved an in vitro reconstitution system to decipher the mechanism of the interaction of T5 phages and its *E. coli* receptor FhuA contained in a proteoliposome (Böhm et al., 2001). At that time, the widespread belief in the field was that the viral DNA is transferred to the bacterial host via diffusion through the FhuA channel. However, Bohm et al. demonstrated that the tip of the phage tail undergoes a conformational change when it contacts FhuA and shrinks in length, acting like an "injection needle" to transfer the viral DNA to the host (Böhm et al., 2001). Subsequent cryo-ET studies of phage infection in the naturally slender *Prochlorococcus marinus* and *E. coli* minicells further revealed more details about the mechanism of DNA injection into the hosts (Liu et al., 2011, 2010). These studies demonstrated the distinct mechanisms of structural alterations that different phages deploy to trigger the release of their genome into the respective host. Another cryo-ET study combined elegant microbiological assays to determine the mechanism of infection of *C. crescentus Siphoviridae* phages that have an elongated head (60 nm in diameter and 200 nm in length) and a large genome (>200 kb) (Guerrero-Ferreira et al., 2011). The work showed that these phages use their head filament to attach to the bacterial flagella and subsequent flagellar rotation allows the phage tails to irreversibly contact the bacterial cell surface on pili portals to release their genome.

More recently, integration of newer optics and sample thinning strategies have enabled visualization of phage replication inside their bacterial hosts. Dai et al. imaged the maturation process of a dsDNA cyanophage Syn5 inside *Synechococcus* in a TEM equipped with a Zernike phase plate (Dai et al., 2013). A phase plate is essentially a thin film of carbon placed in the back focal plane of the objective lens with a small central aperture that is able to recover some of the low spatial frequencies, enhancing the image contrast compared to conventional TEM images (Danev and Baumeister, 2017). This was the first study that described the structural features of different intermediates in viral assembly inside its host using in situ cryo-ET. We recently studied the mechanism of replication of jumbo phages in *Pseuodomonas* by combining cryo-FIB milling to cryo-ET workflow coupled with genetics and fluorescence microscopy. These complementary cell biological studies revealed that jumbo phages belonging to phiKZ family enclose their genome in a protein shell that functionally resembles a eukaryotic nucleus, with DNA replication and transcription localized inside the shell and DNA translation outside in the cytoplasm (Chaikeeratisak et al., 2017; Erb et al., 2014; Kraemer et al., 2012). Further, these phages encode a tubulin-based spindle and the capsids traffic along these filaments to the phage nucleus for DNA packaging (Chaikeeratisak et al., 2019). Cryo-FIB-ET also enabled visualization of different assembly intermediates and their structural features at a high-resolution inside *Pseudomonas* as they replicate, from the formation of capsids near the cytoplasmic cell membrane to fully assembled phages with their tails.

We anticipate that future studies aimed at integrating structural biology approaches with cell biological studies will further propel the field toward a mechanistic understanding of phage-host interactions and replication of phages inside the bacterial cells, helping us to understand how phages are able to evade and evolve newer mechanisms to fight host defense machinery and how we can use harness their power to treat multi-drug resistant bacteria.

6.4 Bacterial sporulation

Sporulation is a unique developmental pathway in many Gram-positive bacteria belonging to the phylum Firmicutes (or genera *Bacillus* and *Clostridium*) that results in the production of tough, hardy and resilient endospores (Higgins and Dworkin, 2012; Tan and Ramamurthi, 2014). The pathway is triggered in starvation conditions and is used as a survival strategy by bacteria to stay dormant until the conditions in the environment become favorable again. Sporulation begins with the formation of a septum closer to the cell pole, dividing the cell into two unequal parts – the smaller forespore and the larger mother cell. The septum then curves towards the mother cell and eventually the mother cell membrane migrates forward to engulf the forespore. The migration of the mother cell membrane is mediated by coordinated degradation and synthesis of the cell wall peptidoglycan (PG) at the leading edge by SpoIIDMP (or DMP) complex and PG synthases respectively (Khanna et al., 2018; Ojkic et al., 2016). Upon polar septum formation, the forespore DNA remains trapped at the septum such that only 1/3rd of the DNA is present inside the forespore. SpoIIIE, an ATP-dependent DNA translocase then subsequently transports the remaining 2/3rd of the DNA from the mother cell to the forespore as engulfment proceeds (Wu and Errington, 1997, 1994). Once the forespore is completely inside the mother cell, protective layers of coat and cortex form around the forespore. Ultimately, the mature endospore is released to the environment upon mother cell lysis.

Bacterial spores have been the subject of electron microscopy since the mid twentieth century when researchers started to visualize the beautiful concentric layers of the coat and cortex surrounding the dormant endospores (Ryter, 1965). These methods relied on imaging ultrathin sections of several species involving dehydration, chemical fixation etc. that can introduce artefacts and destroy many of the macromolecular structures. For instance, many researchers visualized structures called “mesosomes” in thin sections of *Bacillus* species which appeared close to the cytoplasmic membrane as invaginations and were thought to be involved in septum formation and engulfment during membrane migration (FITZ-JAMES, 1960). However, later on it was shown that mesosomes were artifacts formed due to chemical fixatives used for traditional EM sample preparation as they were not detected in cells processed using cryofixation and freeze substitution methods that preserve the native cellular structures (Ebersold et al., 1981).

B. subtilis has been the model organism of choice to study sporulation as its natural competency facilitated its genetic and biochemical characterization although they were excluded from high resolution cryo-ET for a long time due to their thickness. The Jensen lab first used cryo-ET to study sporulation in a slender Gram-negative bacterium, *Acetonema longum*, part of the lesser-known family of *Clostridia* (Tocheva et al., 2011). Tocheva et al. imaged different stages of spore formation in *A. longum* cells using cryo-ET. Based on previous thin-section EM images of sporulating Gram-positive cells, it was previously thought that the peptidoglycan (PG) present between the septum was completely degraded starting from the middle of the septum by the DMP degradation machinery and a new PG is synthesized during cortex formation (Illing and Errington, 1991). However, cryo-ET images of *A. longum* cells suggested that a thin layer of PG persisted throughout engulfment and that it is remodeled to produce cortex during spore maturation (Tocheva et al., 2011). Similar observations regarding PG remodeling were obtained later with cryo-ET images of sporulating *B. subtilis* cells which were made thin for cryo-ET by deleting a *ponA* gene encoding for a penicillin-binding protein and later for wild type (Lopez-Garrido et al., 2018; Tocheva et al., 2013). Combined with optical microscopy and bioinformatics, the authors proposed a theory for the evolution of Gram-negative bacteria. Their data suggested that the cytoplasmic mother cell membrane (or the outer forespore membrane) that surrounds the forespore in *B. subtilis* is degraded upon germination to morph into a Gram-positive bacterium whereas in *A. longum*, it is retained and remodeled into the outer membrane of a Gram-negative bacterium (Tocheva et al., 2016, 2011). The authors propose the idea that it is possible that at some point in evolution, certain spore-formers may have retained their outer forespore membrane during germination that gave way to the formation of Gram-negative bacteria.

More recently, we used cryo-FIB milling to visualize wild type *B. subtilis* during different stages of engulfment (Khanna et al., 2019; Lopez-Garrido et al., 2018). In complementation with genetics, light microscopy and biophysical modeling, we suggested the first mechanistic model of engulfment during sporulation. First, our data provided evidence that during translocation of the chromosome from the mother cell to the forespore increases the turgor pressure in the forespore, stretching the septal PG and reshaping the forespore during engulfment (Lopez-Garrido et al., 2018). Second, the septum is homogenously and only slightly thinned when it transitions from flat to curved state which can be attributed to the increased turgor pressure in the forespore upon chromosome translocation (Khanna et al., 2019). Third, the mother cell migrates around the forespore in tiny finger-like projections which are caused due to uneven degradation of the PG by limited number of DMP complexes, resulting in an irregular membrane front (Khanna et al., 2019).

Together, cryo-ET data has significantly advanced our understanding of PG remodeling during an important evolutionary process of sporulation in bacteria.

6.5 Bacterial cytoskeleton

For a long time, the absence of cytoskeletal filaments in prokaryotes was thought of as one of the major elements distinguishing them from eukaryotes as these structures were not seen in EM images of thin-section bacterial specimens prepared using chemical fixatives, heavy metal stains or plastic-embedding. Likely these structures were not preserved when bacterial specimens were subjected to such harsh treatments. However, freeze-substitution and vitrification lead to better preservation of structural features and consequently, cytoskeletal filaments mediating different cellular processes including cell division, elongation and plasmid segragation could be detected in bacteria prepared using these approaches.

FtsZ, a bacterial tubulin homolog is the major cell division protein in almost all bacteria and forms a ring-like structure at the division site, called the Z-ring (Errington et al., 2003; Haeusser and Margolin, 2016). The Z-ring then acts as a scaffold to recruit other cell division proteins to promote its interaction to the membrane and synthesize septal PG. However, the molecular organization of the Z-ring and the mechanism by which the Z-ring mediates the constriction of the membrane is still a matter of debate. Li et al. first visualized FtsZ filaments using cryo-ET in *C. crescentus* as a series of few short arcs (~100 nm) placed arbitrary near the division site (Li et al., 2007). Although, widefield microscopy at that time suggested that the Z-ring formed a continuous band at the septum, super resolution microscopy studies later suggested that the Z-ring is patchy with holes that corresponded to gaps in the ring. Szwedziak et al. later imaged dividing *C. crescentu*s and *E. coli* minicells using TEM instruments equipped with better cameras and the higher-quality images suggested that the Z-rings were mostly continuous for both cell types (Szwedziak et al., 2014). Our cryo-FIB-ET data for dividing *B. subtilis* cells also demonstrate the continuity of the Z-rings. In addition, we also see rings formed by FtsA filaments in *B. subtilis* which were not previously seen in cryo-ET images of the Gram-negative bacteria and could be a consequence of thicker septal PG in *B. subtilis* that requires the scaffolding action of multiple FtsA and FtsZ filaments for constriction of the septum. Also, our data suggest a fundamental difference in the organization of FtsZ filaments during vegetative growth and sporulation. In the former case, FtsZ filaments are present uniformly along the leading edge of the invaginating septum whereas during sporulation, they are only present on the mother cell side. We further showed that a sporulation specific protein SpoIIE that localizes only on the forespore side of the septum restricts the assembly of the divisome to only one side by potentially competing with FtsA and other cell division proteins to bind the Z-ring on the forespore side and in the process dismantling the constriction machinery on that side. This is the first evidence to date in bacteria wherein the polar distribution of a cell fate determinant (SpoIIE) results in the asymmetric localization of the divisome and hence production of cell types with diverse fates.

Cryo-ET studies have also shed light on the architecture of MreB, actin-like filaments involved in maintenance of bacterial cell shape. Based on light microscopy data, MreB was thought to polymerize into long helical filaments in the cytoplasm of many rod-shaped bacteria (Jones et al., 2001). However, cryo-CLEM data suggested that these helices were likely a result of overexpression of MreB due to the N-terminal YFP tag as no helices were observed upon removal of the tag (Swulius and Jensen, 2012). This is also in agreement with recent TIRF microscopy data demonstrating that MreB filaments organize as small patches that move around the circumference of the cell (Domínguez-Escobar et al., 2011).

Several other bacterial filaments have been characterized using cryo-ET and complementary genetic and biochemical studies. The metabolic enzyme CTP synthase CtpS in *C. crescentus* was observed as bundles of filament that interact with an intermediate filament homolog crescentin to regulate cellular curvature (Briegel et al., 2006; Ingerson-Mahar et al., 2010). In vitro and in vivo studies have also shed light on the structure and arrangement of ParM filaments in *E. coli* that are involved in segregating low copy number plasmid R1 by forming a bipolar spindle (Bharat et al., 2015). The actin homolog MamK found in magnetotactic bacteria *Magnetospirillum* forms polar, double-helical filaments that flanks subcellular organelles containing magnetite crystals called magentosomes which in turn are responsible for navigating these bacteria along magnetic field (Komeili et al., 2006; Scheffel et al., 2006). Further studies have identified regulators of the dynamic behavior of MamK and how MamK filaments are remodeled spatiotemporally during cytokinesis, opening up doors for some interesting cell biology in so-called “non-model model organisms” (Draper et al., 2011; Katzmann et al., 2011).

6.6 Multicellularity in bacteria

Recently, cryo-EM modalities have also shed light on decoding principles that govern multicellular behavior in bacteria including *Streptomyces* and *Anabaena* (Celler et al., 2016; Weiss et al., 2019). *Streptomyces* are filamentous bacteria and one of the major sources of natural products including antibiotics and other bioactive compounds. Once germinated, they grow as a complex branched network of hyphae separated by peptidoglycan-based septa or cross-walls. However, the cross-walls are spaced several micrometers apart, hence Celler et al. suspected an alternative mechanism that Streptomyces may use to achieve effective compartmentalization during their life cycle. The authors elegantly used cryo-CLEM and found that the mycelium is compartmentalized by the formation of small membrane vesicles between the cell wall and cytoplasmic membrane, termed as cross-membranes delimiting the hyphae (Celler et al., 2016). Their FRAP experiments also suggested that about one-third of the cross-membranes are protein-impermeable acting as physical barriers between adjacent compartments. In another study, Weiss et al. studied the in situ structure of septal junctions in the filamentous multicellular cyanobacteria, *Anabaena* using cryo-FIB-ET (Weiss et al., 2019). Conventional EM methods revealed the presence of small pores or septal junctions traversing the septum that contains a PG disc surrounded by two cytoplasmic membranes which were thought to be critical for cell-cell communication. Cryo-FIB-ET images suggested that these pores were organized as tubes traversing the septal PG covered by a cytoplasmic cap and a plug-like density appeared in the cytoplasmic membrane. Subtomogram averaging of septal junctions in wild type and strains mutant in different proteins involved in septal junction assembly suggested that these display mechanistic analogy to metazoan gap junctions in that they are gated channels that reversibly block intercellular diffusion of molecules under different stress conditions (Weiss et al., 2019). In combination with FRAP experiments, the authors suggested that the intercellular communication was blocked under stress and the conformational change in the cytoplasmic cap regulated the gating of the channel. Hopefully, future studies in understanding the molecular architecture of multicellular behavior in bacteria will provide a deeper understanding about evolution of cell differentiation, cell-cell signaling and multicellularity in animals.

6.7 Concluding remarks

I have highlighted some of the most prominent studies that use novel cryo-ET modalities as a cell biological tool in combination with genetics, light microscopy, biochemistry and biophysics to understand the cellular process in bacteria at molecular resolution in the native context. With the advent of other novel modalities in the field, we anticipate we will dive deeper into the unknown world of bacteria and even smaller entities like viruses which have been precluded from high-resolution imaging so far.

6.8 References

Abbe E. 1873. Beiträge zur Theorie des Mikroskops und der mikroskopischen Wahrnehmung. *Arch für Mikroskopische Anat*. doi:10.1007/bf02956173

Baddeley D, Bewersdorf J. 2018. Biological Insight from Super-Resolution Microscopy: What We Can Learn from Localization-Based Images. *Annu Rev Biochem*. doi:10.1146/annurev-biochem-060815-014801

Bai X chen, McMullan G, Scheres SHW. 2015. How cryo-EM is revolutionizing structural biology. *Trends Biochem Sci*. doi:10.1016/j.tibs.2014.10.005

Baumeister W. 2002. Electron tomography: Towards visualizing the molecular organization of the cytoplasm. *Curr Opin Struct Biol*. doi:10.1016/S0959-440X(02)00378-0

Beveridge TJ. 1999. Structures of gram-negative cell walls and their derived membrane vesicles. *J Bacteriol*.

Beveridge TJ, Graham LL. 1991. Surface layers of bacteria. *Microbiol Rev* **55**:684–705.

Bharat TAM, Murshudov GN, Sachse C, Löwe J. 2015. Structures of actin-like ParM filaments show architecture of plasmid-segregating spindles. *Nature*. doi:10.1038/nature14356

Böck D, Medeiros JM, Tsao HF, Penz T, Weiss GL, Aistleitner K, Horn M, Pilhofer M. 2017. In situ architecture, function, and evolution of a contractile injection system. *Science (80-)*. doi:10.1126/science.aan7904

Böhm J, Lambert O, Frangakis AS, Letellier L, Baumeister W, Rigaud JL. 2001. FhuA-mediated phage genome transfer into liposomes: A cryo-electron tomography study. *Curr Biol*. doi:10.1016/S0960-9822(01)00349-9

Bouchet-Marquis C, Pagratis M, Kirmse R, Hoenger A. 2012. Metallothionein as a clonable high-density marker for cryo-electron microscopy. *J Struct Biol*. doi:10.1016/j.jsb.2011.10.007

Briegel A, Dias DP, Li Z, Jensen RB, Frangakis AS, Jensen GJ. 2006. Multiple large filament bundles observed in Caulobacter crescentus by electron cryotomography. *Mol Microbiol*. doi:10.1111/j.1365-2958.2006.05355.x

Briegel A, Li X, Bilwes AM, Hughes KT, Jensen GJ, Crane BR. 2012. Bacterial chemoreceptor arrays are hexagonally packed trimers of receptor dimers networked by rings of kinase and coupling proteins. *Proc Natl Acad Sci U S A*. doi:10.1073/pnas.1115719109

Briegel A, Ortega DR, Tocheva EI, Wuichet K, Zhuo L, Songye C, Müller A, Iancu C V., Murphy GE, Dobro MJ, Zhulin IB, Jensen GJ. 2009. Universal architecture of bacterial chemoreceptor arrays. *Proc Natl Acad Sci U S A*. doi:10.1073/pnas.0905181106

Briggs JAG. 2013. Structural biology in situ - the potential of subtomogram averaging. *Curr Opin Struct Biol* **23**:261–267. doi:10.1016/j.sbi.2013.02.003

Buckley G, Gervinskas G, Venugopal H, Taveneau C, Whisstock JC, de Marco A. 2019. Automated cryo-lamella preparation for high-throughput in-situ structural biology. *bioRxiv*.

doi:10.1101/797506

Celler K, Koning RI, Willemse J, Koster AJ, Van Wezel GP. 2016. Cross-membranes orchestrate compartmentalization and morphogenesis in Streptomyces. *Nat Commun*. doi:10.1038/ncomms11836

Chaikeeratisak V, Khanna K, Nguyen KT, Sugie J, Egan ME, Erb ML, Vavilina A, Nonejuie P, Nieweglowska E, Pogliano K, Agard DA, Villa E, Pogliano J. 2019. Viral Capsid Trafficking along Treadmilling Tubulin Filaments in Bacteria. *Cell* **177**:1771-1780.e12. doi:10.1016/J.CELL.2019.05.032

Chaikeeratisak V, Nguyen K, Khanna K, Brilot AF, Erb ML, Coker JKC, Vavilina A, Newton GL, Buschauer R, Pogliano K, Villa E, Agard DA, Pogliano J. 2017. Assembly of a nucleus-like structure during viral replication in bacteria. *Science (80-)* **355**:194–197. doi:10.1126/science.aal2130

Chang YW, Chen S, Tocheva EI, Treuner-Lange A, Löbach S, Søgaard-Andersen L, Jensen GJ. 2014. Correlated cryogenic photoactivated localization microscopy and cryo-electron tomography. *Nat Methods*. doi:10.1038/nmeth.2961

Clokie MRJ, Millard AD, Letarov A V., Heaphy S. 2011. Phages in nature. *Bacteriophage*. doi:10.4161/bact.1.1.14942

Dai W, Fu C, Raytcheva D, Flanagan J, Khant HA, Liu X, Rochat RH, Haase-Pettingell C, Piret J, Ludtke SJ, Nagayama K, Schmid MF, King JA, Chiu W. 2013. Visualizing virus assembly intermediates inside marine cyanobacteria. *Nature*. doi:10.1038/nature12604

Danev R, Baumeister W. 2017. Expanding the boundaries of cryo-EM with phase plates. *Curr Opin Struct Biol*. doi:10.1016/j.sbi.2017.06.006

Dedrick RM, Guerrero-Bustamante CA, Garlena RA, Russell DA, Ford K, Harris K, Gilmour KC, Soothill J, Jacobs-Sera D, Schooley RT, Hatfull GF, Spencer H. 2019. Engineered bacteriophages for treatment of a patient with a disseminated drug-resistant Mycobacterium abscessus. *Nat Med*. doi:10.1038/s41591-019-0437-z

Domínguez-Escobar J, Chastanet A, Crevenna AH, Fromion V, Wedlich-Söldner R, Carballido-López R. 2011. Processive movement of MreB-associated cell wall biosynthetic complexes in bacteria. *Science (80-)*. doi:10.1126/science.1203466

Draper O, Byrne ME, Li Z, Keyhani S, Barrozo JC, Jensen G, Komeili A. 2011. MamK, a bacterial actin, forms dynamic filaments in vivo that are regulated by the acidic proteins MamJ and LimJ. *Mol Microbiol*. doi:10.1111/j.1365-2958.2011.07815.x

Ebersold HR, Cordier JL, Lüthy P. 1981. Bacterial mesosomes: Method dependent artifacts. *Arch Microbiol*. doi:10.1007/BF00527066

Erb ML, Kraemer JA, Coker JKC, Chaikeeratisak V, Nonejuie P, Agard DA, Pogliano J. 2014. A bacteriophage tubulin harnesses dynamic instability to center DNA in infected cells. *Elife*. doi:10.7554/elife.03197

Errington J, Daniel RA, Scheffers DJ. 2003. Cytokinesis in bacteria. *Microbiol Mol Biol Rev* **67**:52-

+. doi:10.1128/mmbr.67.1.52-65.2003

Farley MM, Hu B, Margolin W, Liu J. 2016. Minicells, back in fashion. *J Bacteriol*. doi:10.1128/JB.00901-15

FITZ-JAMES PC. 1960. Participation of the cytoplasmic membrane in the growth and spore fromation of bacilli. *J Biophys Biochem Cytol*. doi:10.1083/jcb.8.2.507

Fu X, Himes BA, Ke D, Rice WJ, Ning J, Zhang P. 2014. Controlled bacterial lysis for electron tomography of native cell membranes. *Structure*. doi:10.1016/j.str.2014.09.017

Fu X, Shih YL, Zhang Y, Rothfield LI. 2001. The MinE ring required for proper placement of the division site is a mobile structure that changes its cellular location during the Escherichia coli division cycle. *Proc Natl Acad Sci U S A*. doi:10.1073/pnas.98.3.980

Guerrero-Ferreira RC, Viollier PH, Ely B, Poindexter JS, Georgieva M, Jensen GJ, Wright ER. 2011. Alternative mechanism for bacteriophage adsorption to the motile bacterium Caulobacter crescentus. *Proc Natl Acad Sci U S A*. doi:10.1073/pnas.1012388108

Haeusser DP, Margolin W. 2016. Splitsville: Structural and functional insights into the dynamic bacterial Z ring. *Nat Rev Microbiol*. doi:10.1038/nrmicro.2016.26

Higgins D, Dworkin J. 2012. Recent progress in Bacillus subtilis sporulation. *Fems Microbiol Rev* **36**:131–148. doi:10.1111/j.1574-6976.2011.00310.x

Illing N, Errington J. 1991. Genetic regulation of morphogenesis in Bacillus subtilis: Roles of σ(E) and σ(F) in prespore engulfment. *J Bacteriol* **173**:3159–3169.

Ingerson-Mahar M, Briegel A, Werner JN, Jensen GJ, Gitai Z. 2010. The metabolic enzyme CTP synthase forms cytoskeletal filaments. *Nat Cell Biol*. doi:10.1038/ncb2087

Jones LJF, Carballido-López R, Errington J. 2001. Control of cell shape in bacteria: Helical, actin-like filaments in Bacillus subtilis. *Cell*. doi:10.1016/S0092-8674(01)00287-2

Jonson AB, Normark S, Rhen M. 2005. Fimbriae, pili, flagella and bacterial virulence. *Contrib Microbiol*. doi:10.1159/000081690

Katzmann E, Müller FD, Lang C, Messerer M, Winklhofer M, Plitzko JM, Schüler D. 2011. Magnetosome chains are recruited to cellular division sites and split by asymmetric septation. *Mol Microbiol*. doi:10.1111/j.1365-2958.2011.07874.x

Khanna K, Lopez-Garrido J, Zhao Z, Watanabe R, Yuan Y, Pogliano K, Villa E. 2018. The molecular architecture of engulfment during Bacillus subtilis sporulation. *bioRxiv*. doi:10.1101/498220

Khanna K, Lopez-Garrido J, Zhao Z, Watanabe R, Yuan Y, Sugie J, Pogliano K, Villa E. 2019. The molecular architecture of engulfment during Bacillus subtilis sporulation. *Elife*. doi:10.7554/eLife.45257

Komeili A, Li Z, Newman DK, Jensen GJ. 2006. Magnetosomes are cell membrane imaginations organized by the actin-like protein MamK. *Science (80-)*. doi:10.1126/science.1123231

Kraemer JA, Erb ML, Waddling CA, Montabana EA, Zehr EA, Wang H, Nguyen K, Pham DSL, Agard DA, Pogliano J. 2012. A phage tubulin assembles dynamic filaments by an atypical mechanism to center viral DNA within the host cell. *Cell*. doi:10.1016/j.cell.2012.04.034

Lawn AM. 1967. Simple immunological labelling method for electron microscopy and its application to the study of filamentous appendages of bacteria [45]. *Nature*. doi:10.1038/2141151a0

Li Z, Trimble MJ, Brun Y V., Jensen GJ. 2007. The structure of FtsZ filaments in vivo suggests a force-generating role in cell division. *EMBO J* **26**:4694–4708. doi:10.1038/sj.emboj.7601895

Liu J, Chen CY, Shiomi D, Niki H, Margolin W. 2011. Visualization of bacteriophage P1 infection by cryo-electron tomography of tiny Escherichia coli. *Virology*. doi:10.1016/j.virol.2011.06.005

Liu J, Hu B, Morado DR, Jani S, Manson MD, Margolin W. 2012. Molecular architecture of chemoreceptor arrays revealed by cryoelectron tomography of Escherichia coli minicells. *Proc Natl Acad Sci U S A*. doi:10.1073/pnas.1200781109

Liu X, Zhang Q, Murata K, Baker ML, Sullivan MB, Fu C, Dougherty MT, Schmid MF, Osburne MS, Chisholm SW, Chiu W. 2010. Structural changes in a marine podovirus associated with release of its genome into Prochlorococcus. *Nat Struct Mol Biol*. doi:10.1038/nsmb.1823

Lopez-Garrido J, Ojkic N, Khanna K, Wagner FR, Villa E, Endres RG, Pogliano K. 2018. Chromosome Translocation Inflates Bacillus Forespores and Impacts Cellular Morphology. *Cell* **172**:758-770.e14. doi:10.1016/j.cell.2018.01.027

Marko M, Hsieh C, Schalek R, Frank J, Mannella C. 2007. Focused-ion-beam thinning of frozen-hydrated biological specimens for cryo-electron microscopy. *Nat Methods* **4**:215–217. doi:10.1038/nmeth1014

Matias VRF, Al-Amoudi A, Dubochet J, Beveridge TJ. 2003. Cryo-transmission electron microscopy of frozen-hydrated sections of Escherichia coli and Pseudomonas aeruginosa. *J Bacteriol*. doi:10.1128/JB.185.20.6112-6118.2003

McDowall AW, Chang J -J, Freeman R, Lepault J, Walter CA, Dubochet J. 1983. Electron microscopy of frozen hydrated sections of vitreous ice and vitrified biological samples. *J Microsc*. doi:10.1111/j.1365-2818.1983.tb04225.x

Milne JLS, Subramaniam S. 2009. Cryo-electron tomography of bacteria: Progress, challenges and future prospects. *Nat Rev Microbiol*. doi:10.1038/nrmicro2183

Ojkic N, Lopez-Garrido J, Pogliano K, Endres RG. 2016. Cell-wall remodeling drives engulfment during Bacillus subtiliss porulation. *Elife* **5**:30. doi:10.7554/eLife.18657

Rudner DZ, Losick R. 2010. Protein subcellular localization in bacteria. *Cold Spring Harb Perspect Biol*. doi:10.1101/cshperspect.a000307

Ryter A. 1965. Etude Morphologique de la sporulation de Bacillus Subtilis. *Ann Inst Pasteur (Paris)*.

Salje J, Zuber B, Löwe J. 2009. Electron cryomicroscopy of E. coli reveals filament bundles involved in plasmid DNA segregation. *Science (80-)*. doi:10.1126/science.1164346

Scheffel A, Gruska M, Faivre D, Linaroudis A, Plitzko JM, Schüler D. 2006. An acidic protein aligns magnetosomes along a filamentous structure in magnetotactic bacteria. *Nature*. doi:10.1038/nature04382

Southward CM, Surette MG. 2002. The dynamic microbe: Green fluorescent protein brings bacteria to light. *Mol Microbiol*. doi:10.1046/j.1365-2958.2002.03089.x

Swulius MT, Jensen GJ. 2012. The helical mreb cytoskeleton in Escherichia coli MC1000/pLE7 is an artifact of the N-terminal yellow fluorescent protein tag. *J Bacteriol*. doi:10.1128/JB.00505-12

Szwedziak P, Wang Q, Bharat TAM, Tsim M, Lowe J. 2014. Architecture of the ring formed by the tubulin homologue FtsZ in bacterial cell division. *Elife* **3**:52. doi:10.7554/eLife.04601

Tan IS, Ramamurthi KS. 2014. Spore formation in Bacillus subtilis. *Environ Microbiol Rep*. doi:10.1111/1758-2229.12130

THORNLEY MJ, HORNE RW. 1962. Electron microscope observations on the structure of fimbriae, with particular reference to Klebsiella strains, by the use of the negative staining technique. *J Gen Microbiol*. doi:10.1099/00221287-28-1-51

Tocheva EI, Lopez-Garrido J, Hughes H V, Fredlund J, Kuru E, VanNieuwenhze MS, Brun Y V, Pogliano K, Jensen GJ. 2013. Peptidoglycan transformations during Bacillus subtilis sporulation. *Mol Microbiol* **88**:673–686. doi:10.1111/mmi.12201

Tocheva EI, Matson EG, Morris DM, Moussavi F, Leadbetter JR, Jensen GJ. 2011. Peptidoglycan remodeling and conversion of an inner membrane into an outer membrane during sporulation. *Cell* **146**:799–812. doi:10.1016/j.cell.2011.07.029

Tocheva EI, Ortega DR, Jensen GJ. 2016. Sporulation, bacterial cell envelopes and the origin of life. *Nat Rev Microbiol*. doi:10.1038/nrmicro.2016.85

Visick KL, Fuqua C. 2005. Decoding microbial chatter: Cell-cell communication in bacteriaJournal of Bacteriology. pp. 5507–5519. doi:10.1128/JB.187.16.5507-5519.2005

Wang Q, Mercogliano CP, Löwe J. 2011. A ferritin-based label for cellular electron cryotomography. *Structure*. doi:10.1016/j.str.2010.12.002

Webb CD, Graumann PL, Kahana JA, Teleman AA, Silver PA, Losick R. 1998. Use of time-lapse microscopy to visualize rapid movement of the replication origin region of the chromosome during the cell cycle in Bacillus subtilis. *Mol Microbiol*. doi:10.1046/j.1365-2958.1998.00808.x

Weiss GL, Kieninger AK, Maldener I, Forchhammer K, Pilhofer M. 2019. Structure and Function of a Bacterial Gap Junction Analog. *Cell*. doi:10.1016/j.cell.2019.05.055

Winey M, Meehl JB, O'Toole ET, Giddings TH. 2014. Conventional transmission electron microscopy. *Mol Biol Cell*. doi:10.1091/mbc.E12-12-0863

Wolff G, Hagen C, Grünewald K, Kaufmann R. 2016. Towards correlative super-resolution fluorescence and electron cryo-microscopy. *Biol Cell*. doi:10.1111/boc.201600008

Wu LJ, Errington J. 1997. Septal localization of the SpoIIIE chromosome partitioning protein in Bacillus subtilis. *EMBO J* **16**:2161–2169. doi:10.1093/emboj/16.8.2161

Wu LJ, Errington J. 1994. Bacillus subtilis spoIIIE protein required for DNA segregation during asymmetric cell division. *Science (80-)* **264**:572–575.

Zachs T, Medeiros JM, Schertel A, Weiss GL, Hugener J, Pilhofer M. 2019. Fully automated, sequential focused ion beam milling for cryo-electron tomography. *bioRxiv*. doi:10.1101/797514

Zhang P. 2013. Correlative cryo-electron tomography and optical microscopy of cells. *Curr Opin Struct Biol*. doi:10.1016/j.sbi.2013.07.017